RICE UNIVERSITY

# Role of mechanical interactions in self-organization behaviors of *Myxococcus xanthus* bacteria

by

**Rajesh Balagam**

A THESIS SUBMITTED
IN PARTIAL FULFILLMENT OF THE
REQUIREMENTS FOR THE DEGREE

**Doctor of Philosophy**

APPROVED, THESIS COMMITTEE:

Oleg A. Igoshin, Chair
Associate Professor of Bioengineering and
Centre for Theoretical Biological Physics

Herbert Levine
Professor of Bioengineering and Centre for
Theoretical Biological Physics

Lydia E. Kavraki
Professor of Electrical and Computer
Engineering

Houston, Texas

March, 2017

# Role of mechanical interactions in self-organization behaviors of *Myxococcus xanthus* bacteria

by

Rajesh Balagam

## Abstract

Coordinated cell movement and intercellular interactions are crucial for bacterial multicellularity and self-organization, and the mechanisms governing these processes are of active scientific interest. Individual cells interact with neighbors through various biochemical and mechanical interactions, but the role of mechanical interactions in coordination and self-organization of bacteria remains unclear. This work investigates the mechanisms underlying various multicellular patterns in *Myxococcus xanthus* bacteria, a model organism to study self-organization in bacteria, and the role of mechanical interactions in these self-organization behaviors using biophysical models of cell motility in an agent-based-simulation framework.

Using this framework, first I studied the mechanism of gliding cell motility in *M. xanthus* by discriminating motility behavior of biophysical model cells during physical cell collisions from two alternative cell motility models proposed in the literature. Comparing the model cell motility behavior with experimental cell collision behavior showed that gliding cell motility in *M. xanthus* requires strong cell-substrate interactions supporting one of the proposed models. New predictions from this model are independently verified in direct experimentation. Next, I investigated the mechanisms responsible for formation and alignment of *M. xanthus* cells in groups and their collective movement in circular and spiral patterns under starvation, by simulating intercellular interactions among a large number of model cells. Results from the simulations show that these collective cell behaviors in *M. xanthus* can be explained through mechanical and bio-

chemical interactions among cells and with the substrate. Finally, I investigated the mechanism for non-monotonic colony expansion behavior observed in *M. xanthus* motility mutants using the agent-based-simulation framework and analyzed individual cell motility behavior from experiments under similar conditions. Results from this work provide evidence that cell-stalling, a crucial assumption made by previous models to explain non-monotonic colony expansion, does not occur due to physical interactions and is not observed in experimental *M. xanthus* swarms.

Results from this thesis work show that many self-organization behaviors in *M. xanthus* can be explained by a combination of mechanical interactions among cells, between the cells and the substrate and biochemical signaling through physical cell-cell contacts. This work improves our understanding of mechanisms governing various self-organization behaviors displayed by *M. xanthus* bacteria and provides a general framework to study self-organization behaviors in other surface motile bacteria.

# Acknowledgments

I would like to express my thanks to all the people who have helped me and made this thesis research work possible. First, I would like to express my sincere gratitude to my research advisor Prof. Oleg Igoshin for giving me the opportunity to work with him and for his guidance through all my years at Rice. I am extremely thankful to him for allowing me to explore different ideas and for his patience in responding to my last-minute queries. I would also like to thank our collaborators Prof. Joshua Shaevitz - Princeton University, Prof. Heidi Kaplan - University of Texas - Houston medical school, Prof. Daniel Wall - University of Wyoming, and Prof. Herbert Levine - Center for Theoretical Biological Physics (CTBP) - Rice University and their group members. Without their contributions and suggestions, many of the results presented here were not possible.

I would like to thank all my thesis committee members for their time and support. I would also like to thank all the current and former members of Prof. Igoshin's group, especially Dr. Abhinav Tiwari, Dr. Pintu Patra, and Dr. Jatin Narula for their many helpful discussions. I am also thankful to my master's research advisor Prof. Narendra Dixit (Indian Institute of Science) for encouraging me to apply to graduate school and for his support. I would like to thank all the Rice-CTBP members for many stimulating conversations. I would like to thank all the members of administrative staff at Rice Bioengineering department and Rice-CTBP for their support. Finally, I would like to thank all our funding sources from National Science Foundation, Rice-CTBP, and Ken-Kennedy Institute at Rice.

# Contents

# List of Figures

# List of Tables

# Chapter 1

# Introduction

## 1.1 Collective behavior and self-organization in biological systems

Collective behavior is a natural phenomenon in which individuals of the same kind work together. Collective behaviors are observed in many living organisms e.g. a flock of birds, fish schools, insect swarms, and a herd of animals [1]. Sometimes collective behavior results in self-organization in the group where a global order emerges from seemingly chaotic individual interactions [2, 3]. Biological systems use self-organization as an advantageous strategy to gather food and to survive in adverse environments [3, 4]. Self-organization is a complex dynamic phenomenon that requires individual's ability to sense and adapt to their surrounding environmental cues [5]. The mechanisms of this dynamic organization have been widely studied in vertebrates [2]. However, self-organization is not limited to higher organisms and is also observed in simple life forms such as bacteria [6, 7].

### 1.1.1 Self-organization behaviors in bacteria

Bacterial cells self-organize into a variety of multi-cellular patterns during formation and expansion of biofilms [8]. Biofilms are bacterial communities that are attached to a surface and are generally surrounded by slime (a polymeric material secreted by cells). Like in higher organisms, collective behavior through biofilms allows bacterial cells to colonize nutrient rich areas and results in cooperative benefits [9, 10, 11]. Self-organization in bacterial cells often results from coordinated cell motility that requires cells to sense, integrate and respond to a variety of intercellular and environmental signals [6, 7]. However, being unicellular organisms, bacteria lack sophisticated communication mechanisms utilized by higher organisms and gener-

ally interact and coordinate with their neighbors through biochemical signaling and mechanical interactions [12, 13, 14].

### 1.1.2 Biochemical signaling in bacterial collective behaviors

Bacterial species are known to secrete various chemical/signaling molecules from their surface in response to change in local environment (e.g. nutrient availability, adverse conditions - heat, chemical, mechanical stress). These signaling molecules stay on the cell surface and/or diffuse into surrounding environment. Other cells in the community recognize these biochemical signals and respond by changing their behavior (move towards the nutrient source, start gene expressions that protect from stress, etc.). Quorum sensing is one of the major mechanisms through which bacteria exhibit collect behaviors [15]. Here cells exhibit a collective response to a self-produced chemical signal in a density-dependent manner, i.e. collective response is activated only when the concentration of the chemical reaches a certain threshold [12, 13, 16, 17]. Quorum sensing is oberved in multiple bacterial species in different collective cell behaviors ranging from bioluminescence in *V. fischeri*, opportunistic host infections in pathogenic bacteria *P. aeruginosa, A. tumefaciens*, and competence in *S. pneumonia, B. subtilis* [13, 18]. Chemotaxis is another mechanism that was widely studied in the context of bacterial collective-behaviors. Here individual cells sense and respond to a chemical attractant or repellent by changing their motility pattern towards or away from the chemical source. When cells respond to chemicals produced by other cells in the community collective behaviors emerge. *E. coli, S. typhimurium* has been shown to form cell aggregates and patterns using this mechanism [19, 20, 21]. Quorum sensing and chemotaxis utilize diffusible chemical signals resulting in short to long range communication in bacterial cell community. On the opposite extreme, direct contact signaling between individual cells that synchronizes cell behaviors is a very-short-range signaling in bacteria.One such example is the exchange of C-signal(contact) among cells during *M. xanthus* development that works through cell-cell contacts and promotes coordinated cell movement that results in cell streams/chains [12].

### 1.1.3 Mechanical forces shape bacterial self-organization

Most studies on bacterial self-organization focus on cell growth and intercellular chemical signaling in liquid cultures or on solid surfaces under laboratory conditions. However, most bacteria in nature survive inside biofilms attached to surfaces and are subject to various physical forces. Recent studies have shown that mechanical forces also play a significant role in bacterial collective behaviors [22] and their self-organization in biofilms [14, 23, 24]. At individual cell level *C. crescentus, P. aeruginosa, E. coli* bacteria are shown to be adapting to their local mechanical environment either by changing their gene expressions or harnessing the local mechanical forces to their advantage that maximize their adhesion and subsequent colonization on surfaces [25, 26, 27, 28, 29]. When transferred from liquid medium to a solid surface some bacterial cells observed to be differentiating into specialized swarmer cells that are hyperflagellated to maximize their collective movement on solid surfaces [30, 31, 32, 33]. Mechanical stresses generated during biofilm expansion modify the internal cellular organization and result in changes to subsequent global biofilm morphology. Wrinkled structures produced on *B. subtilis* biofilms are a direct consequence of buckling of biofilm in confined spaces [34]. Local cell death inside biofilm also generates mechanical stresses from the surrounding biofilm material leading to a local collapse of the biofilm and wrinkling pattern on the surface of *B. subtilis* biofilms [35]. Mechanical stresses produced by fluid flow around the biofilms deform their structure and influence their overall morphology. Streamer structures (long filamentous biofilms) formed by *P. aeruginosa, S. aureus* at sharp curvatures in flow fields (e.g. bends in pipes) are shown to be mainly due to the positive feedback between the decrease in flow with increase in biofilm mass [36, 37].

Many genes and proteins that are involved in the bacterial signaling pathways have been identified [8], yet how these signaling pathways lead to self-organization of cells in many bacterial systems is still unknown. Furthermore, the influence of mechanical forces on bacterial self-organization is discovered only recenlty[14]. Understanding the role of mechanical interactions and the combination of chemical and mechanical factors in shaping bacterial collec-

tive behaviors and their self-organization is of current scientific interest. Additionally, many pathogenic bacteria evade antibiotic treatments and immune response by forming a surface coat in their biofilms [38]. Disruption of these biofilms requires breaking the underlying cell-cell communication and coordination mechanisms. Thus, we need to understand the mechanisms that result in self-organization in bacterial biofilms. To this end, we study the self-organization mechanisms in a model bacterium *Myxococcus xanthus* ("Myxo") [39, 40].

## 1.2 *Myxococcus xanthus* as a model organism for bacterial self-organization

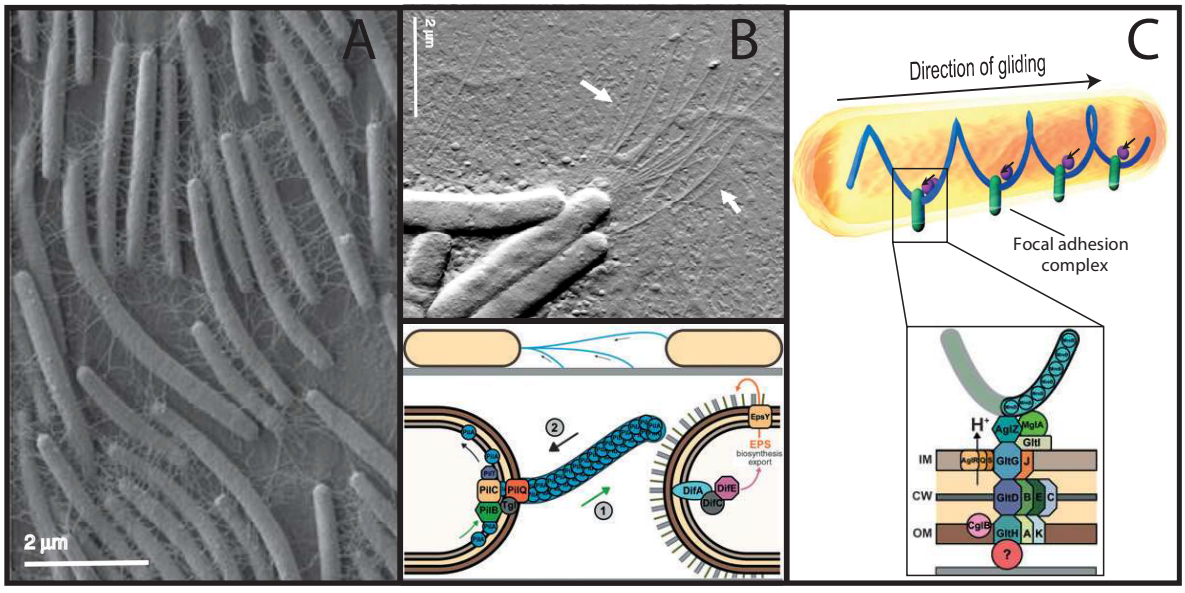


Figure 1.1: *M. xanthus* cells on a surface and its motility systems. (A) Scanning electron microscopy image showing multiple *M. xanthus* cells on a solid surface. The web-like material between cells is the dried extracellular matrix material secreted by cells. (B) (Top panel) Atomic force microscopy image showing type IV pili at the leading poles of individual *M. xanthus* cells. (Bottom panel) Schematic showing S-motility through extension and retraction of pili at cell poles and different proteins involved in S-motility. (C) Schematic showing gliding motility through proposed focal-adhesion-complex model and various proteins involved in gliding motility. (Adapted from [41, 42, 43] with permission)

*M. xanthus* is a rod-shaped ($\approx$ 5 - 7 µm in length and 0.5 µm in diameter), gram-negative, soil bacterium that belongs to the delta group of proteobacteria family [40, 46, 47] (Figure 1.1). *M. xanthus* is a social bacterium i.e. it prefers to live in groups. *M. xanthus* cells collectively

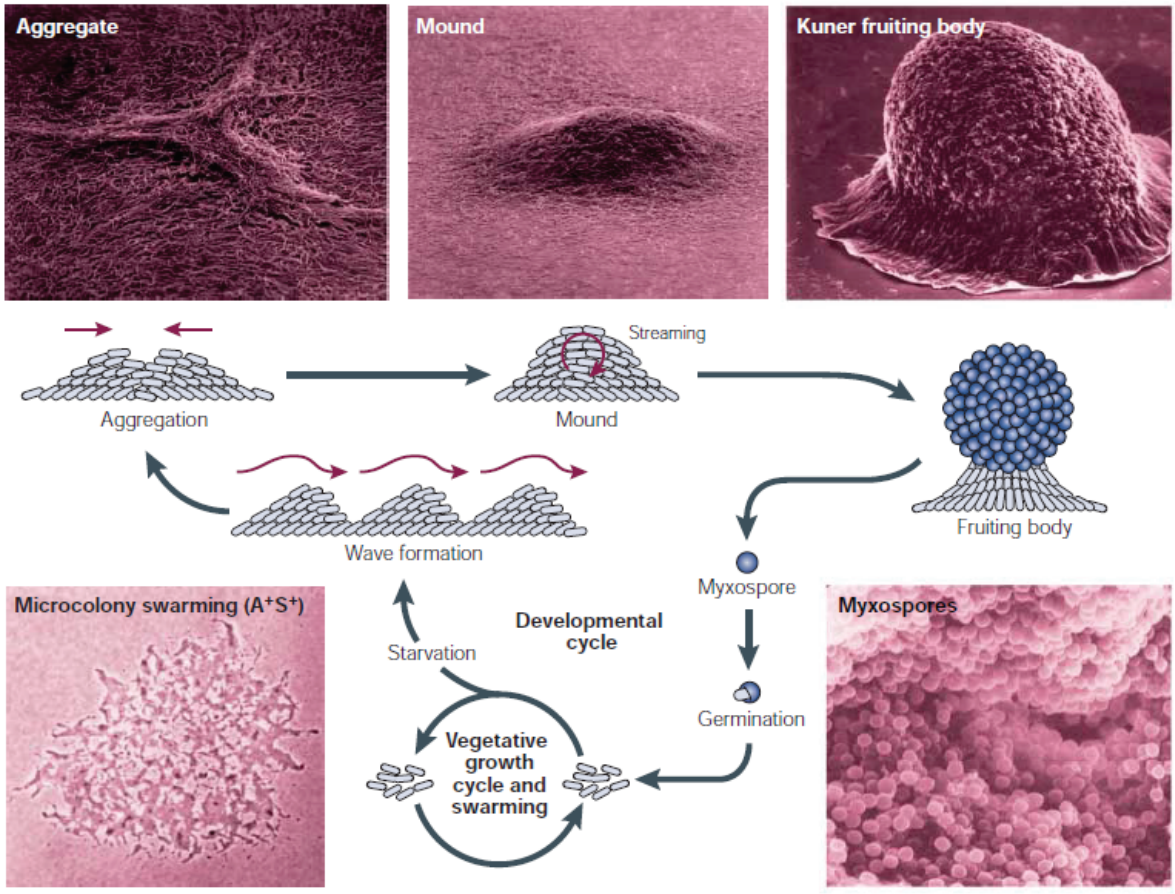


Figure 1.2: *M. xanthus* life cycle showing various multi-cellular structures formed at different stages of its lifecycle. Under nutrient-rich conditions, rod-shaped myxo cells follow a vegetative growth cycle where they divide and collectively swarm. In the natural environment, myxo cells predate on other bacteria by secreting enzymes that lyse other bacterial cells and absorbing the resulting nutrients. At high-density myxo cells, when in contact with these prey cells, exhibit traveling waves structures (predatory ripples) that maximize their predation efficiency [44]. Under starvation *M. xanthus* cells undergo a developmental cycle that spans multiple stages involving traveling waves (developmental ripples), small cell aggregates and fruiting bodies containing $\approx 10^5$ cells. Cells inside fruiting bodies transform into spherical, environmentally resistant myxospores. When nutrients become available again these spores germinate and start the vegetative cycle. (Figure reproduced from [45] with permission)

predate (feed) on other bacteria by forming groups called swarms. During predation, they secrete enzymes into their environment that lyse other bacteria and absorb the resultant nutrient molecules. The efficiency of their predation is directly related to their collective movement to prey-rich areas [44]. During its life cycle, *M. xanthus* cells exhibit various self-organization behaviors depending on surrounding nutrient levels (Fig. 1.2). Due to its capacity to form com-

plex multi-cellular structures through self-organization *M. xanthus* is considered as a model organism for studying bacterial self-organization. Its biology and self-organization behaviors are extensively studied.

### 1.2.1 Self-organization behaviors in *M. xanthus*

- Under nutrient-rich conditions, *M. xanthus* cells swarm (cooperative cell movement in organized groups of cells) and expand outward from the initial cell colony [45, 48, 49, 50].
- Under high cell density conditions and when in contact with prey, *M. xanthus* cells exhibit coordinated rhythmic movement that resembles traveling waves (called predatory ripples) [39, 51, 52].
- Under nutrient starvation, *M. xanthus* cells undergo a developmental program that proceeds through various stages of multi-cellular patterns containing traveling high cell density waves (called developmental ripples, [53, 54, 55]), cell aggregates and finally form spore-filled fruiting bodies (aggregates containing more than $10^5$ cells) [56, 57, 39, 58].

Formation of these multi-cellular structures requires coordinated cell motility and inter-cell communication [45, 44]. Cell machinery responsible for motility and communication in *M. xanthus* has been studied extensively in the past [45, 39].

### 1.2.2 *M. xanthus* motility

*M. xanthus* cells are non-motile in liquid medium as they lack flagella (typical motility organelles for bacteria). *M. xanthus* cells move on solid surfaces using gliding motility - a smooth movement without any visible change in cell shape [45]. Two different and independent motility systems were discovered in *M. xanthus* [59, 60, 39, 61]: Adventurous (A) motility - responsible for individual cell movement and Social (S) motility - responsible for group cell movement. These two motility systems act independently in *M. xanthus* cells i.e. deletion of either set of

motility genes does not stop cell movement completely [60, 45]. However, the two motility systems are shown to work synergistically for *M. xanthus* cell collective movement [60, 62, 63] and provide a selective advantage to cells depending on substrate hardness [64].

**Adventurous motility**

Adventurous (A) motility powers the individual *M. xanthus* cell movement on solid surfaces and it does not utilize any visible external organelles. The exact mechanism of A-motility appears to be somewhat unique and is still under investigation [41, 65, 66, 67, 68]. Genetic studies identified many proteins involved in *M. xanthus* A-motility and based on the location and distribution of these proteins multiple mechanisms were proposed for A-motility [69, 70, 71]. Earlier studies argued that A-motility is powered by the secretion and subsequent expansion of exopolysaccharide material (slime) from the trailing end of the cell that pushes cell forward [71]. Recent studies show that slime secretion is not localized to cell poles [72, 73] and the proteins involved in A-motility appear to be distributed along the cell length [69, 74, 75]. Based on recent experimental evidence two alternative mechanisms for gliding/A-motility[1] are proposed: Helical-rotor-model (HRM) [69] and Focal-adhesion-model (FAM) [70, 74] (Fig. 1.1C). In both the mechanisms A-motility motor proteins move along helical cytoskeleton tracks and interact with the underlying substrate. However, the nature of this interaction differs in these two models: In HRM motor proteins interact with the substrate through frictional forces generated by surface undulations; in FAM motor proteins interact with the substrate through focal adhesion protein complexes that span the cell membrane and attach to substrate through adhesive bonds. Neither mechanism was completely proven to be correct for *M. xanthus* motility. Additionally, the proteins involved in A-motility also regulate other cellular processes [43], and this complicates the identification of their function in cell motility.

[1] Smooth movement of cells along their long-axis on solid surfaces without using any visible external organelles is referred as gliding motility in other bacteria[76]. Here, we use A-motility and gliding motility interchangeably.

**Social motility**

Social (S) motility powers the movement of *M. xanthus* cells in groups i.e. *M. xanthus* mutants containing only S-motility genes remain non-motile as individual cells but are capable of moving in cell groups. During S-motility *M. xanthus* cells use type IV pili (concentrated on the leading pole of the cell, Fig. 1.1B) to bind to exopolysaccharides material on neighbor cells surface or on the substrate and move forward by retracting the pili inward [77, 78, 79, 80, 81]. During a cell reversal (described next) pili at the leading pole retract inward and new pili extend from the other pole. The mechanism of S-motility is better understood as it is analogous to twitching motility in other bacteria and many proteins involved in S-motility have been identified [41]. Though individual cell movement through S-motility is well studied, however, it is currently not known how collective cell motility is achieved in S-motility particularly at a colony edge where no cells are present in front of the edge cells [82, 63, 83].

**Periodic reversing of travel direction**

Wild-type *M. xanthus* cells periodically reverse their direction (reversal period $\approx$ 6-10 min) by switching the roles of leading and lagging poles [39]. Cell reversals require regulation of both A and S motility systems and are controlled by *frz*A-G (a set of seven genes) [39, 84, 85]. Though the functions of the individual Frz proteins are identified, the mechanism by which Frz pathway regulates the cell motility is currently unknown [39]. Deletion of individual *frz* genes results in hyper or hypo reversal mutants [39, 84, 86]. *M. xanthus* cells also observed to be regulating their reversal periods based on surrounding nutrient conditions [45] and in the presence of chemo-attractant/repellents [39, 87]. The presence of Frz system genes are shown to be essential for many self-organization behaviors of *M. xanthus* [39, 88, 53, 89, 85], but the exact the role *frz* genes in these multi-cellular behaviors is not completely established.

**Slime-trail-following**

*M. xanthus* cells secrete slime from their surface that is deposited on the underlying substrate as long trails during cell movement [90]. It is observed that *M. xanthus* cells tend to follow their own trails after a reversal and when in contact with slime trails deposited by others, cells can reorient and follow these trails[91]. However, the exact mechanism that allows *M. xanthus* cells to follow slime-trails has not been established.

### 1.2.3 Intercellular signaling in *M. xanthus*

During cell motility, *M. xanthus* cells exchange various chemical signals with their neighbors [92, 93] by contact or by diffusion in the immediate neighborhood (short-range signal). C-signal (Contact) is exchanged through end-to-end contacts on cell surfaces [39] and is known to increase the reversal frequency of cells during developmental rippling phase [94]. By contrast, cells that are aligned parallel exchange side-to-side signal (through FrzCD clusters) that results in a reversal in one of the cells [53]. This signal is mainly observed during predatory rippling. During aggregation phase, cells exchange A-signal [95] that causes cells to initiate developmental program in a density dependent manner i.e. similar to quorum sensing mechanism. Many of these signals directly affect cell motility during self-organization of cells into multicellular structures [96]. But how these signals are activated in response to specific environmental conditions and result in coordinated cell movement is unknown.

## 1.3 Modeling self-organization in *M. xanthus* and other biological systems

Self-organization is an emergent property of the system and thus cannot be explained by identification of individual components. This requires understanding the interactions among individual components in both spatial and temporal coordinates. Experimental approaches are instrumental in identifying the individual components of the system. However, modeling approaches can

complement experiments in identifying the interactions that result in self-organization in *M. xanthus*. Earlier modeling work by Igoshin et al. on *M. xanthus* self-organization used mean field models based on partial differential equations [97, 88, 98]. These models mainly addressed the formation of traveling waves and aggregation patterns during development. They used interactions resulting from cell-cell contact signaling, change in cell reversals based on cell density, random noise in cell motility, and the existence of refractory period (a brief time interval after a reversal where the cell is unresponsive to further signaling) to study the self-organization patterns. But at cell densities relevant to the studied phenomena mean field assumptions in these cell systems may not be appropriate. Since then several studies have used agent-based modeling and cellular automata models to investigate the self-organization behavior in *M. xanthus* [99, 44, 73, 100, 101, 102, 103, 89, 104, 105, 106]. These models mainly studied the behavior of cells in swarms, the formation of rippling patterns and aggregate formation. Many of these studies were successful in explaining the observed cell patterns under specific experimental conditions. But many questions still remain unanswered [107]. Further, most of these studies used phenomenological approaches for simulating intercellular interactions and not considered mechanical interactions that are shown to play a significant role in self-organization behaviors of biological systems.

### 1.3.1 Modeling studies on physical interactions driving self-organization in biological systems

Multiple modeling and experimental studies have shown that physical characteristics and mechanical interactions play a significant role in collective and self-organization behaviors of biological systems at small length scales. These studies span a wide variety of areas ranging from proteins, microtubules [108, 109, 110, 111], bacterial and other eukaryotic cells [112, 113, 114, 24]. These studies considered various mechanical aspectes e.g. physical features of the cells and interactions among cells (shape of cells [115], alignment with neighbors, adhesive interactions among cells [116], cell density or confinement [117, 118]) and with their

environment (viscosity and surface tension of surrounding fluid, hardness and roughness of the underlying substrate, geometry) to investigate their effect on overall cell organization [119, 120, 121, 122, 123, 124, 125, 126, 127]. Studies in the field of active matter physics are instrumental in elucidating many self-organization behaviors governed by physical interactions [128, 129, 130, 131, 132, 133, 134, 135, 136]. Individual-cell-based models or agent-based models are particularly benefical in simulating and understanding [137, 138] intercellular interactions that lead to emergent patterns. These studies provide basis and motivation for understanding the role of physical interactions in bacterial self-organization.

## 1.4 Specific research objectives

**Investigating self-organization behaviors in *M. xanthus* using biophysical cell motility models and agent-based-simulation framework**

My research on self-organization behaviors in *M. xanthus* relies on a reverse engineering approach that uses a combination of computational models, image processing techniques, and experimental testing (performed by our collaborators). The cornerstone of the approach is a biophysically realistic model of individual cell motility which is then extended to study interactions in small groups of cells and finally, to study the self-organization in large cell groups. A brief of description of the biophysical cell motility model for *M. xanthus*, other cell processes involved in computational framework and specific research objectives are described below.

In this thesis work, we [2] investigated self-organization mechanisms in *M. xanthus* bacteria by constructing biophysical models of *M. xanthus* cell and using these model cells as individual agents in an agent-based-simulation framework [139, 140, 141] to study intercellular interactions that result in observed multi-cellular patterns. Each model cell/agent consists of multiple

[2] Due to interdisciplinary nature of this work combining computational models and experimental testing (performed by our collaborators), in general 'we' is used to signify that research work presented here is the product of discussions with collaborators and colleagues. However, all the theoretical, computational work and scientific analysis presented in this thesis are performed by me. Contributions from others are appropriately acknowledged at such places where presented.

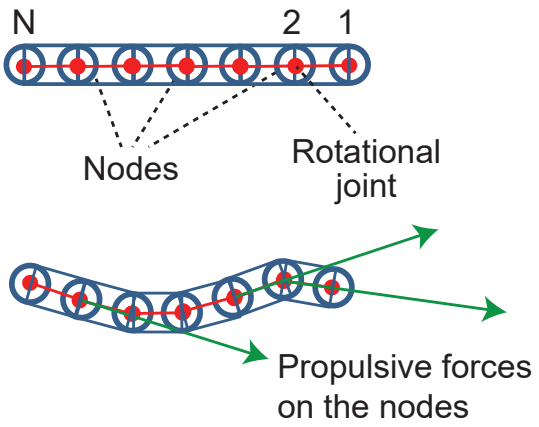


Figure 1.3: Schematic of biophysical cell motility model for a single *M. xanthus* cell in simulation represented as a connected string of nodes with rotational joints between neighbor nodes. Cell moves forward due to propulsive forces acting on nodes tangential to cell nodes in current cell travel direction.

segments enabling a realistic mechanical model of a single *M. xanthus* cell. We represent each agent as a connected string of nodes (1,2,...,N, see Fig. 1.3). Neighbor nodes are joined by rotational joints consisting of linear and angular springs. Linear springs between nodes resist elongation or compression to keep the agent length constant. Angular springs resist bending of the agent from straight line position and thus simulate elastic nature of cell bending. For simplicity, we only implement only gliding (A) motility of *M. xanthus* cells in our model. For this, we use the distributed force generation along cell length through multiple motor protein complexes as indicated by recent models [69, 70, 74, 73]. Thus, agents move forward through propulsion forces ($\boldsymbol{F}_p$) acting on nodes tangential to the agent length towards next node in the current agent travel direction. Agents periodically reverse their travel direction by reversing the order of nodes in the model $(N, ..., 2, 1)$

The direction of the propulsive force on the head node is influenced by other contributing factors: *M. xanthus* cells are known to follow slime-trails of other cells (slime-trail-following). We model this by reorienting a fraction of propulsive force on head node in the direction of the underlying slime-trail left by other agents. *M. xanthus* cells also exhibit a random change of their travel direction (random turning noise). We model this by reorienting propulsive force on the head node randomly either clockwise or counter clockwise for a short time interval.

Viscous drag forces arising from the surrounding fluid act on nodes opposing their motion and are proportional to the node velocities. Adhesive attachments (modeled as linear springs) with the underlying substrate at nodes resist lateral displacement of nodes during collisions. These attachments represent the adhesion complexes in focal adhesion model of gliding motility in *M. xanthus* [74]. At low densities, *M. xanthus* cells are known to move in a monolayer. Therefore, collisions among agents are resolved by applying appropriate forces on nodes that keep agents from overlapping. Using this biophysical cell motility model including various cell processes that affect cell motility we simulate interactions among a large number of cells moving on a 2-D surface and study their collective and self-organization behaviors. Specific implementation details of biophysical cell motility model and other cell processes are presented in Appendix A.

In this thesis work, I combine approaches of agent-based-simulation that gives the flexibility to include complex intercellular interactions and biophysical model of cell motility that accurately describes the cell motility on a surface. Using the above cell motility model and agent-based-simulation framework that simulates intercellular interactions, I have investigated mechanisms for individual cell motility in *M. xanthus* and other self-organization behaviors in *M. xanthus*. Specific research objectives investigated in this work are as follows:

### 1.4.1 Biophysical mechanism of gliding-motility in individual *M. xanthus* cells

Though mulitple models for gliding cell motility are proposed in literature, the mechanism of gliding motility (A-motility) in *M. xanthus* is not completely understood [43]. Recent experiments suggested two possible mechanisms for cell motility which differ in the way a cell interacts with underlying substrate [70, 69]. We hypothesize that the motility behavior of cells during mechanical interactions between cells will be affected by the nature of cell-substrate interactions. Thus, we will simulate these interactions (e.g. cell-cell collisions) using our biophysical model of the cell for the two mechanisms of cell motility to discriminate model cell motility behavior from the two mechanisms. Comparing the model cell behavior with experi-

ments will allow us to identify the mechanism underlying *M. xanthus* gliding cell motility.

### 1.4.2 Mechanism for collective alignment of cell clusters during swarming

During colony growth at low cell density, *M. xanthus* cells form aligned cell clusters, cell groups containing hundreds of cells oriented in the same direction. These clusters are important in formation of other multi-cellular structures later at high cell densities. The process by which these clusters form is presently unknown. Cell alignment can be a direct consequence of pure mechanical interactions between cells [142, 143]. However, a recent study questioned the validity of this mechanism [105]. We hypothesize that the mechanical interactions between cells combined with cells following slime trails (a polymeric material secreted by cells) cause the cells to align thereby forming aligned clusters. We investigate this mechanism of cell alignment using our biophysical model of cell motility in our agent-based-simulation framework. We will use the model to simulate the interactions among cells in initial stages of the colony growth. Comparing the cell behavior in low-density clusters in experiments with model behavior under similar conditions will allow us to identify the mechanism governing aligned cell cluster formation.

### 1.4.3 Mechanism for circular cell aggregate formation in developmental *M. xanthus* swarms

Developmental *M. xanthus* cells in swarms (cell groups) occasionally aggregate and self-organize into transient circular or spiral shaped multi-cellular structures - circular cell aggregates. Recent experiments with *M. xanthus* cells that over-express TraA/B protein formed multiple stable circular cell aggregates during development[144]. At present we do not know the mechanism underlying this circular movement of cells and why over-expression of TraA/B protein stabilizes these cell aggregates. We hypothesize that circular/spiral movement of cells is a result of confined movement and self-closing of cell streams (cells following others like a chain) that are normally observed during *M. xanthus* development. We investigate this mechanism

for circular cell movement using our biophysical cell agent-based-simulation framework under slime-trail-following by cells and identify the cell processes that result in stable circular cell aggregates. From these results we hypothesize the specific cell processes directly affected by TraA/B over-expression and investigate whether these changes results in multiple stable circular cell aggregates in our simulation as observed in experiments.

### 1.4.4 Collective expansion dynamics of *M. xanthus* swarms

Under vegetative growth conditions, *M. xanthus* cells in a colony divide and collectively move in swarms and the cell colony expands at a constant rate [83]. Interestingly, the swarm expansion rates of different *M. xanthus* mutants found to be varying non-monotonically with the cell reversal period [103]. Specifically, swarm expansion rate for mutants that reverse frequently than wild-type cells increased with increase in cell reversal period. But swarm expansion rate for mutants that reverse less frequently than wild-type cells decreased with increase in cell reversal period suggesting that wild-type *M. xanthus* cell reversal period is optimized for maximum swarming efficiency. Currently we do not know the exact mechanism resulting in this non-monotonic swarm-expansion behavior of *M. xanthus* cells. Some studies in literature suggested that decrease cell movement in high cell density regions results in reduced swarm expansion [102, 103]. We investigate the expansion dynamics of *M. xanthus* swarms and mechanism of cell-stalling in high cell density regions using a combination of agent-based-simulation framework and continuum models. Additionally, we analyze cell motility behavior from data collected by tracking individual *M. xanthus* cells in swarms from experiments to identify the mechanisms that explain the decrease in swarm expansion for cells with high-reversal periods.

# Chapter 2

# Mechanism of gliding motility in *M. xanthus* bacteria


**Abstract**

*Myxococcus xanthus* is a model organism for studying bacterial social behaviors due to its ability to form complex multicellular structures. Knowledge of *M. xanthus* surface gliding motility and the mechanisms that coordinate it are critically important for our understanding of collective cell behaviors. Although the mechanism of gliding motility is still under investigation, recent experiments suggest that there are two possible mechanisms underlying force production for cell motility: the focal adhesion mechanism and the helical rotor mechanism which differ in the biophysics of the cell – substrate interactions. Whereas the focal adhesion model predicts an elastic coupling, the helical rotor model predicts a viscous coupling. Using a combination of computational modeling, imaging, and force microscopy, we find evidence for elastic coupling in support of the focal adhesion model. Using a biophysical model of the *M. xanthus* cell, we investigated how the mechanical interactions between cells are affected by interactions with the substrate. Comparison of modeling results with experimental data for cell-cell collision events pointed to a strong, elastic attachment between the cell and substrate. These results are robust to variations in the mechanical and geometrical parameters of the model. We then directly measured the motor-substrate coupling by monitoring the motion of optically trapped beads and find that motor velocity decreases exponentially with opposing load. At high loads, motor velocity approaches zero velocity asymptotically and motors remain bound to beads indicating a strong, elastic attachment[1].


[1]Research work shown in this chapter is already published[145]. Text presented here is from the published manuscript. Contributions from our experimental collaborators are appropriately acknowledged where presented.

## 2.1 Introduction

*Myxococcus xanthus* is a predatory soil bacterium that has been widely used as a model organism for studies of bacterial social behaviors [45]. Under different environmental conditions *M. xanthus* cells display a range of complex multi-cellular behaviors, including groups of cells moving together (often referred to as swarms), periodic bands of high cell density traveling waves (termed ripples), and aggregates of more than $10^5$ cells containing environmentally-resistant myxospores (termed fruiting bodies) [39]. Formation of these complex self-organized patterns requires coordination and collective motility among the cells. The biophysical mechanisms underlying the cell motility and intercellular interactions that generate these collective behaviors are still not completely understood.

*M. xanthus* cell movement is limited to translocation on solid surfaces using two different flagella-independent motility systems[60]. Gliding motility, previously termed adventurous (A) motility, is defined as active surface translocation along the long cell axis without the aid of flagella or pili and is responsible for individual cell movement. Twitching motility, previously termed social (S) motility, appears similar to gliding motility, but is limited to cells within at least a cell length of another cell and is known to be powered by type IV pili extension and retraction [78]. The biophysical mechanism of gliding motility in *M. xanthus* and other bacteria is the subject of active research.

Earlier studies on the mechanism of gliding motility hypothesized that the exopolysaccharide (EPS) slime secretion at the cell's lagging pole and the expansion of slime due to hydration was responsible for the motility [146, 90, 69]. However, subsequent experimental studies [72, 73], indicated that force generation in gliding motility is likely to be distributed along the cell length.

Recently, an alternative view of the gliding motility mechanism has emerged. Using fluorescently tagged proteins recent experiments identified a few components of the machinery responsible for the distributed force-generation: gliding motility regulatory protein (AglZ) [74]

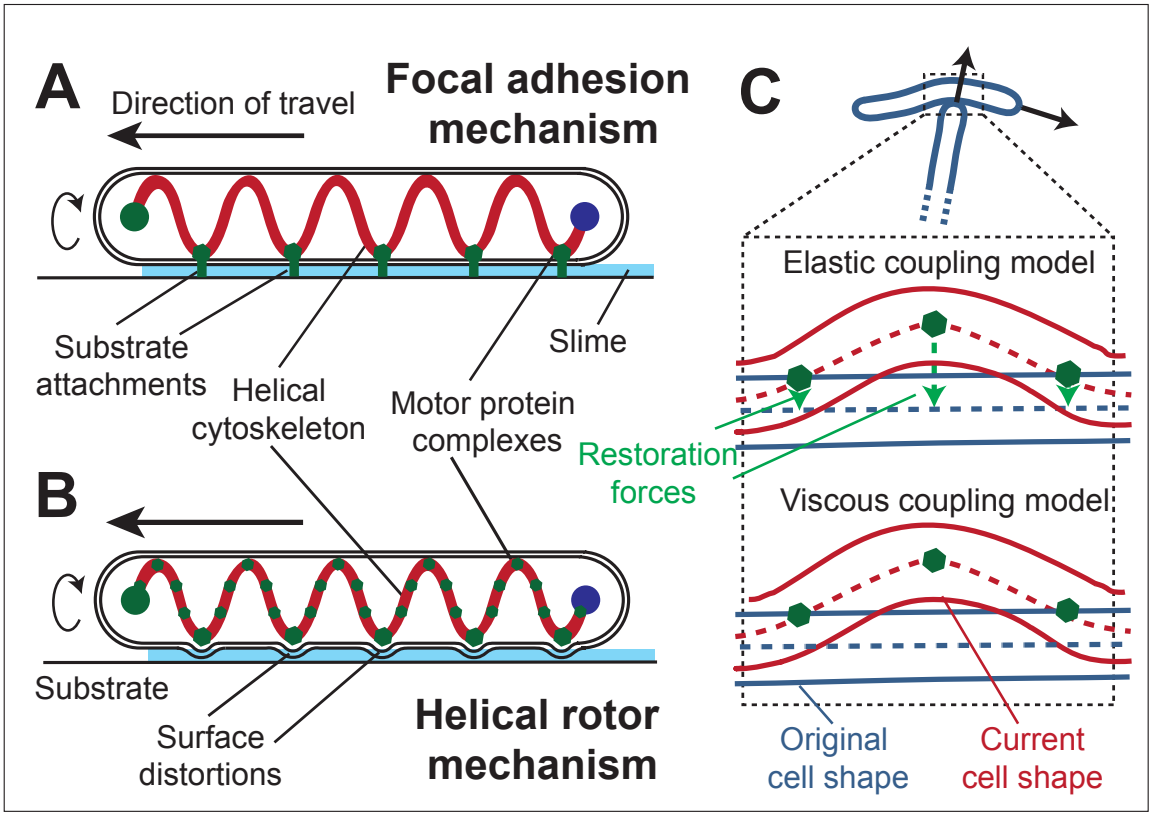


Figure 2.1: Schematics of alternative mechanisms of gliding motility and their representation in biophysical models of the *M. xanthus* cell. (A) Focal adhesion mechanism (FAM) - Multi-protein complexes (green bars) spanning from the cytoplasm to the outside of the cell attach to the underlying substrate at specific points. Cells move forward as a result of the force generated by the components of these complexes against cytoskeleton (B) Helical rotor mechanism (HRM) - Motor proteins (green dots) tracking on a helical cytoskeleton create distortions in cell wall. These distortions generate drag forces between the substrate and the cell surface and result in cell movement. (C) Distinctions in cell-substrate interactions for the two alternative models of gliding motility. In the elastic coupling model during a cell-cell collision, a restoration force acts on the cell at the cell-substrate interaction points (green dots) in the direction perpendicular to cell axis. No such force exists in the viscous coupling model.

and motor proteins (AglRQS) [70]. These studies showed clustering of these proteins at regular intervals along the cell length. These clusters appear to form at the cell's leading pole and disperse at the lagging pole, while remaining stationary with respect to the substrate during cell movement. Further, depolymerization of the cell cytoskeleton elements (MreB) dispersed these clusters and inhibited the gliding motility [70]. Based on the above observations, a focal adhesion mechanism (FAM) of gliding motility was proposed [74, 70] (Fig. 2.1A). The

mechanism hypothesizes that intracellular motor proteins moving on helical cytoskeletal filaments are somehow connected to the focal adhesion complexes attached to a substrate. The cell movement is therefore generated by motors pushing against these focal adhesion complexes. However, it is not clear which molecules adhere cells to the substrate and how their connection to the motor complex is able to move through the peptidoglycan of cell wall.

Another study observed that AgmU, a gliding motility protein, is part of a multi-protein complex that spans cell's inner membrane and periplasm [147]. Additionally, it was found that AgmU decorates a looped continuous helix that rotates as the cell moves forward [69]. It was shown that rotation of the helix stopped when MreB cytoskeletal filaments were depolymerized [69]. The authors also observed that a periodic distortion of cell wall that is consistent with periodicity of the MreB helices. Based on these observations, a helical rotor mechanism (HRM) [69, 43] (Fig. 2.1B) of gliding motility was proposed. In this mechanism motor proteins (AglR) [148] distort cell surface by interacting with the gliding motility proteins (AglZ, AgmU) in protein clusters and create drag forces between cell surface and substrate. These drag forces propel the cell forward.

Even though these studies provide ample evidence for both FAM and HRM mechanisms of gliding motility, neither mechanism has been conclusively proven or eliminated. We note that the major biophysical distinction between the mechanisms is in the nature of cell-substrate interactions – elastic force coupling in FAM vs. viscous drag coupling in HRM. Hence, by studying the mechanical interactions of motile cells it may be possible to distinguish between the two mechanisms of gliding motility. We tested the effect of mechanical forces on motility in two ways: (i) by examining the outcome of physical collisions between moving cells, and (ii) by probing the effect of applied load to the motion of individual motor complexes.

We hypothesize that the outcomes of mechanical collisions between a pair of cells will be different in the two models of motility because of the differences of the nature of cell-substrate interaction (see Fig. 2.1C). Specifically, during a cell-cell collision FAM-based cell motility would offer high resistance to the cell displacement because of the adhesive attachment be-

tween the cell and substrate. In contrast, HRM-based cell motility would result in a larger cell displacement, as the resistance due solely to viscous interactions would be weak.

To test this hypothesis, we built a computational model (see Appendix A for details) that represents the biophysical characteristics of *M. xanthus* cells and used it to investigate how the outcomes of cell-cell collisions depend on the gliding motility mechanism. Since the individual components and their interactions are not completely known at present, we simplified the two mechanisms of gliding motility in our model to focus exclusively on their cell-substrate interactions. As such we employed the viscous coupling model (VCM), which is similar the HRM and the elastic coupling model (ECM), which is similar to the FAM. We analyzed the modeling results for both mechanisms of cell - substrate interactions and compared them with quantified experimental data on isolated cell-cell collisions. Furthermore, we investigated the robustness of our results to variations in mechanical and geometrical parameters of the collision events.

As an additional test of the coupling of motors to the substrate, we used optically trapped beads to directly test the mechanics of motor coupling and the effect of load on motor movement. While the details of how applied hindering load affects the speed of the gliding motors themselves remains unknown, the two models of motility make qualitatively different predictions near the motor stall force due to the difference in coupling. Regardless of the shape of the motor force-velocity relationship, as the force is increased to high enough levels, the VCM predicts that beads should cease motion at the stall force and move backwards for higher loads. In contrast, the ECM predicts that applied force should stop bead motion even for loads well above stall.

## 2.2 Results

### 2.2.1 Distinct cell-cell collision behaviors of two alternative gliding motility models

[2]Refer to [145] for supplemental movies.

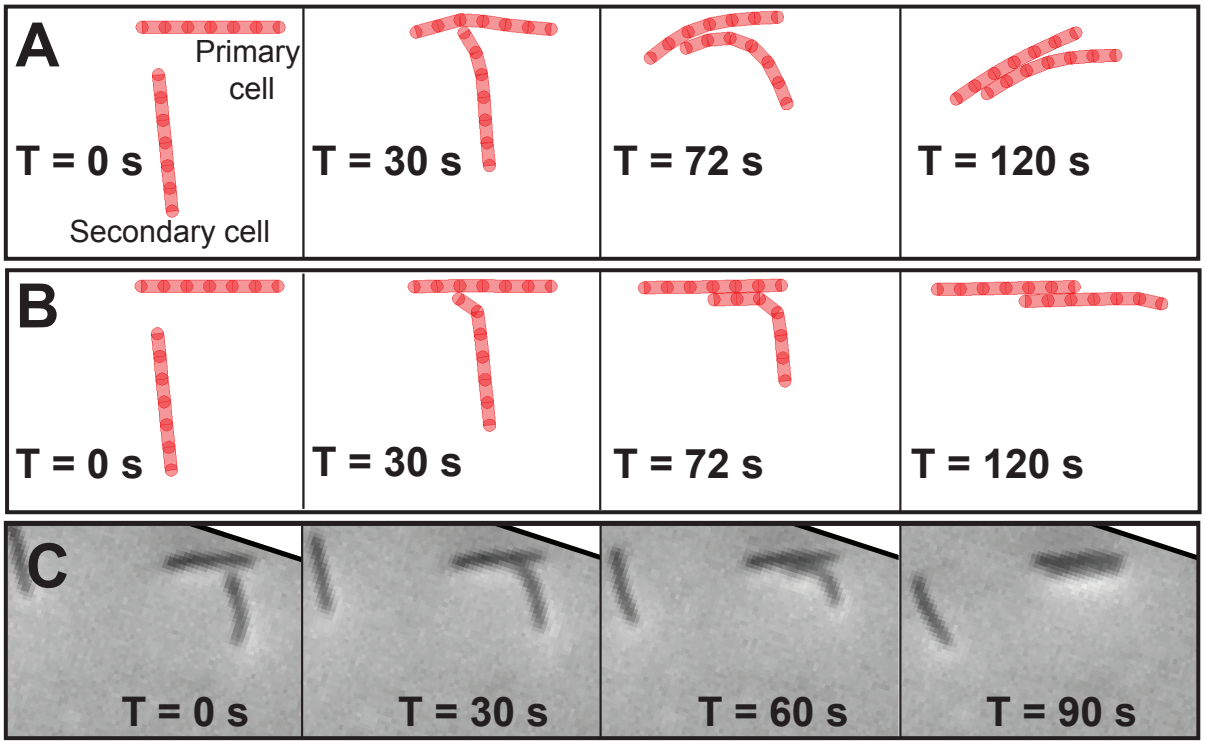


Figure 2.2: Mechanical interactions between two cells during head-to-side collisions in the biophysical models and experiments. (A) Viscous coupling model – both cells change directions. (B) Elastic coupling model – only the secondary cell changes direction. (C) Experimental time-lapse images (rotated to match with simulation configuration) showing collision between two isolated cells where only the secondary cell changes its direction. See videos S1-3 for corresponding movies[2].

To study the mechanical cellular interactions, we simulated a head-to-side collision between two cells moving on crossing paths. To differentiate the two mechanisms of gliding motility, we assumed strong attachments between the cell and the substrate in the ECM. The results show qualitatively distinct interaction behaviors of cells for the two alternative mechanisms (Fig. 2.2A and 2.2B). In these simulations, we define a primary cell as the one whose side is hit by the first node of another (secondary) cell. We observed that in the simulations of both the mechanisms, primary and secondary cells align with each other and move in a common direction after the collision. However, this common direction differed in the two mechanisms. In the VCM (Fig. 2.2A), both the cells changed their direction after the collision. In contrast, in the ECM (Fig. 2.2B), the new common direction is the same as the direction of the primary

cell before collision. Thus, the primary cell maintained its direction, whereas the secondary cell aligned with the former.

This contrasting cell-cell collision behavior in the two mechanisms can be explained by observing the cell's resistance to shape deformation (bending). During collision the primary cell nodes are displaced due to the contact with the secondary cell, thereby leading to local deformation of the primary cell. This deformation results in counter forces on the cell nodes. In both of the mechanisms cell deformation produces viscous drag forces and angular spring forces on nodes. In addition, in case of the ECM a strong restoring force acts on nodes due to the substrate attachments. These forces do not allow the deformations to propagate to the front nodes of the primary cell and as a result limits its change in direction. Since no such force exists in VCM, cell-cell collision results in cell deformation that propagates to its front node, and in turn significantly changes the cell travel direction.

To identify which of the two scenarios resembles the behavior of colliding *M. xanthus* cells, we examined similar collisions in the time-lapse images[3] of wild-type *M. xanthus* cells under low cell density ($8 \times 10^7$ cells/ml). We chose these conditions to easily identify isolated cells and their pairwise interactions. Figure 2.2C shows a typical cell-cell collision observed in experiments. In this case, the direction of the primary cell has not changed after collision. This behavior is similar to the simulations using the ECM of gliding motility. Thus, comparison of our simulations with experimental observations indicates there is an elastic coupling between the cell and substrate for *M. xanthus* gliding cells. Nevertheless, these conclusions may be sensitive to the parameter values used in our simulations or to the particular collision geometry. We therefore examined the robustness of these results.

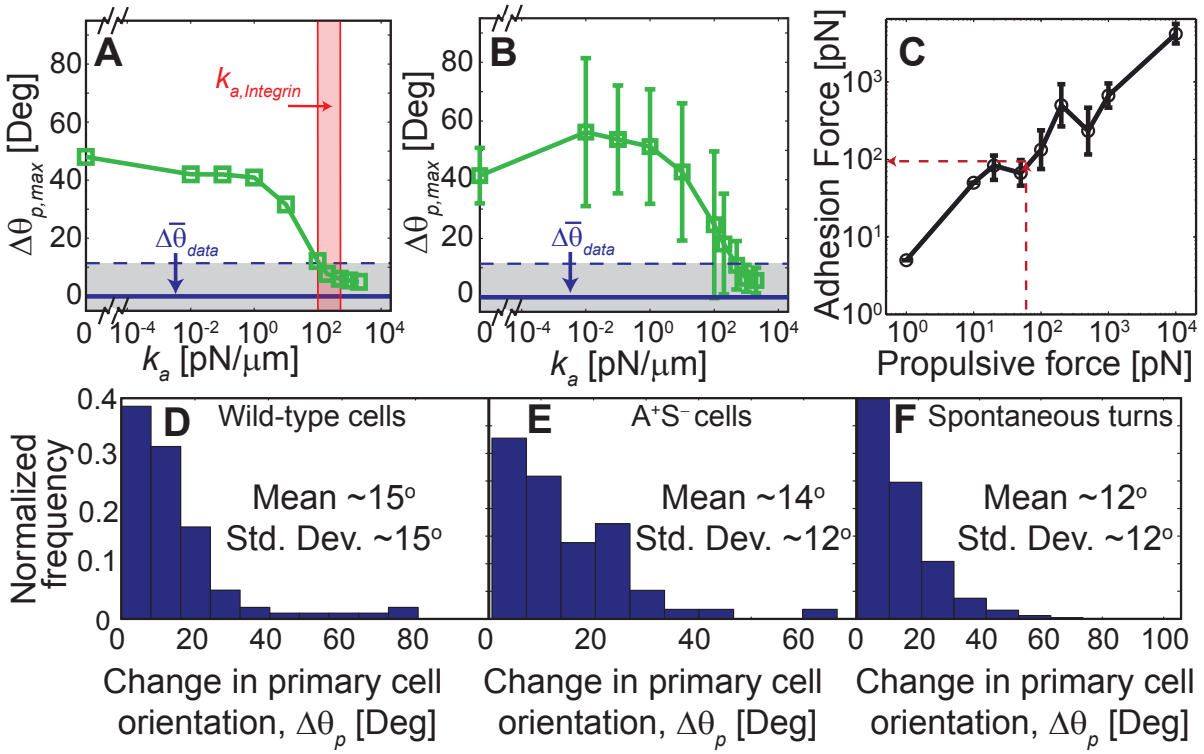


Figure 2.3: Strong adhesive attachments between cell and substrate are required to match experimental observations. (A) Maximum change in primary cell orientation ($\Delta\theta_{p,max}$) as a function of the strength of substrate attachments ($k_a$). Red band represents the range of bond strengths observed for integrin bonds in other biological systems (22-24). Horizontal solid line ($\Delta\bar{\theta}_{data} = \overline{|\theta_{data} - \bar{\theta}_{basal}|}$) represents the mean value of change in primary cell orientation from experimental cell collisions after subtracting the spontaneous cell turning and the dashed lines represent one standard deviation variation in the experimental data. (B) Same as (A) but with mean and standard deviation from aggregated simulations with varied model parameters. (C) The minimum adhesive strength of attachments matching experimental data closely matches with the cell propulsion force. Error bars represent variation in the results for different cell flexibilities. (D) The distribution of $\Delta\theta_p$ values in experimental data of wild-type cells (DK1622, collision events, N=97) and (E) cells lacking twitching motility (DK10407, N=58). (F) The distribution of spontaneous cell orientation change for mean cell collision time of ≈2.9 min measured from trajectories of isolated cells (DK1622, N=4018, see Fig. B.3A for additional details).

### 2.2.2 Distinct cell-cell collision behaviors require strong adhesion strength of substrate attachments but are robust to variation in other parameters

To further investigate the role of substrate adhesions during cell-cell collision we needed a quantitative metric to characterize the outcome of collision events. Since the major difference

[3]Experimental images are taken by Douglas Litwin, graduate student in Dr. Heidi Kaplan Lab, University of Texas - Houston Medical School

between the two mechanisms is the change in the primary cell orientation during collision, we focused on this value (see SI in AppendixB for details). We note that the collision outcome greatly depends on some aspects of the collision geometry, especially the collision position (defined from leading end of the cell, see Fig. B.2A) and collision angle. Therefore, we set the collision angle as ≈90 deg (that produces maximum change in cell orientation) and choose the maximum change in cell orientation ($\Delta\theta_{p,max}$) from all possible node collision positions ($n = 2, 3, ..., N-1; N = 7$) as the metric that describes the cell-cell collision behavior for a specific parameter set. Nodes $1$ and $N$ were excluded from this analysis since we assume no adhesion complexes at these nodes (see AppendixB for details). Figure 2.3A depicts how $\Delta\theta_{p,max}$ varies in the ECM model as a function of attachment strength. Each adhesive attachment is modeled by an elastic spring with a spring constant $k_a$ and a bond-breaking distance $L_{max}$. By keeping the bond-breaking distance constant we vary the elastic spring constant ($k_a$) and thereby change the maximal force to break the bond. $k_a = 0$ corresponds to the case in which no bond is formed with the substrate, and therefore only viscous interactions with substrate exist (VCM). Intermediate values of correspond to weak and non-specific interactions with substrate therefore may correspond to viscoelastic properties of EPS slime surrounding cells. Large values of $k_a$ correspond to a strong specific binding which resembles the ECM. Figure 2.3A shows that the value of $\Delta\theta_{p,max}$ starts at approximately 40 degrees for $k_a = 0$ and then decreases to values below 15 degrees for $k_a > 100$ pN/μm. $k_a = 100$ pN/μm corresponds to a bond-breaking force of 50 pN ( $L_{max} = 0.5$μm), which is roughly the order of integrin bond-breaking forces (≈50-250 pN) [149, 78]. This behavior is expected as the adhesion complex force will only be relevant if it resists the force generated by cell motility (≈ 60 pN). When the attachment strength exceeds this threshold it results in small node displacements and hence small changes in cell orientations after collision.

For comparison we quantified the change in primary cell orientation ($\theta_{data}$) in isolated cell collisions under experimental conditions for 97 cell pairs (Fig. 2.3D). As these measurements also contain the spontaneous change in the orientation of cells, we measured the mean sponta-

neous orientation change ($\bar{\theta}_{basal} \approx 12$ deg) of isolated cells (measurements from $\approx 50$ cells; see AppendixB and Figure 2.3F and B.2 for details) and subtracted it from experimental data ($\theta_{data}$). The mean value and standard deviation of the net change in cell orientation ($|\theta_{data} - \bar{\theta}_{basal}|$) from experimental images is shown in Figure 2.3A (gray area). Since these experimental results were based on wild-type cells that exhibit both gliding and twitching motility, we replicated the analysis with DK10407 ($\Delta pilA A^+ S^-$) cells that exhibit only gliding motility. The results from 58 isolated collision events for DK10407 cells are shown in Figure 2.3E. We observed that the mean change in primary cell orientation in isolated cell collision events for pure gliding motility cells is $\approx 14 \pm 12$ deg (n=58). This value is very close to that of the wild-type cells ($\approx 15 \pm 15$ deg). These results indicate that the contribution of twitching motility to our analysis of gliding motility is negligible which is expected as twitching pili are located only at the poles and should not affect cell bending. Thus we used only wild-type cell data in our further analysis.

We observe that the modeling results match with the experimental observations only for adhesion strength ($k_a$) values greater than 200 pN/μm (Fig. 2.3A). Whereas, model results with no adhesion complexes ($k_a = 0$, VCM) show very large changes in cell orientation and do not match the experimental observations for the chosen parameters. However, we are uncertain whether the results will hold if some mechanical parameters (see Table A.1 for model parameters) of the model are changed. We therefore systematically varied the model parameters over two orders of magnitude (from 0.1x to 10x, see Table B.1) and investigated their effect on cell-cell collisions. These results are combined in Figure 2.4B, which shows the mean values and standard deviations of the cell orientation changes for different adhesion strengths ($k_a$). As before, we find that only the ECM model at very high adhesion strength values ($k_a > 500$ pN/μm) matches the experimental values. We also noted that despite the large variability of the parameters, the standard deviations in the model results at high adhesion strengths are quite small. Thus, we conclude that our results are robust to variation in all model parameters except the strength of adhesion complex.

We have also quantified the minimum strength ($F_{min}^{adh}$) required for a focal adhesion complex

in the cell model to match the experimental cell orientation change in a collision for different cell propulsive force ($F^p$) (Fig. 2.3C). The results indicate that $F^{adh}_{min}$ values increased with an increase in the cell propulsive force and are similar in magnitude to that of propulsive force.

### 2.2.3 Distinct cell-cell collision behaviors are observed using the two gliding motility mechanisms over a range of collision geometries

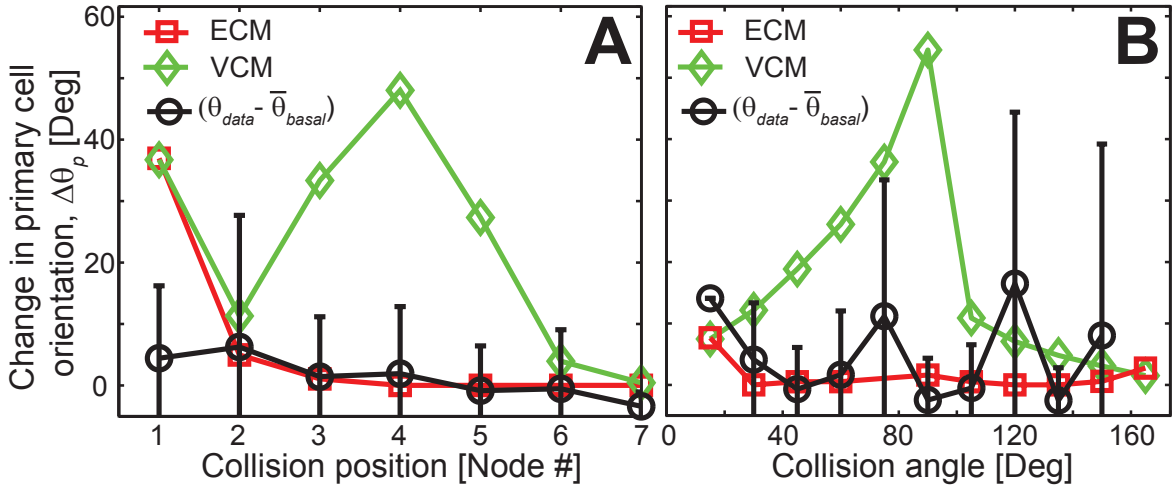


Figure 2.4: Distinct cell behavior from the two cell models for variation in collision geometries. (A) The change in primary cell orientation ($\Delta\theta_p$) as a function of collision position from the leading end of the primary cell and (B) as a function of collision angle.

As noted earlier, the outcome of cell-cell collisions depend on the mechanical parameters of the cell and on the collision geometry, specifically the collision position along the cell length and collision angle (the angle between the cell orientations at the start of the collision) (Fig. 2.4, B.3). To this point, our analysis focused on the maximum change in cell orientation as we varied the position of the colliding nodes and used a collision angle near 90 degrees at which the maximal cell deformation is expected. However, it is not clear if the experimental collision events correspond to these amplified effect scenarios or whether it is possible that a model with very weak or no elastic coupling can be consistent with the experimental collisions at some conditions. Thus, we systematically explored how variability in the geometrical model parameters affects the outcome of the collision. In these simulations we chose for the adhesion strength

value ($k_a$) of 2000 pN/μm in the ECM, a value for which the model results closely match the experimental observations. In addition, all the experimental observations were corrected for spontaneous orientation change of cells ($\bar{\theta}_{basal}$).

First, we compared the orientation change from the two mechanisms as a function of the collision position for the default parameter set (Fig. 2.4A). We note that both models produced a much smaller change in cell orientations for collisions near the lagging end of the primary cell. This is an expected behavior of the model, as small node displacement near the lagging end of the cell may not produce sufficient cell deformation to significantly change the cell travel direction. However, collisions in the forward and middle section of the cell produced significantly larger orientation changes for the VCM model as compared to the ECM model. We note that the collision at the first node of primary cell produced very large orientation change in both mechanisms. This large change is due to the assumption that no adhesive attachment present at the first node of the cell (see SI for details). As a consequence we observed a large displacement of nodes even in the ECM. Thus, we excluded the first node collisions from our analysis. For comparison, we next quantified the changes in cell orientation as a function of the collision position from experiments (black circles in Fig. 2.3A). We note that only the results of the ECM model match with the mean experimental values for all collision node positions, whereas the results of the VCM model deviated significantly from the experimental values. We also found that these results are also robust to variation in mechanical parameters of the model (see Fig. B.4A) and for small perturbations in collision positions (see Fig. B.4B).

Next, we investigated the effect of collision angle on cell-cell collision behavior. We varied the collision angle between 15 – 165 deg (corresponding to the experimental data, see Fig. B.3C) and measured the maximum orientation change of the cell across all node collision position at each collision angle. We observed that the cell orientation changes with both the mechanisms are similar at both extremes of the collision angle range, but vary significantly in the middle (Fig. 2.4B). We compared these results with the observations from experimental cell collisions as a function of collision angle. We determined that results from the ECM model

match closely with the experimental observations, whereas the results from the VCM model deviated significantly (Fig. 2.4B).

We also observed similar results for variation in cell length and number of adhesion complexes per cell (see Fig. B.3C,D). Thus, the results from the VCM model consistently showed large cell orientation changes compared with the ECM model for various collision geometries. Further, the results from the ECM model match with mean values from the experimental data for all the collision scenarios considered.

### 2.2.4 The effect of force on motor velocity is consistent with an elastic motor-substrate coupling

**Experimental results presented below are performed by Fabian Czerwinski, Mingzahi Sun in Dr. Joshua Shaevitz Lab, Princeton University**

To directly test the coupling of single motor complexes to external objects such as the gliding substrate, we applied controlled loads to micron-sized beads being transported by gliding motors on immobilized cells[70]. We designed a transient force clamp that isolates the effects of force on the motor-driven 'runs' even from the complex pause dynamics and occasional directional reversals seen in bead motion (Fig. 2.5A, see [70] and SI for experimental procedure). This procedure uses an optical trap to apply fixed loads to beads, but only after being triggered by a motor-driven displacement of 63 nm in less than 3 s. Trap position feedback was then used to maintain a constant force on the bead for approximately 8 s after which the trap was shut off. If the bead velocity and direction before and after force application was nearly the same, we concluded that the motor did not reverse or pause during the force-clamped period.

Fig. 2.5B-D show the measurements of bead linear velocities under various loading conditions in force clamp experiments. We observe that after some initial period of inactivity bead starts moving (green lines) at which point a preset opposing force is applied on the bead. We found that opposing forces of $\approx$12pN (Fig. 2.5C) causes stalling of the bead whereas for forces below 12pN (Fig. 2.5B) bead movement is continued albeit slower than load free conditions.

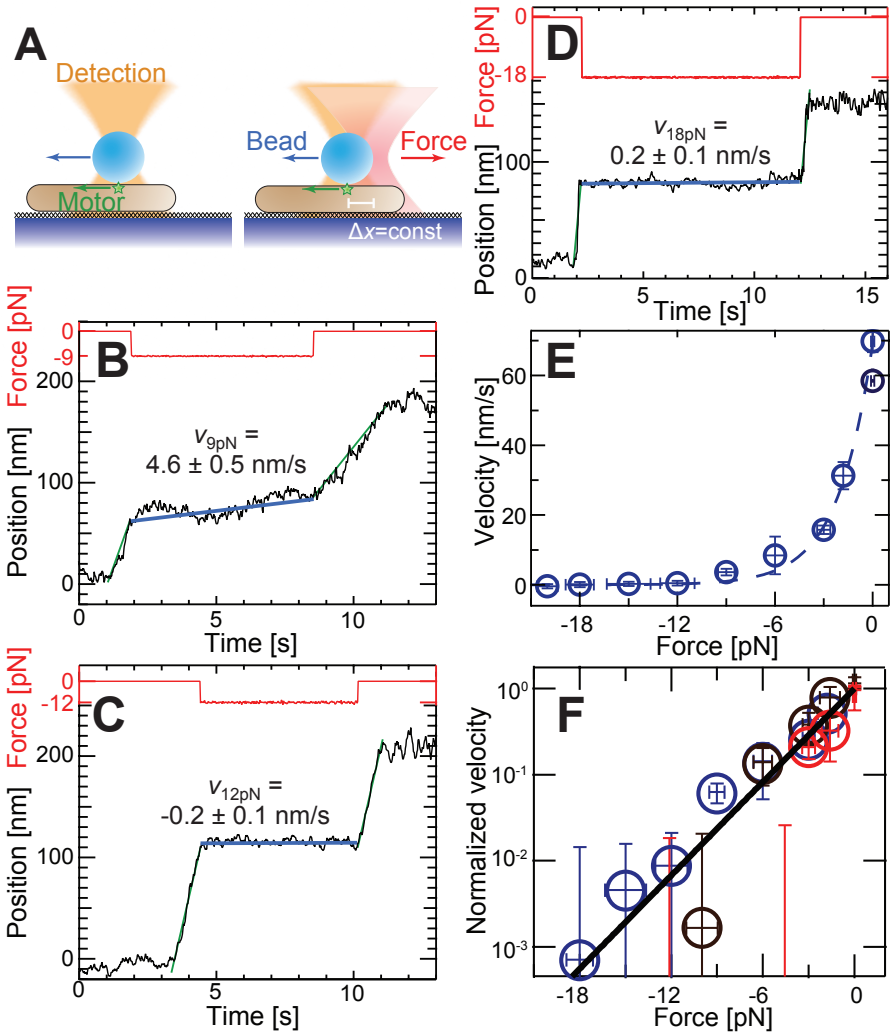


Figure 2.5: Bead/molecular motor motility behavior under optical trap loading. (A) A gliding motor moves a bead along the cell axis. Past a preset threshold movement, the shutter in front of the optical trap is opened, pulling the bead in the direction opposite to the motor by the preset force, resulting in a slowing of bead movement. (B-D) For opposing forces of 12 pN or greater (18 pN) bead movement has stopped and for lower forces (9 pN) bead movement is slowed down but not completely stopped. Here an experiment is associated with the activity of a single motor only if the bead moves before and after trapping with the same direction and speed (green lines). A linear fit to the position versus time during force application provides the velocity (blue lines). (E) Bead velocity decreases exponentially with force but never becomes negative consistent with an elastic coupling and inconsistent with a viscous coupling between the bead and motor. The dashed lines are an exponential fit to the data. Error bars represent the standard error of the mean across trials (> 6 trials per data point). (F) Force-velocity curves normalized by unloaded velocity corresponding to different nigericin concentrations (blue circles – 0 µM, brown circles – 10 µM, red circles – 20 µM; see Fig. B.5 for individual curves) collapse on to a single line on a semi-log plot.

We estimated this stall force by finding those events in which the linear velocity was zero within twice the standard error of the linear velocity measurement. Interestingly, beads remained motionless for loads well-beyond the stall force (18 pN, Fig. 2.5D) and we never observed a bead to reverse its direction in response to high loads over the eight seconds of force application. The lack of backwards motion at super-stall forces is consistent with the ECM, but inconsistent with the viscously-coupled VCM model which predicts significant backwards motion at these loads.

We measured the force-velocity response of at least 108 motor complexes on 40 different *M. xanthus* cells. We chose the preset force to probe the complete force-velocity relationship for opposing loads from 0 to 20 pN (Fig. 2.5E) and also varied the concentration of nigericin (a drug that reduces pH gradient/ proton motive force across cell membrane there by decreases the motor function/bead motion [70]) in solution. We find that opposing loads slow gliding motors exponentially with a characteristic decay force of $2.3 \pm 0.1pN$. In addition, we find that with increasing nigericin concentration, bead velocity decreased but force production did not (Fig. B.5A-C). When normalized by the unloaded velocity, force-velocity curves from different nigericin concentrations collapse onto a single exponential curve (Fig. B.5D) with characteristic force independent of nigericin. This is again inconsistent with the VCM in which decrease in velocity would lead to decrease in force production.

## 2.3 Discussion

Despite progress in elucidating the mechanism of *M. xanthus* gliding motility, its biophysical mechanism is still not fully understood. Based on recent experimental evidence two alternative mechanisms: FAM and HRM of gliding motility are proposed but to date neither model has been conclusively proven. A key difference between the two models is in the biophysics of the interactions between cells and substrate. We hypothesized that this difference will affect cell behavior during cell-cell collisions. To test this, we constructed mathematical models of the *M. xanthus* cell with either viscous (VCM) or elastic (ECM) interactions with substrate and

studied the mechanical behavior in isolated cell-cell collision events. As expected, we found that both models differed in their cell interaction outcome, which was quantified by cell orientation changes. We compared the results from both the models with experimental observations of isolated cell-cell collisions events under similar conditions. We found that experimental cell behavior differs from that of the VCM model and agrees with the ECM model in which there is strong adhesion between the cell and substrate. Variations of the mechanical and geometrical parameters in the cell model for the collision process further confirmed these findings and indicated the robustness of the model. Thus our analysis predicts strong elastic attachments between the cell and substrate, which is consistent with a focal adhesion mechanism for gliding motility. As a further test of the mechanics of cell attachment, we then studied of the effect of load on motor attachment and speed. We found that motors stalled to zero speed for loads about12 pN. Even when the load exceeded these stall force value (up to 20pN), the beads remained strongly attached to the cells and did not show motion in the opposite direction. This behavior is expected in an elastic-coupling model. In total, our simulations and measurements are consistent with the ECM and inconsistent with the VCM.

The strong attachment between cell and substrate indicated by our analysis are realistic and are similar in the range of other biological cell-substrate interactions (e.g. integrin focal adhesions in eukaryotic cells [149, 78]). Further, we observed that the minimum adhesive strength per node required to match the experimental observations increased with an increase in cell propulsive force, but remained within same magnitude (0.5x – 5x) of cell propulsive force. Based on the force-clamp experimental estimate of $\approx$12pN force generated at each focal adhesion node, and assuming $\approx$5 adhesion nodes per cell [74, 147], we estimate the gliding motility apparatus generates $\approx$60pN of force. This estimate is of the same order as the force generated by the twitching motility engine [150, 151] which is not surprising given that *M. xanthus* cells using either gliding or twitching motility move at approximately the same speed [63]. In light of this estimate, our model (Fig. 2.3C) would predict at least 80pN of adhesion force. In support of this, force-clamp experiments never observed bead detachments for forces

up to 20pN.

While the work here probed the attachment of motor bound-bead cargos to immobilized cells, it should be possible in the future to directly test the ECM model using optical tweezers and moving cells to measure the cell detachment force along the cell length. Large detachment forces with the existence of multiple peaks in the cell displacement curve along the cell length would provide support for multiple strong attachment sites.

Although our biophysical model that includes strong adhesion, similar to the FAM, explains the observed experimental cell collision behavior, a number of issues remain unresolved regarding the focal adhesion model of gliding motility. First, while it is observed that clusters of AlgZ proteins, which are predicted to form the focal adhesions, remain stationary during cell movement [74, 69, 44], this behavior requires that the adhesion complexes move through the peptidoglycan layer. Second, the adhesive proteins/molecules that bind the motor complexes to the substrate have not been identified. A recent study by Durcet et al.[152] speculated that slime acts as a binding agent between the cell and substrate. In this context it is worth noting that our biophysical cell model incorporates a simplistic viscoelastic model for cell-substrate interactions. However, a non-isotropic viscoelastic model for attachment may provide a better description of the substrate interactions [153]. Third, strong cell-substrate attachments pose an additional problem for cell by restricting its movement at the lagging pole. Since the attachments remain stationary during cell movement, the elastic nature of the attachment at the lagging pole would be expected to cause an increasingly opposing force for cell movement as the cell moves forward until the attachment is broken causing its lagging pole to snap back. This type of jerky motion is commonly seen in fibroblasts that utilize substrate attaching lamellopods for movement [154, 155, 156]. However, since this type of motion is absent in *M. xanthus* gliding, it suggests that the cells actively destroy attachment complexes at the lagging pole.

The critical role of substrate adhesion in the mechanism of gliding motility of *M. xanthus* may have analogues in other bacteria. Recent studies have demonstrated that gliding motility

in *Flavobacterium johnsoniae* is dependent of the cell-surface adhesion protein SprB [31]. As in *M. xanthus*, these adhesion proteins appear to rapidly move along the cell surface on helical filaments and this movement is powered by the PMF [157]. *F. johnsoniae* cells are also capable of binding and propelling latex beads[158] but the force-velocity relationship has not been measured. These observations bring an intriguing possibility that the biophysical mechanism of gliding motility in evolutionary distant *F. johnsoniae* and *M. xanthus* could share some similarities.

Is there any physiological role for the strong adhesion with substrate? We speculate that the strong attachment between the cell and substrate helps the cells align at high cell density. Indeed, the simulations of Janulevicius et al.[105] lacking substrate adhesion, indicated that *M. xanthus* cells with the bending modulus reported in literature [159, 160] cannot maintain alignment. In our model we have observed that when strong substrate adhesion is included the orientation of one of the cells remains unchanged during cell collisions, whereas the orientation of the other aligns to this orientation. This reflects the natural arrangements of high density *M. xanthus* cells that self-organize into well-aligned clusters [161, 99]. As new cells join and align with the existing cells in a cluster, strong substrate attachments prevents the change in orientation of the cell clusters, thus preserving the mean orientation of the cluster. This effect appears to explain that flexible cells can maintain their alignment using strong adhesive attachment with the substrate.

# Chapter 3

# Mechanism of collective cell alignment in *Myxococcus xanthus* bacteria

**Abstract**

*M. xanthus* cells self-organize into clusters, aligned cell groups, at various stages of its lifecycle. Formation of these clusters is crucial for complex dynamic multi-cellular behavior of these bacteria. However the mechanism underlying the cell alignment and clustering is not fully understood. Motivated by studies of clustering in self-propelled rods, we hypothesized that *M. xanthus* cells can align and form clusters through pure mechanical interactions among cells and between cells and substrate. We test this hypothesis using an agent-based simulation framework where each agent is based on biophysical model of individual *M. xanthus* cell. We show that model agents, under realistic cell flexibility values, can align and form cell clusters but only when periodic reversals of cell directions are suppressed. However, by extending our model to introduce observed ability of cells to lay and follow slime trails, we show that effective trail following leads to clusters in reversing cells. Furthermore, we conclude that mechanical cell alignment combined with slime-trail-following by cells is sufficient to explain the distinct cell clustering behavior observed for wild-type and non-reversing *M. xanthus* mutants in recent experiments. Our results are robust to variation in model parameters, match with the experimentally observed trends and can be applicable to understand surface motility patterns of other bacterial species[1].

[1]Research work shown in this chapter is already published [162]. Text presented here is from the published manuscript. Refer to [162] for supplemental movies.

## 3.1 Introduction

*M. xanthus* is a model organism for studying self-organization behavior in bacteria [45]. These rod-shaped bacteria are known for their ability to collectively move on solid surfaces. Depending on environmental conditions, this collective movement allows cells to self-organize into a variety of dynamic multi-cellular patterns [58, 40]. For instance, when nutrients are abundant, cells collectively swarm into surrounding spaces [45]. When cells come in direct contact with other bacteria that can serve as their prey, *M. xanthus* cells self-organize into ripples i.e. bands of traveling high cell density waves [88, 51, 44]. Alternatively, if nutrients are limited, cells initiate a multi-cellular development program resulting in their aggregation into 3-dimensional mounds called fruiting bodies [163, 92].

Self-organization in *M. xanthus* requires coordination among cells and collective cell motility [88, 45, 97, 73, 44]. Despite decades of research, mechanisms that allow for motility coordination in *M. xanthus* are not fully understood. In particular, ability of cells to collectively move in the same direction is crucial to the observed multi-cellular behavior at various stages of its life cycle [164, 53, 161]. Given that individual rod-shaped *M. xanthus* cells move along their long axis, coordination of cell direction in a group can be achieved by forming aligned cell clusters. Such clusters are observed in a variety of environmental conditions: low-density swarming [161], aligned high cell density bands in ripples [53] and long streams of aligned cells during initial stages of aggregation [165, 166]. But the mechanisms responsible for this collective cell alignment are not completely clear.

Another important aspect of *M. xanthus* motility is the periodic reversal of cell's travel direction by switching cell's polarity and flipping head and tail poles. Recent experiments indicate that clustering behavior of *M. xanthus* cells is dramatically affected by variation in cell reversal frequency [167, 168]. Starruß et al.[167] observed that, above certain cell density non-reversing *M. xanthus* mutants ($A^+S^-Frz^-$) form large moving clusters whereas reversing wild-type cells organize into interconnected mesh-like structure. In a recent study, Thutupalli

et al.[168] observed that starving wild type *M. xanthus* cells increased their reversal frequency with time which resulted in change in their clustering behavior from aggregates (large clusters) to streams (elongated clusters). In addition, this study indicated that reversing and non-reversing cells differ in their dynamic behavior inside clusters. Reversing (wild-type) cells form stream-like clusters that appear stationary and the cells move within the clusters. In contrast, non-reversing ($\Delta$*frzE*) mutants form flock like isolated clusters that move around and the cells inside clusters appear to be moving with the same velocity as the clusters.

Therefore, our ability to explain cell alignment in to clusters and variation of cell clustering behavior with change in reversal frequency is essential for successful models of all self-organization phenomena. Several prior studies [169, 167, 170] attempted to understand the cell clustering process in *M. xanthus* using mathematical and computational approaches. Starruß et al.[167] developed a kinetic model, inspired from coagulation theory for colloidal particles, in which cell clusters dynamics resulted from their fusion, splitting, growth-decay processes. Using this model they were able to explain the observed cluster size distribution for non-reversing cells. However, this model could not explain the cell clustering behavior for wild-type (reversing) cells. In another study, Harvey et al.[170] showed symmetry breaking between free cells (uniform gas phase) and nematically ordered cell clusters (dense phase) using a multi-phase continuum model. However, this model did not explicitly study the effects of changing reversal frequency on clustering and the equations developed are limited to 1-D and quasi-1D settings. Further, both the models follow phenomenological approaches and do not provide a clear relationship between the model assumptions and individual cell behavior.

In this study, we overcome the limitations of previous approaches by connecting the individual cell behavior with collective cell motility through a biophysical agent-based model. Our overarching hypothesis is that cell clustering can be explained solely via mechanical interactions among cells and between cells and substrate. In other words, the observed patterns do not rely on biochemical signals such as chemotaxis. To test this hypothesis, we simulate interactions among a large number of cells through an agent-based-simulation(ABS) framework.

Using this framework, we first study the formation of aligned cell clusters in non-reversing *M. xanthus* cells and later extend our investigation to reversing cells. Furthermore, we investigate the effect of cell-substrate interactions such as slime-trail-following on the clustering patterns. The results of our simulation are compared with experimental data from literature and can be applicable to other bacteria that display surface motility.

## 3.2 Results

### 3.2.1 Non-reversing flexible cells form clusters due to steric alignment

First, we investigated whether mechanical interactions among *M. xanthus* cells would be sufficient to induce aligned cell cluster formation. This approach was motivated by our previous study [145], which demonstrated alignment in cell pairs as a result of the head-to-side collision, and soft-condensed matter models showing clustering in self-propelled rigid rod particles [171, 143, 142]. We hypothesized that successive collisions of cells with previously aligned cell clusters will result in formation of even larger clusters. Thus, we simulated mechanical interactions among non-reversing cells, similar to self-propelled rod models, but with realistic cell flexibility values. For this step, we have used the bending stiffness value ($k_b$) for *M. xanthus* cells, from our previous study [145], which reproduces realistic pair-wise collision behavior in model agents. Under these estimates of $k_b$, we studied clustering behavior of the model *M. xanthus* cells in our ABS framework at different cell densities ($\eta$, defined as the fractional area occupied by all cells in the simulation region).

To simulate mechanical interactions of cells moving on 2D surface we extended our previously developed framework (see AppendixA for further details). In this framework, each agent consists of multiple segments enabling a realistic mechanical model of a single *M. xanthus* cell. To this end, we use a connected string of nodes with linear and angular springs between nodes to simulate elastic behavior. Agents move forward through propulsive forces acting on the nodes tangential to the cell length (towards the next node). This is similar to the force generation

through multiple motor protein complexes distributed along cell length as observed by recent models of *M. xanthus* gliding motility [74, 73, 69, 70]. Agents experience drag forces opposing their motion due to the surrounding fluid. Adhesive attachments with underlying substrate at nodes resist lateral displacement of agents during collisions (the focal adhesion model of gliding motility [70]). At low densities, *M. xanthus* are known to move as monolayer of cells. Therefore, collisions among agents are resolved by applying appropriate forces on nodes that keep agents from overlapping. Agents move over a 2D simulation space with periodic boundary conditions according to the net forces acting on their nodes. We introduce random noise in agent travel direction by altering the direction of the propulsive force on the front node. We observe the agent behavior by solving the Newton's equations of motion on nodes to get their position and velocity at each time step of the simulation. We use Box2D [172] physics library to solve these equations of motion and efficiently handle the excluded-volume forces.

We start the simulation by initializing the cells one by one in the simulation region at random positions and with random orientations until desired cell density is reached. While initializing, we accept only the cell configurations that do not result in cell overlap. As soon as the simulation begins, cells start moving and colliding with their neighboring cells and as a result align along their major axis [145]. This alignment is nematic [173] – aligned cells can move in the same or opposite directions depending on the initial orientation of cells. When aligned cells move in the opposite directions, they separate; however, when they move in the same direction, a small cluster of aligned cells is formed. These clusters grow in size as more cells join through collisions or due to merging with other cell clusters. Clusters shrink in size as peripheral cells leave the cluster due to a random change in their travel direction (Movie SM1, SM2). We quantify the evolution of clusters through cluster size distribution (CSD, see Appendix C Text). After about 180 min of simulation time CSD is stabilized (Fig. C.3), and we observe that cells in the simulation regions are distributed among clusters of different sizes while few cells remain isolated.

Depending on the cell density ($\eta$), we observe a variation in the clusters size distribution

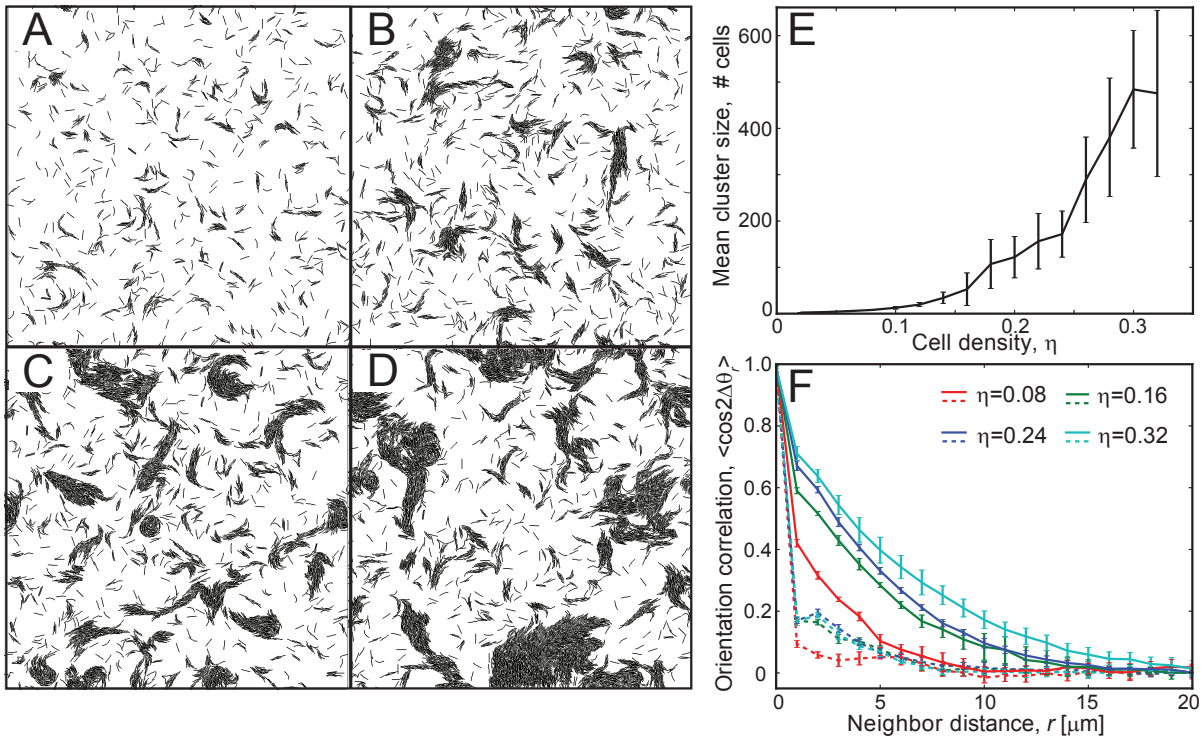


Figure 3.1: Clustering behavior of non-reversing flexible agents in simulations. (A-D) Snapshots of the simulation region at 180 min of simulation time for different cell densities, $\eta$. (A)$\eta$=0.08, (B)$\eta$=0.16, (C)$\eta$=0.24, (D)$\eta$=0.32. Flexible agents formed aligned clusters at moderate to high cell densities ($\eta \geq 0.16$). (E) Mean cluster sizes, $\langle m \rangle$, from simulation as a function of cell density, $\eta$. The error bars indicate the standard deviation in the data. The results are averaged over 5 independent simulation runs. The mean cluster sizes increased with increases in cell density. (F) Orientation correlation $\langle cos2\Delta\theta_r \rangle$ among cells as a function of neighbor cell distance, $r$. $\Delta\theta_r$ is the angle deviation between orientations ($\theta$) of a pair of neighbor cells separated by a distance $r$. Orientation correlation ($cos2\Delta\theta_r$) values from all cell pairs are binned based on $r$(bin width = 1 μm) and averaged. Dashed and solid lines represent orientation correlation values at 1 min and 180 min of simulation time, respectively. Agents in clusters showed higher neighbor alignment at larger distances compared to the initial randomly oriented cells. Furthermore, the alignment increases with increases in cell density.

and in the number of isolated cells. Cells formed stable clusters (containing $> 10^2$ cells) only for sufficiently high cell densities ($\eta \geq 0.16$) (Fig. 3.1A-D), while cells largely remain isolated for lower densities ($\eta = 0.08$). We have quantified the effect of increasing in cell density ($\eta$) on clustering behavior by measuring the mean cluster size $\langle m \rangle$ (refer to Appendix C for details on quantification procedures) at each cell density value. We observe that increase in cell density resulted in increased mean cluster size (Fig. 3.1E). We have quantified the alignment within the cell clusters using mean cell orientation correlation, $C(r) = \langle cos(2\Delta\theta_r) \rangle$, as a function of

neighbor cell distance $r$ (Fig. 3.1F). Here $\Delta\theta_4$ is the angle deviation between the orientations ($\theta$) of a pair of agents whose center nodes are separated by distance $r$ (see Appendix C). We use $2\Delta\theta$ to ensure correlation values in parallel and anti-parallel alignment configurations remain same [105]. The orientation correlation results confirm that in comparison with initial distribution clustering results in longer-distance orientation correlation for high cell densities. We observe that immediately after the start of the simulation (1 min), cells exhibit very low correlation with their immediate neighbors ($r = 2 - 3$μm). However after long simulation time, we observe a large increase in cell orientation correlation with neighbor distances (except for $\eta = 0.08$, Fig. 3.1F) indicating formation of larger aligned clusters. (Refer to Fig. C.4 for evolution of orientation correlation with time)

To test the robustness of our results, we have varied the cell flexibility ($k_b$) values over a wide range (0.1x – 10x) and studied the cell clustering behavior in our simulations. We observed that our model agents formed clusters except for very high cell flexibility value (0.1x, $k_b = 10^{-18} N.m$) (Fig. C.5A-F). Further mean cluster sizes increased with increase in cell densities for all cell flexibility values (Fig. C.5G). Interestingly, increases in cell flexibility decreased the mean cluster sizes.

Thus, we observe that flexible agents can form aligned clusters through mechanical collisions for sufficiently high cell densities ($\eta \geq 0.16$), similar to self-propelled hard rods [169]. Furthermore, these cell clusters from our simulations are very similar to the isolated cell clusters experimentally observed for non-reversing *M. xanthus* (*frz*$^-$) cells [169, 167].

### 3.2.2 Periodic reversals destroy clustering

Next, we investigated the effect of cell reversals on clustering behavior. We introduced periodic reversals of cell travel direction (reversal period = 8 min [52]) in our model agents. Similar to *M. xanthus* cells, each reversal results in switching of the agent polarity, i.e. switching of the head and tail nodes. Surprisingly, with addition of periodic cell reversals, cells failed to form of large clusters even after long simulation time (180 min) (Fig. 3.2A, Movie SM3). Furthermore,

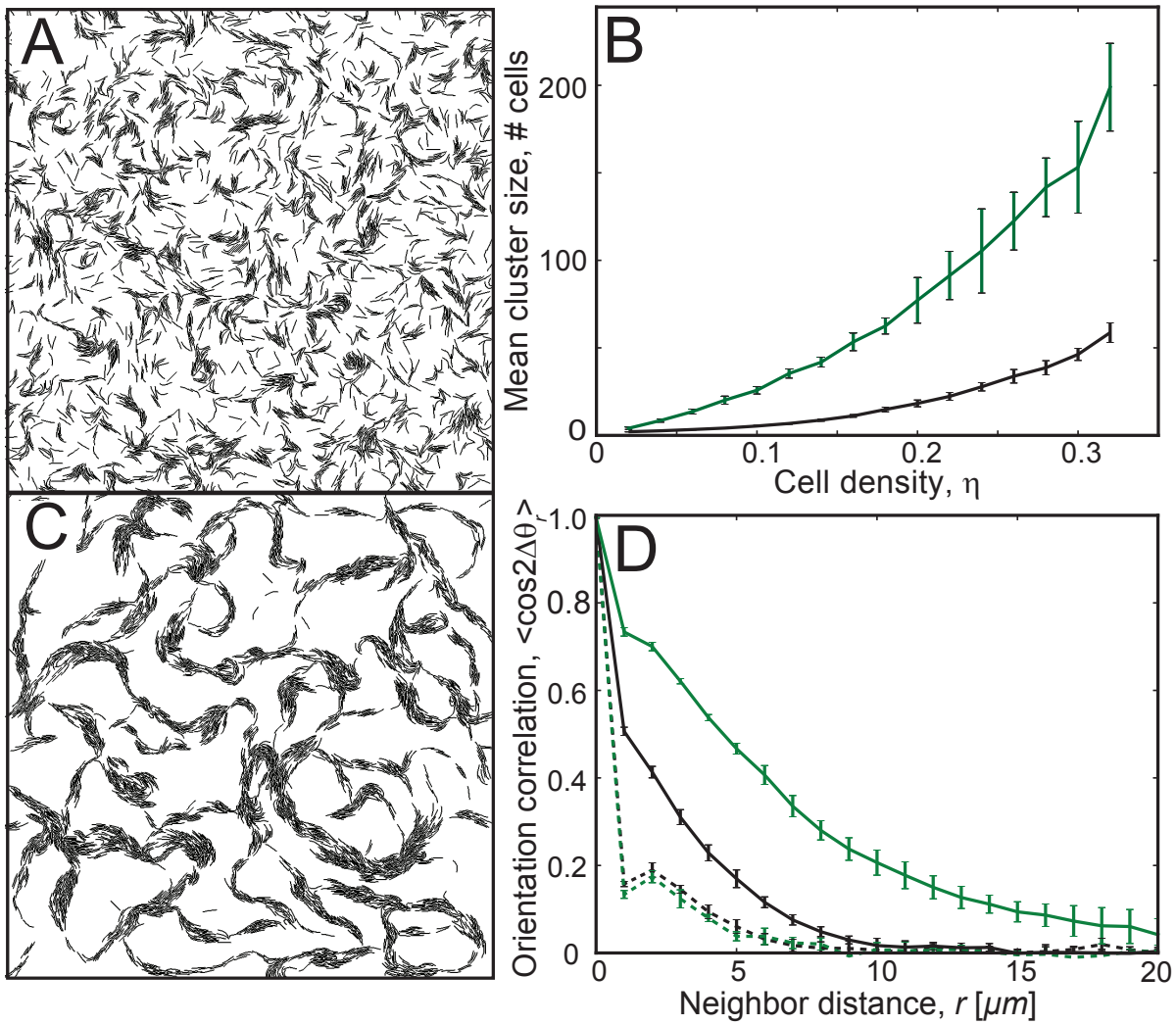


Figure 3.2: Clustering behavior of periodically reversing agents in simulations. (A) Snapshot of the simulation with periodically reversing agents ($\eta$=0.24) at 180 min of simulation time. Reversing agents did not show significant clustering. (B) Mean cluster sizes, $\langle m \rangle$, in simulation as a function of cell density, $\eta$, for agents following slime trails (green line) and agents without slime trails (black line). Agents following slime trails showed a significant increase in mean cluster size compared to agents without slime-trail-following. (C) Snapshot of the simulation for periodically reversing cells with the slime-trail-following mechanism ($\eta$=0.24, $L_s$=11 μm, $\epsilon_s$=1.0, refer to Methods for details) at 180 min of simulation time. Agents show improved clustering compared to those without the slime-trail-following mechanism. (D) Orientation correlation $\langle cos(2\Delta\theta_r) \rangle$ among agents for reversing cells (black) and reversing cells with the slime-trail-following mechanism (green). Dashed and solid lines are orientation correlation values at 1 min and 180 min of simulation time, respectively. Orientation correlation with neighbors improved for larger neighbor distances with the slime-trail-following mechanism.

we observe that increase in cell density did not improve mean cluster sizes significantly (Fig. 3.2B, black line). Even when we started with cells that initially formed clusters by simulating

non-reversing cells first for 90 min and then turned on cell reversals, we observe destruction of existing cell clusters within about 30 min (Fig. C.6). Thus, our simulations results indicate that steric alignment is not sufficient for formation of aligned clusters in population of periodically reversing agents. However, given that wild-type *M. xanthus* cells reverse their polarity but still form clusters, additional interactions must be included in our model to explain *M. xanthus* clustering behavior.

In our first attempt to correct this, we tested whether cohesive interactions among *M. xanthus* cells [174] can rescue clustering. Studies on colloidal particles indicate that adhesion between particles can lead to their clustering [175]. *M. xanthus* cells secrete exopolysaccharide (EPS) proteins and fibrils on their surface and these are observed to a form network with other cells' surface fibrils that are in close contact resulting in cell-cell cohesion [174, 176]. These cohesive interactions can keep cells together and thus may lead to clustering in reversing *M. xanthus* cells. We investigated this mechanism, by introducing lateral adhesion forces between neighboring agents nodes in our simulations (Refer to AppendixA). However, we observe that adhesive interactions between neighbor cells did not lead to significant cell clustering for reversing cells even at high adhesion forces (Fig. C.7). Thus, lateral adhesions are not sufficient to stabilize the clusters of reversing cells.

To understand the rationale of why cell reversals prevent the formation of large clusters we examined the cell clustering dynamics in our simulations with and without cell reversals. For non-reversing cells, we observe that, clusters grow in size due to collision with new cells and cells inside the clusters are unable to leave the cluster. At steady-state, cluster size is determined by a balance between the flux of peripheral cells leaving the cluster and new cells joining the cluster similar to kinetic theory developed in Ref. [169]. In contrast, for reversing cells we observed that even though mechanical collisions often lead to transient formation of small clusters, these clusters fail to grow and stabilize. This occurs because upon reversal cells from interior of the cluster move through the other cluster cells in the opposite direction and leave the cluster. Further, random changes in their travel direction prevent them from returning

to their original clusters after another reversal. This also explains why adhesive cell interactions failed to result in clustering of cells in our simulation. Lateral adhesive interactions do not stop cells from leaving the clusters after reversal and cannot influence the direction of cell movement once it leaves from the existing cluster.

### 3.2.3 Slime-trail-following by cells rescued clustering for reversing cells

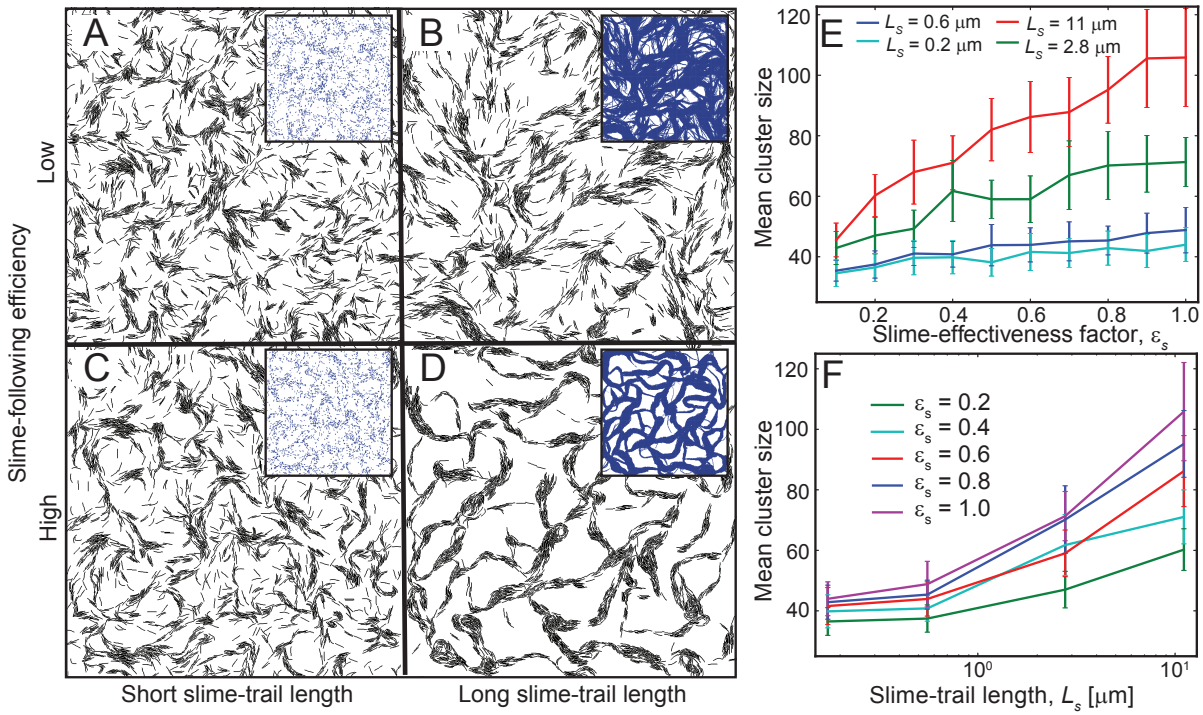


Figure 3.3: Robustness of the slime-trail-following mechanism for cell clustering. (A-D) Snapshots of simulations showing agent clustering behavior ($\eta$=0.24) for variation in the slime effectiveness value and slime trail length at 180 min of simulation time. Only agents with high slime-trail-following efficiency and long slime trails show significant clustering behavior (D). Inset figures show the slime distribution in the simulation region. The mean cluster sizes in the simulations (E) as a function of the slime effectiveness factor, $\epsilon_s$ for different slime trail lengths and (F) as a function of the slime trail length, $L_s$, for different slime effectiveness factor values. Cell clustering improved with increases in the slime effectiveness factor (E), provided the slime trails are sufficiently long, and with increases in the slime trail length (F).

Based on the results thus far, we conclude that an additional mechanism that could reduce random orientation changes in the cells could help overcome destabilizing effects of reversals on clustering. A possible mechanism for this is suggested by the observations of slime-trail-

following by *M. xanthus* cells. *M. xanthus* cells secrete slime, a polymeric gel, from their surface, and it is deposited on the underlying substrate as long trails during cell movement [90]. Furthermore, cells tend to follow their own trails after reversal, and, when in contact with slime trails deposited by others, cells can reorient and follow these [91]. Accordingly, we hypothesize that slime trails act as orientation memory that reduce cells' ability to randomly change travel direction and assist in clustering for reversing cells.

We investigated above mechanism of cell clustering based on slime-trail-following using our ABS framework. As the mechanistic basis of slime-trail following by *M. xanthus* cells is not fully clear, we opt for phenomenological model of slime-trail-following by reorienting part of the propulsive force on cell's leading pole (head node) parallel to the slime trail it is crossing (Refer to Appendix C text for more details). Results of these simulations indicate that slime-trail-following mechanism rescued clustering for reversing cells (Fig. 3.2C, Movie SM4). This is reflected by significant increase in mean cluster sizes (green line in Fig. 3.2B) for slime-trail-following cells compared to cells that do not follow slime trails (dashed line). Additionally, slime-trail-following also increased large-distance orientation correlations of cells indicating formation of aligned cell clusters (Fig. 3.2D).

Notably, the cell clusters in our simulations for reversing cells with slime-trail-following mechanism resemble an interconnected mesh-like structure (Fig. 3.2C). These clusters are distinct form the freely moving isolated cell clusters for non-reversing cells (Fig. 3.1C). However, these interconnected cell clusters in our simulations are very similar to the interconnected mesh-like structure observed for wild-type (reversing) *M. xanthus* cells in experiments [167].

### 3.2.4 Effective slime-following and long slime trails required for clustering in reversing cells

To investigate the robustness of clustering to the values of unknown parameters and demonstrate key features of the model that are essential for clustering, we investigated effects of variation in slime-trail-following ability of cells. For this, we perturbed the parameters that affect the slime-

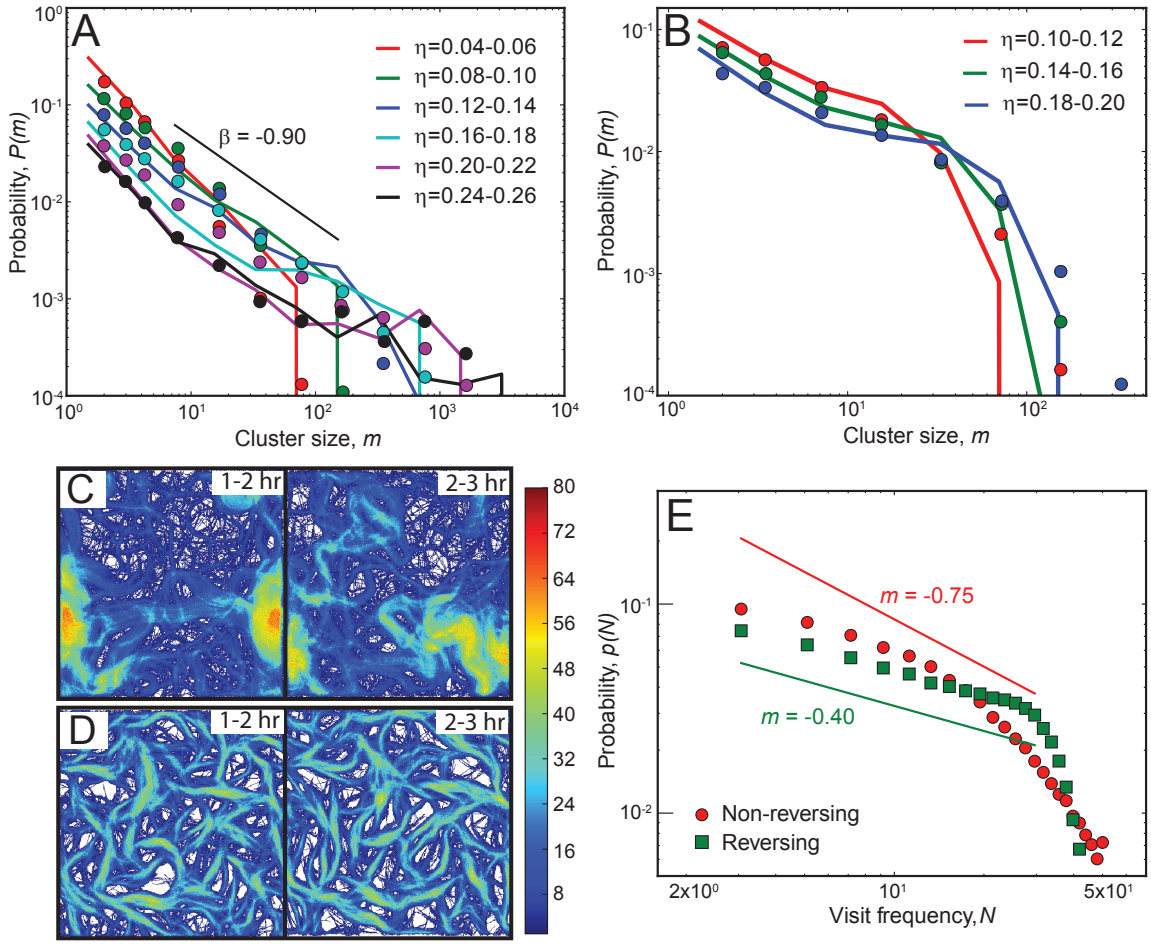


Figure 3.4: Comparison of cell clustering behavior in simulations with experiments. (A-B) Comparison of cluster size distributions (CSD) from simulations (lines) with experimental data (symbols, digitized from Starruß et al. [167]) for non-reversing (A) and reversing (B) cells. Probability, $p(m)$, of finding a cell in a cluster is plotted as a function of the cluster size $m$. We use different sets of slime-trail-following mechanism parameters for non-reversing ($L_s$=0.6 μm, $\epsilon_s$=0.5) and reversing ($L_s$=11 μm, $\epsilon_s$=0.2) agents. CSD results from simulations show a similar trend to that of the experimental data. (A) Non-reversing cells show a power-law-like CSD, whereas reversing cells show a monotonically decreasing CSD (B). (C-D) Heat maps of cell visit frequencies over the simulation region for 2 consecutive hours ($\eta$=0.24). The color bar represents the number of cell visits per hour at a particular location. Non-reversing cells show a dynamic cluster pattern with changes in cell traces (C), whereas reversing cells show a static cluster pattern with the pattern of cell traces remaining approximately the same over time (D). (E) Probability of cell visits, $p(N)$, as a function of visit frequency, $N$, for non-reversing (red) and reversing cells (green) over a 1-hr simulation time (120-180 min). Reversing cells show a large fraction of sites with high visit frequencies compared to non-reversing cells.

trail-following mechanism in our model: slime effectiveness factor ($\epsilon_s$) that controls the ability of a cell to follow a slime trail, and slime trail length ($L_s$) which controls memory effect of cell path (refer to AppendixA for details). High $\epsilon_s$ values decrease a cell's chance of escaping from the slime trail whereas high $L_s$ values increase the chance of a cell to encounter slime trails from other cells. We have varied both parameters over a wide range in our simulations: $\epsilon_s$ (0.1 to 1.0) and $L_s$ (0.16 to 11 μm).

For short slime trail length ($L_s$ =0.16μm) and with low slime effectiveness value ($\epsilon_s = 0.1$), reversing cells show dispersed cell pattern with minimal cell clustering (Fig. 3.3A). This dispersed cell pattern is very similar to the situation for cells without slime-trail-following(Fig. 3.2A). The underlying pattern of slime distribution in the inset shows minimal slime paths in the simulation that do not effectively result in cells to follow others. Increasing slime trail length to higher value ($L_s$=11μm) but keeping the slime effectiveness values low ($\epsilon$=0.1) did not improve cell clustering significantly (Fig. 3.3B). Although cells are able to leave longer slime trails, creating an interconnected slime network (inset), low slime effectiveness ($\epsilon_s$) values allow cells to easily escape from the slime paths and the slime-trail-following cannot effectively stabilize the formed clusters. In the same fashion, an increased slime effectiveness value ($\epsilon_s$=1.0) but with low slime trail length ($L_s$=11μm) also did not result in significant cell clustering (Fig. 3.3C). Here even though cells are able to follow slime trails effectively, slime trails are not long enough that other cells can follow and thus cells are more or less separated except for small cell clusters. However, with high slime effectiveness ($\epsilon_s$=1.0) and long slime trails ($L_s$=11μm), cells are able to produce normal cell clustering pattern for reversing cells (Fig. 3.3D). Here, long slime trails allows for cells to follow other cells' slime trails thus produce a network of interconnected slime network and high slime effectiveness factor prevent cells from escaping from slime paths and thereby results in mesh-like clustering of cells. Thus, we observe that high slime-trail-following efficiency and sufficiently long slime trails allows for reversing cells to form cell clusters.

To further investigate the robustness of slime-trail-following mechanism on agent clustering

behavior, we have measured the mean cluster sizes in simulation for variation in slime effectiveness and slime trail length over a wide range of values ($\epsilon_s = 0.1 - 1.0; L_s = 0.2 - 11$μm - 64x change in slime production rate – see SI Text for details). Our results indicate that, except for very short slime trails ($L_s \geq 1$μm), increase in slime effectiveness values increased the mean cluster sizes (Fig. 3.3E). Similarly, increase in slime trail length resulted in significant increase of mean cluster sizes except for very low slime effectiveness values (Fig. 3.3F). Thus reversing agents along with slime following mechanism can form clusters over a wide range of model parameters.

### 3.2.5 Mechanical clustering model reproduces many features of observed *M. xanthus* cell behavior

To further assess our model of clustering we decided to quantitatively compare our model predictions with the available experimental data on clustering behavior for both reversing and non-reversing strains of *M. xanthus*. To this end we quantified the cell clustering behavior in our simulations by measuring cluster size distribution, cell path maps, and cell visit frequency distribution from our simulations and compared our results with experiments reporting similar metrics [167, 168].

First, we compared cell cluster size distribution from our simulations with experiments of Starruß et al.[167]. For this, we performed simulations with the same cell density as in experimental conditions for both reversing and non-reversing cells. We measured the cluster size distribution (CSD) from our simulations and plotted the probability, $p(m)$, of finding a cell in a cluster of size $m$ as a function of cluster size (solid lines in Fig. 3.4A, B) and compared with experimentally observed distribution (symbols). We observe that our simulation results qualitatively follow similar trend as experimental data. We chose model parameters, slime effectiveness, $\epsilon_s$, slime trail length, $L_s$ to produce an approximate match. Global parameter optimization could further improve the agreement but was not performed. At small cell densities ($\eta = 0.08$) both reversing and non-reversing cells show a monotonically decreasing CSD with

large number of cells are either isolated or belong of small clusters ($m \approx 10 - 10^2$). However, no clusters larger than $10^2$ cells are observed. Nevertheless, with increases in cell density ($\eta$), non-reversing cells show a power-law distribution for CSD ($m^\beta, \beta = -0.90$ – closely matches with the result $\beta = -0.88$ from Starruß et al.[167]), and a significant number of cells now belong to large clusters ($m \approx 10^2 - 10^3$). In contrast, reversing cells show a decreasing CSD with increases in cluster size, and the largest clusters formed are limited to $< 400$ in size even at high cell densities.

Next, inspired by recent experimental studies indicating that wild-type (reversing) and $\Delta$*FrzE* (non-reversing) *M. xanthus* mutants form distinct cell clusters that differ in their shape and dynamic behavior [168], we investigated this phenomena in our simulations. For this, we traced the cell paths over time and plotted cell visit frequency of sites in the simulation region as a heat map for 2 consecutive hours after an initial transition period of 60 min (Fig. 3.4C and D). We observe localized high frequency visit areas and changing shape of cell trace paths over time for non-reversing cells (Fig. 3.4C) indicating formation of large clusters that move all over the simulation region (Movie SM5). In contrast reversing cells organized into interconnected clusters that resemble a mesh-like structure and shape of the structure itself remained approximately the same over time (Fig. 3.4D, Movie SM6). Further the gap regions in the mesh structure (white areas) mostly remain free of cells or show very low visit frequency indicating that reversing cells are confined within the cluster network (clearly seen for high slime-trail-following efficiency parameters, $L_s$ =11μm, $\epsilon_s$ =1.0 – see Movie. SM4). Additionally, we have quantified the probability of cell visits,$p(N)$, as a function of visit frequency, $N$, in our simulations for both motility mutants (Fig. 3.4E). We observe that simulations with reversing cells show large fraction of sites with high visit frequencies ($N = 20-50$ visits for 60 min interval) compared to non-reversing cells. Thus reversing cells in simulation region frequently visit specific sites indicating stationary cluster structures. These results are qualitatively consistent with observations of Thutupalli et al.[168] on dynamic behavior of clusters.

## 3.3 Discussion

Aligned cell clusters are crucial for the formation of multicellular structures observed during *M. xanthus* life cycle [165, 166, 53]. However, mechanisms responsible for the cell alignment and clustering were not completely clear. Inspired by the studies of clustering in self-propelled hard-rods through mechanical collisions [171, 143, 142], we have developed an agent-based-simulation framework to investigate mechanical collisions based cell clustering in *M. xanthus*. In this framework, each agent is based on a biophysical model of individual *M. xanthus* cell that realistically mimics flexible cell motility behavior. Results from our simulations show that non-reversing flexible model agents can form clusters through mechanical collisions alone under realistic cell bending stiffness values of *M. xanthus* cells. However, addition of periodic cell reversals destroyed cell clusters in our simulations. Thus we observe that mechanical collisions alone are insufficient for cell clustering for reversing cells. We hypothesized an additional mechanism of cell clustering based on slime-trail-following by *M. xanthus* cells. As expected, slime-trail-following by cells rescued clustering for reversing cells. By varying the parameters in our model, we observe that effective slime following along with long slime trails are required for cell clustering using slime following mechanism. We quantified cell clustering behavior from our simulations and compared our results with experiments for both non-reversing and reversing cells. We observe that our simulation results qualitatively agree with experimental cell clustering behavior. Thus our analysis show that *M. xanthus* cells can form aligned clusters through mechanical collisions and slime-trail-following.

We believe that the following mechanism enables the reversing *M. xanthus* cells to form clusters through slime trail following (Fig. 3.5): a single *M. xanthus* cell leaves a slime trail while moving on a substrate and traces back its own trail while reversing and thus reinforces its own slime trail. When other cells cross this trail they reorient and align with this slime trail and start following it. This results in a positive feedback mechanism where newly joined cells in the slime trail further reinforce the trail with their own slime causing more cells to join the trail.

Thus more cells, aligned with the original slime trail, are recruited into the trail resulting in cluster of aligned cells. Within a cluster, cells maintain alignment with neighbor cells through mechanical interactions.

In the current study, we limited cell densities ($\eta$) to 0.32 due to the limited availability of experimental data [167]. However, to extrapolate our conclusions, we have simulated the clustering behavior of cells for higher densities (up to $\eta = 0.60$). Results from these simulations indicate that cell alignment and clustering trough mechanical interactions also occur at these high densities (Fig. C.8). Interestingly we observe clustering of reversing cells at high cell densities even without slime-trail-following by cells (Fig. C.8B). These results suggest diminished role of slime trails in collective cell alignment at these conditions as the whole area covered by cells is likely to contain slime. However, we have opted not to investigate these conditions at greater depth due to limitations of our current 2D simulation framework and cluster quantification metrics for such conditions. At high densities cells in our simulations form large continuous clusters such that separating and characterizing individual clusters is practically impossible. Moreover at high cell densities real M. xanthus cells are capable of moving on top of one another resulting in a multi-layered biofilm whose dynamics are different from that of low cell density scenario. These effects would be explored in depth elsewhere.

Our simulations show that distinct clustering behaviors observed in *M. xanthus* mutant strains can be explained through mechanical interactions alone. Quantitative results from our simulations (CSD, cell visit frequency) follow the general trend as observed in experimental data [167, 168]. Even though our results do not exactly match with the experiments, this is understandable as we were aiming to explain the observed cell clustering phenomena with a minimal interaction model. In our current model, we ignored many other interactions that exist among *M. xanthus* cells e.g. twitching of *M. xanthus* that uses type IV pili to pull cells together. Addition of these processes along with further optimization of unmeasurable parameters and choosing others model parameters from direct experimental observations (e.g. distribution of cell orientation changes, reversal time distribution) could further improve our current model

but is beyond the scope of this study.

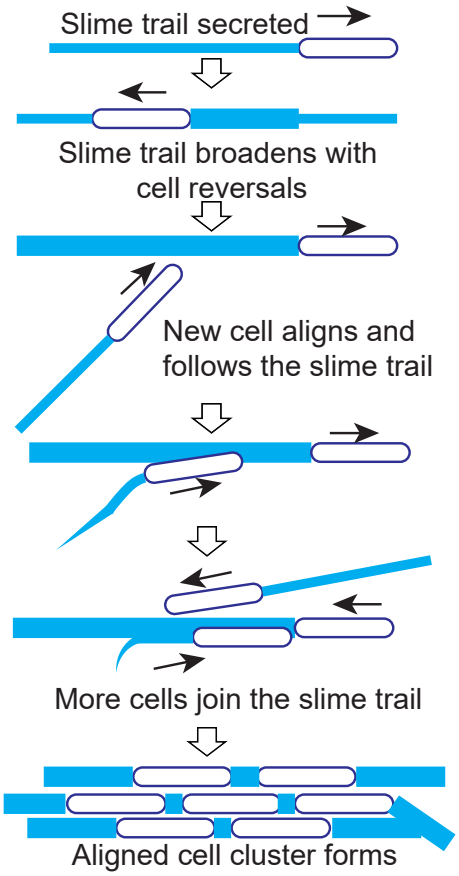


Figure 3.5: Hypothetical mechanism of cell clustering through slime-trail-following in reversing *M. xanthus* cells.

Cell clustering and alignment of cells inside the clusters play major role in *M. xanthus* physiology. *M. xanthus* are predatory bacteria that feed on other bacteria by secreting proteolytic enzymes into their surroundings. To maximize their predation these cells form groups that move together. Alignment of cells inside these groups allows for dense packing of cells per given area there by increasing their predation efficiency. Further, variation in cell clustering behavior observed by Thutupalli et al.[168] with concomitant change in cell reversal frequency may enable starving cells to optimize search for nutrients. During initial phase of starvation, *M. xanthus* cells exhibit low reversal frequency that allows them to form flock like clusters that explore their surroundings for nutrients. Once nutrients are found, cells switch to high reversal frequency thus enabling cells to form stationary cluster structures that allow them for optimal

nutrient gathering.

Notably, cell clustering through slime following is observed in other bacterial systems. A recent study by Zhao et al.[177] showed that *P. aeruginosa* also uses slime-trail-following mechanism to form initial cell clusters. Using cell-tracking algorithms and by fluorescently staining the secreted Psl exopolysaccharides (slime), they concluded that *P. aeruginosa* cells form cell clusters by depositing slime trails that influence the motility of their kin cells, that encounter these trails, to follow them resulting in a positive feedback. Our study shows that *M. xanthus* cells use similar mechanism to form aligned cell clusters. Furthermore, our results show that differences in surface motility mechanisms (e.g. reversals or ability to follow trails) lead to distinct cell clustering behaviors. These distinctions can be used to identify the nature of cell motility from snapshot images of bacteria for which direct observations on individual cells are difficult. Therefore the mechanistic model of cell clustering and alignment developed here can be applicable to a wide class of bacteria displaying surface motility.

# Chapter 4

# Mechanism of circular cell aggregates formation in developmental *M. xanthus* swarms


**Abstract**

Recent experiments with developmental *M. xanthus* mutants that over-express TraA/B protein produced a large number of circular cell aggregates compared to wild-type cells. *M. xanthus* cells in these aggregates self-organize and move in circular/spiral formations that span multiple cell layers. At present we do not have a clear mechanism for this circular movement of *M. xanthus* cells and the increased formation of cell aggregates from TraA/B protein over-expression. In this work, we investigate the mechanism for circular cell aggregate formation in *M. xanthus* cells using our agent-based simulation framework. Our results show that circular cell aggregate formation in *M. xanthus* cells requires a combination of multiple factors such as strong cell reversal suppression, slime-trail-following of cells and neighbor cell alignment through mechanical cell-cell collisions. Our simulation results qualitatively match with the observed motility behavior of cells inside circular aggregates and the overall dynamics of cell aggregates, in contrast to the predictions of a previous model in literature. Further, we show that the increased cell aggregate formation in TraA/B over-expressed *M. xanthus* cells is due to the synergistic effects of TraA/B-mediated physical cell-cell adhesion and the contact based suppression of cell reversals.

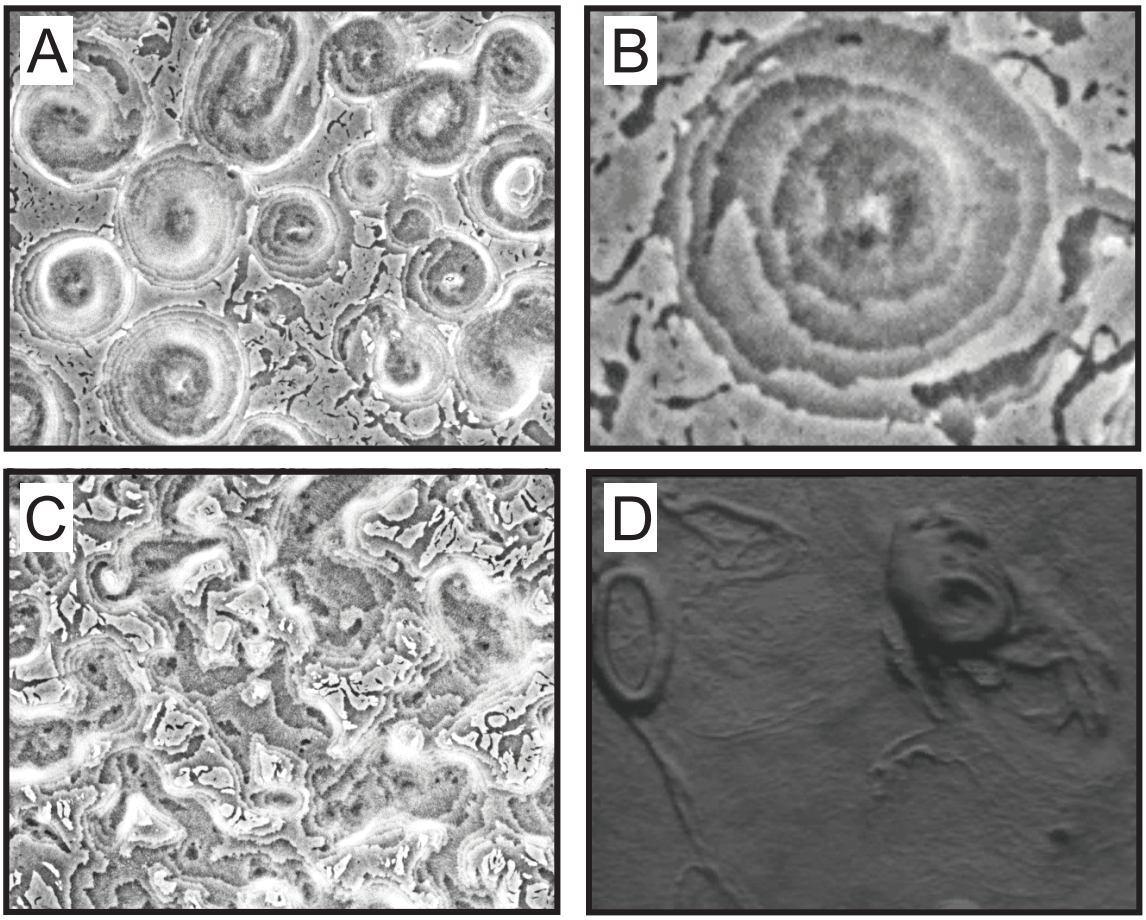


Figure 4.1: Circular cell aggregates observed in *M. xanthus* developmental cell swarms. (A) A large number of circular cell aggregates formed by TraA/B over-expressed *M. xanthus* mutants (B) Close-up view of a single circular cell aggregate. Cells self-organize into circular formations in multiple layers. Multiple cell layers may rotate in synchrony or rotate with different speeds independent of other layers. Consecutive layers in a single stack may also rotate with opposite spins. (C) Relatively few number of circular aggregates (many not completed formed into a circular shape) produced by wild-type *M. xanthus* cells (TraA/B expressed at wild-type cell level). (D) Large circular/spiral cell aggregates formed in wild-type *M. xanthus* developmental swarms. Pictures A, B, C are taken by Pengbo Cao - graduate student in Dr. Daniel Wall Lab, University of Wyoming (unpublished work). Picture D is a snapshot of circular cell aggregates from Reichenbach H et al. [178, 179] myxo movies.

## 4.1 Introduction

### 4.1.1 TraA/B over-expressed *M. xanthus* cells produced large number of circular cell aggregates

Recent experiments from Dr. Daniel Wall Lab, University of Wyoming, with developmental *M. xanthus* mutants that over-express TraA/B protein produced a large number circular cell

aggregates (CCA) (Fig. 4.1A, unpublished results [144]. Work presented in this chapter is performed in collaboration with Dr. Wall lab). TraA/B is a recently discovered two component system protein that facilitates exchange of materials between cells through fusion of their outer membranes [180, 181, 182, 183, 184]. CCAs are also observed in wild-type *M. xanthus* developmental swarms (Fig. 4.1C) [178, 179], albeit to a less extent than swarms with TraA/B over-expressed cells. *M. xanthus* cells in these aggregates self-organize and move in circular/spiral formations that span multiple layers (Fig. 4.1B). Interestingly, cells in individual layers are observed to be moving independently to the overall rotation of the aggregate [144]. Sometimes consecutive cell layers within the same aggregate are observed to be rotating with opposite spins [144]. It is believed that some of these cell structures serve as initial seed centers for much larger 3-dimensional cell aggregates (fruiting bodies) in later stages of *M. xanthus* development process [185, 165]. What makes *M. xanthus* cells aggregate and move in these circular formations is currently unknown.

Cell aggregation during *M. xanthus* development is a well-known multi-stage process spanning over several hours ($\approx 42$ hr) culminating in large 3-dimensional multicellular structures called fruiting bodies, where some of the inner cells of these aggregates turn into environmentally resistant spores. Cell aggregation process in *M. xanthus* was well studied in the literature. A recent study by Xie et al.[186] using image analysis techniques on time-lapse images of *M. xanthus* aggregation identified various metrics that predict the fate of initial cell aggregates maturing into larger fruiting bodies and showed that cell aggregates are dynamic structures. Various other modeling studies also identified the mechanisms underlying cell aggregation process [98, 89, 73]. However, most of these studies concentrated on late stages ($\approx 20 - 40$ hr post starvation) of *M. xanthus* development, and circular cell aggregates are mainly observed during initial stages (below $\approx 20$ hr post starvation) of *M. xanthus* development with transiently formed cell aggregates. A recent study by Cotter et al.[187], by analyzing cell motility patterns during initial stages of aggregate formation, identified that individual cell movement significantly differs while traveling towards and away from the aggregates. However, our current

understanding of the exact mechanisms that govern the initial cell aggregate formation during *M. xanthus* development are still unclear: we currently do not understand why some aggregates stabilize and others disperse with time; why cells move towards aggregates in long cell streams; what are the locations of aggregate formation etc.

### 4.1.2 Mechanism of *M. xanthus* circular cell aggregate formation is not clear

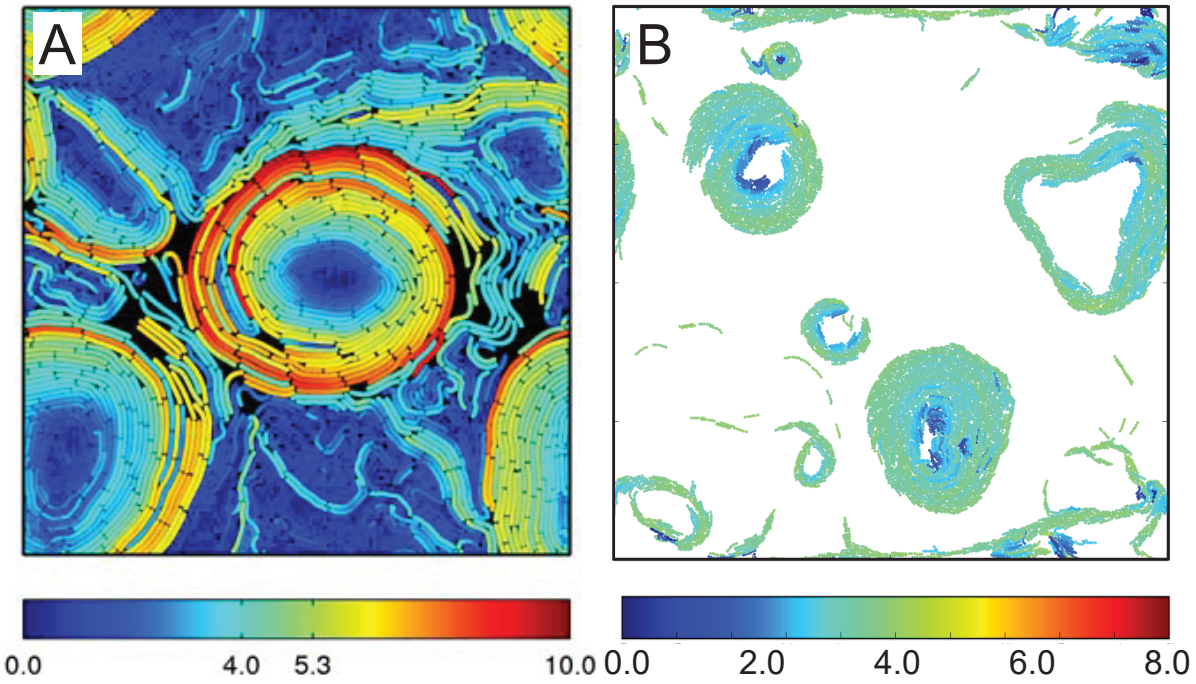


Figure 4.2: Circular cell aggregates formed by model cells in simulations. (A) Circular cell aggregates formed by model *M. xanthus* cells under active guiding forces between cell poles (Reproduced from [106]) (B) Circular cell aggregates formed by model *M. xanthus* cells in our cell clustering simulation (Chapter 3) without active cell guiding forces (Non-reversing model cells with the slime-trail-following mechanism, $L_s$=11 μm, $\epsilon_s$=1.0, $\eta = 0.24$). Color bars represent cell speed in μm/min. Cells in circular aggregates maintain their natural speed ($\approx 4$ μm/min or lower at center of aggregate due to restricted cell movement) in our simulation compared to unrealistically large speeds ($\approx 10$ μm/min) shown by cells at the aggregate edge in Janulevicius et al. model [106].

Circular or spiral movement of cell groups and circular aggregate formation in *M. xanthus* developmental swarms was observed only as a transient process during initial stages of cell aggregation in wild-type *M. xanthus* cells. However, this phenomenon gained recent scientific

interest due to the multiple stable defined patterns produced by *M. xanthus* cells under TraA/B protein over-expression. At present, we do not have a clear understanding of the mechanism behind the circular movement of cells and the formation of these large cell aggregates. During developmental phase, *M. xanthus* cells are known to move in long-chains or streams that lead towards cell aggregate centers [188, 189]. This collective movement of cells in streams towards aggregates requires suppression of normal periodic cell reversals in *M. xanthus* cells [189, 190, 191, 192]. Reversal suppression in *M. xanthus* cells is previously observed in developmental *M. xanthus* cells, but the exact reason for cell reversal suppression is not known. It is assumed that during development, a short-range C-signal is exchanged among cells that inhibits cell reversals [193]. However, the actual components of C-signal or the exact mechanism of this signal exchange were not completely established [39, 93]. Further, CCAs are observed only occasionally during *M. xanthus* development but cell stream formation, through decrease in reversal frequency, is a prominent feature during development. Thus increase in cell reversals alone may not be a sufficient condition to produce CCAs in developmental *M. xanthus* swarms. We currently do not understand how change in cell reversal behavior results in circular movement of cells and which other cell processes contribute to CCA formation in *M. xanthus* cells.

A recent simulation study by Janulevicius et al.[106] using flexible mass-spring model cells showed that CCAs could be formed through short-range active guiding forces between cell poles (Fig. 4.2A). This study assumed that the cell-guiding forces could arise from either physical adhesion between cell poles (tail and head poles of leading and lagging cells in a chain respectively) or through additional cell forces generated in the lagging cell that allows it to actively seek and maintain a constant distance from the leading cell. Further, results from this study indicate that passive-cell-following (lagging cell only turns toward the direction of leading cell but does not actively follow) or any long-range guiding mechanism (e.g. slime-trail-following) did not result in CCAs in their model. Additionally, complete cell reversal suppression between cells that are in end-to-end contact is required for forming CCAs in their

model. Without reversal suppression, their model failed to produce circular cell aggregates. We observe that there is no biological evidence of additional force generation in *M. xanthus* cells that allows them to actively seek other cells. Specifically, the cell motility forces required to maintain the large cell speeds ($\approx$ 10 μm/min at the outer edge of an aggregate in their simulation, see Fig. 4.2A) are biologically unrealistic. Additionally, rigid-body rotation of cell aggregates in their model is different from experimental cell aggregate movement where individual cells are seen to be moving independent of aggregate rotation. Further, based on the proposed mechanism in this model, we can not explain why TraA/B over-expression results in a large number of CCAs.

### 4.1.3 Circular cell aggregates occasionally formed in our *M. xanthus* clustering simulation without active cell forces

In our previous simulation study aimed at investigating *M. xanthus* cell clustering mechanism (Chapter 3) we occasionally observed CCAs in our simulations (Fig. 4.2B) with non-reversing cells under slime-trail-following. Interestingly these aggregates formed without using any additional cell forces in our simulations indicating that active cell guiding forces are not required for CCA formation. However, formation of these cell aggregates in our simulations is not robust i.e. not all simulations with non-reversing cells produces CCAs. In this work, we investigate the conditions for stable CCA formation in our simulations and the mechanism underlying the formation of multiple cell aggregates in TraA/B over-expressed *M. xanthus* strains using our ABS framework.

## 4.2 Results

### 4.2.1 Circular cell aggregates in our simulation do not rotate as rigid bodies

First, we examined the cell motility behavior in simulations that formed circular aggregates. We observe that cells inside the circular aggregates (except for few cells close to the center)

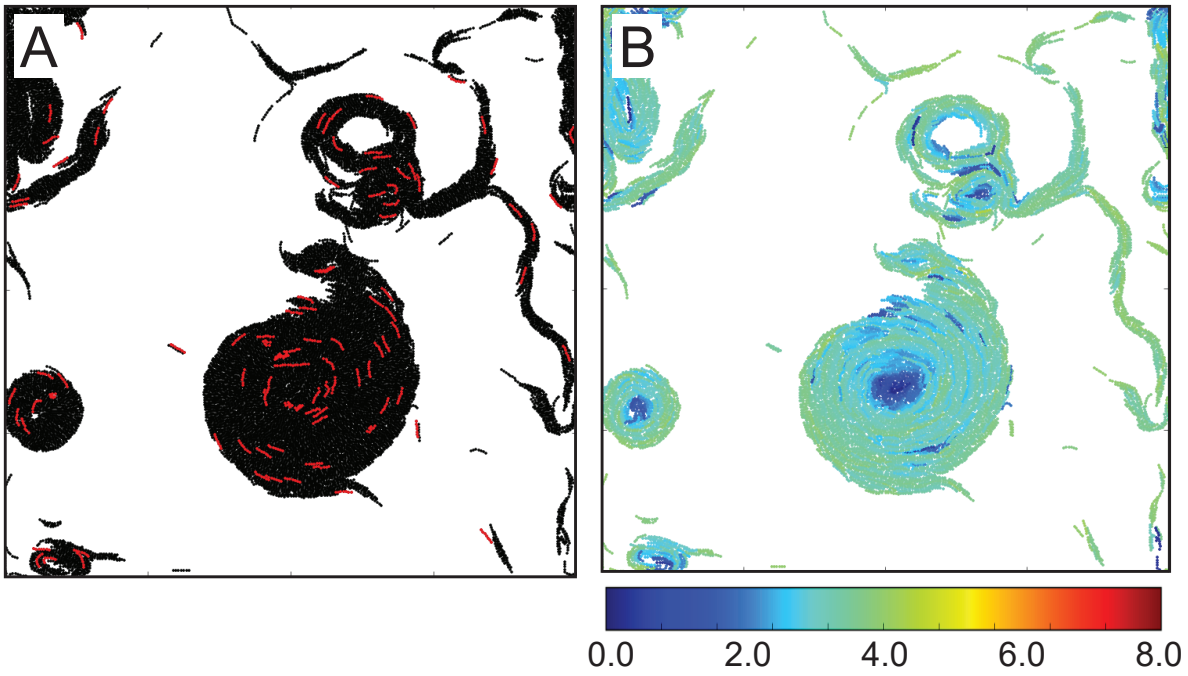


Figure 4.3: Individual model cell motility behavior in circular cell aggregates. (A) Close-up view of circular aggregates formed by model *M. xanthus* cells in our simulation. 3% of model cells are colored red to for easy visualization of individual cell movement. (B) Visualization of cell speeds in simulations. Color bar represents cell speeds in μm/min. Cell speeds inside circular aggregates are similar to cells outside the aggregates in the simulation. Further speed of a cell is independent of its position from the aggregate center (except few cells at the center whose movement is restricted) in contrast to the results of the previous model[106] indicating rigid-body rotation of cell aggregates. Further cells are observed to be sliding past each other inside the aggregate in our simulation. Simulation parameters: non-reversing model cells with the slime-trail-following mechanism, $L_s$=11 μm, $\epsilon_s$=1.0, $\eta = 0.24$.

move with similar speeds ($\approx$ 4μm/min) independent of their position from the center and easily slide past each other. This cell motility behavior is in contrast to the rigid body rotation of circular aggregates predicted by the Janulevicius et al. model [106] where a cell speed inside the aggregate is proportional to its distance from the aggregate center (see Fig. 4.3). Further, this rigid body rotation of aggregates in their model resulted in biologically unrealistic cell speeds ($\approx$ 10 μm/min) in their model. Qualitative observations from experiments also show that cells move with similar speeds and can slide past each other inside the aggregates[144].

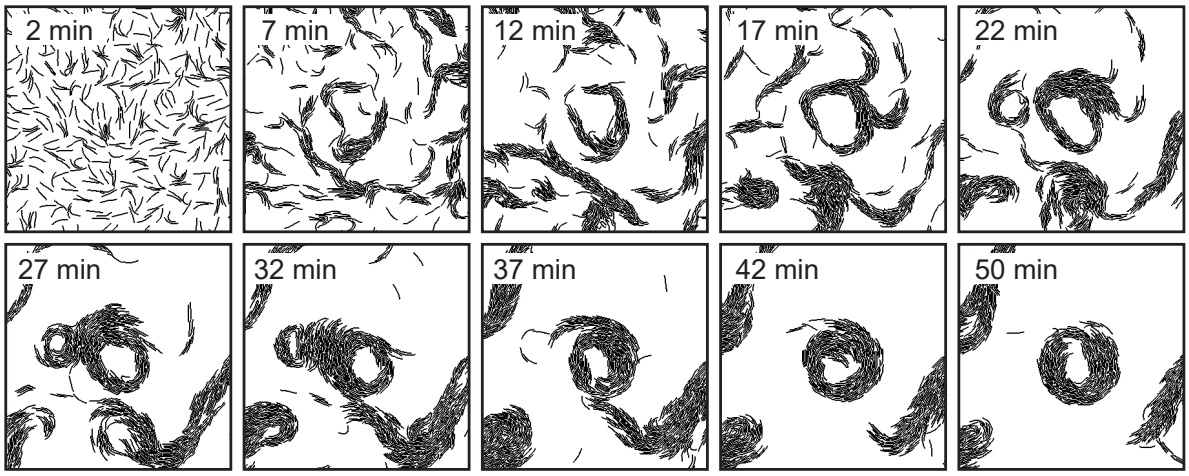


Figure 4.4: Dynamics of circular cell aggregate formation in simulations. Snapshots of simulations showing the formation of initial circular cell aggregates with non-reversing cells. Cells initialized with random positions and orientations (2 min) align with neighbors through collisions and form small cell clusters (7 min). Cells in these clusters follow slime-trails left by other cells and form cell streams (12 min). Occasionally a single cell stream closes on itself by following slime-trail of previous cells and forms an initial circular cell aggregate (12 - 22 min). This initial cell aggregate grows and stabilizes by addition of new cells from neighboring cell streams (17 - 42 min). Not all initial aggregates stabilize and grow. Some aggregates disperse and join other neighbor aggregates (smaller cell aggregate left of central cell aggregate in snapshots from 22 - 42 min)

### 4.2.2 Dynamics of circular cell aggregate formation

Careful observation of cell behavior in simulations with non-reversing model cells under slime-trail-following revealed that initial CCAs form primarily through two mechanisms in our simulations: A single cell stream closing on itself by following its own slime-trail and start moving in a circular fashion (Fig. 4.4) or through the merging of two anti-parallel moving cell streams. These initial CCAs either disperse after some time or stabilize and grow into larger aggregates through joining of other cell streams into the aggregate.

### 4.2.3 Formation of stable circular cell aggregates require strong slime-trail-following, mechanical cell collisions and long cell reversal periods

We observed that not all initial CCAs stabilize and grow into larger cell aggregates. Some of the initial aggregates dispersed with time. So we investigated the conditions required for stable

cell aggregate formation in our simulations. Our results indicate that stable circular aggregates form in our simulations when cells move with low reversal frequency (long reversal periods) under moderate to strong slime-trail-following efficiency and align with neighbor cells through mechanical interactions.

**Circular aggregates are not observed under weak slime-trail-following**

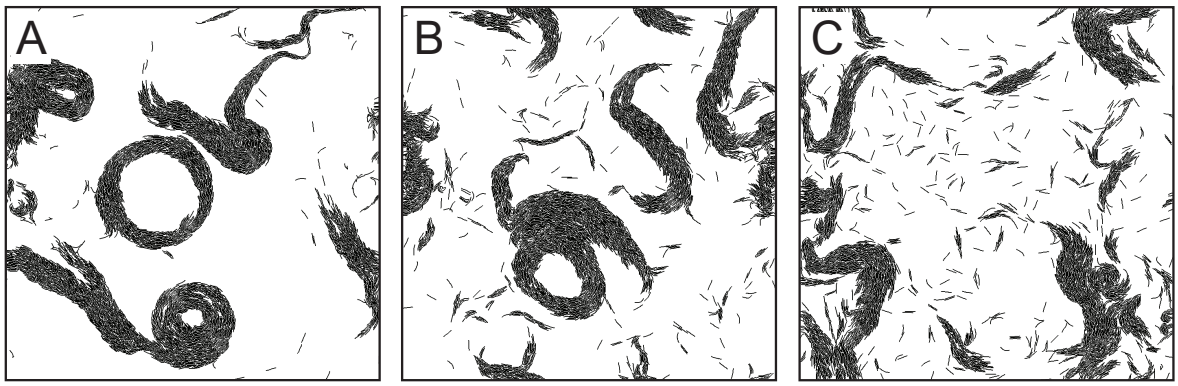


Figure 4.5: Effect of cell slime-trail-following efficiency on the circular aggregate formation. Non-reversing cells readily form circular cell aggregate under strong (A, $L_s$=11 μm, $\epsilon_s$=1.0) and moderate (B, $L_s$=2.8 μm, $\epsilon_s$=0.5) cell slime-trail-following efficiency but failed to form any circular cell aggregates under weak cell slime-trail-following (C, $L_s$=0.6 μm, $\epsilon_s$=0.2)

Since initial cell aggregates in our simulation formed by self-closing of a cell stream, we hypothesize that cell stream formation is essential for circular cell aggregate formation. Cell streams form in our simulations as cells follow other cells through slime-trails. So we systematically varied cell slime-trail-following efficiency and studied CCA formation in our simulations. Since we primarily observed CCAs with non-reversing cells in clustering simulations, we first studied the effect of variation in cell slime-trail-following efficiency with non-reversing model cells.

We observed that under moderate ($L_s$=2.8 μm, $\epsilon_s$=0.5) to strong ($L_s$=11 μm, $\epsilon_s$=1.0) cell slime-trail-following efficiency non-reversing cells readily formed circular aggregates in our simulations (Fig. 4.5A, B). Further, under strong ($L_s$=11 μm, $\epsilon_s$=1.0) slime-trail-following by model cells, CCAs are formed in simulation independent of cell density in simulation region

(SI Fig. D.1). Additionally, CCAs formation in our simulation is robust under strong slime-trail-following i.e. reproduced in all simulation runs (SI Fig. D.2). However, under weak slime-trail-following non-reversing model cells, though formed cell streams, failed to form any circular aggregates in our simulations (Fig. 4.5C). Further, decreasing the slime-trail-following efficiency decreased the formation of CCAs in our simulation (SI Fig. D.4). Thus we observe that CCA formation requires the ability of cells to follow slime-trails with good efficiency.

**Reversing wild-type model cells failed to form circular cell aggregates in simulation**

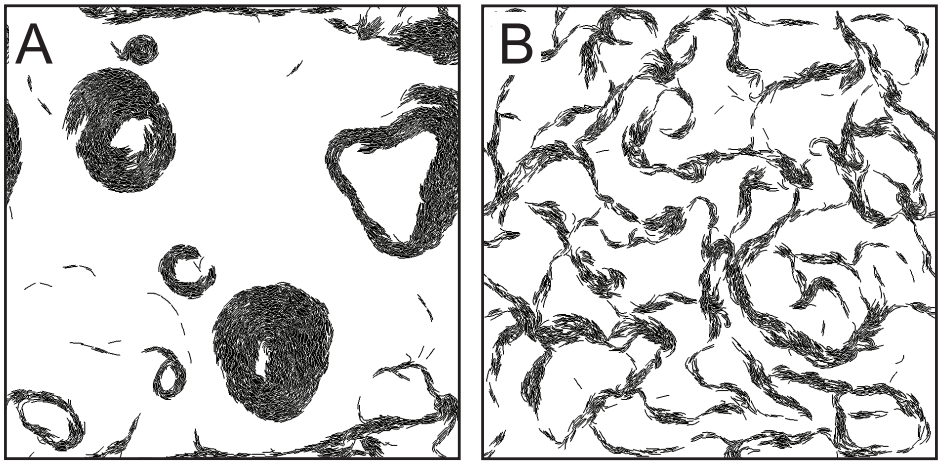


Figure 4.6: Effect of cell reversals on the circular aggregate formation. Non-reversing model cells readily form circular cell aggregate under slime-trail-following ($L_s$=11 μm, $\epsilon_s$=1.0) (A), but reversing wild-type cells (reversal period, $\tau_r = 8$ min) failed to form circular cell aggregates under similar conditions (B)

Next, we studied the effect of cell reversals on CCA formation in our simulations by systematically varying the cell reversal period. We observe that under periodic cell reversals ($\tau_r = 8$ min, wild-type) model cells only formed connected cell clusters and small cell streams but failed to form any circular aggregates (Fig. 4.6). However, we observed an increased probability of forming circular aggregates with increase in cell reversal periods in our simulation (Fig. 4.7). Thus we observe that CCAs form in our simulation for cells with high reversal periods.

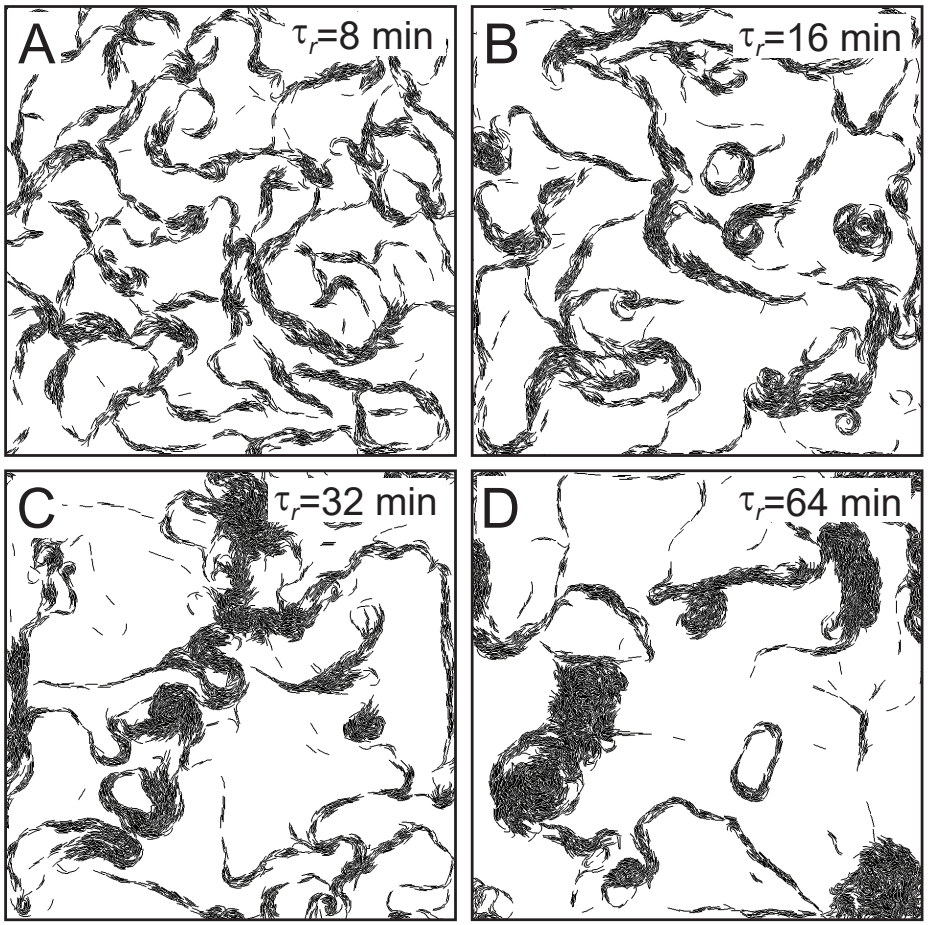


Figure 4.7: Effect of cell reversal period ($\tau_r$) on circular cell aggregate formation (A-D). Increasing cell reversal period increased the probability of CCA formation under strong slime-trail-following ($L_s$=11 μm, $\epsilon_s$=1.0).

**Cell alignment through mechanical cell collisions is essential for CCA formation**

To understand the role of mechanical interactions in CCA formation, we studied cell clustering process with and without mechanical interactions among model cells in our simulation. We observe that removing mechanical interaction among cells (cell-cell collisions turned off) results in decreased collective movement of cells in our simulation. Specifically, non-reversing model cells under strong slime-trail-following (Fig. 4.8A, B) collapsed into narrow streams in absence of cell-cell collisions. These streams sometimes form circular aggregates of single cell width. However, under weak slime-trail-following (Fig. 4.8C, D) non-reversing cells did not

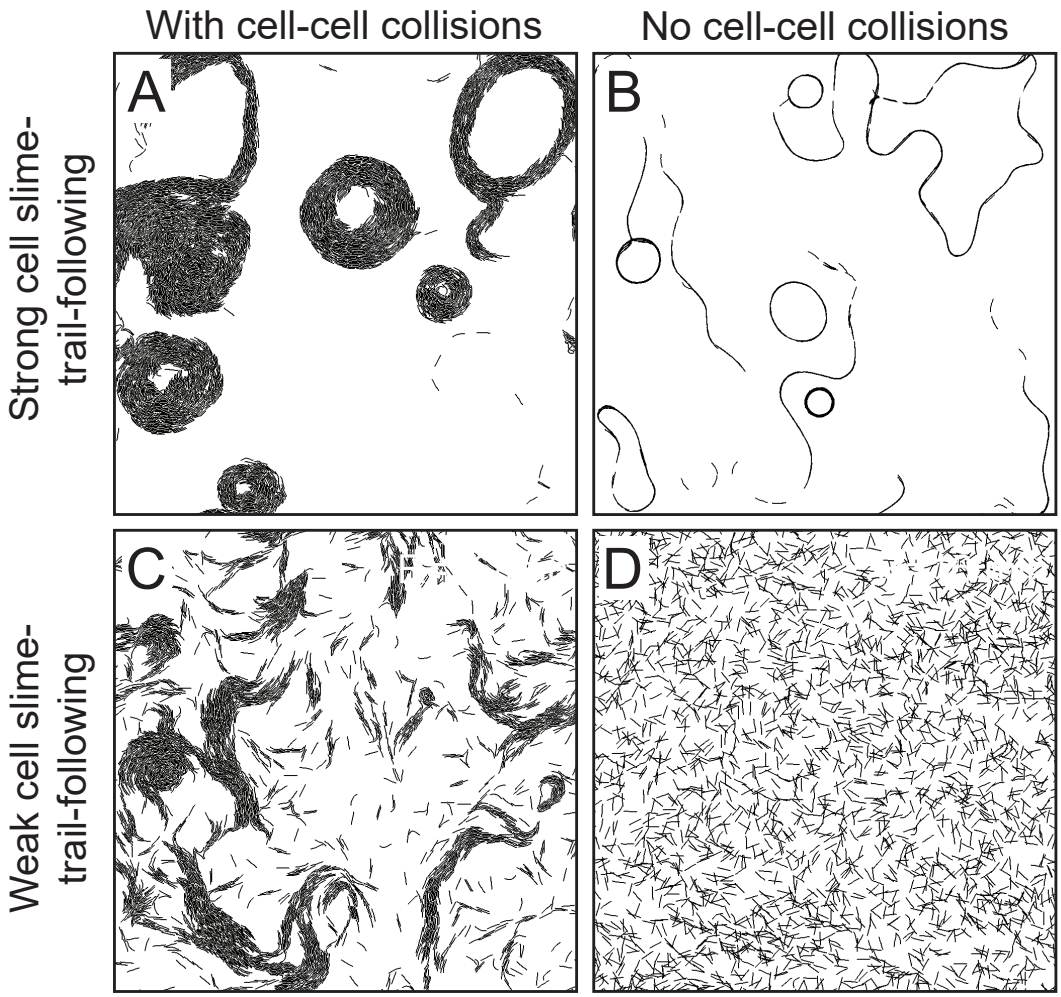


Figure 4.8: Effect of cell-cell mechanical interactions on CCA formation in simulation under different cell slime-trail-following conditions. Disabling cell-cell collisions under strong cell slime-trail-following ($L_s$=11 μm, $\epsilon_s$=1.0, top row) in simulation collapsed all cells into single cell width streams and failed to produce large CCAs as observed in experiments. However under weak cell slime-trail-following ($L_s$=0.6 μm, $\epsilon_s$=0.2, bottom row) and disabling cell-cell collisions resulted in cells moving randomly independent of other neighbor cells and failed to produce any collective movement.

show any collective cell behavior and move randomly. We observe that this lack of collective cell behavior is mainly due to the absence of cell-cell collisions that normally result in cell alignment and subsequent clustering. Thus we observe that neighbor cell alignment through mechanical interactions among cells is essential for cell clustering and CCA formation.

Additionally, we studied the effect of other cell processes on CCA formation and observed that formation of stable circular aggregates requires the presence of cell-substrate attachments

(SI Fig. D.7). Further, we investigated the robustness of our predictions of the conditions (strong slime-trail-following, large cell reversal periods and mechanical cell collisions) required for stable CCAs. For this, we initialized model cells in spiral formations (as a circular aggregate) and studied the stability of CCA under variation of cell processes. Results of these simulations are presented in Appendix D and confirm our predictions of the conditions required for stable CCA formation.

Our simulations results indicate that wild-type reversing cells fail to produce CCAs and the formation of stable CCA requires long cell reversal periods. Thus we need an additional mechanism in our simulation that results in increased cell reversal periods. To this end, we first investigated whether physical (adhesive) interactions among cells lead to increased cell reversal periods.

### 4.2.4 Physical cell-cell interactions fail to produce circular cell aggregates

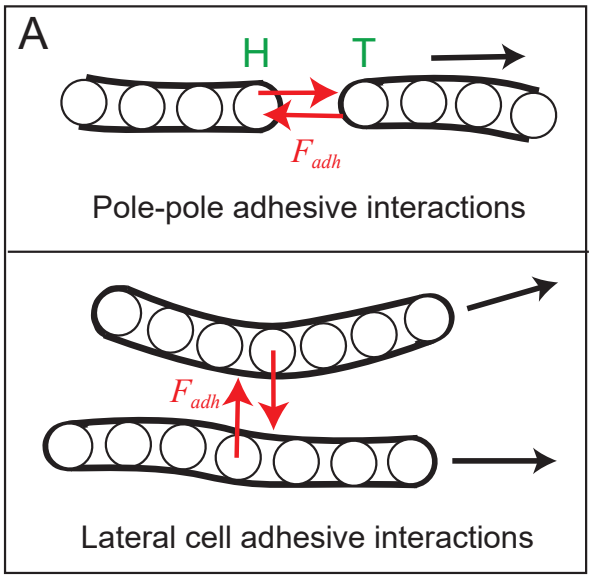


Figure 4.9: Physical adhesive interactions in our cell model (A) Pole-pole adhesion (B) Lateral cell adhesion between adjacent cell nodes

Adhesive interactions among cells can arise through membrane fusion during TraA/B-mediated material exchange. Further, experiments from Dr. Wall Lab show an increased CCA formation

with TraA/B over-expressed cells i.e. increased adhesive interactions among cells. Thus we hypothesized that adhesive interactions among cells affect cell movement. Particularly, strong adhesive bonds between a pair of cells that are moving in tandem (pole-pole) can prevent cell movement during reversal of one of the cells. This altered cell movement effectively increases the reversal period for one of the cells. So we implemented two types (pole-pole and lateral, Fig. 4.9) of adhesive interactions in our cell model and studied their effect on CCA formation in our simulations. These adhesive cell interactions are modeled as linear springs that form when cells are in contact and break under a threshold bond breaking force $F_{max}^{adh}$. Refer to Appendix D for implementation details.

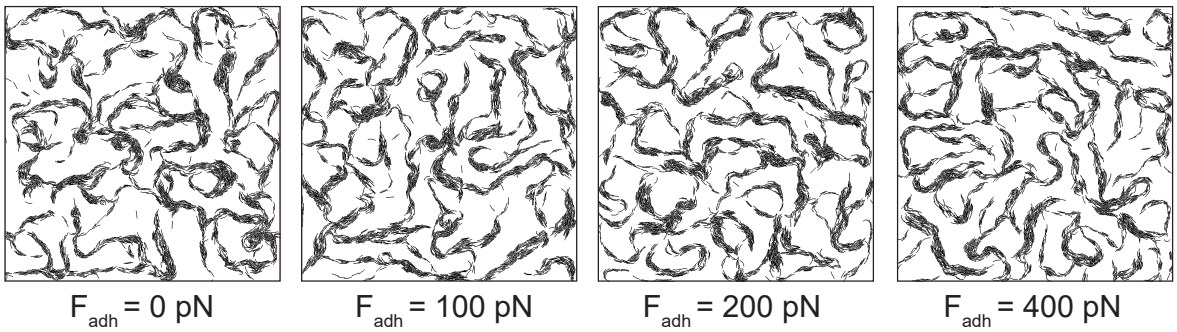


Figure 4.10: Effect of cell-cell adhesion at poles at different adhesion strength values ($F_{adh}$) for periodically reversing cells ($\tau_r = 8$ min)

First, we introduced pole-to-pole adhesive cell interactions in our simulations and studied the clustering behavior of periodically reversing cells moving under strong slime-trail-following conditions under different threshold bond breaking strengths ($F_{max}^{adh}$=100-400pN). We observe that even under very large adhesive interactions ($F_{max}^{adh}$=400 pN) reversing model cells only formed connected cell clusters and did not exhibit any circular cell aggregation. These results are similar to the case without cell-cell adhesive interactions for reversing cells, and we did not observe any significant change in cell clustering behavior. However, non-reversing cells under similar conditions form multiple stable circular aggregates (SI Fig. D.9) similar to the case with no cell-cell adhesive interactions present.

Above results aimed at understanding the effect of adhesive interactions on CCA formation

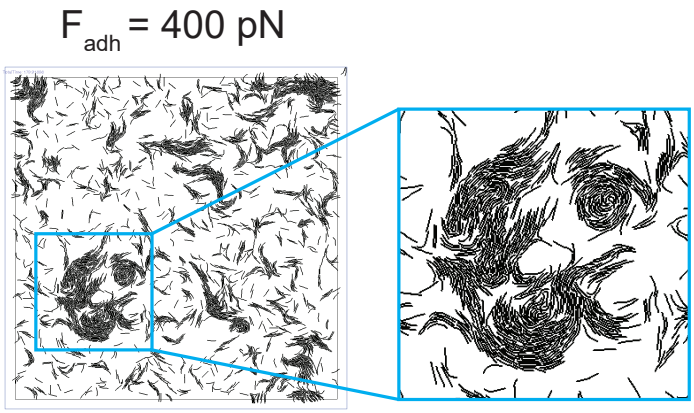


Figure 4.11: Cell-cell adhesive interactions at cell poles result in small circular aggregates. However, these initial aggregates fail to grow and stabilize.

are confounded by the presence of slime-trail-following by cells. To understand the effect of cell-cell adhesions on motility of cells, we introduced adhesive cell-cell interactions in the absence of slime-trail-following by cells and studied cell clustering behavior (see Appendix D). We observe that the adhesive interactions between cell poles make the trailing cells to follow the leading cells and the resulting cell behavior is similar to slime-trail-following by cells with very short slime trails. So we expected the formation of some circular aggregates in our simulation. However, at the end of the simulation (180 min) we did not observe any significant stable circular cell aggregates for both reversing and non-reversing cells even at high threshold bond breaking forces (400 pN, SI Fig. D.10). Careful examination of the cell behavior in these simulations shows that end-to-end adhesions result in formation of small circular aggregates (Fig. 4.11). However, these initial cell aggregates fail to grow due to the absence of long-range guiding mechanism typically provided by slime-trails. Note that we have observed stable circular cell aggregates only for under strong slime-trail-following by cells (Fig. 4.5). We observe that physical adhesions between cells only provide short range guiding mechanism and thus does not stabilize the circular movement of cells in the aggregates.

Next, we studied the effect of lateral cell adhesive interactions and combination of both pole-pole and lateral cell adhesive interactions on CCA formation in our simulations. We observe that in both the cases cells failed to produce any CCAs in our simulation (Fig. 4.12).

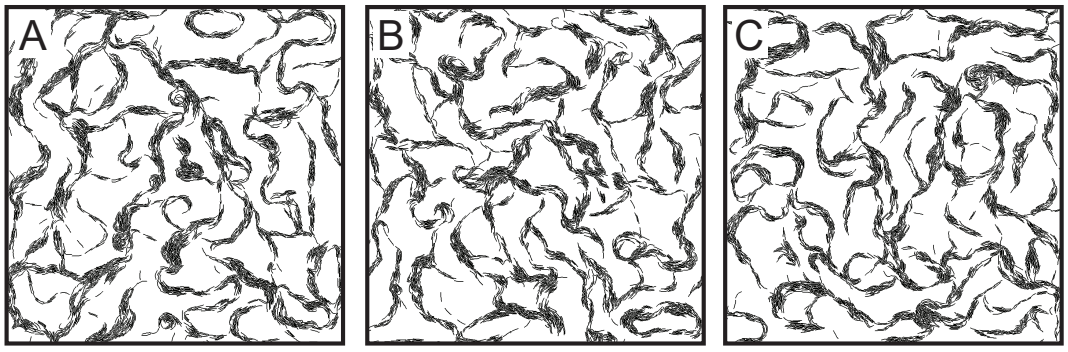


Figure 4.12: Effect of cell-cell adhesion at poles and lateral cell adhesion on circular cell aggregate formation. Simulation snapshots at 180 min for reversing cells with slime-trail-following under (A) pole-pole cell adhesive interactions (B) lateral cell adhesive interactions (C) both pole-pole and lateral cell adhesive interactions. Physical adhesive interactions among reversing model cells failed to produce circular cell aggregates in our simulations.

Increase in cell reversal periods during *M. xanthus* development is well characterized, but the precise mechanism leading to the increased cell reversal periods or reversal suppression among cells is not known. It is assumed that the cell reversal suppression results from the exchange of a C-signal through end-to-end cell contacts. However, the exact cell components involved in this signal exchange are not established. We implement this cell reversal suppression using a phenomenological cell signaling mechanism in our simulation, and investigate whether cell reversal suppression lead to CCA formation in our simulation.

### 4.2.5 Reversing cells form circular cell aggregates under cell-cell contact based reversal suppression

Our results show that physical adhesion between cells is not strong enough to influence cell motility and the resulting cell reversal behavior to produce circular cell aggregates. So next we turn to short range chemical signaling between cells that can affect cell reversals. As mentioned earlier, C-signal exchange among *M. xanthus* cells during development decrease their reversal frequency and results in cell stream formation. Since the exact mechanism of C-signal exchange in not clear, we hypothesize that C-signal exchanges through TraA/B-mediated material transfer between cells that are in contact. We implement the TraA/B mediated cell reversal suppression

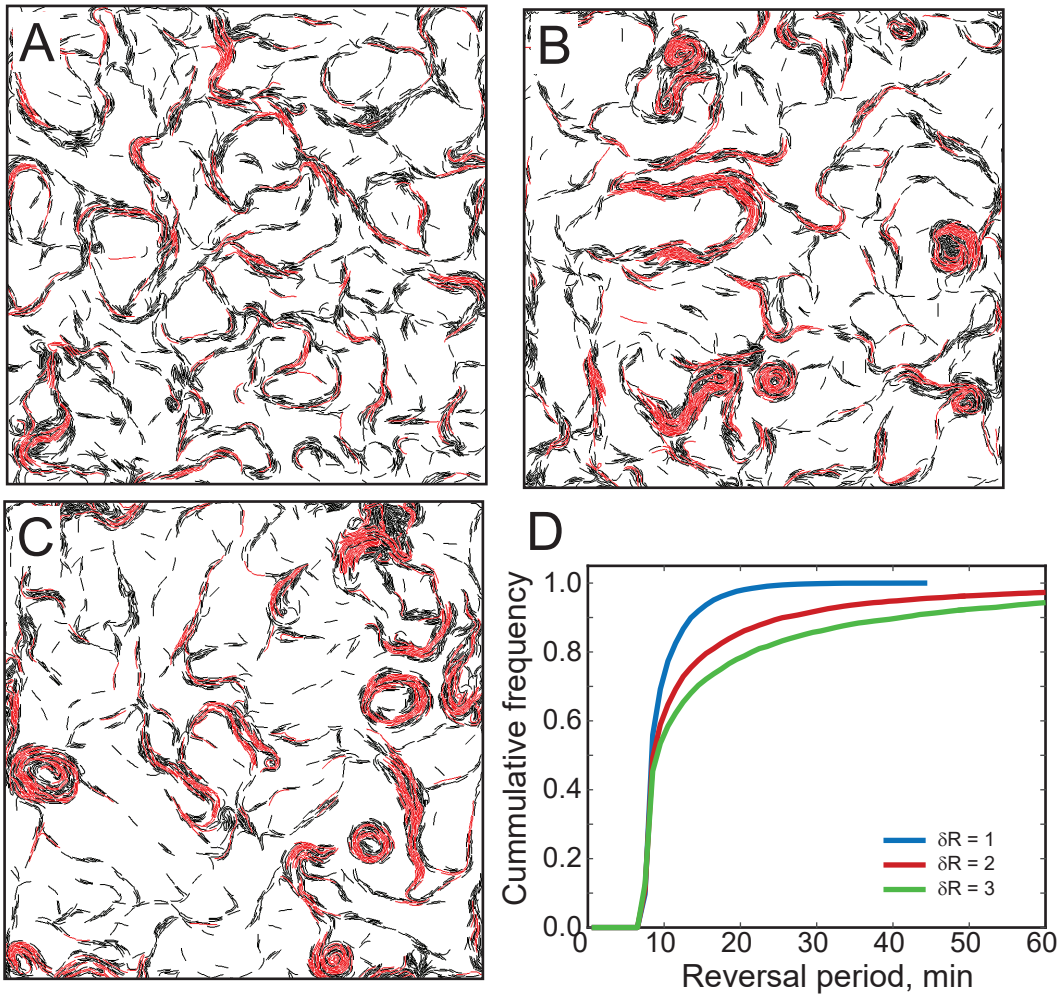


Figure 4.13: Effect of contact based reversal suppression in reversing cells on CCA formation. Periodic reversing cells ($\tau_r$=8 min) produced circular cell aggregates under strong cell reversal suppression. Increasing reversal suppression amount (A) $\delta R = 1$ (B) $\delta R = 2$ (C) $\delta R = 3$ increased circular cell aggregate formation in simulation. Snapshots of simulation at 180 min. Black cells represent normal reversing cells and red cells represent reversal suppressed cells. (D) Cumulative distribution of cell reversal periods in simulation for different cell reversal suppression amounts. Results show an increase cell reversal period distribution to the right with an increase in cell reversal suppression factor. All cells move with wild-type reversal period ($\tau_r$=8 min) in the absence of reversal suppression. Other simulation parameters: $L_s$=2.8 μm, $\epsilon_s$=1.0, $\eta = 0.24$.

in our model using a phenomenological approach where physical contact between cells result in suppression of cell internal reversal clock by a fixed amount in model cells i.e. cell reversal clock is reversed by a fixed amount (reversal suppression factor, $\delta R$) for every time step that cells are in contact. We justify the assumption of turning back of reversal clock in our model by

noting that actual cell reversals in *M. xanthus* cells are maintained through chemical reactions and the transfer of C-signal reverses direction of this reaction. Further, we hypothesize that over-expression of TraA/B results in increased signal exchange among cells that are in contact and thus results in increased circular aggregate formation in *M. xanthus* cells.

First, we tested our hypothesis in our simulation with reversing cells at wild-type TraA/B expression. Since we do not know the contribution of adhesive interactions through TraA/B system, we assume that at wild-type expression level of TraA/B, cell-cell adhesive interactions are minimal (basal level, $F_{max}$=0 pN). Under these conditions, we simulated the clustering behavior of periodically reversing cells ($\tau_r = 8$ min) moving with strong cell slime-trail-following efficiency ($L_s$=11 μm, $\epsilon_s$=1.0) for different cell reversal suppression factor values (Fig. 4.13). We observe that with an increase in cell reversal suppression ($\delta R$ =1-3), connected clusters produced by periodically reversing cells changed to uni-directional moving cell streams and started forming circular cell aggregates under strong cell reversal suppression ($\delta R = 2, 3$). Thus we observe that contact based cell reversal suppression in periodically reversing cells results in CCA formation in our simulation.

**Increased circular cell aggregates in TraA/B over-expressed cells is due to synergistic effects of cell-cell adhesion and contact based cell reversal suppression**

Next, we investigated the effect of over-expression of TraA/B proteins in our simulation by including additional cell-cell adhesive interactions. For simplicity, we maintain the reversal suppression factor ($\delta R = 3$) of TraA/B system at the same level as wild-type TraA/B expression level that resulted in CCA in our simulation. We observe that under additional cell-cell adhesive interactions (due to TraA/B over-expression) model cells in our simulation readily formed multiple stable CCAs (Fig. 4.14). Here, we believe that the additional adhesive interactions due to TraA/B over-expression increase the cell-cell contacts i.e. keeps cells in contact for longer than the wild-type expression level. This increased cell-cell contacts act synergistically with the contact based cell reversal suppression in *M. xanthus* cells and result in increased circular cell

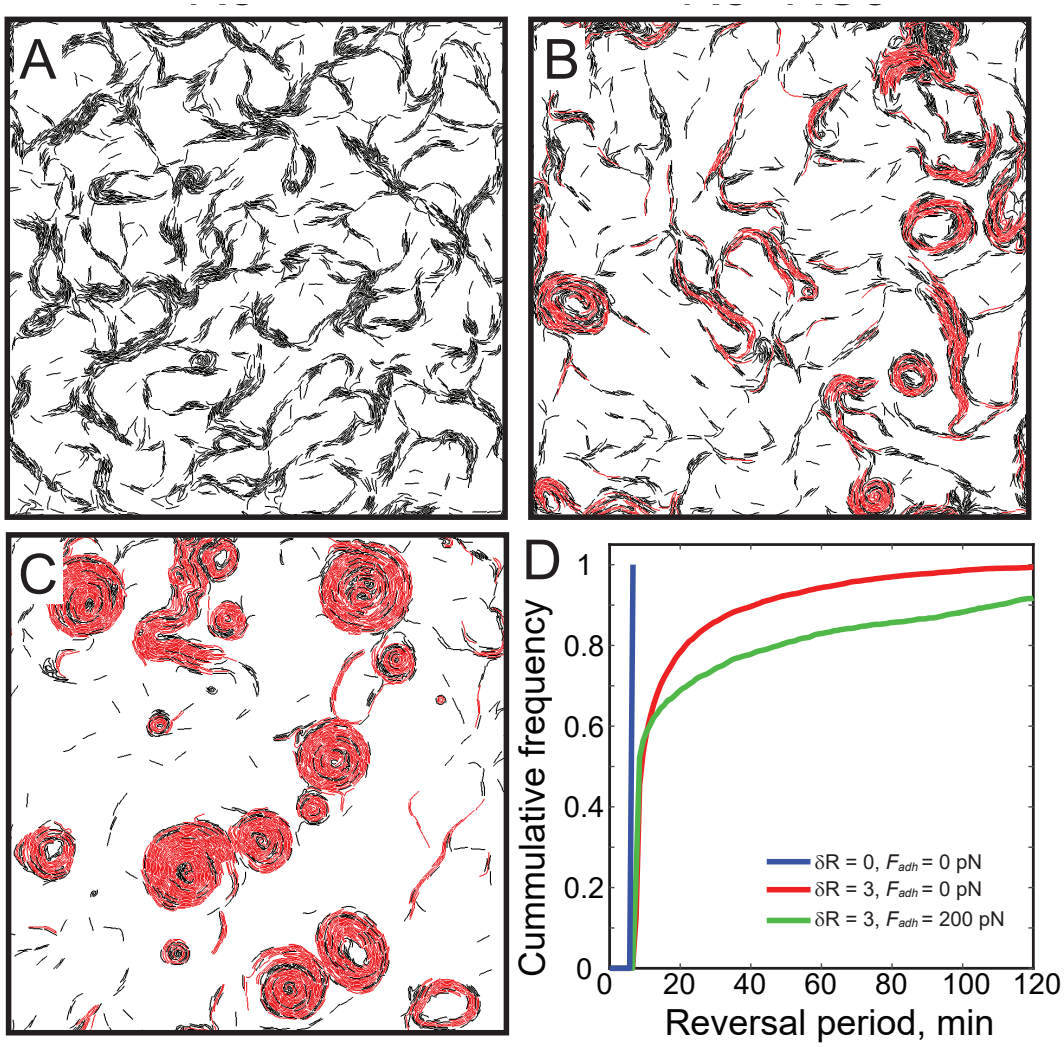


Figure 4.14: Effect of TraA/B over-expression on model cell clustering behavior in simulations. Cell clustering behavior (A) in the absence of cell reversal suppression $\delta R = 0$, (B) under strong cell reversal suppression, $\delta R = 3$ and (C) strong cell reversal suppression, $\delta R = 3$, combined with cell-cell adhesive interactions. Strong cell reversal suppression combined with cell-cell adhesive interactions produced a large number of circular aggregates in our simulation similar to the case of TraA/B over-expressed *M. xanthus* cells in experiments. (D) Cumulative distribution of cell reversal periods for different cell reversal suppression factors. Results show an increase cell reversal period distribution towards right with an increase in reversal suppression. Cells move with wild-type reversal period ($\tau_r$=8 min) in the absence of reversal suppression. Other simulation parameters: $L_s$=2.8 μm, $\epsilon_s$=1.0, $\eta = 0.24$.

aggregates formation in TraA/B over-expressed cells. Thus our proposed mechanism, through contact based cell reversal suppression mediated by TraA/B proteins in *M. xanthus* cells, explains the formation of CCAs in wild-type reversing cells and the increased formation of CCAs

in TraA/B over-expressed cells.

## 4.3 Summary and Future work

In this work, we investigated the mechanism of circular cell aggregate formation in *M. xanthus* developmental swarms using our agent-based-simulation framework. We showed that formation of stable CCAs requires long cell reversal periods or reversal suppression among periodically reversing cells, strong slime-trail-following efficiency of cells and neighbor cell alignment through mechanical interactions among cells and between the cell and the underlying substrate. Cell motility behavior inside circular aggregates in our simulation is qualitatively similar to the cell motility behavior in cell aggregates from experiments i.e., cells inside aggregates are observed to be sliding past one another and moving with similar cell speeds independent of their position from the center of the aggregate. Further, we showed that strong cell reversal suppression leading to large cell reversal periods, an essential requirement for CCA formation, in periodically reversing wild-type cells ($\tau_r$=8min) could not be achieved by physical cell interactions alone. We hypothesized that cell reversal suppression observed in developmental *M. xanthus* swarms is due to the result of an unknown signal exchange between cells that are in contact and this signal exchange is facilitated by TraA/B membrane exchange proteins. Our simulation results show that wild-type periodically reversing cells can readily form CCAs under strong contact based reversal suppression mediated by TraA/B proteins. Further, our results indicate that the increased CCA formation in TraA/B over-expressed cells is due to the synergistic effect of contact based cell reversal suppression and physical adhesive interactions between cells mediated through TraA/B system.

### 4.3.1 Future work

Our current simulations results qualitatively match with experimentally observed cell motility behavior and overall cell aggregate formation in *M. xanthus* developmental swarms. Further, our proposed mechanism for circular aggregation for *M. xanthus* cells is directly testable in

experiments. For future work, we plan to develop methods to measure and quantify cell aggregates formation in cell swarms and overall cell motility behavior to compare our simulation simulations with experimental observations. Specifically, we develop methods to quantify cell aggregation process based on various measurable quantities in both experiments(using image processing techniques) and simulation e.g. aggregates density (number of aggregates), size and distribution of the aggregates, spatial distribution of the aggregates, time required for the aggregate formation, speed and rotation direction of aggregates etc. Additionally, our hypothesis of contact based cell reversal suppression through TraA/B system can tested by quantifying individual cell motility behavior by measuring cell reversal periods for both individual cells and in cells in groups. Quantifying cell motility behavior in experiments, specifically in high-density cell groups, require advance cell tracking and image analysis methods. For this, we plan to collaborate and use advanced cell tracking algorithms for *M. xanthus* cells developed by Dr. Joshua Shaevitz group, Princeton University. For quantifying cell behavior in high-density cell aggregates, we plan to use fluorescent cell tracking techniques where a small fraction ($\approx 1\%$) of total cells are fluorescently labeled that allows tracking of individual cells inside the aggregates.

**Proposed experiments**

We hypothesize that TraA/B system mediates the contact based cell reversal suppression in *M. xanthus* cells during the developmental phase and this effect is enhanced through physical adhesion among cells through TraA/B membrane fusion. We propose to test whether TraA/B mediates *M. xanthus* cell reversal suppression, by observing cell aggregation behavior among modified *M. xanthus* mutants with TraA/B deleted genome ($\Delta$TraA/B) but with additional TraA/B protein analogs that provide cell-cell adhesion. If contact based cell reversal suppression is mediated by TraA/B system, we expect no CCAs in these modified *M. xanthus* mutants.

Next, we propose to test whether TraA/B system itself causes cell reversal suppression i.e., fusion of TraA/B proteins activates reversal suppression in *M. xanthus* cells or it mediates the exchange of another protein that causes cell reversal suppression. This can be tested by con-

structing ΔTraA/B *M. xanthus* mutants containing two-component membrane exchange proteins from other bacteria. If TraA/B system itself activates cell reversal suppression, we expect no CCA formation in these new mutant *M. xanthus* cell swarms.

Additionally, we propose experiments to quantify the effect of cell reversal suppression as a function of TraA/B expression, quantify cell motility behavior (specifically cell reversals periods) for individual cells (no contacts) and when cells are in groups (contacts potentially resulting in cell reversal suppression). Another testable prediction from our simulation results is the requirement of strong cell reversal suppression among cells. This can be tested in experiments by artificially inducing cell reversals under an external chemical control with TraA/B over-expressed *M. xanthus* cells. Since long cell reversal periods resulting from strong cell reversal suppression is negated by induction of artificial cell reversals in this system, we expect a decrease in CCA formation in these experiments.

# Chapter 5

# Expansion dynamics of *M. xanthus* swarms


**Abstract**

During vegetative growth, swarms (cell groups) of *M. xanthus* cells collectively expand into nutrient-rich regions at a constant rate. Interestingly, cell swarm expansion rate for different *M. xanthus* mutants is found to be varying non-monotonically with cell reversal period. Notably, the swarm expansion rate increases with reversal period for strains of cells that reverse more frequently than wild-type cells and then decreases for cells reversing less frequently. This observation suggests that wild-type reversal period is optimized for maximal swarming efficiency of *M. xanthus* bacteria. However, a clear mechanism resulting in this maximum cell swarming efficiency for wild-type cell reversal periods is lacking. In this work, we investigate the mechanism behind the non-monotonic expansion behavior of *M. xanthus* cell swarms using our agent-based-simulation framework based on realistic *M. xanthus* cell motility behavior. In contrast to experiments, our simulation results show an increase in swarm expansion rate with increase in cell reversal period even beyond wild-type cell values. Therefore, an additional mechanism that slows down collective cell motility at high cell reversal periods is needed. A previous study indicated that *M. xanthus* cells slowdown/stall in cell groups during collisions with other cells and these collisions are resolved by cell reversals resulting in overall high collective cell movement for frequently reversing cells. However, by analyzing individual cell motility behavior in experimental *M. xanthus* swarms of wild-type cells and mutants with very large reversal periods, we show that cell stalling is not present in *M. xanthus* swarms. We conclude that the non-monotonic swarm expansion behavior by *M. xanthus* cells is due to an unknown complex signaling mechanism acting in high cell-density regions.

## 5.1 Introduction

### 5.1.1 *M. xanthus* cells in colonies swarm and expand at a constant rate

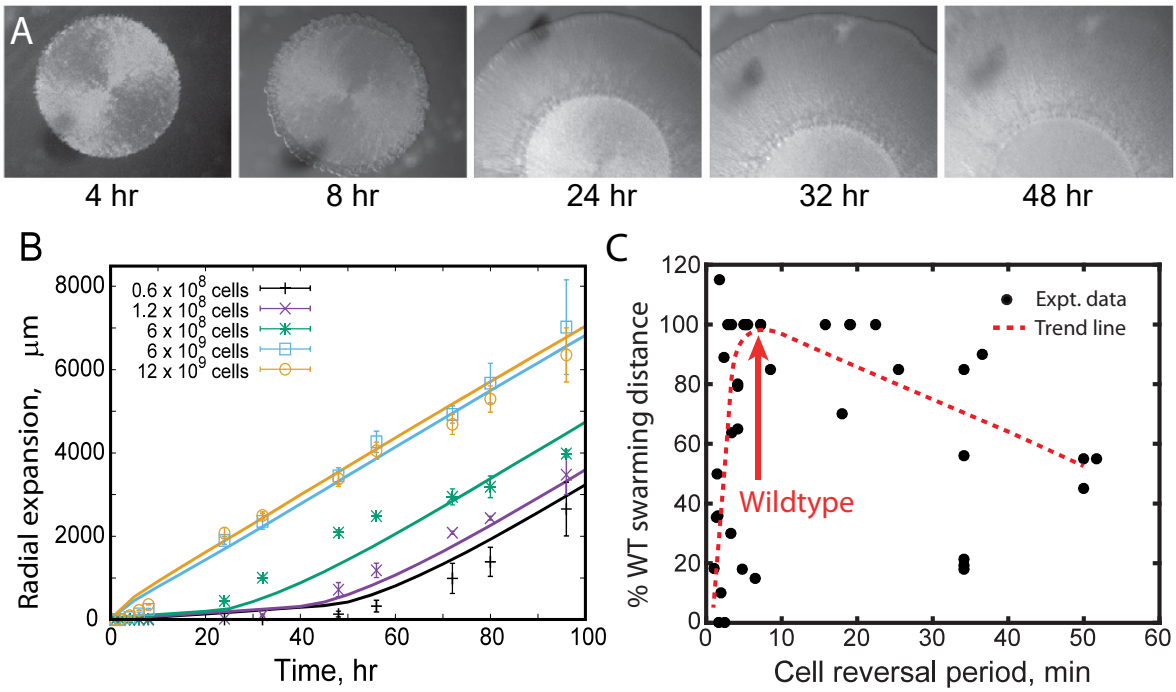


Figure 5.1: *M. xanthus* colony expansion in experiments. (A) Snapshots of *M. xanthus* colony expansion on agar surface with time. Under vegetative growth, starting from an initial cell colony, *M. xanthus* cells divide and swarm outward at a constant rate. (B) *M. xanthus* colony expansion behavior for different initial cell densities in the colony. A *M. xanthus* colony expands at a constant rate with time. However, at lower initial cell densities (black, purple and green lines) colony expansion is preceded by a lag-phase until the cell density reaches a threshold amount and then the linear colony expansion resumes (Panels A, B are reproduced from Patra et al. [83]). (C) Swarm expansion behavior (relative to wild-type) for different *M. xanthus* mutants in experiments (dots - experimental data [194, 195, 196, 197, 198, 103], dotted line - qualitative trend line for the data). *M. xanthus* mutants with reversal periods ($\tau_r$) below wild-type cells ($\tau_r = 8$ min) showed an increasing relative expansion distance with increase in cell reversal periods. However, for *M. xanthus* mutants with reversal periods above wild-type values relative swarm expansion decreased with increase in cell reversal period. Moreover, cell swarming efficiency is maximum for cells with reversal periods close to wild-type *M. xanthus* cell reversal period ($\approx 8$ min). Data is partially compiled by Christopher Cotter, graduate student in Dr. Lawrence Shimkets group, University of Georgia.

*Myxococcus xanthus* is a social bacterium, known for its rich display of dynamic self-organization behaviors under different environmental conditions. These dynamic cell behav-

iors are the result of collective swarming of cells utilizing cell-cell coordination and signaling. Though many signaling systems in *M. xanthus* are discovered, we are still exploring the mechanism of cell swarming and how variation in cell swarming behaviors achieve different *M. xanthus* cell self-organization behaviors.

On a solid agar plate *M. xanthus* cells, starting from an initial cell colony, grow and divide by consuming nutrients and expand outward in a symmetrical fashion (Fig. 5.1A). The speed of *M. xanthus* colony expansion is found to be constant with time (Fig. 5.1B). Interestingly, *M. xanthus* colony expansion was also observed to be dependent on initial cell density of the colony where colonies with lower initial cell density exhibit a lag phase before resuming linear expansion [64, 63, 199]. A recent study by Patra et al.[83] using social motile *M. xanthus* cells ($A^-S^+$) showed that the *M. xanthus* swarm expansion requires a threshold amount of exopolysaccharide material (EPS; secreted by cells). Further, they showed that, the presence of a lag phase in some colonies is due to the low levels of initial EPS content in the colony (low initial cell density) and needs to reach the threshold EPS level before the colony resumes linear expansion behavior. Experiments with a larger initial density of cells, in their study, showed an immediate colony expansion behavior without the lag phase (Fig. 5.1B). However, this study only considered social (S) motility of *M. xanthus* cells and we do not know how addition of adventurous (A) motility in wild-type *M. xanthus* cells affect swarm expansion behavior.

### 5.1.2 Swarm expansion rates for different *M. xanthus* mutants vary non-monotonically with cell reversal period

Cell colonies belonging to different *M. xanthus* motility mutants show different expansion rates in experiments (Fig. 5.1C). Interestingly it was observed that swarm expansion rate of a colony varies non-monotonically with the corresponding cell reversal period of the mutants. Specifically, swarm expansion rate for mutants with lower reversal periods than wild-type cells increased with increase in cell reversal period. However, swarm expansion rate decreased for mutants with reversal periods above wild-type values with increase in cell reversal period. These

observations suggest that wild-type *M. xanthus* cell reversal periods ($\tau_r = 8$ min) are optimized for maximum swarming speed of cell colonies. We currently do not know the reasons for this maximum swarming efficiency for wild-type *M. xanthus* cells. A previous simulation study [103] indicated that frequent stalling of cells in cell groups is the reason for the decrease in swarming efficiency for cells with high reversal periods. This study suggests that cell speeds decrease in high cell density regions due to frequent collision with other cells. When a cell collides with another cell this collision resolved only when the other cell passes or the current cell reverses and the colliding cell stalls until the collision is resolved [103]. Thus frequent cell reversals resolve cells out of cell stalls/jams resulting in better swarming for cells with low cell reversal periods. However, qualitative observations based on cell motility behavior in large cell aggregates e.g. fruiting bodies indicate that cells can move freely even under very high-density conditions [200]. From these observations, the validity cell-stalling explanation in collective cell motility is questionable specifically in the context of *M. xanthus* swarming where cell density is much lower compared to fruiting bodies.

In this work, we investigate the mechanism of cell swarming in wild-type *M. xanthus* cells and study the expansion dynamics of cell swarms for different motility mutants of *M. xanthus*. First, we study expansion dynamics of periodically reversing *M. xanthus* cells using a simple 1-D continuum model. Next, we investigate the swarm expansion behavior at a colony edge by simulating the collective motility of a large number of model cells using our agent-based-simulation (ABS) framework. We compare our simulation results with experimental swarm expansion behavior for different *M. xanthus* mutants with varying cell reversal periods. Additionally, we revisit the cell stalling process in *M. xanthus* swarms proposed in a previous study to understand the discrepancy between swarm dynamics from our current ABS framework with experimental cell swarm dynamics. We analyze individual cell motility data from high-resolution cell tracking of *M. xanthus* cells in swarms from experiments to verify the validity of the cell-stalling process. Finally, we compare cell motility behavior from experimental *M. xanthus* swarms with results from our ABS framework and a Monte-Carlo simulation model

with cell-stalling assumptions.

## 5.2 Results

### 5.2.1 A simple continuum model for *M. xanthus* swarm expansion shows a monotonic swarm expansion rate with cell reversal period

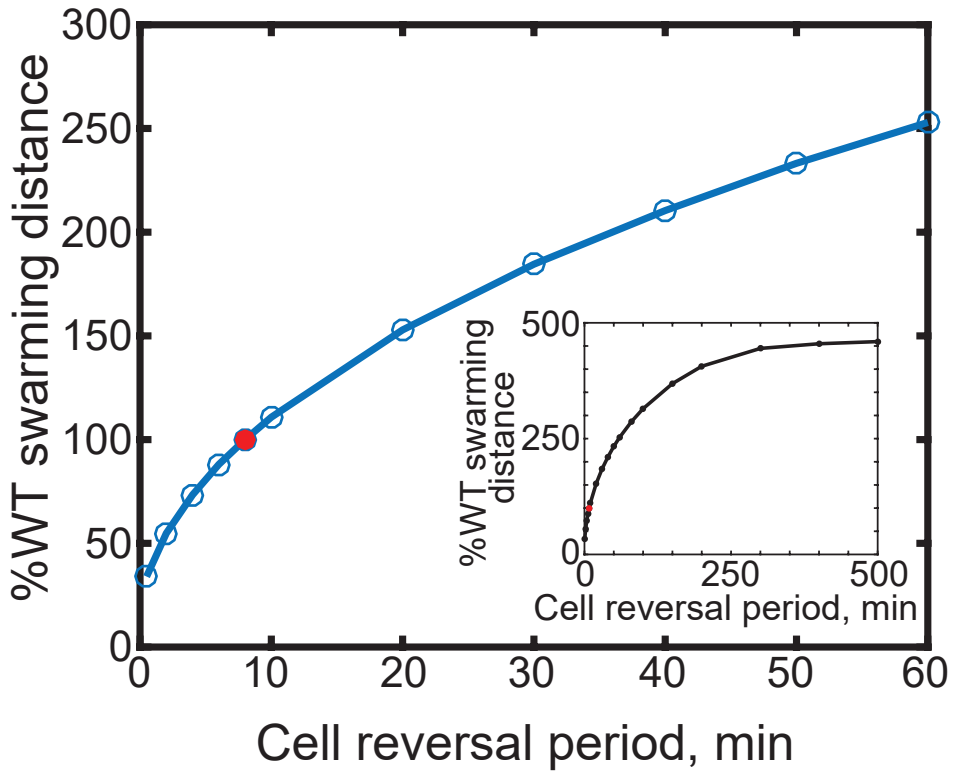


Figure 5.2: Swarm expansion behavior (relative to wild-type cells, red dot - 8 min reversal period) from a simple 1-D continuum model for *M. xanthus* cells as a function of cell reversal period. Cells in the model swarm/expand through a combination of cell growth, motility and cell reversals. At low cell reversal period values, swarm expansion increased with increase in cell reversal period up to wild-type cell values similar to experiments. However, in contrast to experimental observations, swarm expansion rate in model increased with increase in cell reversal periods for reversal periods beyond wild-type values. Further, we observe that swarm expansion rate saturates for very high cell reversal periods (≈500 min; see inset).

To understand the expansion behavior of *M. xanthus* cell colonies with reversing cells, we developed a simple 1-D continuum model[1] of colony expansion based on telegraph equations

[1]Some initial calculations based on this model are preformed by Maria Lalata, under-graduate summer intern

[201]. Cells in this model swarm/expand through a combination of cell growth, motility and cell reversals. Movement and expansion behavior of such a cell colony can be described by a set of partial differential equations (Eqn. 5.1). Here the movement of a colony of reversing cells in a 1-D channel is described by two separate cell groups of left and right moving cells (densities $\rho^+(x,t),\ \rho^-(x,t)$ respectively). Cells move with a net speed of $v$, and random noise in cell movement is described by the diffusion process (diffusion coefficient $D$, [202]). Cells grow (growth rate $g$ growth rate) and divide by consuming nutrients and we describe cell growth kinetics using logistic growth model (saturation constant or carrying capacity $K$ [203]). Cells switch/reverse from left to right moving (and vice versa) at a rate $\lambda$ (cell reversal frequency, $1/\lambda$ - cell reversal period). Refer to Appendix E for details on solution procedure of these equations and colony expansion dynamics resulting from these equations.

$$\begin{aligned}
\frac{\partial \rho^+}{\partial t} + v\frac{\partial \rho^+}{\partial x} &= D\frac{\partial^2 \rho^+}{\partial x^2} + g\rho^+(1-\rho^{tot}/K) + \lambda(\rho^- - \rho^+) \\
\frac{\partial \rho^-}{\partial t} - \underbrace{v\frac{\partial \rho^-}{\partial x}}_{\text{Movement}} &= \underbrace{D\frac{\partial^2 \rho^-}{\partial x^2}}_{\text{Diffusion}} + \underbrace{g\rho^-(1-\rho^{tot}/K)}_{\text{Growth}} + \underbrace{\lambda(\rho^+ - \rho^-)}_{\text{Reversals}}
\end{aligned} \tag{5.1}$$

We observed that total cell density ($\rho^{tot} = \rho^+ + \rho^-$) in the colony increases due to cell growth and the colony expands forward at a constant rate (see Fig. 5.2A) after an initial transient period. These results are similar to the observations of constant rate colony expansion from experiments and previous modeling studies [83]. Next, we measured the steady-state colony expansion rate at different cell reversal periods and calculated the relative swarming distance of the colony (after a fixed amount of time, 96 hr) with respect to the wild-type cell colony expansion distance. We observe that with an increase in cell reversal period, relative swarm expansion distance increased for values below wild-type cell values similar to experiments. However, for cell reversal periods beyond wild-type cell values we observed a continued increase in colony expansion with increase in cell reversal period. This is in contrast to the experimentally ob-

in CTBP FIS program

served decreasing colony expansion behavior with increase in cell reversal period at high cell reversal period values (> wild-type cell values). Further, our model shows a saturation behavior for colony expansion at very large cell reversal period values (see Fig. 5.2 inset).

We observe that our 1-D continuum model for *M. xanthus* colony expansion failed to reproduce the observed non-monotonic colony expansion behavior with varying cell reversal period. However, *M. xanthus* colonies grow and expand on 2-D surfaces and also includes many other complexes cell processes (e.g. cell orientation change during movement resulting in non-linear expansion with time than simple 1-D channel, cell-cell collisions resulting change in overall travel direction of the cell group, *M. xanthus* cells following slime trails of other cells) which our simple continuum model does not describe. To better understand *M. xanthus* colony expansion behavior under complex cell-cell interactions on 2-D surfaces, we study the swarm expansion behavior of *M. xanthus* cells using our ABS framework with realistic cell motility and volume exclusion interactions.

### 5.2.2 Agent-based-simulation with excluded volume interactions produces a monotonic swarm expansion behavior with increasing cell reversal period

An expanding *M. xanthus* cell colony typically contains $10^6 - 10^8$ cells. Simulating such large number of cells with realistic interactions is not computationally feasible. So we study the expansion dynamics of *M. xanthus* swarm at a colony edge in our simulation (similar to a previous simulation study[103] in literature). In this setup, cell swarm expansion is studied in a rectangular simulation region ($L_{sim}/W_{sim} > 5$) (Fig. 5.3A) with cells initially positioned in a constant cell density region (shaded area) at the bottom edge of the rectangle. This region in our simulation represents a small region at the outer edge of a full circular cell colony. We employ periodic boundary conditions at the left and right boundaries to simulate continuum around colony edge. We use reflective boundary conditions i.e. we rotate the travel direction of a cell by 180° when the cell touches this boundary. Reflective boundaries at bottom edge simulate high cell-density conditions in the interior of the cell colony beyond the bottom edge where

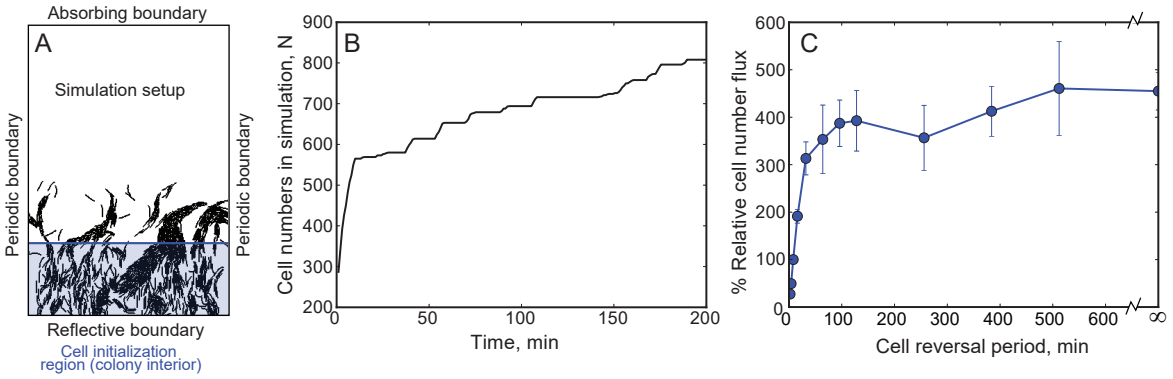


Figure 5.3: Model cell swarm expansion behavior in agent-based simulations. (A) Schematic of simulation setup in a rectangular region representing cell swarming behavior out of colony edge with biophysical cell model simulation. Cells are initialized in the constant cell density region (shaded area) representing colony interior. Cells swarm out from the initial region and new cells are added to the initialization region to maintain cell density constant in the initial region. (B) Cell number flux increase in the simulation with time as cells leave the initial region (simulation results with reversing cells, $\tau_r = 8$ min). (C) Relative swarm expansion behavior of cells in ABS as a function of cell reversal period

space is limited for cell movement and a dynamic equilibrium between cells moving in and out of the interior region exists i.e. equivalent number of cells move in and out of the colony interior to the edge. We maintain the initial region (shaded region, Fgi. 5.3A) at a constant cell density, to simulate high-density colony interior and edge, by adding additional cells to the region when cells swarm out beyond the upper edge of the initial region. We employ absorbing boundary conditions at the top edge of the simulation region which removes cells from simulation i.e. cells moved out of the region of interest. We remove the cells from beyond region of interest to minimize the computational cost.

Starting from random positions and orientations cells in the initialization region move and interact with other cells through collisions and form cell clusters. When these cell clusters swarm out of the initial region, additional cells are added to the initial region to keep the cell density constant. Thus the total number of cells in the simulation region increases as cells swarm out of the colony edge. We measure the total number of cells in the simulation region as a function of time. We observed that, with time, cells swarm out of initialization region and the cell numbers ($N$) increased at a constant rate with time (Fig. 5.3B). We studied swarm

expansion behavior of different mutants in our simulation by measuring the cell number flux ($(N_{final} - N_0)/T_{sim}$ i.e. number of new cells added to system/total simulation time, a measure of swarm expansion rate) for different cell reversal period values. We plotted the relative cell number flux (with respect to wild-type cell reversal period) as a function of cell reversal period ($\tau_r$). We observe that the relative swarm expansion rate monotonically increased with increase in cell reversal period (Fig. 5.3C), beyond wild-type cell reversal periods, saturating at ≈500% for non-reversing cells ($\tau_r = \infty$, as predicted by 1-D model). Specifically, we did not observe a decrease in swarm expansion behavior at high cell reversal periods. Thus our biophysical cell simulation model with realistic cell interactions failed to capture the non-monotonic cell swarm expansion dynamics observed in experiments.

Based on our results from the continuum model and biophysical cell simulations, we observe that swarm expansion behavior of reversing cells monotonically increases with increase in cell reversal period. We believe that the decrease in *M. xanthus* cell swarm expansion for cell reversal periods beyond wild-type cell values is due to an additional mechanism acting in *M. xanthus* swarms. Thus we need a mechanism that slows down swarm movement at high cell reversal period values. Frequent cell stalling in cell groups with high reversal periods is suggested to be the reason for the decrease in swarm expansion rate in literature [103]. We explore this mechanism of cell-stalling in *M. xanthus* swarms next.

### 5.2.3 Swarm expansion behavior under cell-stalling process

A previous study by Wu et al. [103] based on qualitative observations of individual *M. xanthus* cell motility behavior indicated that *M. xanthus* cells stall (stop moving) during collisions with other cells specifically for pole-to-lateral cell collisions. Cell collisions are resolved when the other cell passes or the current cell reverses. Thus this study suggested that cells with high cell reversal periods frequently stall in cell groups and the cells with frequent reversals are able to resolve cell collisions better resulting in high collective cell movement. This study reproduced the non-monotonic expansion behavior of *M. xanthus* cells with reversal period by simulating

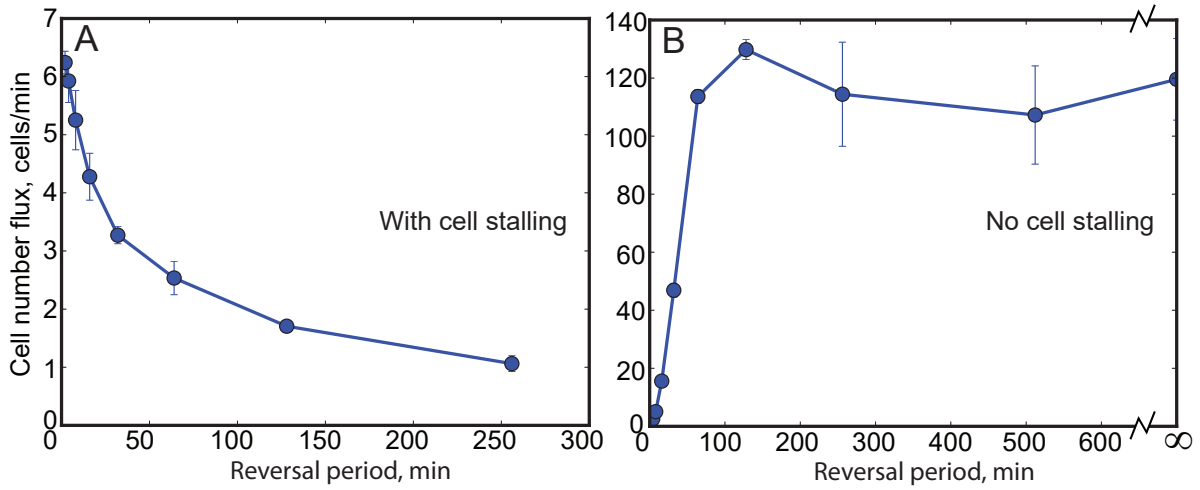


Figure 5.4: Swarm expansion rate in Monte-Carlo simulation model with cell-stalling process present (A) and in the absence of cell-stalling process (B). Under cell-stalling process, swarm expansion rate (cell number flux) decreased with increase in cell reversal period similar to the observations of Wu et al.[103]. However, in the absence of cell-stalling process, Monte-Carlo simulation model produced an increase in swarm expansion rate with cell reversal period similar to the results from biophysical cell model, Fig. 5.3C.

model *M. xanthus* cell swarm expansion behavior under above cell-stalling process using a Monte-Carlo simulation framework.

In our previous simulations aimed at understanding cell clustering process (Chapter 3), we did not observe any significant decrease in model cell speeds inside cell clusters or stalling of cells during collisions for both reversing ($\tau_r$ =8 min) and non-reversing cells (SI Fig. E.5) even for high cell densities ($\eta$=0.4). To understand the discrepancy in cell motility behavior and the resulting swarm expansion behavior between our simulation and the previous study with cell-stalling process [103], we replicated the Monte-Carlo simulation model for *M. xanthus* cells from Wu et al. [103] study (refer to Appendix E details) and studied swarm expansion behavior of *M. xanthus* cells under cell-stalling conditions. Using this model we simulated swarm expansion of model *M. xanthus* cells from a colony edge (similar to simulation setup in Fig. 5.3A) and measured the total number of cells in simulation region with time. Here, similar to our agent-based-simulation for swarm expansion, we maintain the cell density in the initial region constant by adding new cells to this region as cells swarm out.

We observe that wild-type ($\tau_r = 8$ min) model cells in simulation collectively swarm out

of the initial region and the cell numbers increased with time (SI Fig. E.7). Next, we varied the reversal period of cells and studied the swarm expansion behavior by measuring the cell number flux from initial cell region. We observe that with cell-stalling present during cell collisions, swarm expansion rate decreased with increase in cell reversal period (Fig. 5.4A) at high cell reversal period values similar to the results from Wu et al. study. However, we did not observe the increase in swarm expansion rate with cell reversal period for low cell reversal period values (< 8 min). Next, we simulated the swarm expansion behavior from a colony edge with a mix of reversing and non-reversing model cells similar to the previous study. We measured the steady-state swarm expansion rate in our simulation for varying fraction of non-reversing cells. We observe a decrease in swarm expansion rate with increase in non-reversing cell fraction in Monte-Carlo simulation (Fig. E.8) indicating that reversing cells are able to swarm better than non-reversing cells. Our results from agent-based-simulation under similar conditions are in contrast to the results of Monte-Carlo simulation model, and showed an increasing swarm expansion rate with increase in non-reversing cell fraction indicating a better swarm expansion efficiency for non-reversing cells.

Both our agent-based simulation (ABS) and the Monte-Carlo simulation (MCS) simulate the motility behavior of model *M. xanthus* cells under similar cell processes i.e. individual cells are move through A-motility in their long-axis direction, cells follow slime-trails of other cells, cells align with neighbor cells through mechanical collisions (ABS) or phenomenological rules (MCS). We believe that the contrasting cell expansion behavior from our agent-based-simulation and the Monte-Carlo simulation model is mainly due to the additional cell-stalling process in Monte-Carlo simulation. To test this hypothesis, we turned-off cell-stalling in MC simulation and studied the swarm expansion behavior under varying cell reversal period values. In the absence of cell-stalling process, swarm expansion showed an increase in swarm expansion with increase in cell reversal periods similar to the results from ABS (Fig. 5.4B).

Thus we observe that the decrease in cell swarm expansion behavior at high cell reversal periods in the previous study is mainly due to the cell-stalling assumptions in the simulation.

Another interesting observation from our MC simulation (also observed in Wu et al.'s study) is that simulations with non-reversing cells alone moving under cell-stalling process resulted in zero swarm expansion rate i.e. cell movement completely stopped in the simulation. However, non-reversing *M. xanthus* mutants in experiments show motility in swarms [168]. Further cell movement is observed in *M. xanthus* developmental aggregates where cells are packed at high-density into 3-dimensional cell mounds [200]. Thus the cell-stalling assumptions may not be completely true in *M. xanthus* cell swarm movement. So we next look into the validity of the cell-stalling assumptions in *M. xanthus* swarms.

### 5.2.4 Cell-stalling not present in *M. xanthus* swarms

**Experimental cell speeds distributions do not indicate significant decrease in cell speeds in *M. xanthus* swarms**

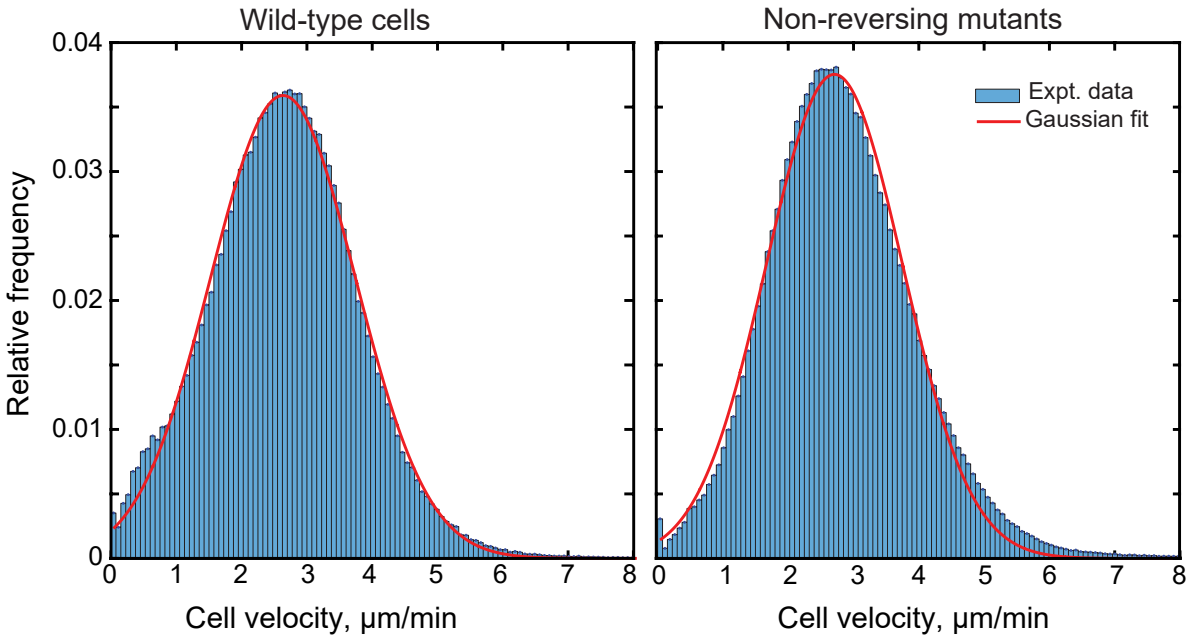


Figure 5.5: *M. xanthus* cell velocity distributions from experiments for (a) wild-type (reversing, $4.5 \times 10^5$ data points from $n$=4791 cell tracks) and (b) non-reversing cells ($8.0 \times 10^5$ data points from $n$=18628 cell tracks). Red line shows Gaussian fit to the cell velocity histograms for wild-type ($\mu = 2.63$ μm/min, $\sigma$=1.11 μm/min) and (b) non-reversing ($\mu = 2.71$ μm/min, $\sigma$=1.04 μm/min) cells

To understand cell stalling process and the collective cell behavior in *M. xanthus* swarms we analyzed the motility behavior of individual cells in *M. xanthus* swarms for both reversing and non-reversing cells. If cells are frequently stalled in cell swarms, we expect a large fraction of cells to have very low velocities. The experimental cell motility data [168] is provided by Dr. Joshua Shaevitz Lab at Princeton University. This data is obtained by applying high-resolution cell tracking methods [204] on time-lapse microscopy images of *M. xanthus* swarms. From this cell tracking data (provided as positions ($\boldsymbol{r}$) of cells in each frame) we calculated the distribution cell velocities after noise filtering (see Appendix E for data analysis methods) for both reversing ($n$=5038 cell tracks) and non-reversing mutants ($n$=19600 cell tracks). These cell velocity distributions are shown in Fig. 5.5. We observe that cell velocities are normally distributed with a mean at ($\mu = 2.7$ μm/min) indicating that most cells move with normal cell velocities ($\approx$ 3 μm/min). Further, the fraction of cells with near zero velocities are very small indicating that cell stalling is rare in *M. xanthus* swarms.

**Some cells inherently move with low velocities**

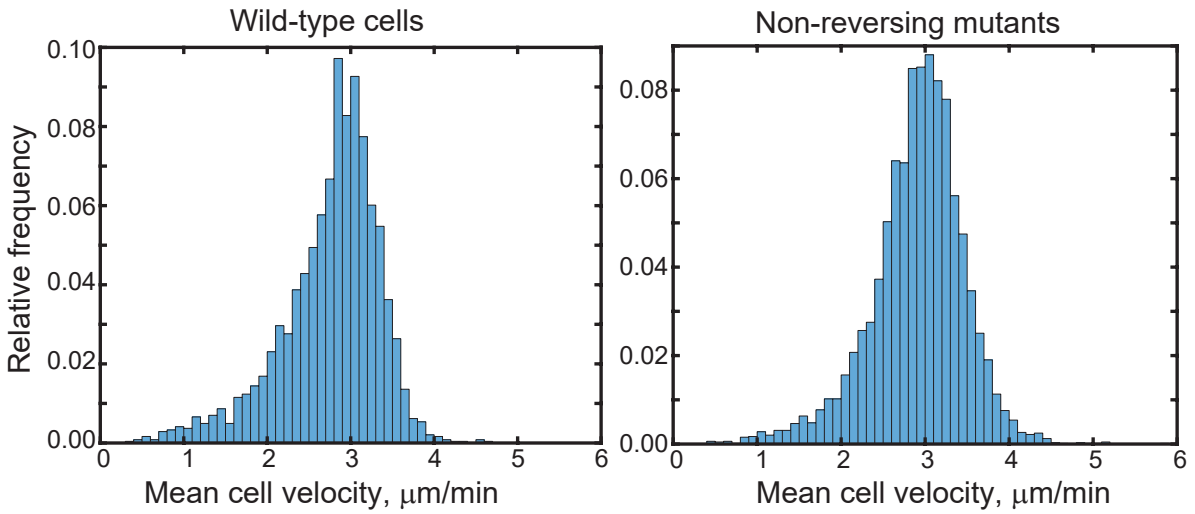


Figure 5.6: Mean/inherent cell velocity distributions for (a) wild-type reversing cells (n=2428) and (b) non-reversing mutants (n=6466). Cells inherently move with different velocities

To further understand the source of lower cell velocities in the cell motility data (Fig. 5.5)

we calculated the total distance traveled by each cell (from cell track data) as a function of time (SI Fig. E.11). We observe that the distance traveled by a cell is linear with time and the slope of the line (from linear regression, SI Fig. E.12) gives the mean velocity of that cell. From this data, we observe that different cells have different mean or inherent velocities i.e. there exists an inherent variation of velocity among cells. We calculated the mean/inherent velocities for all cells in the data and the distribution of these inherent cell velocities for both reversing and non-reversing cells are shown in Fig. 5.6. We observe that a fraction of cells inherently move with lower velocities and the small cell velocities observed in Fig. 5.5 is mainly due to the inherent low cell velocities but not due to cell stalling in crowded cell groups.

**Individual cell velocities are not correlated with their neighbor cell densities**

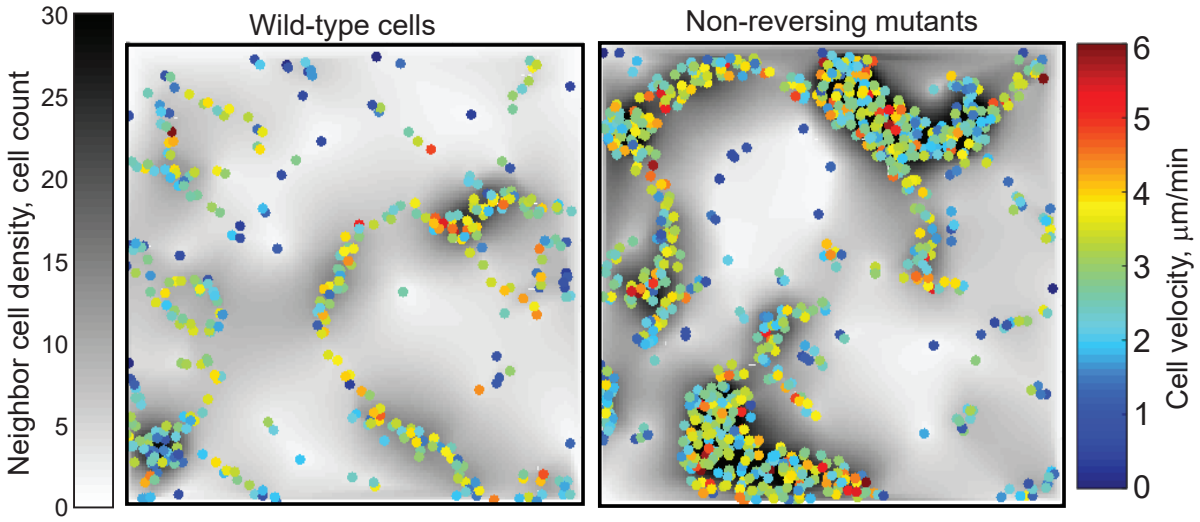


Figure 5.7: Qualitative visualization showing effect of neighbor cell density on individual cell velocities. Cells represented as point particles (colors indicate cell velocity) in a specific time-lapse image frame with their neighbor cell densities (number of neighbor cells within a circle area of one cell length radius) represented as background gray-scale intensity for wild-type and non-reversing cells. No obvious correlation observed for cell velocities with their neighbor cell densities.

To further understand the effect of cell crowding on cell velocity, we calculated the neighbor cell density (cell counts) for each cell along its track from the cell tracking data. A qualitative visualization showing the effect of neighbor cell density on cell velocities are shown in Fig.

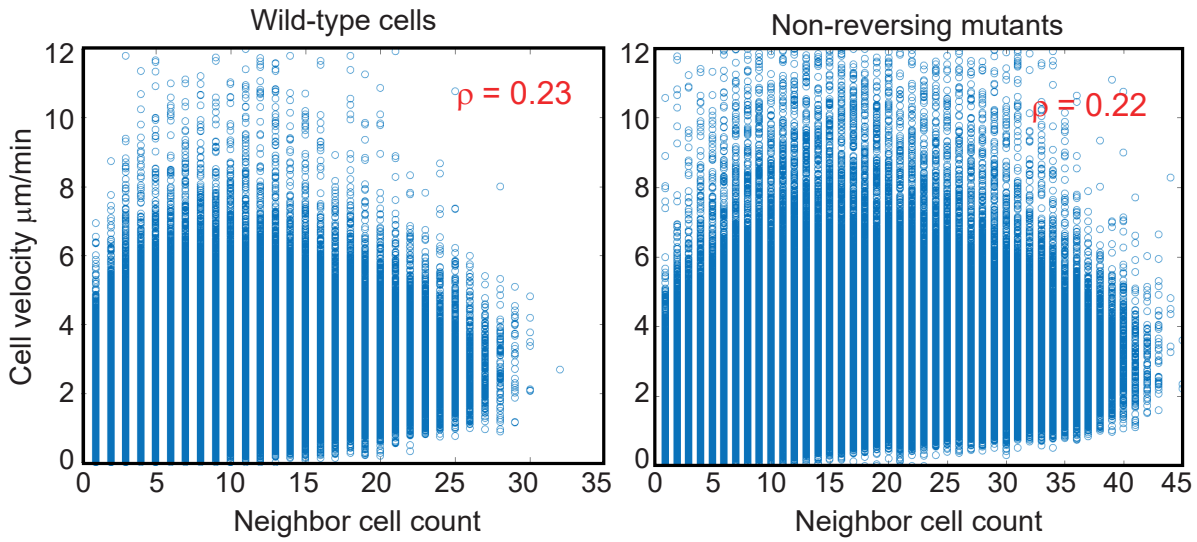


Figure 5.8: Quantitative measurements showing effect of neighbor cell density on individual cell velocities. Individual cell velocities are plotted as a function of their neighbor cell densities for wild-type and non-reversing cells. We expect a negative correlation between cell velocity and its neighbor cell density if cells are stalling is swarms. We observed a small positive correlation ($\rho \approx 0.2$) between cell velocity and neighbor cell density indicating that cell velocity do not decrease with increase in neighbor cell density as expected due to cell crowding.

5.7. Here the cell positions are shown as colored points (color represent cell velocity) in a specific time-lapse image frame. The neighbor cell densities are shown as the underlying gray intensity cloud (darker areas indicate higher cell densities). If cells slow down due to crowding, we should see a decrease in cell velocities in high cell density areas. However, we observe no qualitative correlation between cell velocities and their neighbor cell densities. To quantify the relation between cell velocities and neighbor cell density we measured the Pearson's correlation ($\rho$) between these quantities from the data of all cells. If cell stalling/slowing down is present, we should observe a negative Pearson's correlation between cell velocity and neighbor cell density. However, we observed a small positive Pearson's correlation ($\rho \approx 0.22$) for both reversing and non-reversing cells indicating that there is no cell crowding effect in *M. xanthus* swarms i.e. cell velocity did not decrease with increase in neighbor cell density.

Based on the results from above analysis, we conclude that cell stalling is not present in *M. xanthus* swarms.

### 5.2.5 Biophysical *M. xanthus* ABS model reproduces experimental cell velocity distributions

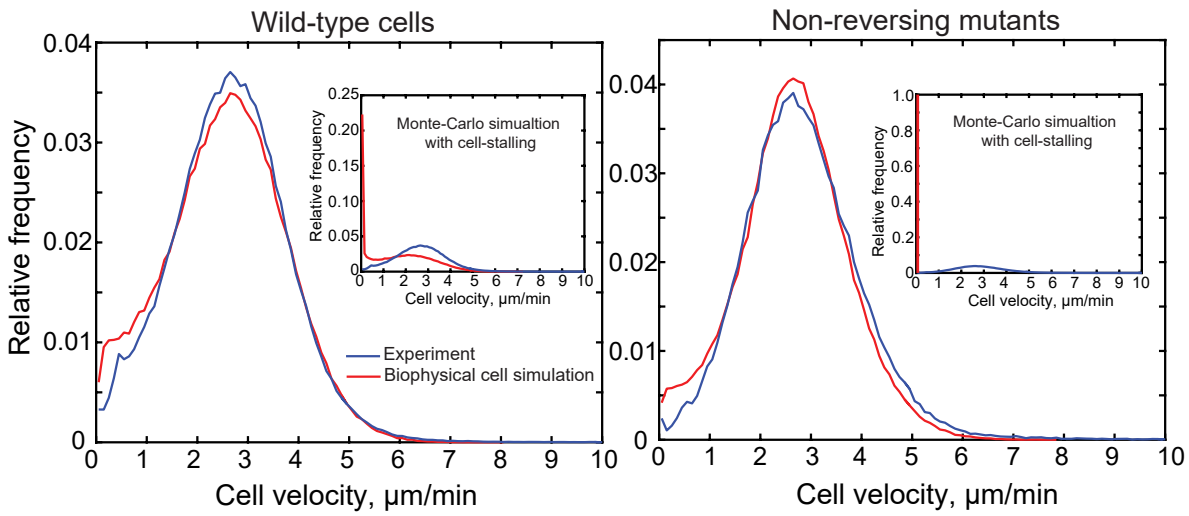


Figure 5.9: Comparison of cell velocity distributions from agent-based biophysical cell simulation and Monte-Carlo simulation (inset) with experimental observations for reversing and non-reversing cells. Results from biophysical cell simulations quantitatively match with experimental data whereas results from Monte-Carlo simulations fail at the same (inset).

To better understand cell swarming behavior in experiments we compared cell motility behavior in swarms from our ABS with cell tracking data from Dr. Shaevitz's lab. For this, we simulated the swarming behavior of model cells (both reversing and non-reversing cells) in a square simulation region with periodic boundary conditions (to simulate continuum). Here we initialized the cells (density $\eta = 0.24$) in random positions with random orientations and simulated their collective cell behavior for 180 min. We observe that with time, model cells formed cell clusters through mechanical interactions with neighbor cells under slime-trail-following and collectively swarmed. We measured the resulting model cell velocities under collective cell swarming in 1 min intervals for the last 60 min of simulation time and calculated the distribution of cell velocities as a histogram for both reversing and non-reversing cells (Fig. 5.9). We observe that our agent-based simulation framework reproduces (after adjusting the velocity of the model cells to mean cell velocities from experiment) the experimental cell velocity distributions for both reversing and non-reversing cells (Fig. 5.9). However, under similar

conditions, Monte-Carlo simulation with cell-stalling assumptions failed to reproduce the cell velocity distributions for both reversing and non-reversing cells (Fig. 5.9 inset). Specifically for non-reversing cell case, cell velocities are entirely concentrated at zero indicating that cell motility is completely stopped (an artifact of cell stalling assumptions) which is not indicative of the actual motility behavior of cells in experiments. Thus we show that our biophysical cell-based simulations reproduce the experimental *M. xanthus* cell swarming behavior indicating that our simulation framework accurately describes the actual *M. xanthus* cell swarming behavior.

## 5.3 Summary and Discussion

In this work, we investigated the mechanism for non-monotonic variation of *M. xanthus* colony expansion with change in cell reversal period as observed in experiments. We studied *M. xanthus* colony/swarm expansion behavior under a simple 1-D continuum model for reversing *M. xanthus* cells based on telegraph equations and a more complex biophysical cell simulations that include various *M. xanthus* cell processes. In both the models, we observed only a monotonic expansion behavior of *M. xanthus* swarms with an increase in cell reversal period. Specifically, we fail to reproduce the decrease in swarm expansion behavior for cells with reversal periods beyond wild-type cell values.

Next, we explored for additional mechanisms in literature that can decrease the swarm expansion at high cell reversal period values. We find that a previous study by Wu et al. [103] reproduced the decrease in swarm-expansion rate for cells with high reversal periods using a Monte-Carlo simulation model [205, 206]. To understand the cell behavior from this model, we replicated their model and studied swarm expansion behavior of model *M. xanthus* cells. Results from these simulations show that the observed decrease in swarm expansion rate with increase in cell reversal periods is mainly due to cell-stalling assumptions present in the model. In absence of cell-stalling, the Monte-Carlo simulation produced the monotonic swarm expansion behavior similar to the results of ABS. Since cell movement is observed even in very

high cell-density conditions in experiments, cell-stalling assumptions in *M. xanthus* swarms are questionable.

To test the validity of cell-stalling assumptions, we analyzed individual cell motility behavior in experimental *M. xanthus* swarms and showed that the cell-stalling is not present *M. xanthus* swarms. Additionally, our biophysical cell agent-based simulation quantitatively reproduced the cell motility behavior observed in experiments. Monte-Carlo simulation with cell-stalling assumptions under similar conditions fail to reproduce the experimental cell motility behavior. Based on these observations, we conclude that the decrease in cell swarming efficiency at large reversal periods observed by the previous simulation study [103] is mainly due to the cell stalling assumptions in the their model. Results from our ABS and experimental cell motility data analysis indicate that cell stalling is not present in *M. xanthus* swarms. Further, our ABS with biophysical cell motility model reproduced the experimentally observed cell motility behavior, but fail to reproduce the decrease in cell swarming efficiency for large cell reversal periods. Thus, we conclude that physical interactions among cells do not result in cell-stalling in *M. xanthus* swarms and do not reproduce the decreased cell swarming behavior with increase in cell reversal period beyond wild-type cell values. We believe that the reduced cell swarming efficiency is probably due to an additional, currently unknown, mechanism specifically acting in *M. xanthus* cells with large cell reversal periods. Additionally, it is possible that this mechanism is only activate under high-cell density conditions present in cell colonies further complicating its identification.

# Chapter 6

# Summary

Most bacterial species self-organize and exhibit collective behaviors in biofilms. These behaviors require coordination and collective movement of participant cells. Understanding the mechanisms that enable bacterial cells to work in a coordinated fashion and move collectively is crucial for understanding bacterial self-organization. Being single cell organisms, bacteria lack sophisticated communication mechanisms that are available in higher organisms and coordinate with their peers through biochemical signaling and mechanical interactions. Biochemical cell signaling in the context of bacterial self-organization was studied extensively in the literature, but the role of mechanical interactions are still under investigation. In this thesis work, I investigated the mechanisms underlying self-organization behaviors exhibited by a model bacterium *Myxococcus xanthus* and the role of mechanical interactions in its collective behavior.

Individual-cell-based models (or) agent-based-models were particularly proven to be useful in understanding the effect of intercellular interactions in bacterial self-organization. In this work, I studied *M. xanthus* self-organization behaviors by constructing biophysical models of *M. xanthus* cell motility and simulating interactions among large number of these models cells as individual agents in an agent-based-simulation framework. I followed a multi-stage approach where I first investigate the mechanism of individual cell motility, then extend this model to study interactions in small cell groups and finally to study collective behaviors in large cell groups. Results from each of the studies are summarized below.

**Mechanism of individual cell motility in *M. xanthus***

Mechanism of *M. xanthus* gliding motility is still under investigation. Based on recent experimental evidence two alternative mechanisms of gliding motility (Helical-rotor-model, HRM

and Focal-adhesion-model, FAM) were proposed in the literature. However, neither mechanism was conclusively proven to be the actual mechanism for gliding cell motility. Physically, these two mechanisms differed in how a cell interacts with the underlying substrate: In HRM a cell moves through pure friction forces between the cell surface and the surrounding fluid whereas, in FAM a cell moves through adhesive interactions between the cell surface and the underlying substrate. We hypothesized that difference in cell-substrate interactions results in different cell motility behaviors during cell-cell collisions. We simulated cell-cell collisions using our biophysical models of cell motility and studied resulting cell motility behavior for the proposed two models of gliding motility. Comparing cell motility behavior during collisions in simulations with experimental cell-cell collision behavior under similar conditions showed that cell motility in *M. xanthus* requires strong adhesive interactions between cell and substrate as indicated by focal-adhesion-model of gliding motility. Our results are robust to variation in model parameters. Further, our predictions of strong attachments between cell and substrate are proven to be true in direct experimentation (performed by our collaborators) using optical-trap loading. Additionally, a recent experimental study by Faure et al. [67] proved that force transmission in *M. xanthus* gliding motility occurs through focal adhesion complexes.

**Mechanism of collective cell alignment in *M. xanthus* groups**

*M. xanthus* cells moving on a solid surface at low cell density conditions form cell groups (clusters) and move collectively. Individual cells in these clusters are observed to be aligned with their neighbors parallel to their long-axis. We currently do not the know the mechanism for this collective cell alignment. Multiple studies in active-matter physics literature indicate that rod-shaped particles moving along their axis can align with others through pure steric interactions (mechanical collisions). We hypothesize that being rod-shaped cells, *M. xanthus* cells form aligned clusters through mechanical interactions. However, these studies consider particles to be rigid and move along their axis without reversing whereas *M. xanthus* cells are flexible and periodically reverse their travel direction. We investigated the mechanism of aligned cell

cluster formation in *M. xanthus* under cell flexibility and periodic reversals by simulating mechanical interactions among model cells based on our biophysical model of cell motility in an agent-based-simulation framework.

We observe that flexible non-reversing model cells formed aligned cell clusters through collisions with other cells similar to self-propelled-rod studies in the literature. However, under periodic cell reversals, we did not observe any significant cell clustering in our simulation. Careful analysis revealed that we need an additional mechanism that guides cells to clusters during cell reversals and hypothesized that slime-trail-following by cells observed in *M. xanthus* is such mechanism. Under slime-trail-following periodically reversing model cells formed aligned cell cluster in our simulations. Additionally, our simulations reproduce, both qualitatively and quantitatively, variation in shape and spatial distribution of cell clusters and their collective motility behavior for reversing and non-revering *M. xanthus* cells as observed in experiments. Thus our simulation results show that mechanical interactions among cells and between the cell and substrate resulting from slime-trail-following are sufficient to explain the distinct aligned cell cluster pattern formation observed in *M. xanthus* motility mutants.

**Mechanism of circular cell aggregate formation in *M. xanthus* developmental swarms**

*M. xanthus* cells in developmental swarms (large cell groups moving collectively) occasionally aggregate and move in circular or spiral formations, called circular-cell-aggregate (CCA). CCA formation is a known transient phenomenon during *M. xanthus* developmental phase, but the mechanism underlying this cell self-organization behavior was not well understood. Recent experiments, from Dr. Daniel Wall Lab at University of Wyoming, with developmental *M. xanthus* mutants that over-express TraA/B protein formed multiple stable CCA, renewing interest in understanding mechanism for CCA formation. *M. xanthus* cells are known to move in streams (swarms of cells following one another like a long chain) during *M. xanthus* development and we hypothesize that CCAs form due to self-closing of these cell streams following previous slime-trails on the surface. We investigated this mechanism of CCA formation using

our agent-based-simulation framework under slime-trail-following by cells.

We observe that non-reversing model cells readily form CCAs in our simulation under strong slime-trail-following efficiency of cells. However, reversing model cells fail to form either cell streams or CCAs in the simulation. Since it is known that cells in streams move with decreased reversal frequencies, we hypothesize that an additional mechanism suppresses cell reversal frequency in wild-type reversing *M. xanthus* cells. We investigated the effect of various potential physical (adhesive) intercellular interactions that can interfere with cell reversals and lead to decrease in cell reversal frequency. However, physical interactions alone are found to be insufficient to suppress cell reversals to the extent required for CCA formation. TraA/B being membrane bound proteins that facilitate material exchange, we hypothesize that TraA/B mediates the exchange of a signal that suppresses cell reversals through cell-cell contact. We tested this mechanism in our simulation and observe that reversing model cells form CCA under contact based cell reversal suppression. Further, we show that the increased CCA formation in TraA/B over-expressed cells is due to the synergistic effect of contact based cell reversal suppression and TraA/B-mediated cell adhesion that keeps cells in contact for longer periods. Thus our simulation results show that CCA from in *M. xanthus* cells through the combined effect of contact based cell reversal suppression, strong slime-trail-following by cells, and the alignment of cells in streams through mechanical interactions.

**Expansion dynamics of *M. xanthus* swarms**

Under nutrient-rich conditions, *M. xanthus* cells grow, divide and collectively swarm out from an initial cell colony at a constant rate. Interestingly, swarm expansion rate for different *M. xanthus* motility mutants in experiments is found to be varying non-monotonically with cell reversal period and exhibit a maximum swarm expansion rate near wild-type cell reversal periods. We currently do not know the reason for this optimal swarming efficiency of wild-type cells. Previous studies indicated that cells frequently stall/slowdown in high cell density regions and the cells with frequent reversals resolve these cell stalls better and thus show better

swarming efficiency. However, cell stalling in *M. xanthus* has not been well understood and the specific mechanism resulting in cell stalling is currently unclear. Further, in our simulations with biophysical cell interactions, we did not observe any cell stalling indicating that physical interactions are not the cause of cell stalling.

We investigated the non-monotonic swarm expansion of *M. xanthus* cells with cell reversal period by simulating swarm expansion of cells at a colony using a simple 1-D continuum model and agent-based-simulation framework. We observe that in both the models swarm expansion rate monotonically increased with cell reversal period saturating at very high cell reversal periods ($\approx$ 500 min). Specifically, we did not observe the decrease in cell swarming efficiency for cell reversal periods beyond wild-type values (8 min). Further, by replicating a previous study, we observe that the non-monotonic expansion behavior shown by the previous model is mainly due to the cell stalling assumption in the model. Next, we analyzed motility behavior of individual cells in experimental *M. xanthus* swarms (data provided by Dr. Joshua Shaevitz Lab, Princeton University) and showed that cell stalling is not present in *M. xanthus* swarms for both reversing and non-reversing cells. Thus our simulation results and experimental data analysis show that physical cell interactions do not result in cell stalling for *M. xanthus* cells in swarms as indicated by previous studies. We conclude that decrease in swarming efficiency of cells with high reversal periods is due to unknown mechanism that slows down collective motility of cells at high cell densities in cell colonies.

Using the biophysical model of cell motility and an agent-based-simulation framework, we investigated mechanisms and the role of mechanical interactions in individual cell motility and collective behaviors of *M. xanthus* bacteria. Our simulation results show that most of the studied self-organization behaviors in *M. xanthus* can be explained by a combination of mechanical interactions among cells, physical interactions between the cell and the substrate and cell-cell contact signaling. This work improves our understanding of mechanisms governing various self-organization behaviors displayed by *M. xanthus* bacteria and provides a general framework to study self-organization behaviors in other surface motile bacteria.

# Appendix A

# Biophysical cell motility model for *M. xanthus* and the Agent-Based-Simulation framework

## Biophysical model of cell motility

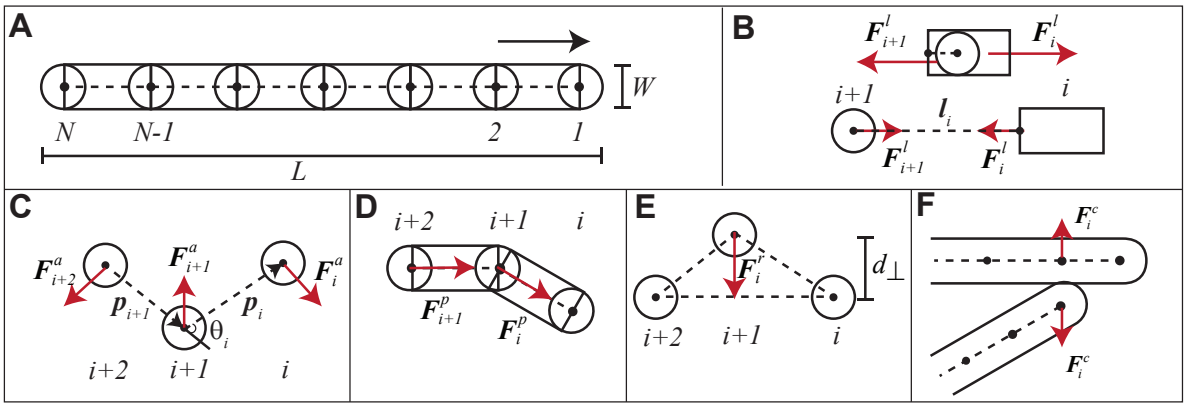


Figure A.1: A biophysical representation of the *M. xanthus* cell as a mass-spring system. (A) Each flexible cell is represented as a connected string of nodes. Circular nodes are similar to the focal adhesion complexes (FAM) or cell wall distortions (HRM) at which cell propulsion force is generated. Circular nodes are spaced apart by rectangular bodies of fixed dimensions. (B) Linear springs join neighboring nodes (circular and rectangular bodies) and maintain the connectivity between the bodies by opposing change in distance between the connected bodies and apply forces ( $\boldsymbol{F}^l$ ) to that effect. (C) An angular spring between three consecutive circular nodes resists bending of the nodes from straight line formation by introducing elastic bending forces ( $\boldsymbol{F}^a$). (D) Cell propulsive forces are applied at circular nodes along the segment joining the next neighbor node in cell travel direction. (E) Adhesive attachments between the node and the substrate are represented by linear springs that introduce a restoration force ($\boldsymbol{F}^r$) on that node when it is displaced from cell's linear axis. (F) Collision forces ($\boldsymbol{F}^c$) act on the nodes that are in direct contact to prevent overlap of bodies.

We developed a biophysical model of the *M. xanthus* cell by extending the linear flexible cell model by Janulevicius et al.[105]. In our model, each cell is represented as a connected string of circular nodes with a total cell length $L$ and width $W$ (Fig. A.1A). Each circular node

is modeled as a rigid body of radius $W/2$. Circular nodes are kept at a fixed distance apart by $M(= N - 1)$ rectangular spacers of length $((L - W)/(N - 1))$ and width $(W)$. Each body of mass $(m_i)$ is identified by its position $(\boldsymbol{r}_i)$ and heading direction$(\theta_i)$. Neighbor circular and rectangular bodies are connected by a rotational joint at the center of the circular node (Fig. A.1B). Each circular node is connected to the neighboring circular nodes by angular springs $(a_i)$ that resist bending of the nodes from straight line position (Fig. A.1C). Spring constants for the angular springs $(k_b)$ can be tuned to achieve the desired flexibility of the cell that matches with the actual bacterium. Various forces $(\boldsymbol{F}_i)$ (e.g. propulsive forces that move cell forward, drag forces on the cell surface due to contact with surrounding fluid) act on the nodes that affect the velocity $(\boldsymbol{v}_i)$ of the nodes. In the following sections we describe the equations that model the cell motion. In these equations letters represent magnitudes and bold letters represent vectors.

**Rotational joints**

Rotational joints between circular and rectangular bodies are modeled as linear springs with zero equilibrium length (Fig. A.1B). Thus, joints resist variation in length (elongation and compression) between connected bodies with counteracting forces $(\boldsymbol{F}_i^l)$ determined by Hooke's law

$$\boldsymbol{F}_i^{l_i} = -k_l \boldsymbol{l}_i = -\boldsymbol{F}_{i+1}^{l_i} \tag{A.1}$$

where $\boldsymbol{l}_i$ is the vector joining the connected bodies at joint $i$ from their respective joint positions ($|\boldsymbol{l}_i|$ = 0 at equilibrium) and is linear spring constant.

**Angular springs**

Angular springs resist bending of the bacterium to simulate elastic behavior of the cell. An angular spring $a_i$ connects every three adjacent circular nodes $i, i + 1$ and $i + 2$ (Fig. A.1C), where $i = 1, 2, \ldots, N - 2$. Each angular spring exerts torques ($\boldsymbol{\tau}_i^{a_i}$ and $\boldsymbol{\tau}_{i+2}^{a_i}$) on the connected

arms ($\boldsymbol{p}_i$ and $\boldsymbol{p}_{i+1}$) of the spring.

$$\tau^{a_i} = k_b \theta_i \boldsymbol{\tau}_i^{a_i} = \left( \left( \boldsymbol{p}_{i+1} \times \boldsymbol{p}_i \right) / |\boldsymbol{p}_{i+1} \times \boldsymbol{p}_i| \right) \tau^{a_i} \tag{A.2}$$

where, $k_b$ is the angular spring constant, $\theta_i$ is the angle between the nodes, $\boldsymbol{\tau}_i^{a_i}$ is the torque acting on the node $i$ , $\boldsymbol{p}_i$ is the vector joining the neighboring circular nodes $i+1$ to $i$. These torques are converted to forces ($\boldsymbol{F}_i^a$) on nodes such that forces acting on node $i$ and $i+2$ cancel out the force acting on node $i+1$ thus producing zero axial movement of the nodes.

$$\begin{aligned}
\boldsymbol{F}_i^{a_i} &= \left( \boldsymbol{p}_i \times \boldsymbol{\tau}_i^{a_i} \right) / p_i^2 \\
\boldsymbol{F}_{i+2}^{a_i} &= \left( \boldsymbol{p}_{i+1} \times \boldsymbol{\tau}_{i+2}^{a_i} \right) / p_{i+1}^2 \\
\boldsymbol{F}_{i+1}^{a_i} &= - \left( \boldsymbol{F}_i^{a_i} + \boldsymbol{F}_{i+2}^{a_i} \right)
\end{aligned}$$

**Cell motility forces**

Motility forces are the forces that are generated internally in the cell and propel it forward. In this model, we consider only the force generation due to gliding motility. In both the proposed mechanisms of gliding motility, cell propulsive force is generated at the motor protein complexes. In our model circular nodes are equivalent to these motor protein complexes. Thus, we apply motility/propulsive force ($\boldsymbol{F}_i^p$) at each circular node (except first and last node) of the cell along the segment connecting next circular node in cell travel direction (Fig. A.1D). We assume that force generated per node due to gliding motility is constant. Here $\boldsymbol{F}_i^p = \left( \boldsymbol{p}_i / p_i \right) F_i^p$, where $\boldsymbol{p}_i$ is the vector joining the neighboring circular nodes $i+1$ to $i$.

**Viscous drag forces**

*M. xanthus* cells secrete slime from their surface, which is deposited on the underlying substrate as long trails [207]. As cells move on the slime they experience drag forces that oppose

their movement. Since the mean speed of *M. xanthus* cells is very low (4 μm/min) [208] and the dimensions of the cell are $0.5 \times 7$ μm [103, 105, 44], the cell movement is in the low Reynolds number flow regime, and thus we assume only a Stokes drag force acts on the cell. Stokes drag force on body is determined using the equation $\boldsymbol{F}_i^d = -c\boldsymbol{v}_i$. Here, $c$ is the drag coefficient between body and slime and $\boldsymbol{v}_i$ is the velocity of the body $i$. Drag coefficient is adjusted such that the terminal speed ($\boldsymbol{v}_f$) achieved by the model cell based on the total force generated matches the mean speed of *M. xanthus* cells observed experimentally.

**Node-substrate interaction force**

Adhesive attachments between the cell and the substrate result in a restoration force ($\boldsymbol{F}_i^r$) on circular node $i$ when the node is displaced from its position due to collision with another cell (Fig. A.1E). These forces restore the displaced node to its original position. Here the attachments are modeled as linear springs, with a spring constant $k_a$, that break if stretched beyond a threshold length ($L_{max}$).

$$\boldsymbol{F}_i^r = \begin{cases} k_a \boldsymbol{r}_i^d & \text{for } r_i^d \leq L_{max} \\ 0 & \text{for } r_i^d > L_{max} \end{cases}, i = 2, 3, ..., N-1 \tag{A.3}$$

where $\boldsymbol{r}_i^d$ is the perpendicular displacement of the node from its original position due to collision. Here we assume that the cell does not form an attachment at the first node as it interferes with the cell's ability to randomly change its direction, which is normally observed in *M. xanthus* cells. Node-substrate interaction forces are absent in VCM (Fig. 2.1C).

When an attachment is broken it reforms after a random waiting time ($\tau$) that is exponentially distributed with a mean of 1/8 min (rate of new bond formation of 8 1/min). The mean waiting time is estimated on the experimentally observed cell speed (4 μm/min) and pitch of helical cytoskeleton ( 0.5 μm) [69]. We assumed that the waiting time corresponds to the time for the arrival of the next motor protein to the next node.

### Collision forces

When two cells collide (i.e. bodies/nodes of two cells are in direct contact) collision resolving forces ($\boldsymbol{F}_i^c$) are applied on the nodes to stop them from overlapping (Fig. A.1F). These forces are applied in the direction normal to their surfaces at the point of the collision. Collision detection and collision resolving forces are handled by a physics engine (see below) in our model.

Additionally, we employ appropriate forces on agent nodes to simulate periodic reversals of cells, noise in cell travel direction, and slime trail following by cells. Implementation details of these processes in our model are presented below.

## Additional cell processes

### Periodic cell reversals

*M. xanthus* cells periodically reverse their travel direction (mean reversal period = 8 min [51]) by switching the roles of its head and tail parts [103, 207]. We mimic this behavior in our model by renumbering nodes, i.e. switching the roles of head and tail nodes at each reversal event and as a result the direction of propulsive force on agent nodes are rotated . Reversals in agents are triggered asynchronously by an internal timer expiring at the end of the reversal period ($\tau_r$). This timer is reset to zero at each reversal. During initialization, each agent's reversal timer is initialized randomly between $[0, \tau_r]$.For all simulations shown here reversals are perfectly periodic, i.e. no noise in $\tau_r$ is introduced. However, introduction of noise in reversals does not affect our conclusions (data not shown).

### Noise in cell travel direction

*M. xanthus* cells exhibit random turns during movement on solid surfaces [145]. What triggers this random change in cell travel direction is not known. We introduce these random cell turns in our model by altering the direction of propulsive force on agents' head node. For simplicity, we only introduce a constant amount of noise in our model. Agents in our model change their

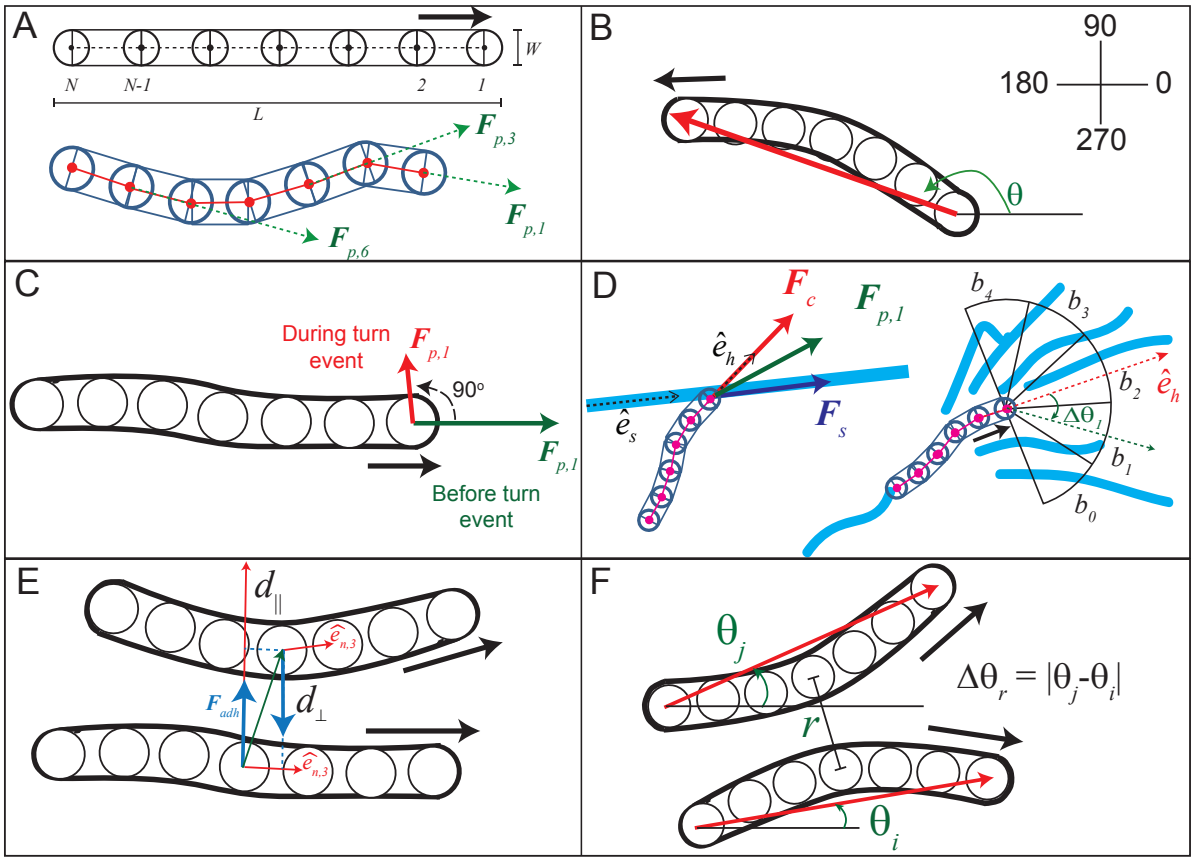


Figure A.2: Implementation of additional cell processes in simulation. (A) Multi-segmented biophysical model of single *M. xanthus* cell as an agent in our simulation framework. Each agent contains 7 nodes connected by joints that simulate the elastic behavior of the cell. Propulsive forces ($\boldsymbol{F}_{p,i}$, green arrows) on nodes in the direction of next node move the agent forward. (B) Orientation ($\theta$) of an agent as the angle made by the vector connecting from its tail node to head node with X-axis. (C) Random noise in agent direction is introduced by reorienting the propulsive force ($\boldsymbol{F}_{p,1}$) on its head node by 90° either clockwise or anti-clockwise randomly for a fixed amount of time (= 1 min). (D) Schematic for implementation for slime-trail following by agents. When an agent encounters a slime trail, a part of the propulsive force on its head node ($\boldsymbol{F}_s$) proportional to the amount of slime in the trail is reoriented parallel to the direction of the slime-trail ($\hat{\boldsymbol{e}}_s$). Remaining propulsive force $\boldsymbol{F}_c(= (F_T/(N-1) - |\boldsymbol{F}_s|)\hat{\boldsymbol{e}}_h)$ acts in current head node direction $\hat{\boldsymbol{e}}_h$. Thus the resulting force on the head node $\boldsymbol{F}_{p,1}$ maintains its magnitude but changes its direction due to slime. In slime-rich regions (slime denoted by blue trails) of simulation, effective slime-trail direction ($\hat{\boldsymbol{e}}_s$) is estimated by dividing a semi-circular slime search region at the head node of the agent into bins ($n = 5$). $\hat{\boldsymbol{e}}_s$ is chosen as the direction (center line) of the bin with high slime volume ($0.8S_{max}$) but with least deviation ($\Delta\theta_s$) from current head node direction ($\hat{\boldsymbol{e}}_h$). (E) Lateral adhesive forces ($\boldsymbol{F}_{adh}$) between a pair of agents acting normal to node propulsion vectors ($\hat{\boldsymbol{e}}_{n,i}$). These forces are implemented for simulations shown in Fig. C.7 only (F) Orientation correlation between a pair of agents, is computed by averaging $cos(2\Delta\theta_r)$ over all agent pairs whose center nodes are separated by distance $r$. $\Delta\theta_r$ is the difference in orientations between the two agents.

travel direction during turn events that are activated asynchronously. During a turn event, we rotate the direction of the propulsion force on an agent's head node by 90° either clockwise or anti-clockwise direction chosen randomly (Fig. A.2C). Each turn event lasts for a fixed time interval (1 min). Similar to periodic reversals, turns events in each agent are activated through an internal timer, expiring after a fixed amount of time ($\tau_t$=5 min). During initialization, each agent's turn event timer is initialized randomly between $[0, \tau_t]$.

**Slime-trail-following by cells**

The exact mechanism for slime trail following by *M. xanthus* cells is currently not known. It is possible that slime tracking by cell is facilitated by attaching the type IV pili at the leading pole of the cell to the substrate [78]. Retraction of the pili inward causes the cell to reorient towards the nearest slime trail. Alternatively, slime-trails may provide low resistance (drag) paths compared to the slime-free areas and thus allow the cells slip into these paths when they cross these slime-trails.

We employ a phenomenological approach for slime trail following in our model where we gradually change the direction of propulsive force ($\boldsymbol{F}_{p,h}$ , Fig. A.2D) on an agent's leading node parallel to the slime trail it is crossing. Here, we assume that cells actively seek slime rich regions on the substrate. Thus, we model a slime field covering the entire simulation region that tracks the amount of slime at each position. This slime field is divided into a square grid area with grid width equal to the cell width ($W_c$). Each agent secretes slime at a constant rate ($S_r$) as it moves forward, that is deposited into the underlying slime field grid elements. Slime exponentially degrades (or dries) in each grid element ($dS/dt = -k_d S$, where $k_d$ is the degradation constant). We assume that cells can only track wet slime (threshold slime detection limit = 1% of original deposit volume). Consecutive grid elements with wet slime represent a slime-trail in our model.

Propulsive force on the head node ($\boldsymbol{F}_{p,1}$) of an agent is influenced the presence of nearby slime trails (Fig. A.2D, left). When an agent encounters a slime trail, total propulsive force on

its head node is rotated with its magnitude preserved and the rotation amount is a function of slime concentration. To implement this we split $\boldsymbol{F}_{p,1}$ into two components: one in current head node direction ($\boldsymbol{F}_c$) and another parallel to the slime trail ($\boldsymbol{F}_s$). The magnitude of force in slime direction is proportional to the fraction of slime remaining in the grid element whereas $\boldsymbol{F}_c$ is computed to keep the magnitude of propulsion force constant $F_T/(N-1)$.

$$\boldsymbol{F}_s = \left[\epsilon_s \left(\frac{F_T}{N-1}\right)\left(\frac{S}{S_0}\right)\right]$$
$$\boldsymbol{F}_c = \left[\frac{F_T}{N-1} - |\boldsymbol{F}_s|\right]\hat{e}_h$$

Here $\epsilon_s$ is slime effectiveness factor, $F_T$ – total propulsive force per cell, $N$ – number of nodes per cell, $S$ – volume of wet slime in grid element, $S_0$ – initial volume of wet slime, $\hat{e_s}, \hat{e_h}$ – unit vectors in the direction of slime trail and head node respectively.

We determine the direction of the dominant slime trail ($\hat{e}_s$) using the following procedure (adapted from Hendrata et al.[209]). A semi-circular region, radius equal to half the cell length, in front of each cell's head node is designated as slime search region (Fig. A.2D, right). This semi-circle area is divided into 5 sectors (bins) and the total slime volume in each bin and the maximum slime volume ($S_{max}$) among the 5 bins are calculated. Finally, we estimate the slime trail direction as the vector along the center line of the bin (sector) with at least 80% $S_{max}$ slime volume and has least angle deviation ($\Delta\theta_s$) from current head node direction ($\hat{e}_h$). If two bins (on opposite sides of $\hat{e}_h$) satisfy the above condition, then we chose either bin randomly.

Slime-trail length ($L_s$) is estimated as the distance travelled by an agent within the time slime deposited at a grid element degrades below a threshold volume ($S_{thr}$ = 0.01). We assume that slime degrades exponentially with time (rate constant, $k_d$). So the amount of slime deposited in a grid element of width ($W_c$) by the time ($\tau_1 = w_c/v_c$; $v_c$ - mean cell speed) an agent crosses the grid element is $S_{\tau_1} = \left(1 - e^{-k_d \tau_1}\right) S_0/k_d$. And the time ($t_{thr}$) required to degrade this initial deposited slime volume ($S_{\tau_1}$) below the threshold volume is $t_{thr} = ln(S_{\tau_1}/S_{thr})/k_d$. Finally,

length of slime trail is calculated as $L_s = t_{thr} v_c$.

To test the robustness of our results using slime trail following mechanism we have varied the length of the slime trail ($L_s$) produced by an agent. For this, we have multiplied production rate of slime ($S_r$) from an agent and slime degradation constant ($k_d$) with same factor so that the net volume of the slime in the simulation region remains constant.

**Lateral cell adhesions**

To simulate adhesive interactions between agents (used only for simulations in Fig. C.7), we apply lateral adhesive forces ($\boldsymbol{F}_{adh}$) on nodes of neighboring agents that are closer than specific threshold distance $d_{thr}$(= 0.75 μm)(Fig. C.3E). Adhesive force on each node is calculated using the following equation.

$$F_{adh} = \begin{cases} 0 & d_\perp \geq d_{thr} \\ \left(\frac{d_\perp - W_c}{d_{thr} - W_c}\right) k_{adh} \frac{F_T}{N} & W_c \leq d_\perp < d_{thr} \end{cases} \tag{A.4}$$

Here $d_\perp$ is the perpendicular distance between the nodes of neighboring agents. These adhesive forces are applied on each node normal to the direction of propulsive force ($\hat{e}_{n,i}$) towards its neighbor agent nodes.

**Equations of motion**

The equations of motion that describe the movement of a cell in the model are as follows. For each body $i$, total force $\boldsymbol{F}_i^T = \boldsymbol{F}_i^l + \boldsymbol{F}_i^a + \boldsymbol{F}_i^p + \boldsymbol{F}_i^c + \boldsymbol{F}_i^r + \boldsymbol{F}_i^d$, total torque $\boldsymbol{T}_i$ acting on it. Angular spring forces ($\boldsymbol{F}_i^a$) and propulsive forces ($\boldsymbol{F}_i^p$) are absent on rectangular bodies. Positions, velocities and orientations of nodes ($\boldsymbol{r}_i, \boldsymbol{v}_i, \theta_i$), are determined by integrating the equation of motion (Eqn. A.5, see below) based on Newton's laws of motion using Box2D physics engine [172].

$$\begin{aligned}
\frac{d\boldsymbol{v}_i(t)}{dt} &= \frac{\boldsymbol{F}_i^T}{m_i} \\
\frac{d\boldsymbol{r}_i^T}{dt} &= \boldsymbol{v}_i^f(t) \\
\frac{d\omega_i}{dt} &= \frac{\boldsymbol{T}_i}{I_i} \\
\frac{d\theta_i}{dt} &= \omega_i \qquad i \in 1, 2, ..., N
\end{aligned} \tag{A.5}$$

**Simulation procedure**

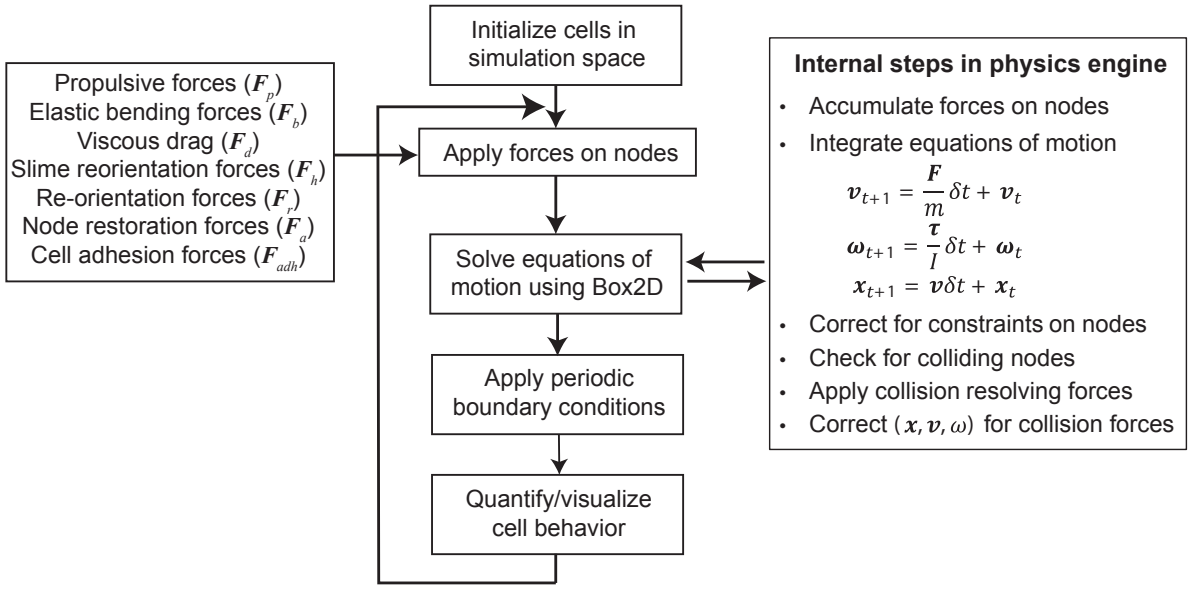


Figure A.3: Flow chart of simulation procedure for our agent-based-simulation framework

We study the clustering behavior of cells by simulating the mechanical interactions among large number ($M$) of agents on a 2D simulation region with periodic boundary conditions in an agent-based-simulation (ABS) framework. Flow chart for our simulation procedure is shown in Fig. A.3.

We initialize agents one by one on a square simulation region (dimension $L_{sim}$) over few initial time steps until desired cell density ($\eta$) is reached. Agents are initialized in random positions over the simulation region with their orientations ($\theta$) chosen randomly in the range

$[0, 2\pi]$. Here, an agent orientation is defined as the angle made by the vector pointing from its tail node to head node with X-axis (Fig. A.2B). Agent nodes are initialized in straight-line configuration. During initialization, agent configurations that overlap with existing agents are rejected. After initialization the head node for each agent is chosen between its two end-nodes ($i = 1, 7$) with 50% probability.

At each time step of simulation, agents move according to the various forces (see Fig. A.3) acting on their nodes. Changes in node positions and velocities are obtained by integrating the equations of motion based on Newton's laws. We use Box2D physics library [172] for solving the equations of motion and for effective collision resolution. Snapshots of the simulation region, orientation of each agent along with its node position are recorded at 1 min time interval for later analysis.

Simulations are implemented in Java programming language with Java port of Box2D library (http://www.jbox2d.org/). Parameters of the simulation are shown in Table A.1. Each simulation is run for 180 mins.

**Box2D physics engine**

We use an open source physics library Box2D (http://box2d.org/) to solve Newton's equations of motion in our model. Box2D is a two-dimensional rigid body dynamics simulator that solves the equations of motion of bodies subjected to various forces, and outputs the position and velocity of the bodies at each time step. We modeled the biophysical cell in Box2D, using the mathematical modeling approach described above. The model parameters were specified as various physical parameters to the simulation engine. The collision forces between the bodies were internally calculated by the physics engine. The cell model is simulated at each time step where the position, orientation and velocity of the nodes are recorded. The parameters used in the model are listed in Table A.1. We scaled the actual cell parameters to the model cell configuration due to the restrictions on the rigid body dimensions that Box2D simulates. These restrictions are introduced primarily to maintain the numerical error within acceptable limits

and for the numerical stability of the simulation. We have also modified the integration scheme used by Box2D to the semi-implicit Euler method from the original explicit Euler method. Refer to Appendix F for implementation details of the cell model and rigid body simulation using Box2D physics engine.

**Simulation parameters**

| Symbol | Description | Value |
|---|---|---|
| $L_c$ | Agent length | 6 μm [44, 105] |
| $W_c$ | Agent width | 0.5 μm [44, 105] |
| $N$ | Number of nodes per cell | 7 |
| $\rho$ | Cell density | 1000 kg/m$^3$ |
| $k_l$ | Linear spring constant | Managed by Box2D |
| $k_b$ | Angular spring constant/bending stiffness | $10^{-17}$ Nm [105, 159, 160] |
| $k_a$ | Spring constant for cell-substrate adhesions | 500-2000 pN/μm [145] |
| $L_{max}$ | Bond breaking length | 0.5 μm (cell width) |
| $L_{sim}$ | Dimension of square simulation region | 200 μm |
| $v_c$ | Mean speed of cell | 4 μm/min [103] |
| $F_T$ | Propulsive force per cell | 60 pN [145] |
| $\mu$ | Viscosity of the slime | $10^{-3}$ kg/m.s |
| $t_{step}$ | Simulation time step | $5 \times 10^{-3} min$ |
| $tau_r$ | Reversal period | 8 min [51] |

Table A.1: Simulation parameters for biophysical cell model

# Appendix B

# Supplementary information for *M. xanthus* gliding motility

## Computational and quantification methods

To simulate the cell motility and cell-cell collisions, we have used our biophysical model of *M. xanthus* cell by extending the linear flexible cell model [105]. In our model, each cell is represented as a connected string of nodes. Neighbor nodes are joined using linear and angular springs that simulate elastic behavior of the cell. Cell propulsive forces are applied at the center of nodes to simulate force generation from motor protein complexes. Cell experiences drag force on its nodes that oppose cell movement as it travels on the slime. Cell nodes interact with the substrate using elastic attachments (in ECM) modeled as linear springs that resist displacement of nodes during cell-cell collision. These attachments are absent in VCM. Collision resolving forces are applied on the nodes when nodes are in direct contact. We solve the equation of motion describing the cell movement by integrating the Newton's laws of motion for all the nodes using an open source physics library Box2D (http://box2d.org/).

### Quantifying cell-cell collision behavior

To quantify the cell-cell collision behavior we used the following procedure. We numbered the nodes in each cell from the leading end (node $1$) to the lagging end (node $N$), and defined a vector ($\boldsymbol{O}$) pointing from lagging to leading node as the travel direction of the cell. Orientation of cell '$i$' at any instance of time '$t$' is denoted by $\theta_i(t)$ and is quantified as the angle difference between the cell's travel direction vector ($\boldsymbol{O}$) and the horizontal axis ($y = 0$) in the

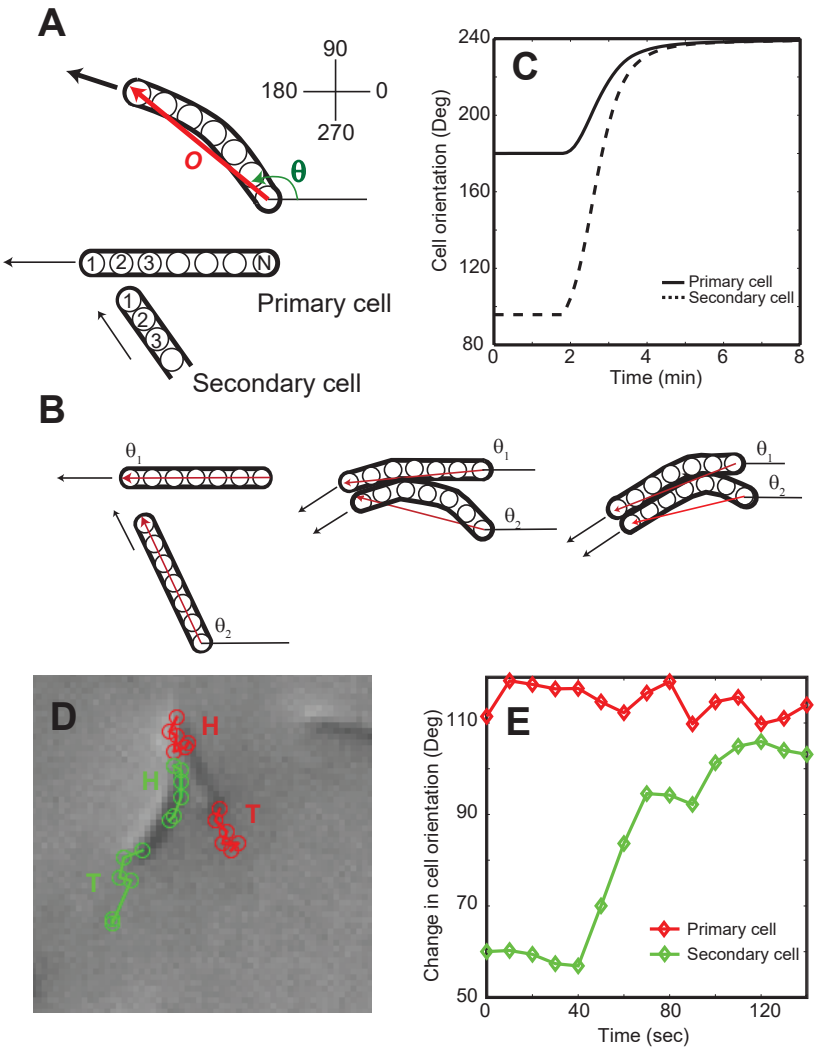


Figure B.1: Quantification of cell-cell collision behavioral data from simulations and experiments. (A) A cell's travel direction is indicated by the vector (***O*** – red arrow) pointing from lagging to the leading end. This direction is converted into the cell orientation ($\theta$) by measuring the angle between the cell direction vector (***O***) and the horizontal axis (y=0) in the anti-clockwise direction. The position of cell collision is identified by the node number of the primary cell where the secondary cell first makes contact. (B) Schematics showing the change in cells' orientations at different instances of time during the collision process. (C) Simulation results show the corresponding change in cell orientations with time. (D) Cell tracking using ImageJ [210] software and MTrackJ plugin [211]. Individual cells (red, green) participating in collision are identified and their leading (H) and lagging (T) ends are marked in consecutive time-lapse images during collision process. The chain of points for each color represents the tracking history of a marked cell's end through the time-lapse images. (E) Orientation of primary (red) and secondary cell (green) as a function of time during a collision event as measured from time-lapse images. Observe that after the collision secondary cell (green line) changes its orientation and aligns with the primary cell (red line).

counter-clockwise direction (Fig. A.1A). We defined a primary cell as the one whose side is hit by the first node of another (secondary) cell. Thus, the change in orientation of both the primary and secondary cells can be recorded as a function of time. We measured the value of the primary cell orientation change ($\Delta\theta_p = |\theta_{t(+\infty)} - \theta_{t(-\infty)}|$) before and after the collision. A schematic showing the quantification of cell collision process and the corresponding change in cell orientations are shown in Figures B.1B and B.1C.

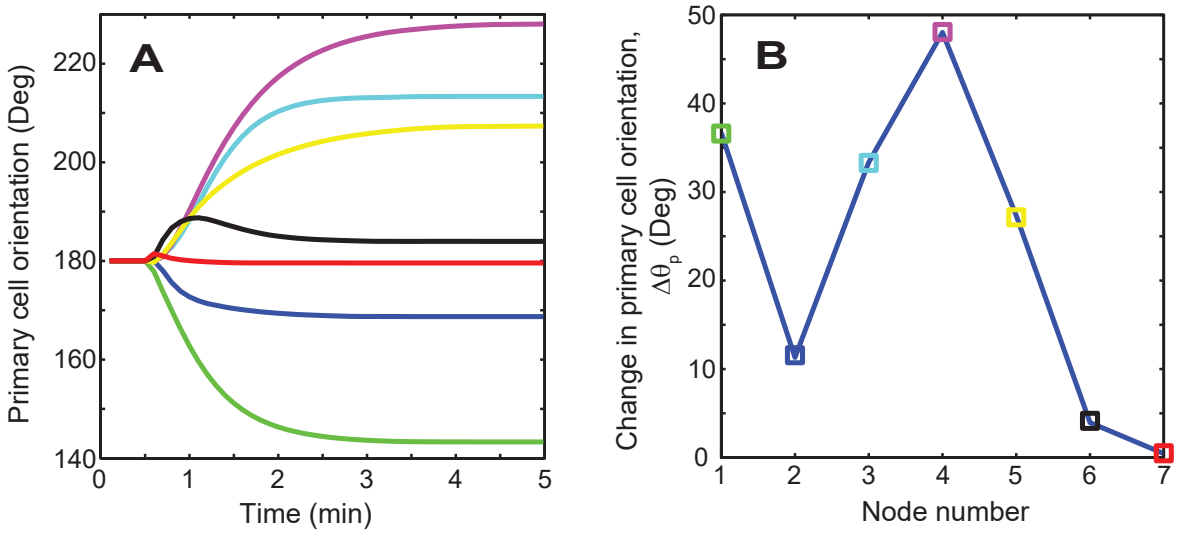


Figure B.2: Cell collision behavior varies for different collision positions. (A) Change in the primary cell orientation with time for different collision node positions (different colors) from the leading end of the primary cell. (Note that collisions occur around 0.5 min). (B) Absolute change in the primary cell orientation before and after the collision as a function of node position. Data points shown in different colors correspond to the lines in panel A.

We observed that the change in the primary cell orientation during the collision process varies based on the collision position (node numbers) along its length (Fig. B.2A and Fig. B.2B). We used the maximum change in cell orientation ($\Delta\theta_{p,max}$) resulting from all possible node collision positions ($n = 2, 3, ..., N-1$) as a metric to compare the model results.

**Quantifying cell collision behavior from experimental time-lapse images**

Cell-cell collision behaviors under experimental conditions were quantified by tracking the cell's position and orientation in time-lapse images during the collision process. We used Im-

ageJ software [210] with MTrackJ plugin [211] for cell tracking. First, we identified cell collision events that were free from interactions with neighboring cells (isolated collision events) in the experimental time-lapse images. Next, we loaded the image stacks corresponding to the collision events from the time-lapse movies into ImageJ. We used MTrackJ (a cell tracking plugin for ImageJ) to track the positions of the colliding cells as a function of time. The individual cell's leading and lagging ends were marked manually for each image in the loaded frame stack. These marked positions were converted to a time-series of $(x, y)$ pixel coordinates by MTrackJ (Fig. B.1C). From the pixel coordinates (the cell's leading and lagging pole positions) we calculated the cell orientations as a function of time (Fig. B.1D, see previous section for details).

**Measuring the spontaneous turning of *M. xanthus* cells**

The change in the primary cell orientation that we measured in our experimental time-lapse images also includes an additional component due to the spontaneous turning of the cells. To estimate the actual change in cell orientation due to collision, we measured the mean orientation change ($\bar{\theta}_basal$) of isolated cells for the duration of mean collision time ($\bar{t}_c$) (Fig. 2.3E, B.3A). We subtracted this value from our experimental estimates of cell orientation change. To measure the mean orientation change of individual cells, we first tracked the orientation ($\theta_i(t)$) of isolated cells over time (Fig. B.3B) from the time-lapse images and then calculated the mean cell orientation change using the following equation.

$$\bar{\theta}_{basal} = \frac{1}{N \times K} \sum_{i=1}^{N} \sum_{t=0}^{T} |\theta_i(t) - \theta_i(t + \bar{t}_c)| \tag{B.1}$$

where N is the total number of cells tracked, $|\theta_i(t) - \theta_i(t+\bar{t}_c)|$ is the absolute orientation change of cell $i$ in the time interval $\bar{t}_c$, and $K$ is the number of such possible measurements for a total tracking time of $T$.

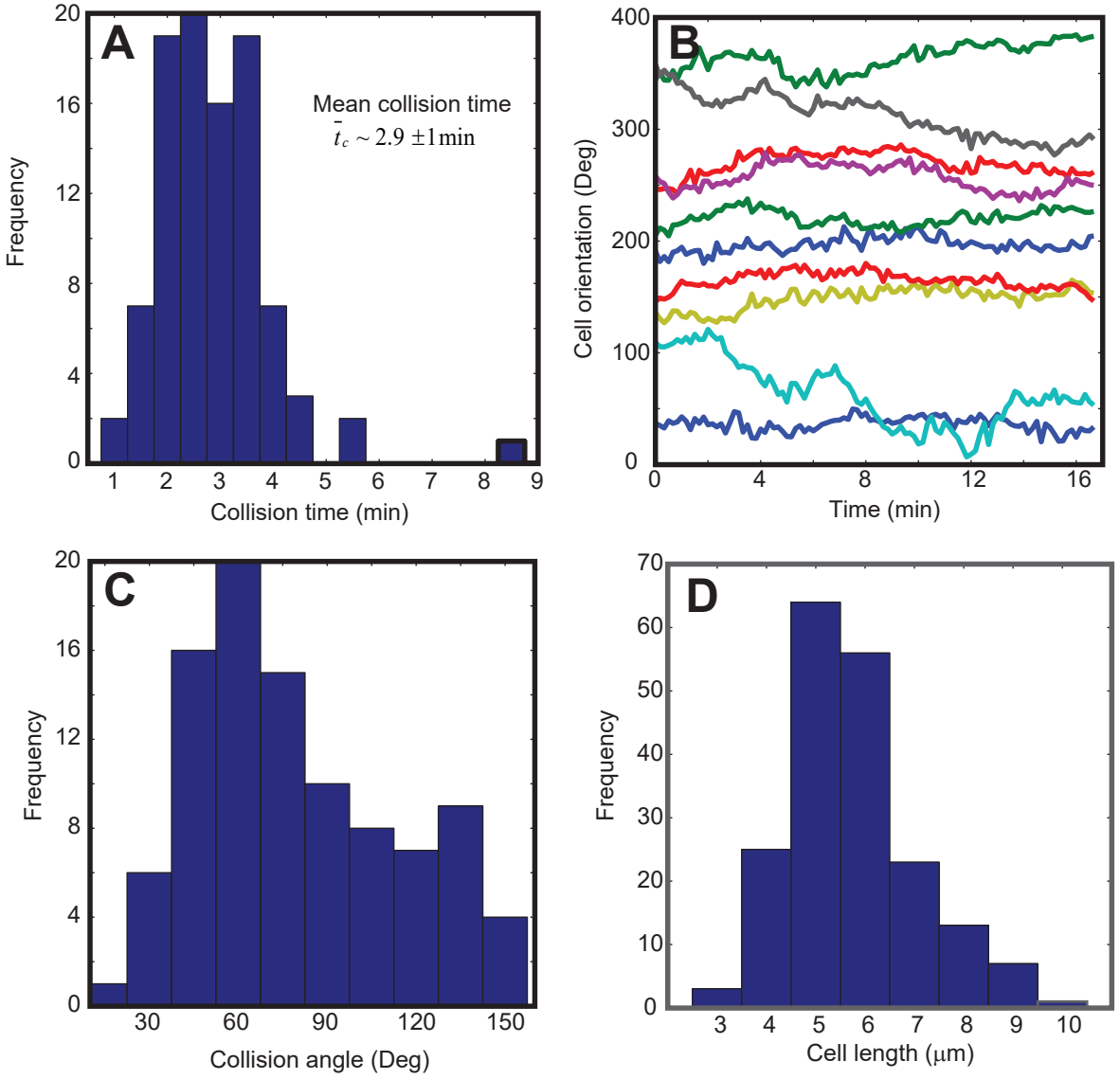


Figure B.3: Cell properties measured in experimental data for wild-type cells. (A) Distribution of collision times from the experimental data of wild-type cells. (B) Tracking history of individual cell orientations over time indicating the spontaneous random cell orientation changes. Each trajectory/color represents measurements from a single isolated cell. (C) The distribution of collision angles and (D) cell lengths from wild-type cell data.

## Experimental methods

In the following section, optical microscopy experiments are performed by Douglas Litwin, graduate student in Dr. Heidi Kaplan Lab, University of Texas - Houston Medical School. Experiments of bead pulling assay with atomic force microscopy are performed by Fabian Cz-

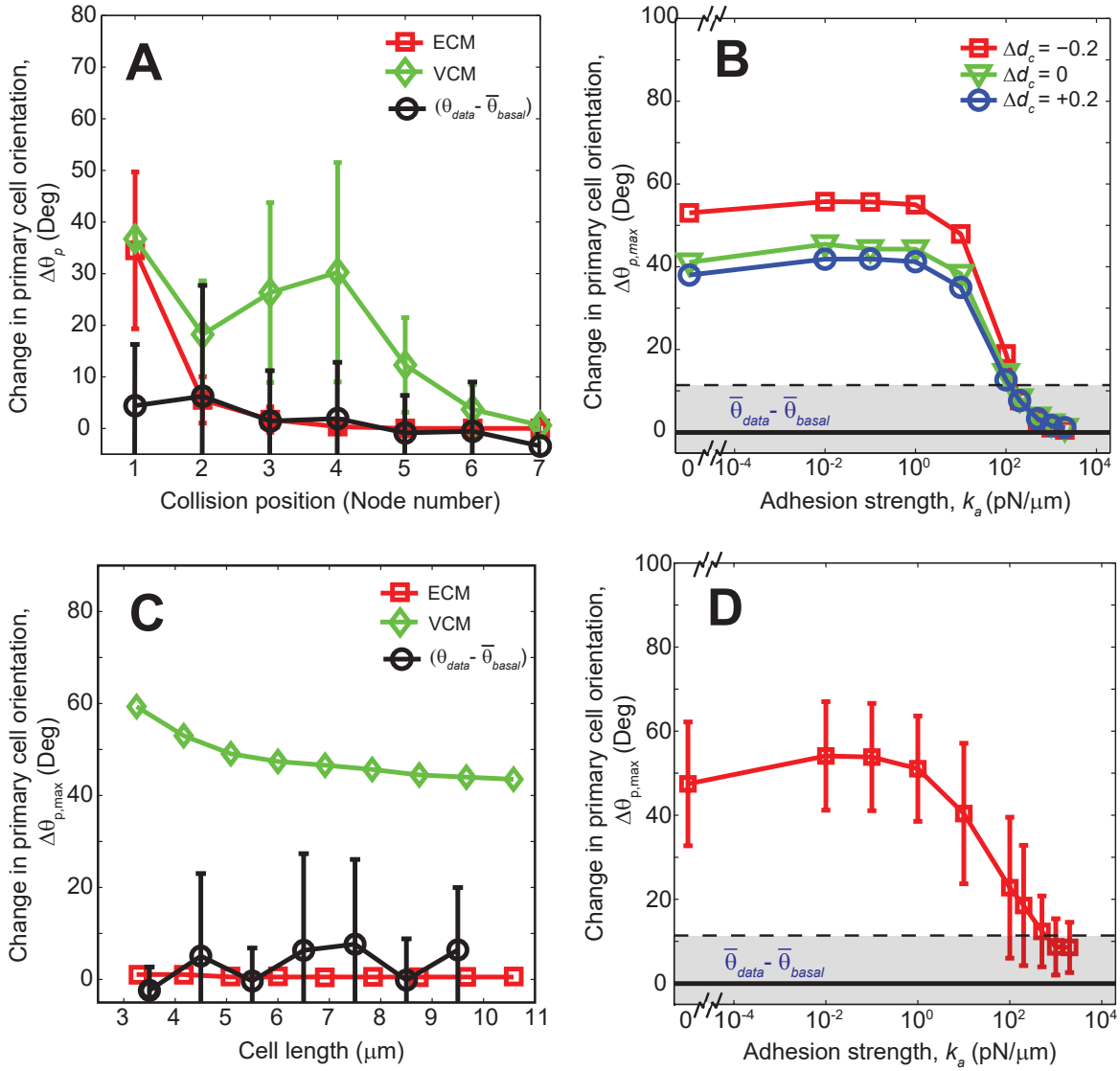


Figure B.4: Cell collision behavior for variations in cell geometrical parameters. (A) Mean and standard deviations in the primary cell orientation changes as a function of cell collision position for variations in the cell mechanical parameters (see Table B.1). Black circles represent mean values from the experimental observations. (B) Variations in the maximum change in the primary cell orientation for small perturbation ($\Delta d_c = \pm 0.2$ mm, $\approx$ half-cell width) of collision position from center of the node. (C) Maximum change in the primary cell orientation in cell collisions as a function of the variation in cell length. Here length of the primary cell is varied while the secondary cell length is fixed at 7 mm. We also find that the results are similar for variation of secondary cell length (data not shown). (D) Mean and standard deviation in primary cell orientation change as a function of adhesive strength for an increased number of adhesive complexes per cell (9 complexes).

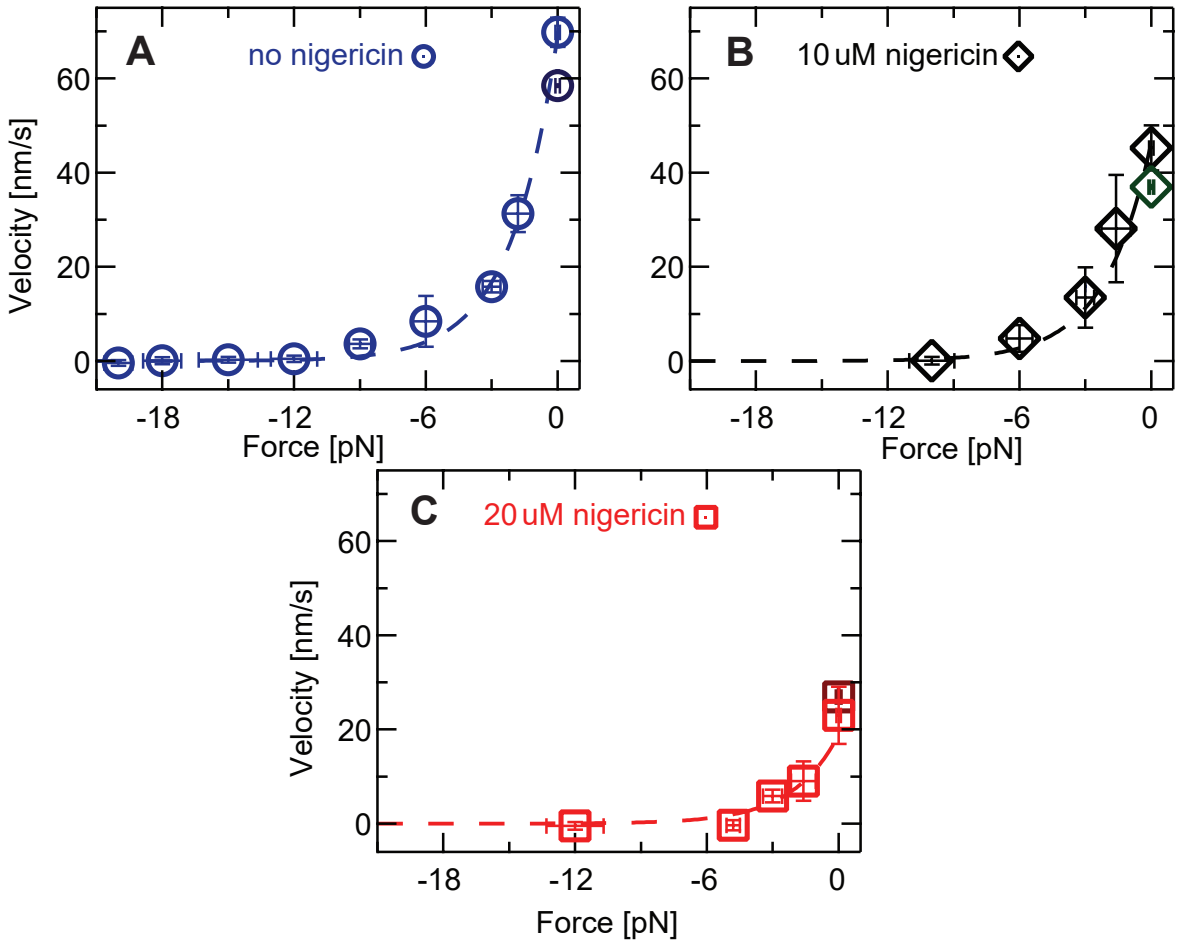


Figure B.5: Force-velocity relation of *M. xanthus* gliding motors at various nigericin concentrations. (A-C) Force velocity curves for three different nigericin concentrations: 0 µM (A, blue circles), 10 µM (B, black diamonds), 20 µM (C, red squares). Velocity decreases exponentially with force but never becomes negative consistent with an elastic coupling and inconsistent with a viscous coupling between the bead and motor. The dashed lines are exponential fits to the data. Error bars represent the standard error of the mean across trials (> 6 trials per data point).

| Symbol | Description | Range varied |
|---|---|---|
| $k_b$ | Angular spring constant/bending stiffness | $10^{-18} - 10^{-16}$ N.m |
| $k_a$ | Spring constant of substrate adhesions | 0-2000 pN/µm |
| $\gamma$ | Drag coefficient between cell surface and substrate attachment | $9 \times 10^{-5} - 9 \times 10^{-3}$ kg/s |
| $L_{max}$ | Bond breaking length | 0.25 - 1.0 µm (cell width) |

Table B.1: Mechanical parameters varied in the model for testing the robustness of model results

erwinski, Mingzhai Sun in Dr. Joshua Shaevitz Lab, Princeton University.

**Cell Growth and Development**

For cell collision experiments *M. xanthus* strains DK1622 (wild-type) and DK10407 ($A^+S^-$) were grown in CTT broth (1% Difco Casitone, 10 mM Tris-HCl pH 8.0, 8 mM MgSO4 and 1 mM KHPO4 pH 7.6) or on CTT agar (CTT broth containing 1% agar) at 32 °C. When *M. xanthus* cells reached mid-log phase ($4 \times 10^8$ cells/ml), the cells were diluted to 20% in TPM buffer (CTT without Casitone).

For optical trap experiments *M. xanthus* strain DZ2 AglZ-YFP ΔpilA [74] was incubated on 1.5% agar plates (CYE medium - 1% peptone, 0.5% yeast extract, 10 mM MOPS, pH 7.8) at 32 °C for 4 days. 10 µl of cells were transferred in 25 ml CYE containing 10 mg/ml tetracycline. Cultures were incubated in a shaker at 32 °C overnight. Prior to experiments, 2 ml cell culture grown to an OD of 0.78 was centrifuged at 8,000 rpm for 5 min, the supernatant removed, and pelet resuspended in 400 µl TPM medium (10 mM Tris, 8 mM MgSO4, 100 mM KH2PO4, pH 7.8).

**Microscopic imaging of cell collisions**

Corning 35 mm tissue culture dishes were prepared for microscopy by drilling a 5 mm hole in the bottom of the dish. A microscope cover slip was then taped over the hole and 5 mls of 1/2 CTT agar was poured into the culture dish. After the agar solidified, the microscope cover slip was removed and 5 µl of the diluted *M. xanthus* (DK1622, DK10407) culture was spotted onto the exposed agar and allowed to dry. The culture dish was then inverted and water was added to the large agar surface. The cells were allowed to acclimate for at least 2 hrs before imaging with an Olympus 81X inverted microscope fitted with a Hamamatsu HD camera. The cells were imaged at 5 or 10 sec intervals for up to 12 hrs. The temperature was maintained at 30°C during the imaging.

**Flow chamber and surface preparation for bead assays with immobilized cells**

Flow chambers were custom-made using double layers of double-stick tape and a cover slide (thickness 1 mm) and a cover slip (#1.5, thickness 100 μm) as described previously [212]. The final chamber volume was approximately 40 μl. 20 μl of 0.7% agarose dissolved in 6 M DMSO were injected into a chamber, incubated at room temperature for 15 min and washed with 400 μl TPM [70]. *M. xanthus* (DZ2) in TPM was injected and allowed to attach firmly to the surface for 30 min. Non-attached cells were washed out thoroughly using 2 ml TPM containing 10 μM glucose. Samples were mounted onto the microscope and ready for experimental use.

For all bead experiments, polystyrene beads (diameter 520 nm) were washed and diluted in TPM medium (0.005% weight/volume) containing 10 μM glucose and injected into the flow chamber. Freely diffusing beads were optically trapped and placed on surface-immobilized cells. For subsequent experiments in the presence of different concentrations of the drug nigericin, TPM medium with the appropriate nigericin concentration was carefully injected into the microscope-mounted flow chamber.

**Optical tracking and trapping**

The optical trap was custom-built onto a Nikon TE2000 microscope equipped with a TIRF objective (NA = 1.49, Nikon). A trapping potential for transparent objects was formed by focusing the TEM00 mode of a high-powered Nd:YVO4 laser (wavelength 1,064 nm, up to 5W output power). A piezo-controlled tip-tilt mirror allowed for precise positioning of the optical trap within the focal plane. The flow chamber was mounted on top of a 3D-piezo stage with a wide working range (200 μm × 200 μm × 200 μm). The experiments were recorded by an EMCCD camera mounted behind a 2.5 times zoom with a field of view of 41 μm × 41 μm.

A low-powered diode laser (wavelength 855 nm, operated at 3 mW output power) was aligned with the optical trap, and the forward scattered light from trapped objects was collected onto a position-sensitive photodiode placed in a plane conjugate to the back aperture of the condenser, pre-amplified at the diode, amplified and filtered (low-pass filter 53 kHz), and recorded

with a data acquisition card. Using this acquisition, we implemented a PID feedback to fix the bead position relative to the detector laser beam focus by moving the piezo. Typically, we recorded positional tracking of bead movement on the cell surface with 10 kHz using stage feedback in the lateral direction with a frequency of 50 Hz to keep the detection/tracking laser focused on the bead. The height was fedback at a frequency of 1 Hz by comparing the bead's image with a look-up table taken prior to the actual tracking. Tracking could be performed for hours without significant drift. We stored the images of the whole field of view at 1 Hz to ensure that no other objects diffused into the path of the detection laser close to the focus. In a post-processing step, the images were used to project the lateral dimensions of the bead trajectories along the cell major axis.

Prior to deposition onto the cell, trapped beads were calibrated by monitoring their Brownian motion at an acquisition frequency of 22 kHz for 10 s in close vicinity to the cell. A standard protocol was employed to extract the harmonic trap stiffness, the linear photodiode-voltage to position conversion factor, and an unbiased measure of the accuracy [213]. The sum signal of the photodiode was used as a measure of bead displacement in the direction perpendicular to the focal plane.

For force-clamp experiments, the optical trap was moved to an off-center position with respect to the detection/tracking laser along the cell axis, but with the shutter closed. The exact distance was chosen under the assumption that the exerted force was linear to the displacement from the trap center [214]. If the bead moved at least 63 nm in one direction along the cell axis within a time interval of less than 3 s and without tracking back, the shutter would open, thus applying the preset force of the optical trap to the bead. Updating the bead position effectively functioned as a force feedback, since the distance was kept constant at the same time. The trap was released after 8 seconds. Runs where the kept if the velocity before and after force application were the same within measurement error.

# Appendix C

# Supplementary information for *M. xanthus* collective cell alignment

## Quantitative measurements of cell clustering

### Cluster size distribution (CSD)

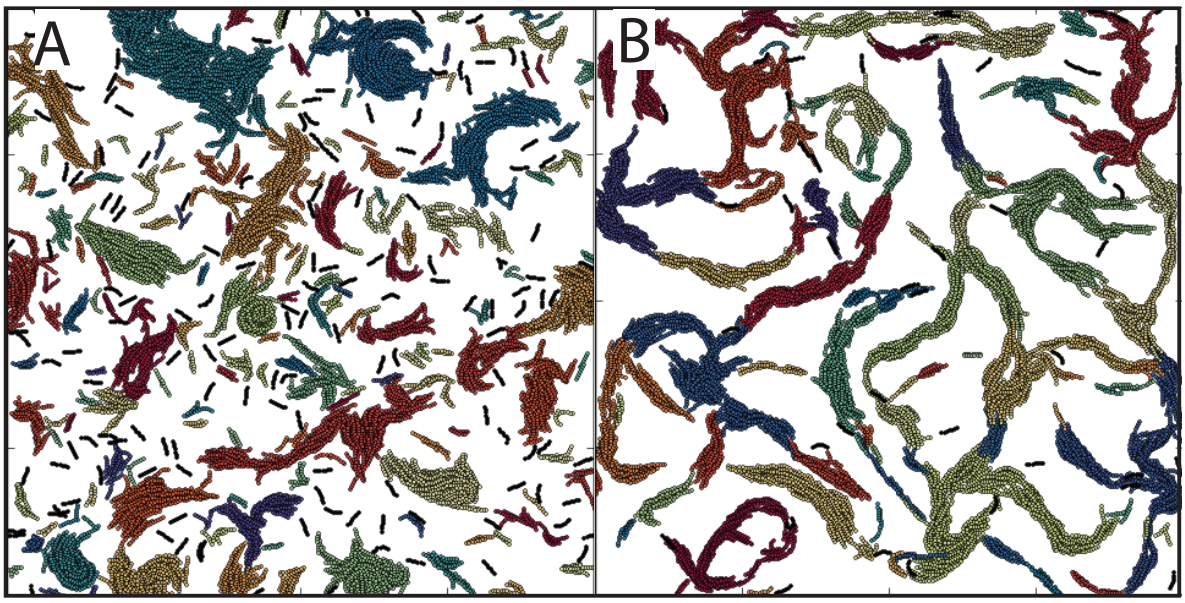


Figure C.1: Identifying cell clusters using DBSCAN algorithm. Different colors represent different clusters of agent nodes identified from their positions that exceed given density threshold. Snapshots of identified clusters for (A) Non-reversing cells (B) Reversing cells with slime-trail-following mechanism ($L_s$= 11 μm, $\epsilon_s$=1.0) at 160 min after simulation started. Cell density $\eta$=0.24

We identify the clusters in the simulation region using a density based clustering algorithm (DBSCAN [215, 216]) applied on agent node positions. This algorithm identifies groups of nodes that exceed given density threshold and classifies them as separate clusters. We chose

the parameters of the algorithm (minimum number of nodes to form a cluster, $k = 21$ i.e. 3 cells, and the minimum neighbor distance, $d_{min}$ = 2) that resulted in good separation (visually) between individual clusters. Using small neighbor distances ($d_{min} \leq 2$) values in this algorithm resulted in large clusters that are actually multiple separate clusters connected by a narrow streams of agents. So we used minimum neighbor distance as $d_{min} = 2$ µm and later process the individual clusters to include short distance ($\leq 2$ µm) neighbor agents.

Next, we determine the agents belonging to each separate cluster of nodes identified by the algorithm. We process partial agents, i.e. only fraction of the agent nodes are included in the cluster, to include in the all nodes of the agents into the cluster. We further process the clusters to include all the nearest neighbor agents ($d_{min}$ <0.75µm) that are missed by the algorithm. We quantify the size of the clusters ($m$) by measuring the number of agents in each cluster. Snapshots of identified clusters (after processing) from simulation are shown in Fig. C.1.

We quantify the cluster size distribution (CSD) by measuring the probability $p(m)$ of finding a cell in a cluster of size $m$. For this, we followed the procedure illustrated in Starruß et al.[167]. After identifying and processing the clusters from simulation, we obtain an array of various cluster sizes ($m_i$) at each time frame. These values ($m_i$) are converted into a normalized histogram ($f_i$) whose bin edges are chosen exponentially i.e. bin $i(= 1, 2, ...)$ contains all agents that belong to clusters of size $10^{(i-1)dm} \leq m < 10^{idm}$, where $dm$=0.33. Thus $f_i$ values represent fraction of all agents found in cluster sizes represented by bin $i$. Finally, probabilities, $p_i$ are calculated by dividing the $f_i$ values with the corresponding bin width $db_i(= 10^{idm} - 10^{(i-1)dm})$.

**Mean cluster size, $\langle m \rangle$**

Due to the sparse nature of cluster size distribution data from simulation, we calculate mean cluster size at each cell density ($\eta$) using data from multiple simulation runs and from multiple time points ($\tau_{ss,t}$) in each simulation run after CSD values reached steady state. We chose time points ($\tau_{ss,t}$) such that the CSD at these time points are sufficiently independent. For

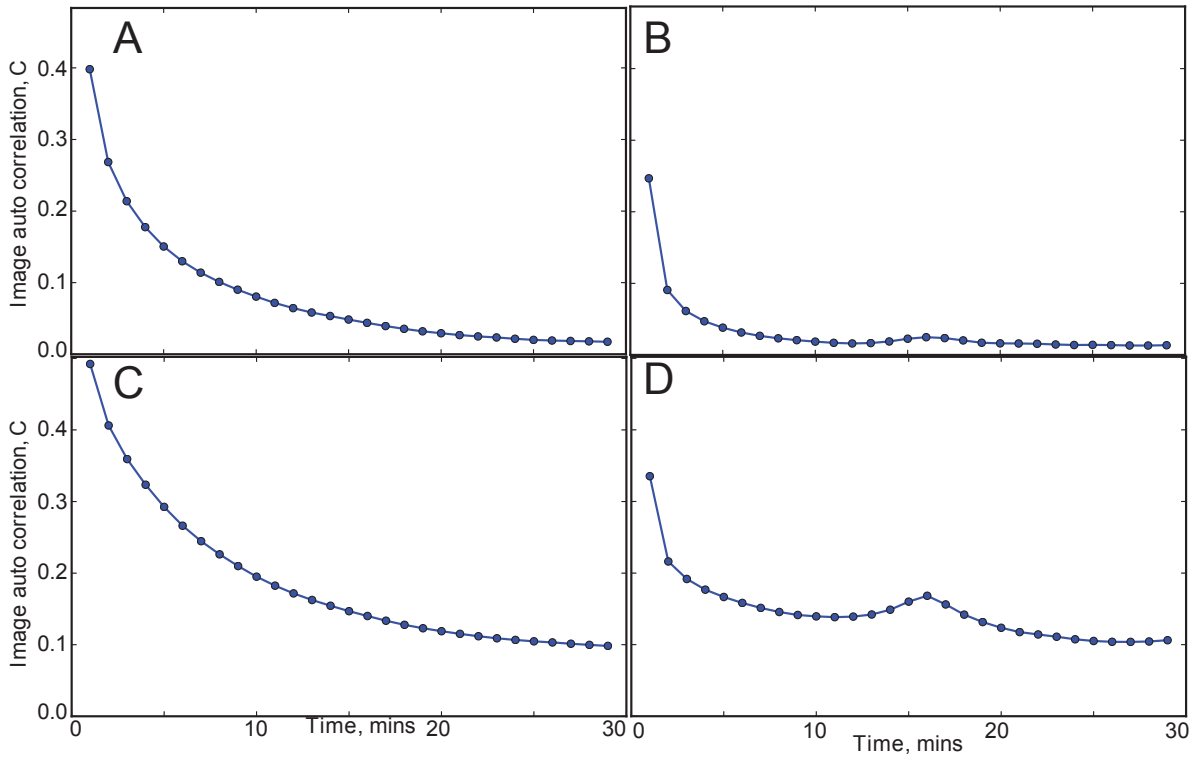


Figure C.2: Auto-correlation of simulation snapshots with time. (A, C) Non-reversing cells (B, D) reversing cells (C, D) simulations with slime-following mechanism ($L_s$=2.8 μm, $\epsilon$=1.0). For all simulations, cell density $\eta$= 0.24. Images from 60 - 180 mins of simulation time are used. Correlation among simulation images dropped to low value (0.1) after 20 mins.

this we measure the auto-correlation between the snapshots of cluster images from simulation as a function of time (Fig. C.2). Image auto-correlation is calculated using Eqn. C.1 where $C_I(t, t+\delta t)$ is the normalized cross correlation between snapshots $(f, g)$ of the simulation at times $t$ and $t+\delta t$, $N_K$ is number of such image pairs. Normalized cross correlation between two images $f, g$ is calculated using Eqn. C.2 where $n$ is the total number of pixels in the image, $f_{i,j}$ – grayscale intensity of pixel at position $i, j$ in image $f$, and $\bar{f}, \sigma_g$ are the average intensity and std. dev. in intensity of pixels in the image $f$.

$$C(\delta t) = \frac{1}{N_K} \sum_{t=1}^{K} C_I(t, t+\delta t) \tag{C.1}$$

$$C_I = \frac{1}{n} \sum_{i,j} \frac{(f_{i,j} - \bar{f})(g_{i,j} - \bar{g})}{\sigma_f \sigma_g} \tag{C.2}$$

Auto-correlation values are measured for snapshots of simulation between 60 to 180 mins after initialization. From these results, we determined that correlation among cluster images dropped to low value (< 0.1) after 20 mins for both reversing and non-reversing cells (Fig. C.2). Thus we take data from steady state time points ($\tau_{ss,t}$) separated by 20 mins as independent trials.

Mean cluster sizes at each time point ($\tau_{ss,t}$) is calculated using $\bar{m}_t = \sum_i p_i m_i$, where $p_i$ is the probability from CSD and $m_i$ is the average cluster size ($= 10^{(i-1)dm} + (10^{(i-1)dm} - 10^{idm})/2$) of bin $i$. Finally, the mean $\langle m \rangle$ and standard deviation in cluster size for specific cell density values is calculated by averaging data from all the stead state time points from multiple simulation runs ($n = 5$).

**Orientation correlation,** $C(r)$

Alignment among neighbor agents is quantified using orientation correlation function $C(r) = \langle cos 2\Delta\theta_r \rangle$. Here $\Delta\theta_r$ is the angle deviation between orientations of a pair of neighbor cell's whose center nodes are separated by a distance $r$ (Fig. A.2F). $\langle\ \rangle$ represents average over all cell pairs that are separated by a distance $r$.

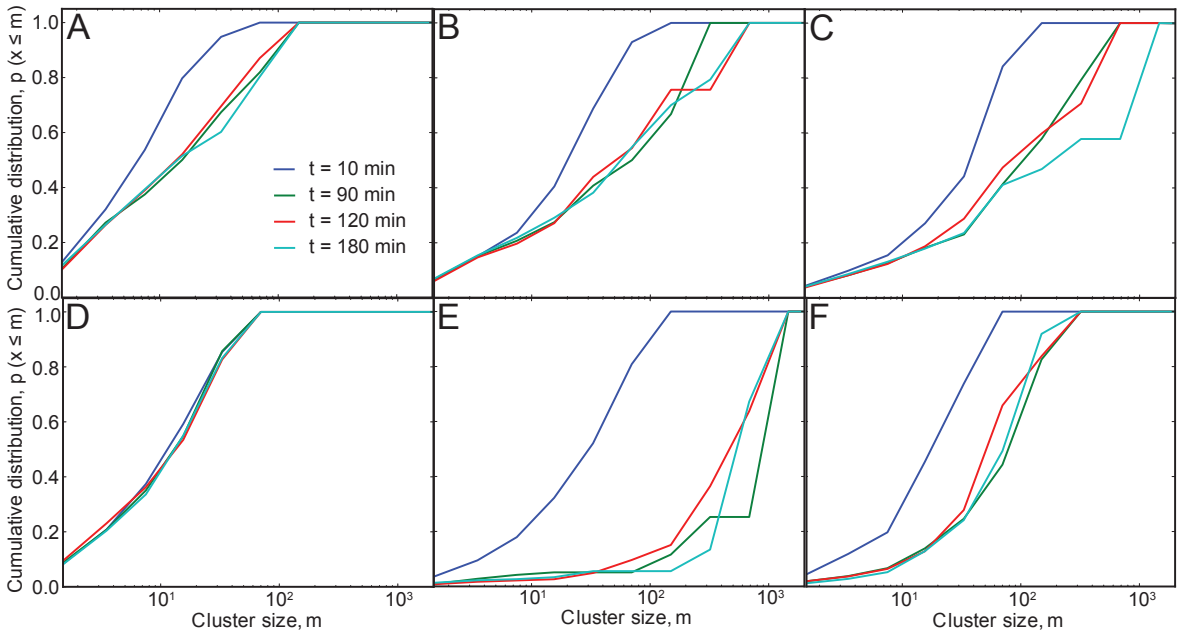


Figure C.3: Evolution of cumulative cluster size distribution (CSD) with time for different model parameters. Non-reversing agents with cell densities (A) η = 0.16 (B) η = 0.24 (C) η = 0.32 (D) Reversing agents with cell density η = 0.24 (E) Non-reversing agents following slime-trails, η = 0.24 (F) Reversing agents following slime-trails, η = 0.24.

| Symbol | Description | Value |
|---|---|---|
| $M$ $(\eta)$ | Total number of agents (corresponding cell densities) | 246-3938 (0.02-0.32) |
| $\epsilon_s$ | Slime effectiveness factor | 1.0 |
| $L_s$ | Slime trail length | 11 μm |
| $k_d$ | Slime degradation constant | 1.0 1/min |
| $V_s$ | Slime production rate | 20 AU |
| $\tau_r$ | Reversal period | 8 min[51] |

Table C.1: Simulation parameters for cell collective alignment

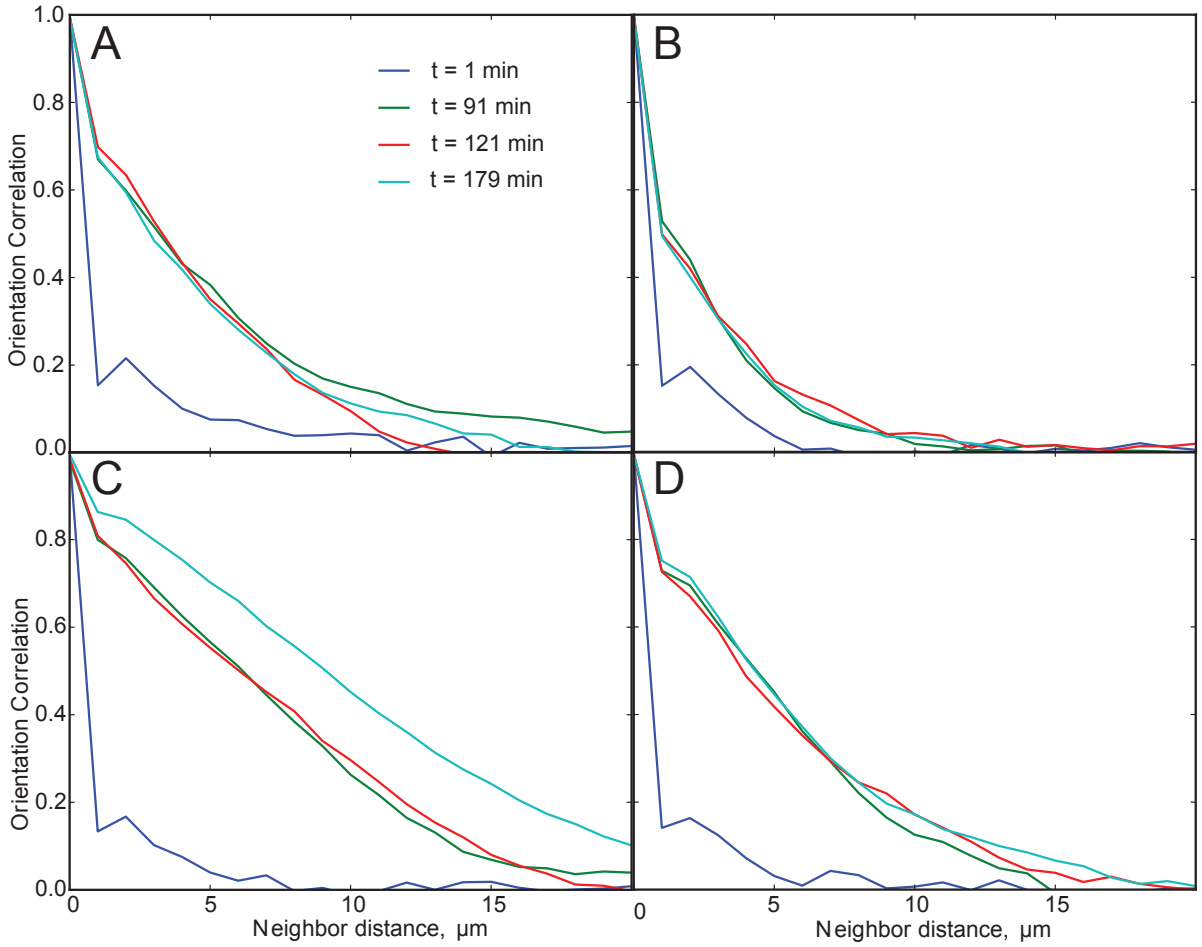


Figure C.4: Evolution of orientation correlation among cells with time. (A, C) Non-reversing cells (B, D) Reversing cells (C, D) cells following slime-trails. All simulations performed at cell density $\eta = 0.24$.

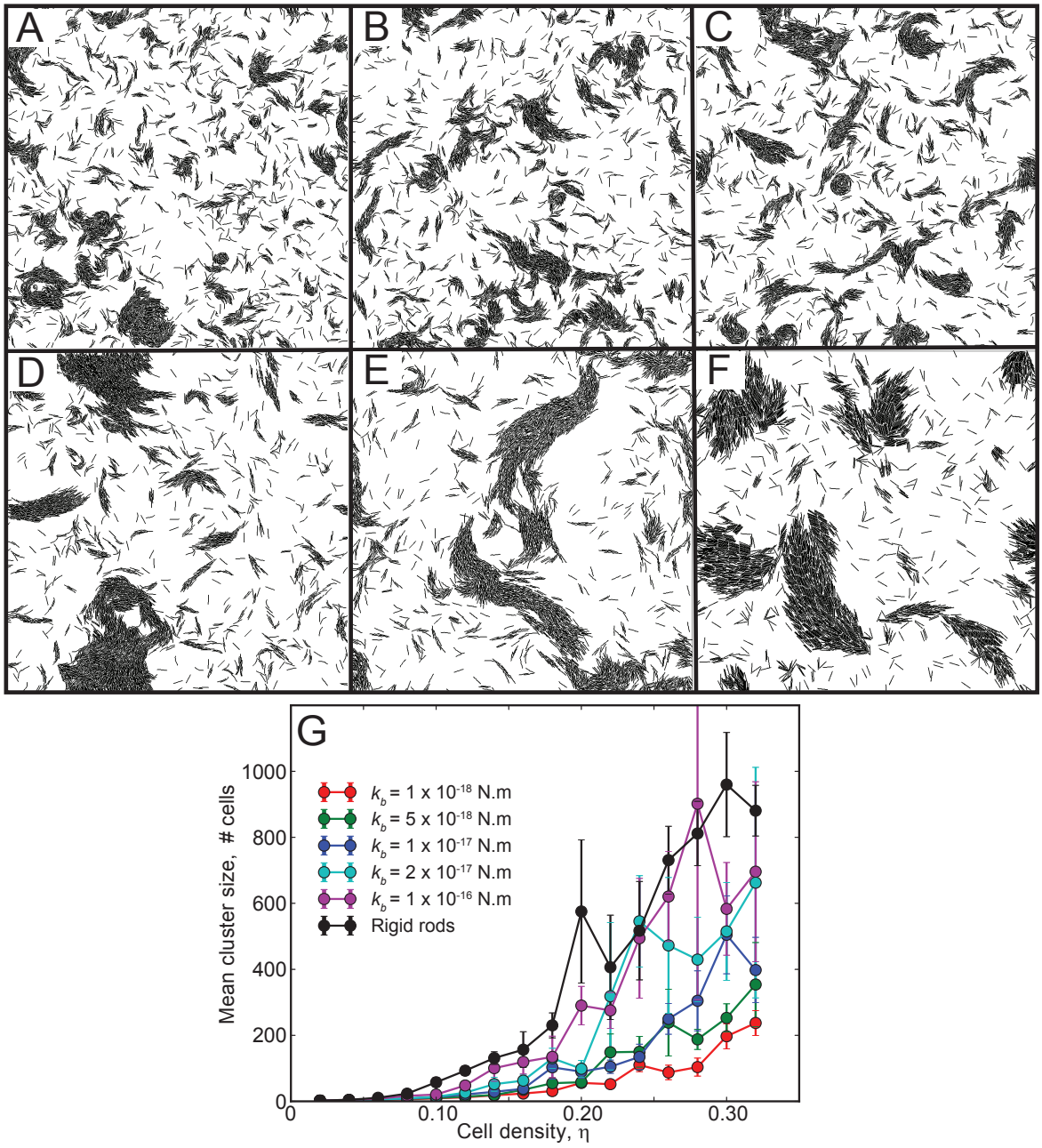


Figure C.5: Clustering behavior of non-reversing agents for variation in cell flexibility. (A-F) Snapshots of cell clusters after 180 min of simulation (cell density, η = 0.24) with bending stiffness ($k_b$) values (A) $10^{-18}$ N.m (B) $5 \times 10^{-18}$ N.m (C) $10^{-17}$ N.m (D) $2 \times 10^{-17}$ N.m (E) $10^{-16}$ N.m (F) Rigid rods (G) Mean cluster sizes in simulation as a function of cell density (η) for different cell bending stiffness values.

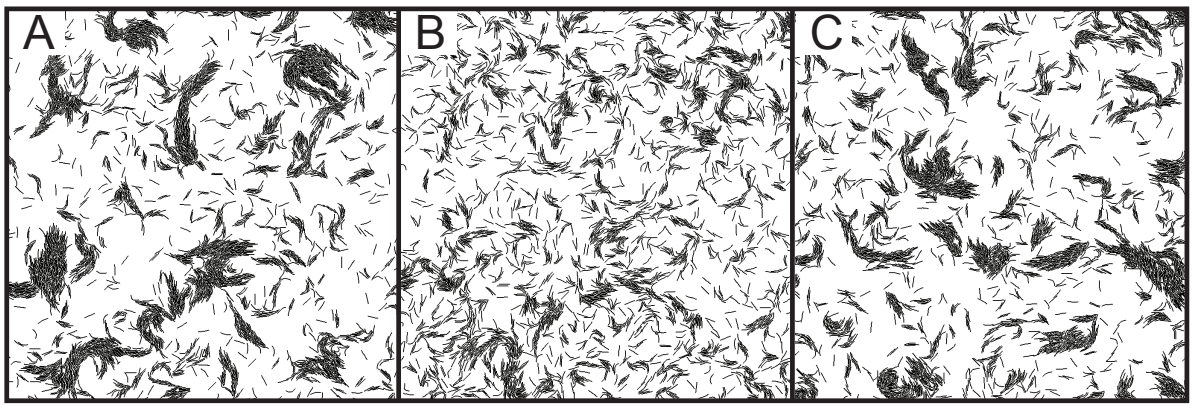


Figure C.6: Clustering behavior of cells with with turning on/off cell reversals. Snapshots of simulation at (A) 90 min (B) 120 min (C) 150 min. Cell reversals were turned-off for the first 90 min of simulation and thereafter are turned-on from 90 to 120 min with reversal period = 8 min. Reversals are turned-off again at 120 min. Cell clusters formed by simulating non-reversing cells for first 90 min (A) are quickly, within 30 min destroyed by cell reversals (B). Suppression of reversals restored clustering of cells after another 30 min (C).

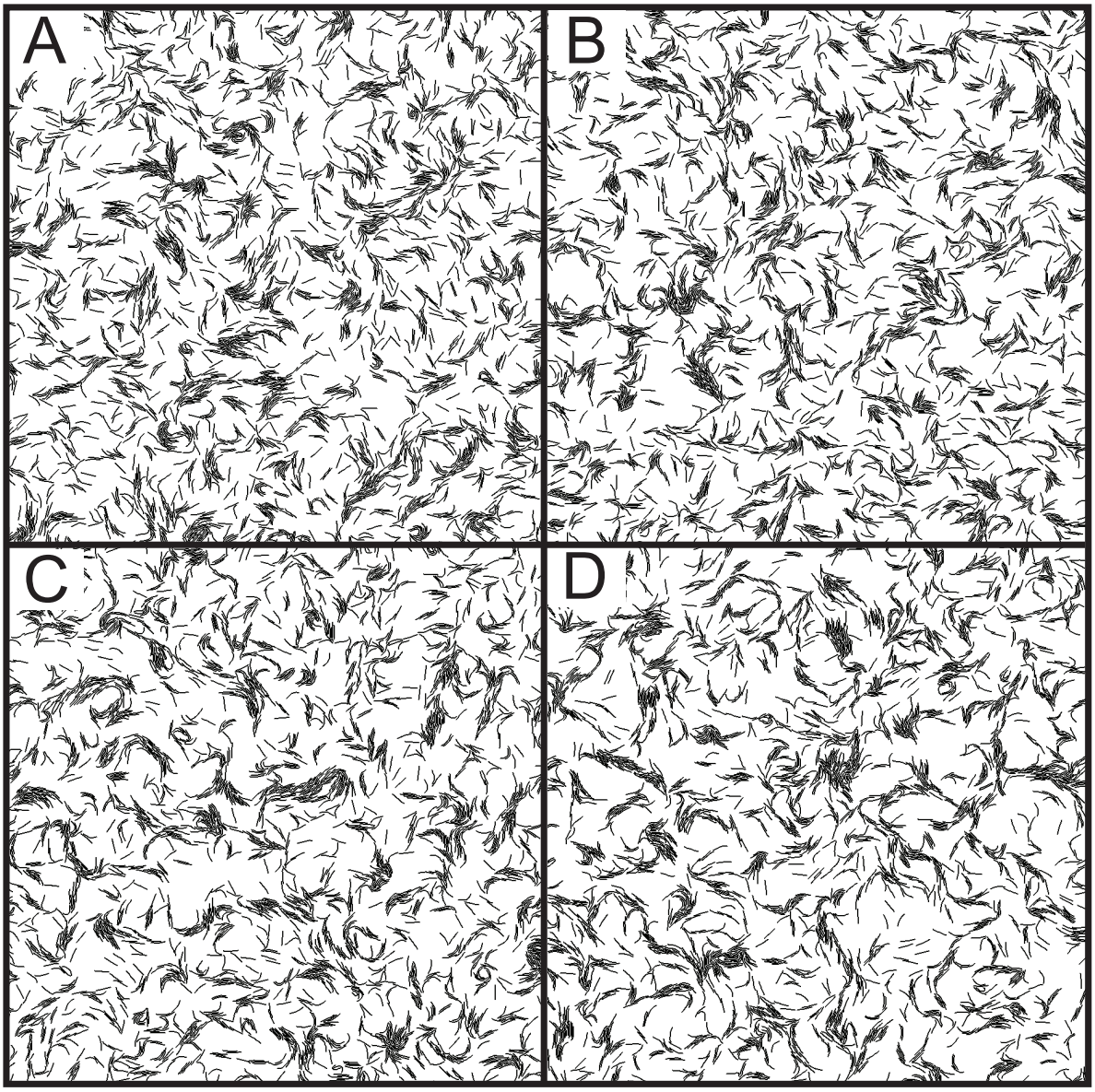


Figure C.7: Clustering behavior of reversing-cells with lateral cell adhesions. Snapshots of simulation at 180 min for different lateral adhesion force values. Adhesion force per cell (A) $F_{adh}$ = 0 pN (B) $F_{adh}$ = 30 pN (C) $F_{adh}$ = 60 pN (D) $F_{adh}$ = 120 pN.

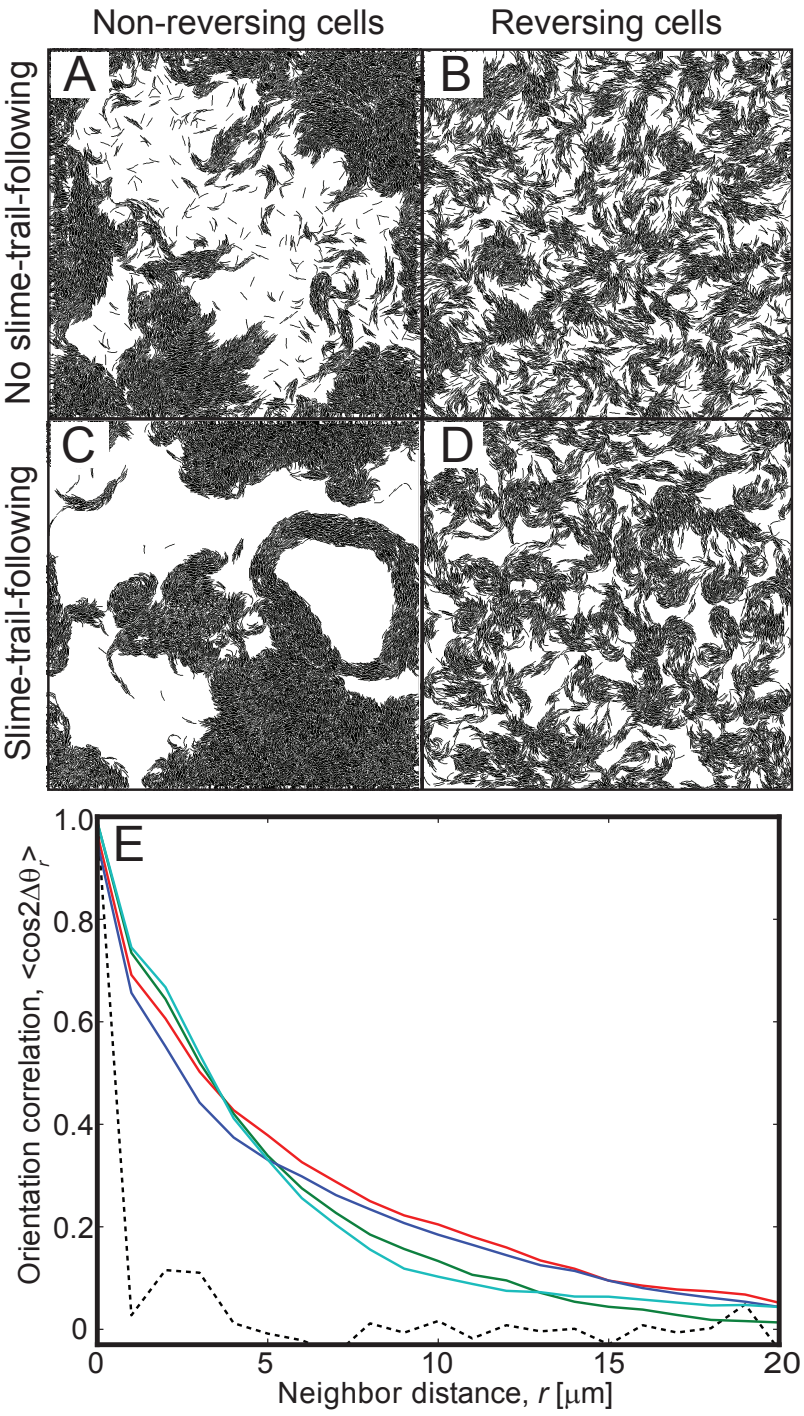


Figure C.8: Clustering behavior of cells at high cell densities. (A-D) Snapshots of simulation at 180 min for cell density $\eta = 0.60$. (E) Orientation correlation among cells at 180 min of simulation time for non-reversing cells (red), reversing cells (green), non-reversing cells with slime-trail-following (blue), and reversing cells with slime-trail-following (cyan). Dotted line represents the orientation correlation values at 1 min simulation time.

# Appendix D

# Supplementary information for *M. xanthus* circular cell aggregates

## Circular cell aggregate formation in simulation under variation of cell processes

### Non-reversing model cells formed circular aggregates independent of cell packing fraction

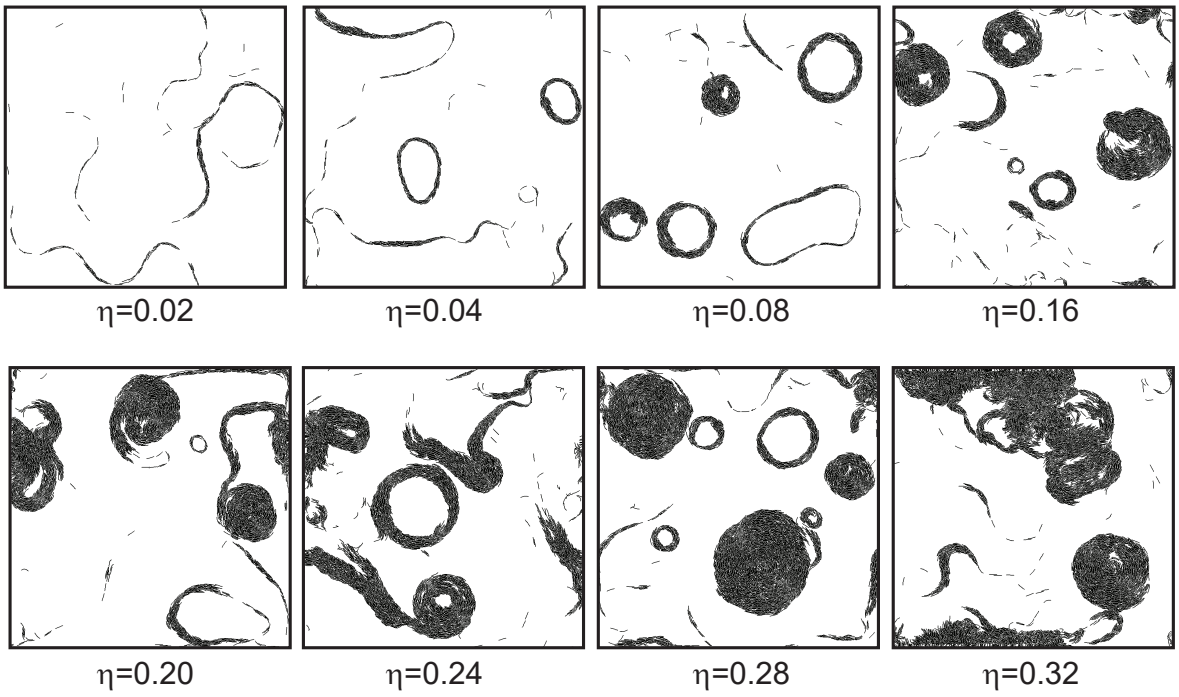


Figure D.1: Effect of cell density on circular cell aggregate (CCA) formation for non-reversing model cells. Snapshots of simulation at 180 min for different cell packing fractions ($\eta$). Non-reversing model cells formed circular aggregates at difference cell packing fraction values under strong slime-trail-following by cells ($L_s$=11 μm, $\epsilon_s$=1.0).

**Circular cell aggregation formation is robust for non-reversing model cells**

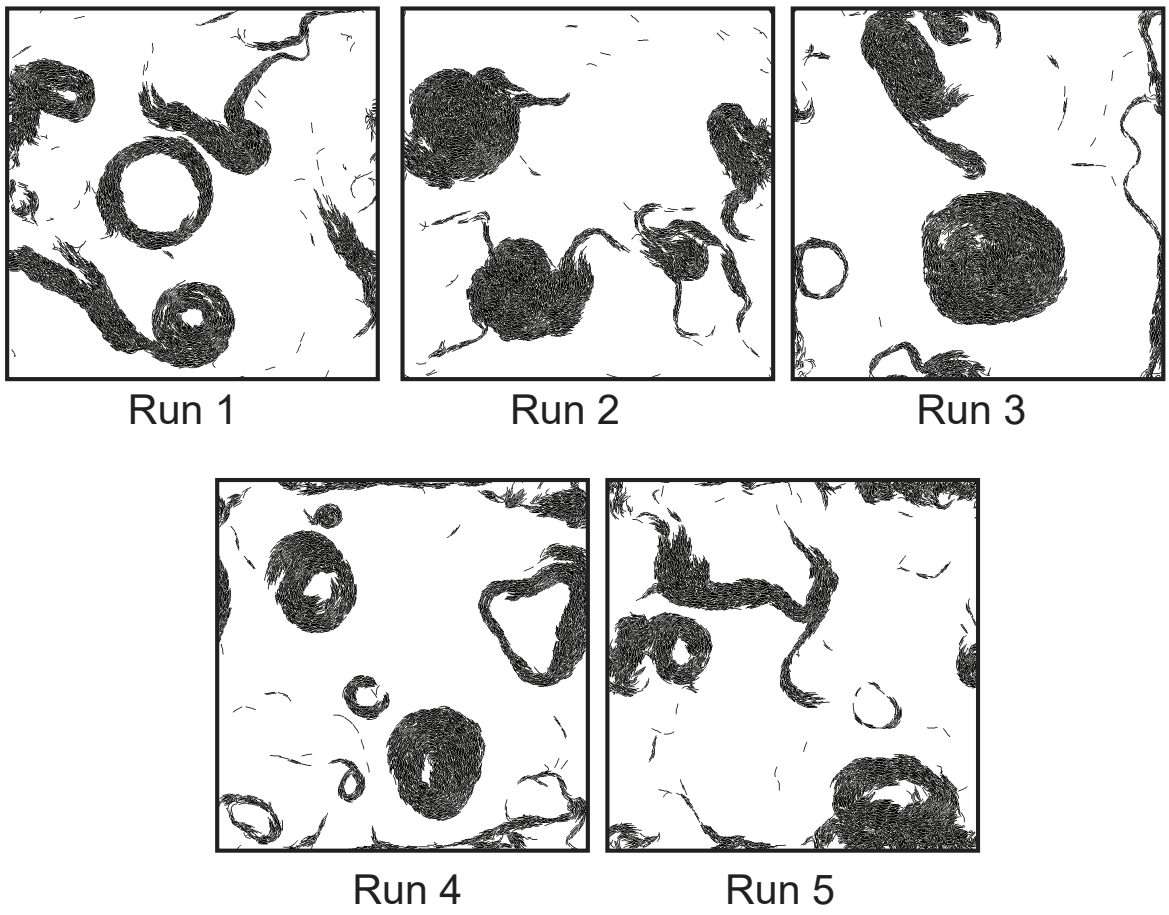


Figure D.2: Circular cell aggregates is reproducible across multiple simulation runs ($n$=5). Snapshots of simulation at 180 mins for non-reversing cells under strong slime-trail-following by cells ($L_s$=11 μm, $\epsilon_s$=1.0) at cell packing fraction $\eta$=0.24.

**Periodically reversing model cells failed to form circular aggregates independent of cell packing fraction**

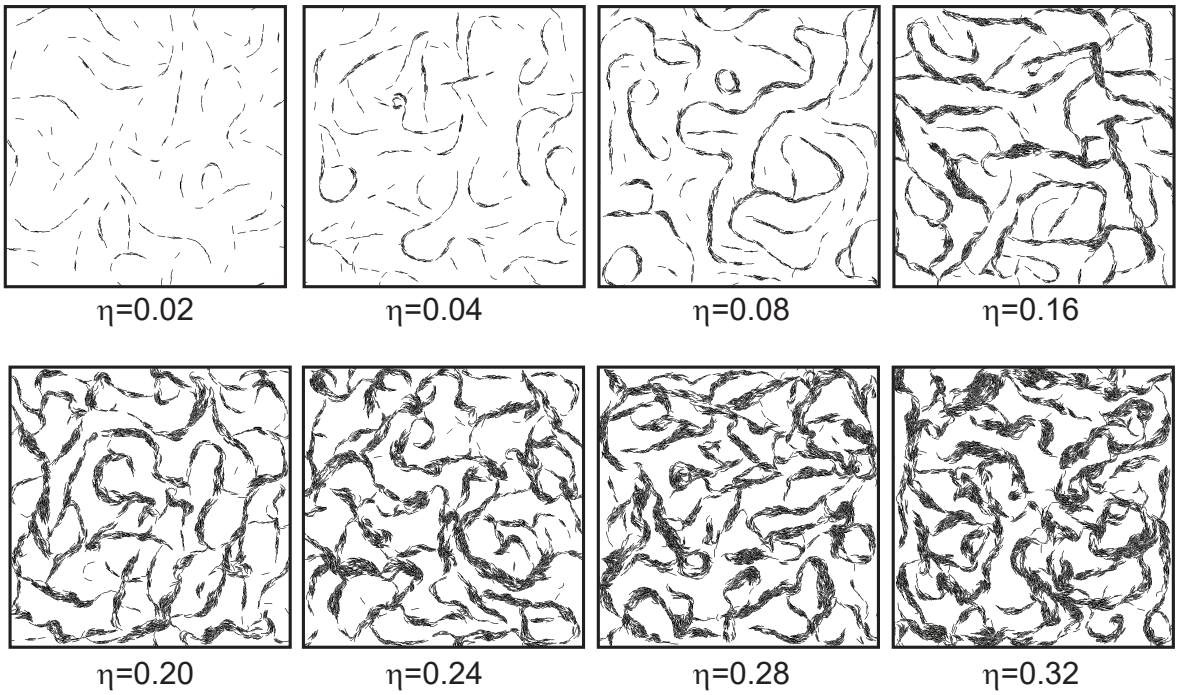


Figure D.3: Effect of cell density on CCA formation for periodically reversing model cells. Periodically reversing cells ($\tau_r$=8 min) moving under strong slime-trail-following ($L_s$=11 μm, $\epsilon_s$=1.0) failed to form circular aggregates at different cell packing fraction values ($\eta$). Snapshots of simulation at 180 min.

**Effect of cell slime-trail-following efficiency on circular aggregate formation**

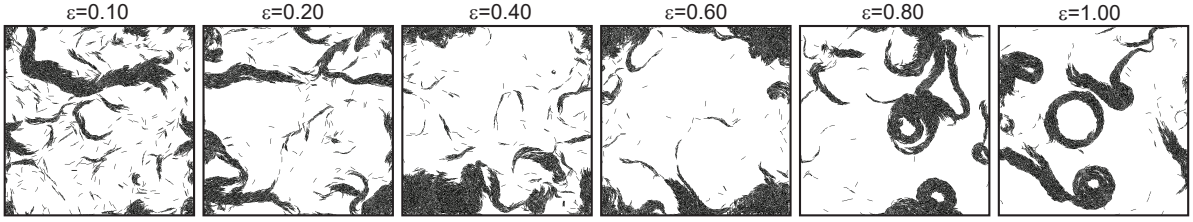


Figure D.4: Effect of slime-trail-following efficiency on CCA formation. CCA formation decreased with decreasing cell slime-trail-following efficiency ($\epsilon_s$, $L_s$=11 μm). Snapshots of the simulation at 180 min.

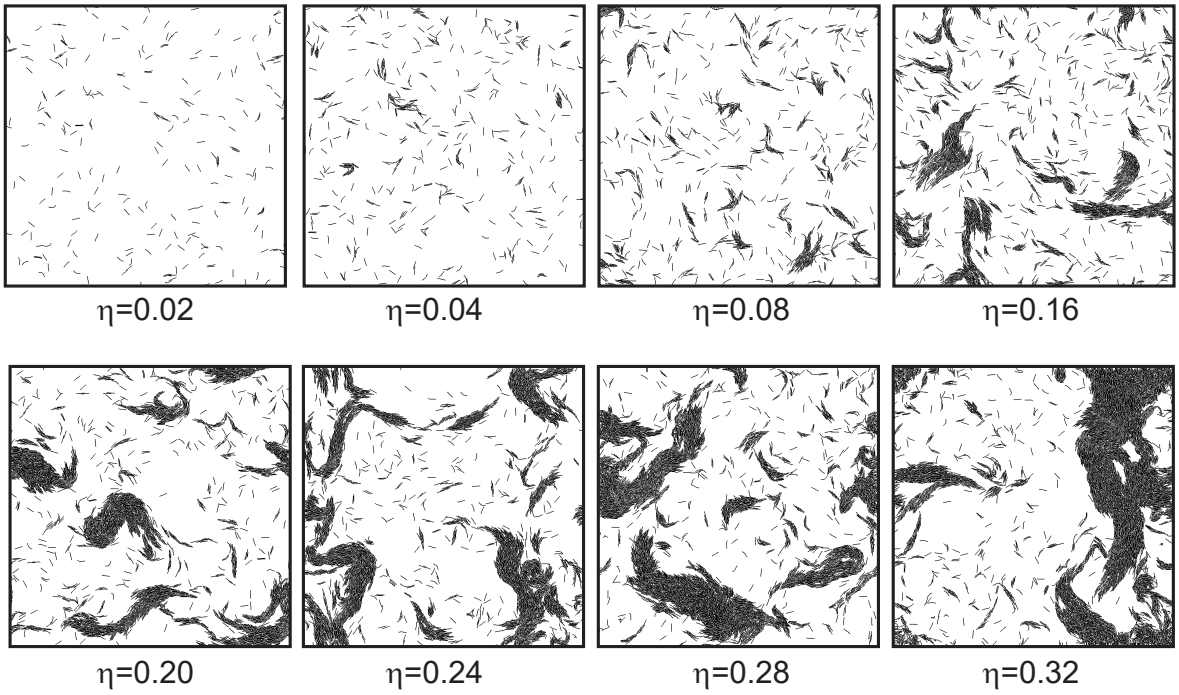


Figure D.5: Effect of cell density on CCA formation for weak slime-trail-following efficiency with non-reversing model cells. CCAs are not observed with non-reversing model cells at weak cell slime-trail-following efficiency ($L_s$=0.6 μm, $\epsilon_s$=0.2) independent of cell packing fraction. Snapshots of the simulation at 180 min.

**Removing cell substrate adhesive interactions decreased circular cell aggregate formation**

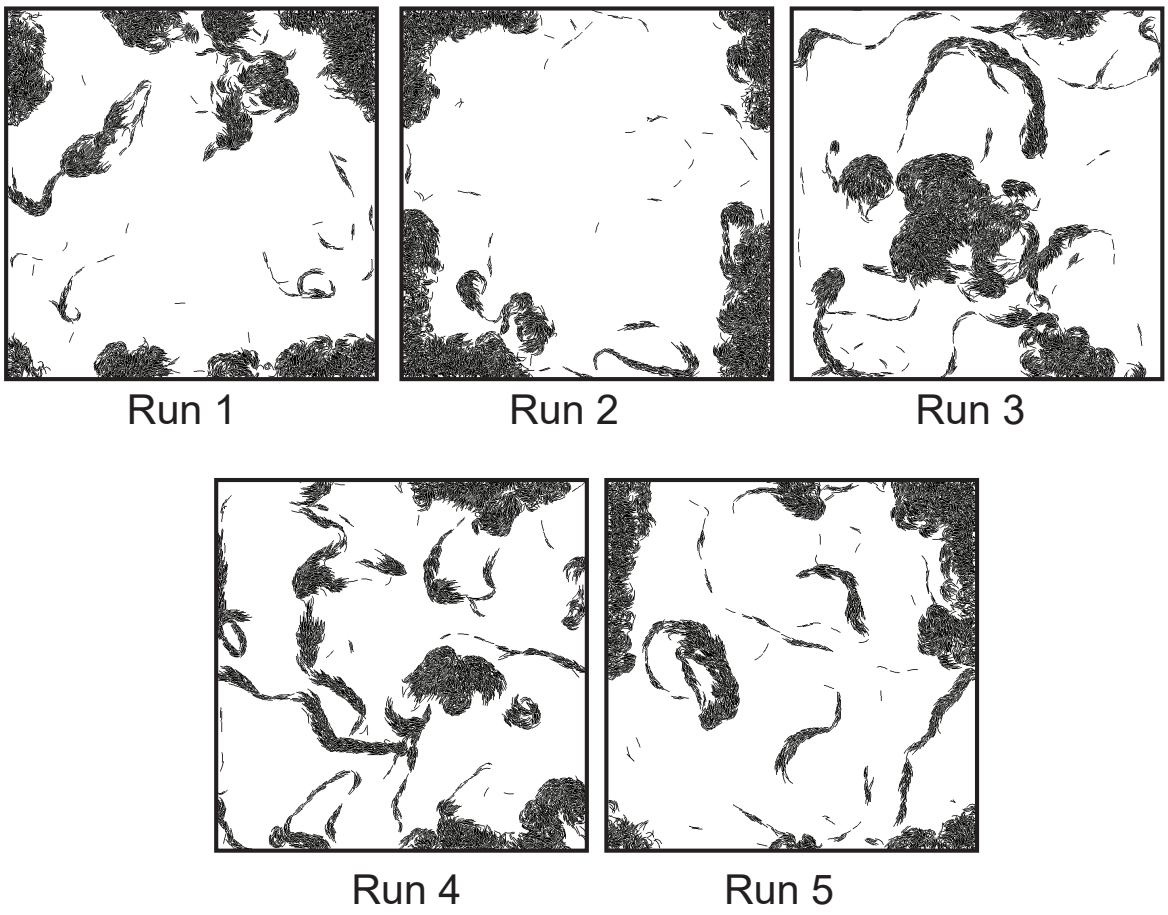


Figure D.6: Effect of cell-substrate attachments on CCA formation. Removing cell substrate adhesive interactions reduced CCA formation in our simulations even under strong cell slime-trail-following conditions($L_s$=11 μm, $\epsilon_s$=1.0, $\eta$ =0.24). Compare with Fig. D.2. Snapshots of the simulation at 180 min.

**Substrate attachments required for circular aggregate formation**

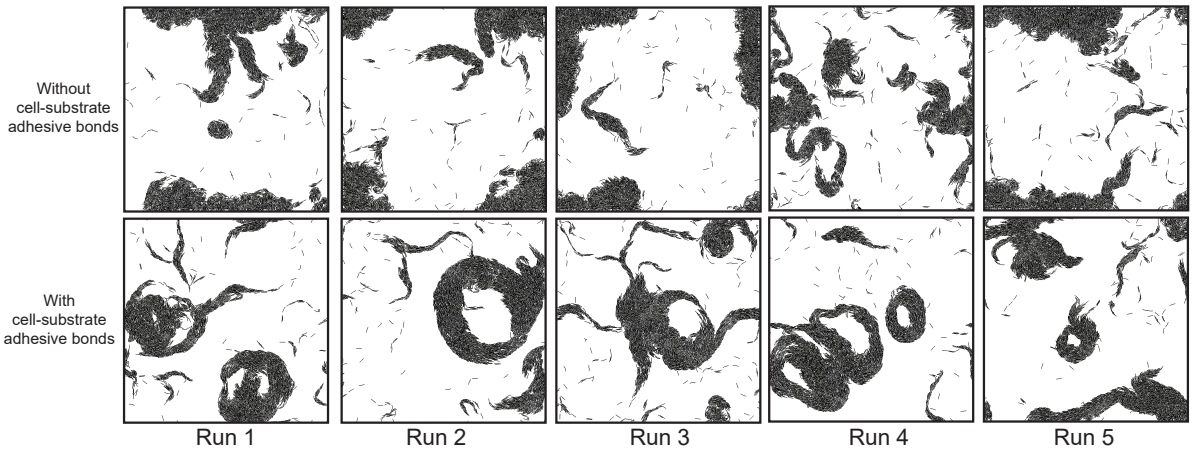


Figure D.7: Effect of cell-substrate attachments on CCA formation in simulation. Cells in simulation failed to form stable CCAs in absence of cell-substrate attachments (top row) whereas cells readily formed CCAs with inclusion of cell-substrate attachments (bottom-row) under similar slime-trail-following conditions ($L_s$ =2.8 μm, $\epsilon_s$ =1.0). Snapshots of simulation at 180 min.

**Pole-pole and lateral cell adhesive interactions**

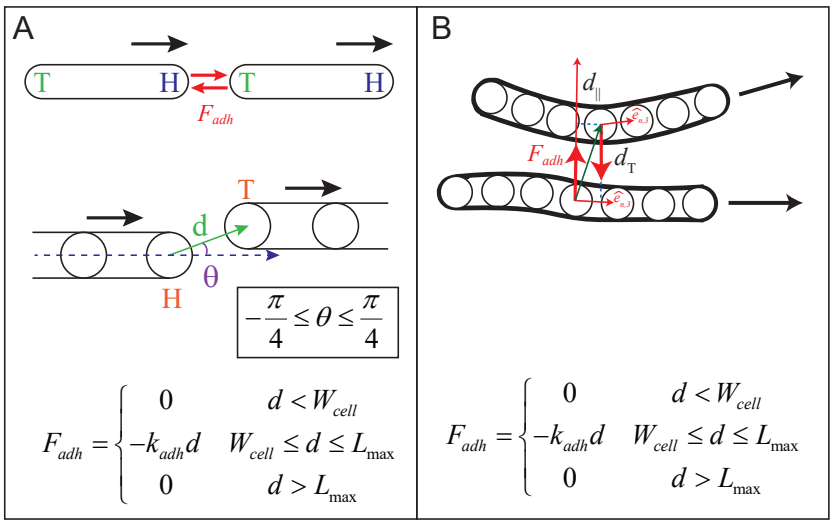


Figure D.8: Cell-cell adhesion implementation in our model (A) Pole-pole adhesion (B) Lateral cell adhesion between adjacent cell nodes

For this we added adhesive interactions between head and tail nodes of lagging and leading

cell pairs respectively. We model these interactions as adhesive attachments (linear springs, $k_{adh}$ - spring constant) that form between the interacting nodes when they come close together. These attachments add additional forces ($F_{adh}$) on the interacting nodes, towards each other, when the distance between the nodes increase. These attachments break when the force between interacting nodes cross a threshold breaking force ($F_{max}$).

**Cell-cell adhesive bonds has minor effect on circular cell aggregate formation for non-reversing cells**

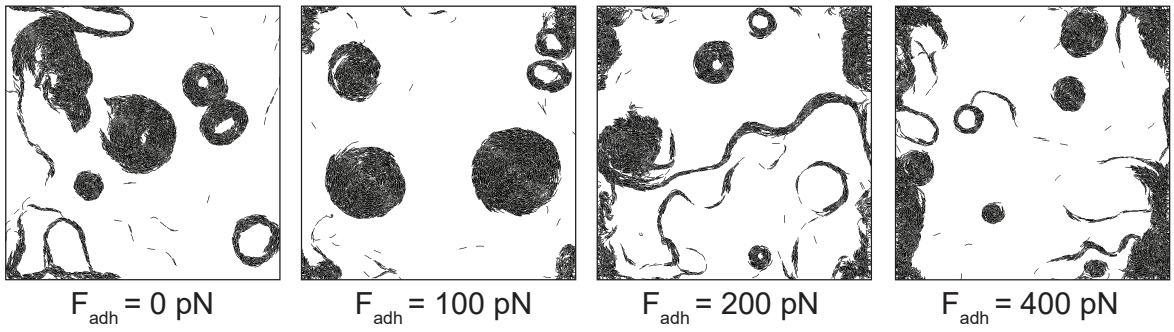


Figure D.9: Effect of cell-cell adhesion at poles at different adhesion strength values for non-reversing model cells ($\tau_r = 8$ min) under strong slime-trail-following conditions ($L_s$ =11 μm, $\epsilon_s$ =1.0). Snapshots of simulation at 180 min.

**Cell-cell adhesive interactions in absence of slime-trail-following by cells fail to produce stable circular cell aggregates**

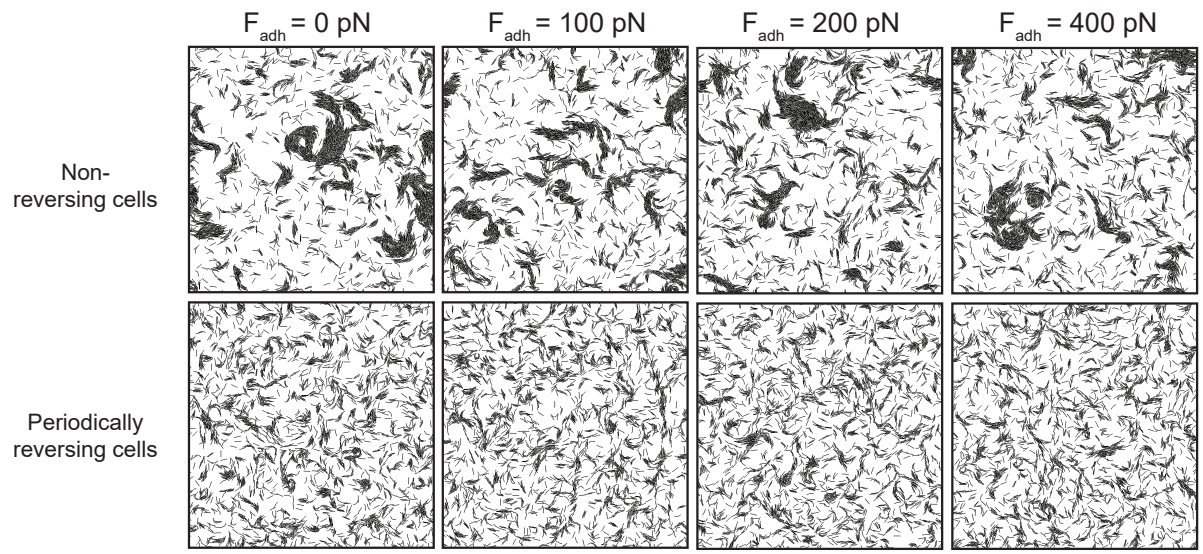


Figure D.10: Effect of cell-cell adhesion at poles for different adhesion strength values in absence of slime-trail-following by cells. Snapshots of simulation at 180 min.

**Spiral cell initialization**

To understand the stability of CCAs in our simulation under various cell processes, we have initialized cells in spiral formation (Fig. D.11, $t = 0$ min) and studied the cell motility behavior with time. We have varied various cell processes that are proven to be critical for stable CCA formation in our simulation i.e., variation of cell slime-trail-following efficiency (Fig. D.11), variation of cell reversals, variation of cell density (Fig. D.12), pole-pole and lateral cell adhesive interactions. Our simulation results with spiral initialized cells confirm our previous predictions that stable circular aggregates require cells moving with long reversal periods with neighbor cell alignment through mechanical collisions under strong cell slime-trail-following.

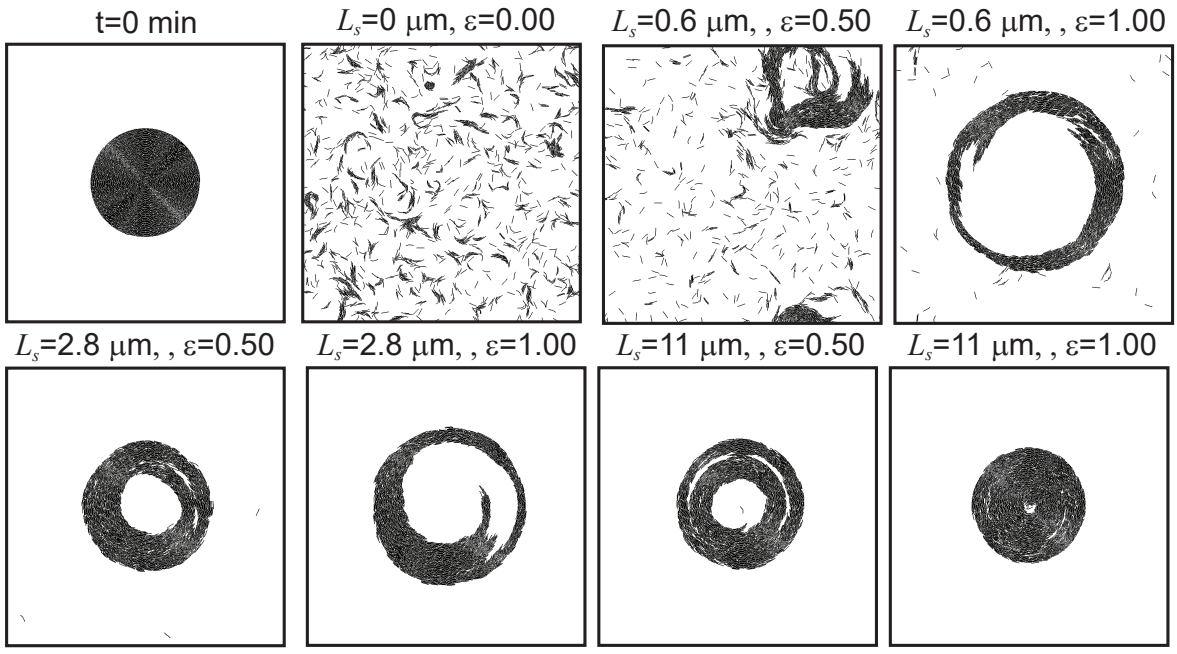


Figure D.11: Stability of circular cell aggregates for variation of cell slime-trail-following efficiency. Snapshots of simulation at 180 min. Left to right panels (top row - no or very small slime trail length ($L_s$=0.6 μm, $\epsilon_s$=0.2), bottom panel - large slime trail length($L_s$=11 μm, $\epsilon_s$=1.0)) indicate increasing cell slime-trail-following efficiency. Increase in cell slime-trail-following efficiency increased stability of circular cell aggregate.

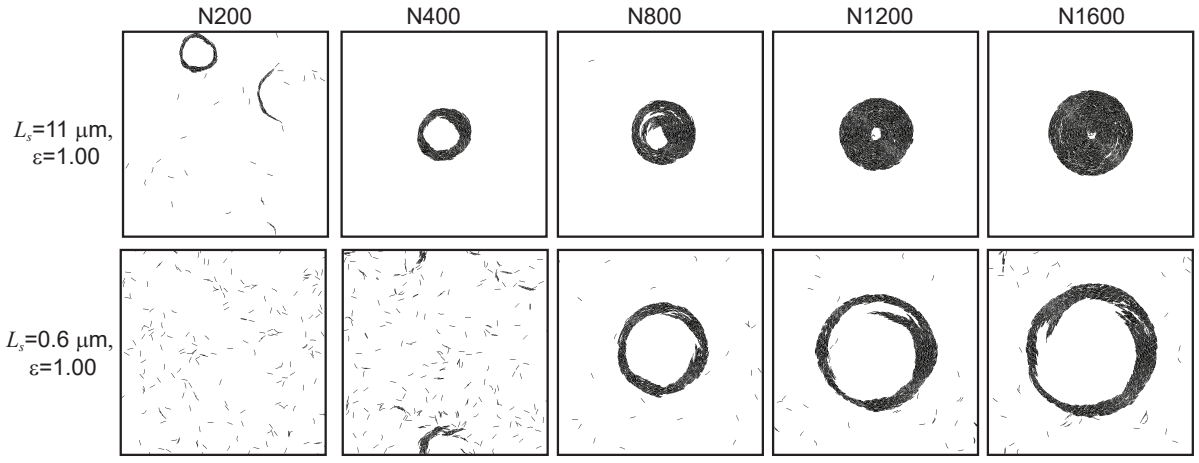


Figure D.12: Stability of circular cell aggregates for variation in cell density. Snapshots of simulation at 180 min. Left to right panels indicate increasing cell density (N = number of cells). Top and bottom panels represent cells moving under strong (top) and weak (bottom) slime-trail-following efficiency respectively.

# Appendix E

# Supplementary information for *M. xanthus* cell swarm dynamics

## 1-D continuum model for *M. xanthus* swarm expansion

$$\frac{\partial \rho^+}{\partial t} + v\frac{\partial \rho^+}{\partial x} = D\frac{\partial^2 \rho^+}{\partial x^2} + g\rho^+(1-\rho^{tot}/K) + \lambda(\rho^- - \rho^+)$$

$$\frac{\partial \rho^-}{\partial t} - \underbrace{v\frac{\partial \rho^-}{\partial x}}_{\text{Advection}} = \underbrace{D\frac{\partial^2 \rho^-}{\partial x^2}}_{\text{Diffusion}} + \underbrace{g\rho^-(1-\rho^{tot}/K)}_{\text{Growth}} + \underbrace{\lambda(\rho^+ - \rho^-)}_{\text{Reversals}}$$

$\rho^+(x,t),\ \rho^-(x,t)$ - density of right and left moving cells respectively; ($\rho^{tot} = \rho^+ + \rho^-$); $v$ - mean speed of cells; $D$ diffusion coefficient of the cells; $g$ - growth rate of cells; $K$ - carrying capacity; $\lambda$ - cell reversal frequency

Above set of partial differential equations are solved using Crank-Nicolson method ($dt = 5\times10^{-3}$ hr, $dx$ =0.02 mm, $t_{final}$ =96 hr, $D = 1.2\times10^{-2}$ mm$^2$/hr, $v$ =2.4 mm/hr, $g$ =0.14 /hr, $K$ =1, $1/\lambda$ =3.33$\times10^{-2} - 8.33$ hr) and the resulting cell density profiles (left and right moving cells) are shown in figure E.1. Corresponding total cell density profile ($\rho^{tot}$) is shown in figure E.2. We observe that colony spread from above equations shows a constant rate expansion (Fig. E.3) with time. Next we studied that final expansion of the colony as a function of cell reversal period $\tau_r$, shown in Fig. E.4. We observe that colony expansion increases linearly with cell reversal period for small cell reversal period values ($\tau_r$ < 50 min) but colony expansion saturated for large cell reversal periods ($\tau_r \approx 500$ min).

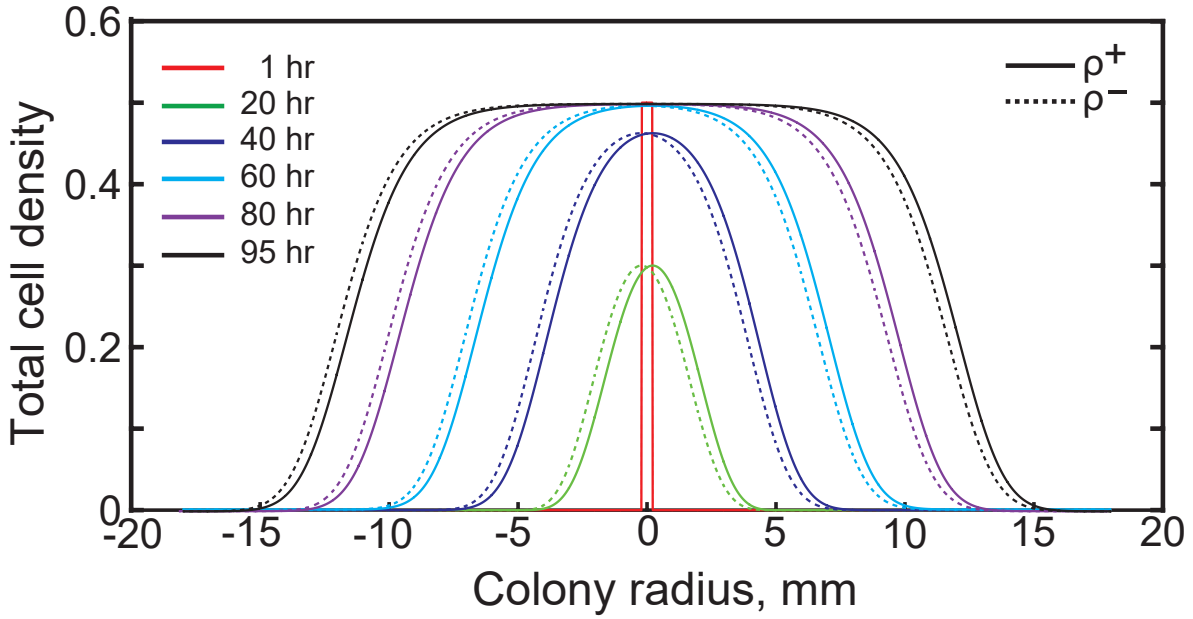


Figure E.1: Cell density profiles in space from 1-D continuum model. Reversal period, $\tau_r = 1/\lambda$=100 min

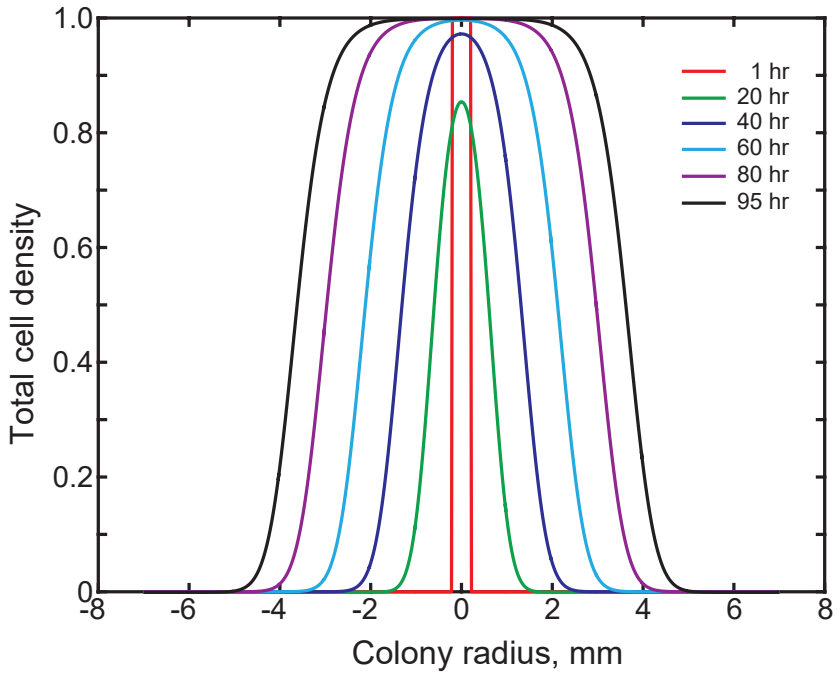


Figure E.2: Total cell density profile in space from 1-D continuum model with time. Reversal period, $\tau_r = 1/\lambda$=8 min

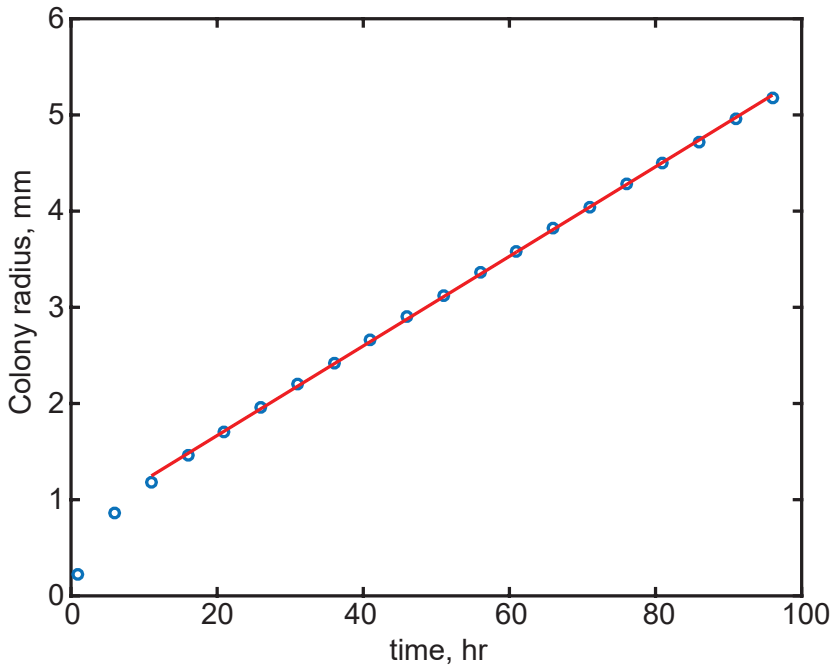


Figure E.3: Colony spread as a function of time from 1-D continuum model. Spread rate = 0.047 mm/hr, cell reversal period $\tau_r = 1/\lambda = 8$ min

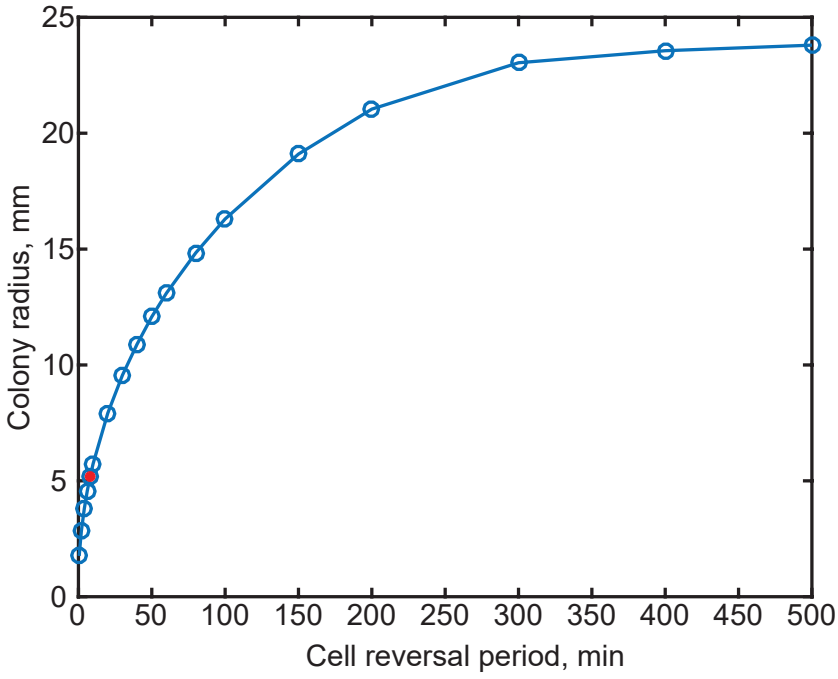


Figure E.4: Final colony radius (at $t$=96 hr) as a function of cell reversal period $\tau_r$

## Cell stalling not observed in biophysical cell simulation at high cell density

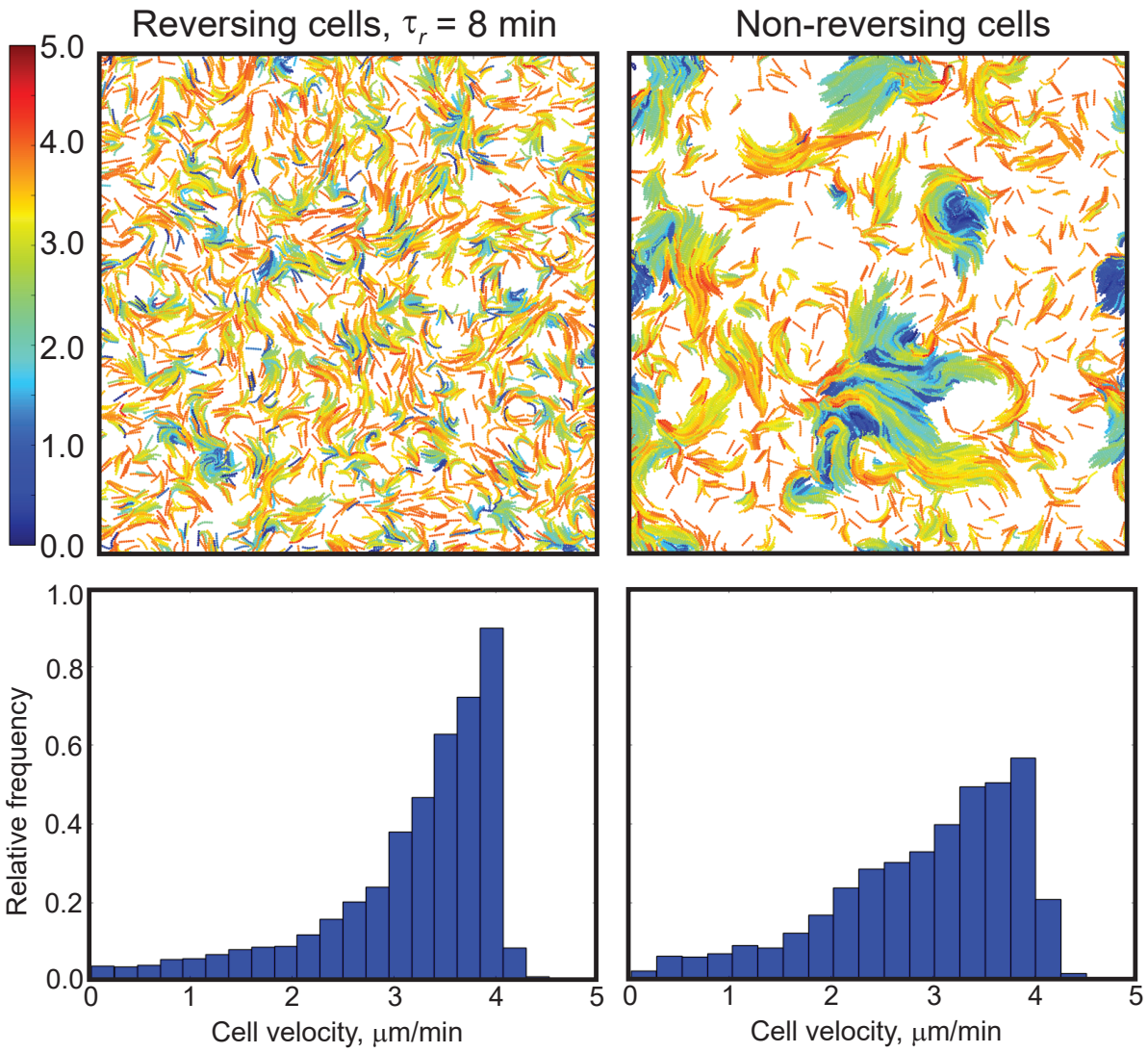


Figure E.5: Visualization of cell velocities in simulations at high cell packing fraction. Snapshots of simulations (top row) and corresponding cell velocity distributions (bottom row) at 180 min for reversing ($\tau_r = 8$ min) and non-reversing cells at high cell packing fraction ($\eta = 0.40$). Color bar represents cell velocities in μm/min.

## Monte-Carlo simulation model for *M. xanthus* swarm expansion

### Flexible cell model

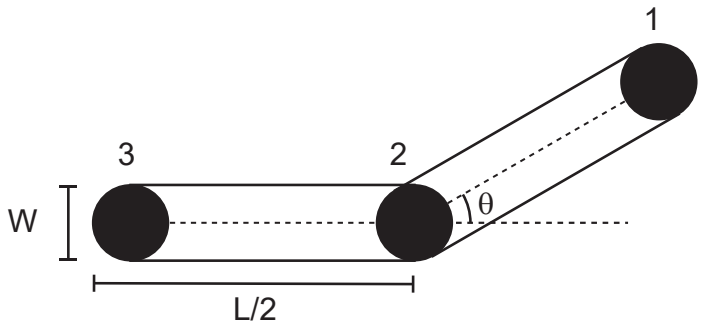


Figure E.6: Schematic of flexible cell model in Monte-Carlo simulation model

We will follow the Monte-Carlo simulation model described by Wu et al. [103, 102, 101] based on 2-D off-lattice flexible model *M. xanthus* cells. Each cell is represented by a string of $N(=3)$ circular nodes $(1, 2, .., N)$ of radius $W/2$ connected by $(N-1)$ equal length linear segments of width $W$ representing a total cell length of $L$ (Fig. E.6). Node $1, N$ are designated as head and tail nodes respectively. Neighboring linear segments have rotational freedom and there are $(N-2)$ such rotational joints whose angles are $\theta_i$ representing angle between each pair of neighbor segments. Relative positions of circular nodes $\boldsymbol{r}_i$ are free to change according to the Monte-Carlo simulation step such that the model cell shows bending and linear elastic behavior.

### Cell movement

At each step of the simulation first the head node is moved to a new position and the remaining cells nodes move according to the Monte-Carlo simulation steps (described later). Movement of head node to a new position ($\boldsymbol{r}_1^{new}$) for a cell $k$ is calculated using Eqn. E.1 based on cell speed $V_0$ in the unit vector direction $\hat{e}_k$ combined with additional rotational noise $\bar{\eta}$ in cell movement. Node movement direction ($\hat{e}_k$) is calculated based on current travel direction ($\bar{A}_k$)

- *M. xanthus* A motility, average direction of neighbor cells ($\bar{S}_k$) - *M. xanthus* S motility and underlying slime orientation ($\bar{L}_k$).

$$\begin{aligned} \boldsymbol{r}_1^{new} &= \boldsymbol{r}_1^{old} + \hat{e}_k V_0 + \bar{\eta} \\ \hat{e}_k &= \frac{\alpha\bar{A}_k + \beta\bar{S}_k + \gamma\bar{L}_k}{|\alpha\bar{A}_k + \beta\bar{S}_k + \gamma\bar{L}_k|} \\ \bar{S}_k &= e^{i<\theta>}; <\theta> = \frac{1}{2n}\sum_{j=1}^{n} \text{sin}2\theta_j \\ \bar{\eta} &= Be^{i\theta} \end{aligned} \tag{E.1}$$

Here cell travel direction ($\bar{A}_k$) is same as the direction of vector from node 2 to node 1. For S-motility, we measure the average nematic orientation $< \theta >$ of neighbor cells (count = $n$ and align the cell $k$ in acute angle with average neighbor cell orientation $< \theta >$ i.e $\hat{S}_k \cdot \hat{e}_{<\theta>} \geq 0$. Each cell leaves a slime trail in its current travel direction while moving on the 2-D surface. Orientation of slime trail ($\bar{L}$) is stored as a 2-D vector field/grid whose values are over-written with each pass of a model cell movement. $\alpha, \beta, \gamma$ are the relative fractional coefficients determining contributions from each process for node movement direction $\hat{e}_k$. $B$ is the orientational noise strength and $e^{i\theta} = \text{cos}\theta + i\text{sin}\theta$ where $\theta$ is chosen randomly in the range $[0, 2\pi]$ with uniform probability.

**Monte-Carlo simulation step**

Each cell configuration is defined by its Hamiltonian energy ($H$) that depends on its node positions ($\boldsymbol{r}_i$) and angles ($\theta_i$) between the segments. A cell's Hamiltonian energy is defined by the equation E.2 where $K_b,\ K_{theta}$ are the linear extension and bending spring constants respectively, $l_i$ is the current segment length and $l_0$ is the equilibrium segment length.

$$H = \underbrace{\sum_{i=0}^{N-1} K_b(l_i - l_0)^2}_{\text{Streching energy}} + \underbrace{\sum_{i=0}^{N-2} K_\theta \theta_i^2}_{\text{Bending energy}} \tag{E.2}$$

Relative cell node positions $\boldsymbol{r}_i$ are updated according to following Monte-Carlo simulation step. At each step of simulation , first the head node a cell is moved to a new position (described later) with a displacement of $\Delta x$ and the following the tentative movements for other nodes are repeated for $2.5N$ times. 1) Randomly choose a node $i$ among $[2, ...N]$ nodes and move the node $i$ in the direction of node $i-1$ for a distance of $\Delta x + \delta n$ where $\delta n$ is small noise displacement. 2) Calculate the Hamiltonian energy change $\Delta H$ from current change in node positions. 3) Accept the change in node positions with probability $P$ based on Metropolis algorithm [206] shown in Eqn. E.3 where $k$ is the Boltzmann constant, $T$ is the system temperature (a parameter that moves the system away from equilibrium).

$$\begin{aligned} P &= 1,\ \Delta H \leq 0 \\ P &= e^{-k\Delta H/kT},\ \Delta H > 0 \end{aligned} \tag{E.3}$$

**Collision resolution**

When the head node of cell $k$ collides/overlap with body of cell $j$, collision is resolved by choosing a new direction for cell $k$. New direction for cell $k$ is chosen randomly such that new direction is in acute angle with cell $j$ direction if head node of $k$ is less than one cell width distance from either of end nodes (head or tail) of cell $j$ i.e. end-end collision. If distance between head node of cell $k$ and end nodes of other cell $j$ is more than one cell width i.e. head-to-side collision, then average direction of cell $k$ and cell $j$ is chosen as new direction for cell $k$ and cell $k$ is stalled till next simulation time step.

Additionally periodic cell reversals are implemented using an internal reversal cell clock that is incremented for every time step of simulation. When the cell reversal clock reaches the

threshold cell reversal period, we reverse the direction of cell travel by reversing the order of cell nodes i.e. cell nodes are ordered $N, N-1, ...1$.

**Simulation setup**

We simulate cell swarm behavior in a 2-D rectangular simulation region (Fig. E.7A). Cells are initialized with random orientation and positions in the constant cell density region at bottom of the box representing the colony interior. Cells move and interact with neighbor cells and collectively swarm out from the initial region. We track the number of cells leaving the initial region as the cell number flux. We add new cells into the initial region to keep the cell density constant.

## Simulation results

### Swarm expansion behavior for from Monte-Carlo simulation

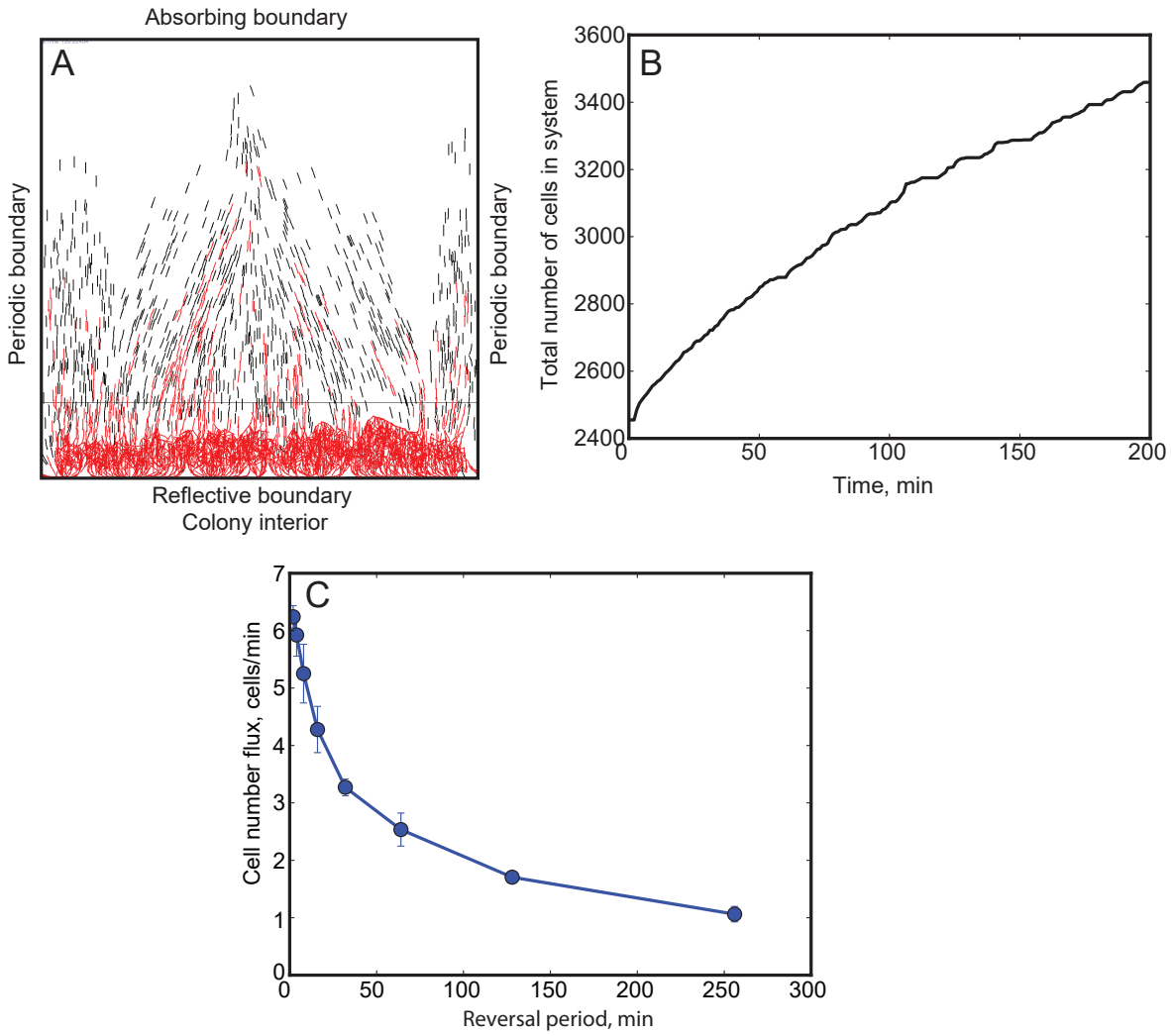


Figure E.7: Swarm expansion behavior of model cells in Monte-Carlo simulations.(A) Snapshot of simulation at 200 min from Monte-Carlo simulation (B) Cell number flux recorded as a function of time in Monte-Carlo simulation model for reversing cells ($\tau_r = 8$ min) with slime-trail-following by cells. (C) Relative cell flux calculated from Monte-Carlo simulation model as a function of cell reversal period.

**Swarm expansion behavior for a mix of reversing and non-reversing cells**

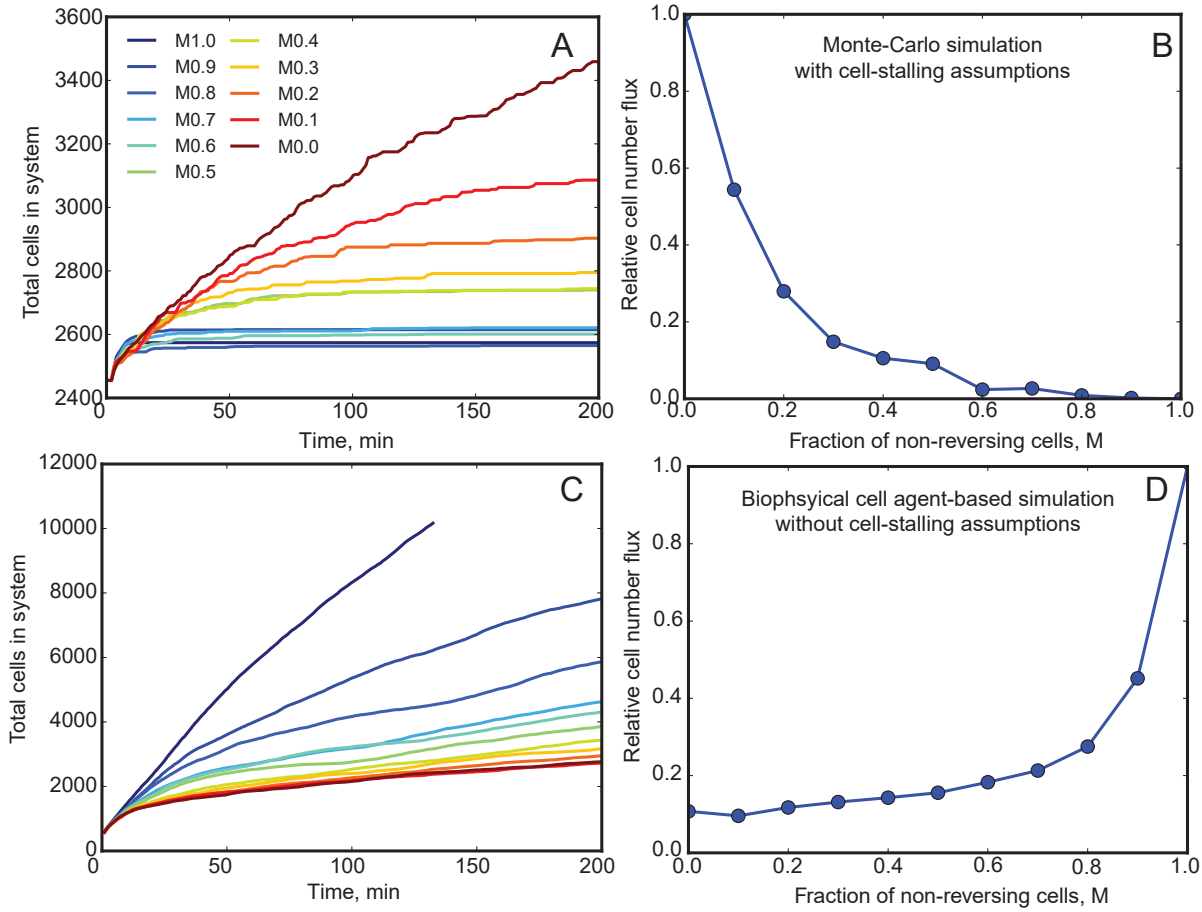


Figure E.8: Swarm expansion behavior of model cells at a colony edge with a mix reversing and non-reversing cells in simulations.(A) Cell number flux recorded from Monte-Carlo simulation model for cell populations with mix of reversing and non-reversing cells. Each colored line represent the results from simulation with different fraction of non-reversing cells. (B) Relative cell flux from Monte-Carlo simulation model as a function non-reversing cell fraction. (C) Cell number flux from biophysical cell agent-based-simulation for cell populations with mix of reversing and non-reversing cells. (D) Relative cell flux from biophysical cell ABS model as a function of non-reversing cell fraction

# Analysis and quantification of cell motility tracking data

## Data filtering and smoothing

*M. xanthus* cell motility tracking data for both wild-type (reversing) cells and non-reversing mutants is provided by Dr. Joshua Shaevizt Lab, Priceton University. This data describes the movement of individual *M. xanthus* cells as they swarm on solid agar surfaces and is obtained by applying high-resolution cell tracking algorithms on time-lapse microscopy images of *M. xanthus* swarms [168, 204]. Cell tracking data is stored in the form of Matlab© cell structures. Each Matlab cell structure contained tracking information for a single *M. xanthus* cell (called cell track). Each row of cell track has 4 data columns: (frame number, cell x position, cell y position, distance moved from previous frame). Cell positions are given in pixels with the following scaling: spatial scale: 1 pixel = 80 nm and frame to frame time interval for images = 10 sec.

## Instantaneous cell velocities from raw data

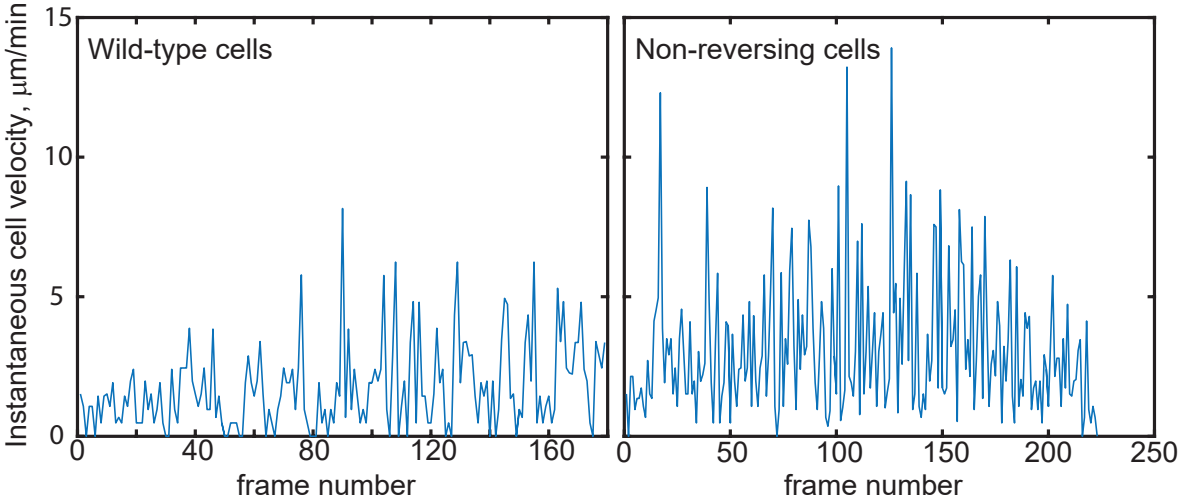


Figure E.9: Instantaneous cell velocities from a single cell track for wild-type and non-reversing *M. xanthus* cells calculated from frame to frame displacement of the cell

First we calculated the instantaneous cell velocities based on cell displacement from frame

to frame and plotted them as a function of frame number for both reversing and non-reversing cells (Fig. E.9). We observe that the instantaneous cell velocities are highly noisy due to errors from microscope drift during imaging and errors from tracking algorithm. To reduce noise we filtered/smoothed cell velocity using a weighted moving average method.

**Data smoothing using weighted moving average method**

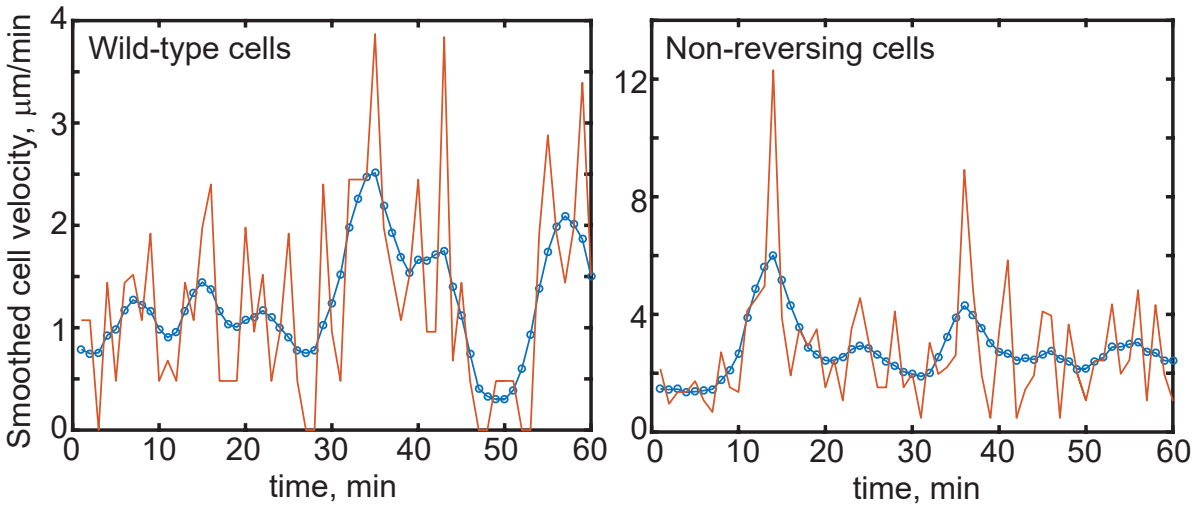


Figure E.10: Smoothed cell velocities (circles) calculated from instantaneous cell velocities (line) using moving weighted average method for a single cell track for wild-type and non-reversing cells

Instantaneous cell velocities values are smoothed using weighted moving average method, where a cell velocity at each time point is estimated as a weighted sum of previous and next time points velocities using following equation.

$$\bar{X} = \frac{\sum_i w_i X_i}{\sum_i w_i} \tag{E.4}$$

where $w_i$ are weights associated with neighbor time points $i = [-n, -n+1, ..., 0, ...n-1, n]$. Here we use weights from a triangular weighting function $w_i = n - |i| + 1$ with $n = 3$ centered at current time point $i = 0$. Resulting smoothed cell velocities are shown in Fig. E.10. We ignore data from cell tracks that are less than 10 min length.

Smoothed cell velocity values from all the cell tracks for each min of cell travel are pooled together and the resulting histograms of cell velocity distributions are shown in Fig. 5.5 for both wild-type cells ($n$=4791 cell tracks) and non-reversing mutants ($n$=18628 cell tracks). We observe that cell velocities follow a normal distribution.

**Mean cell velocities**

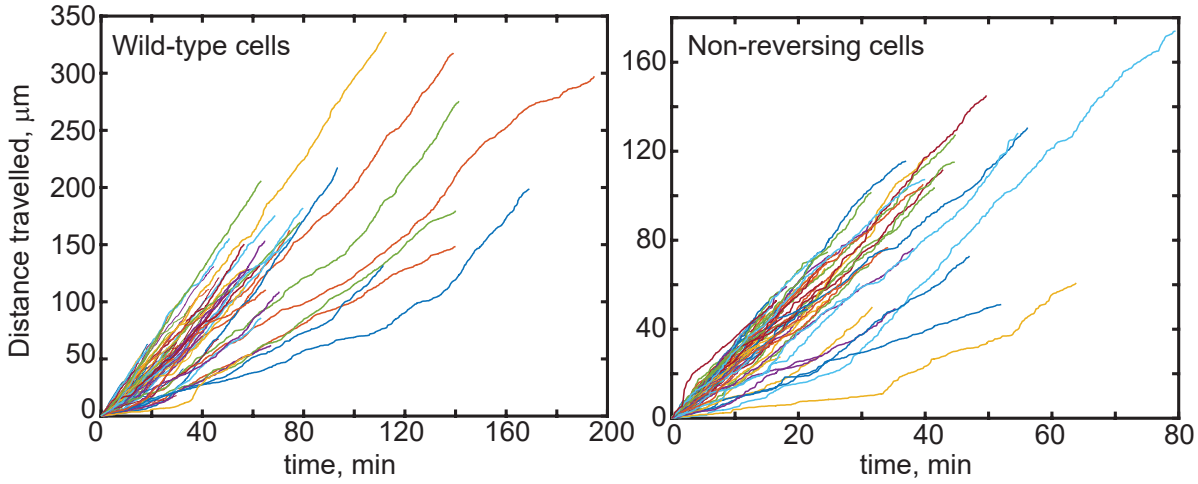


Figure E.11: Cumulative distance traveled by individual cells ($n = 100$) as a function of time for wild-type and non-reversing cells.

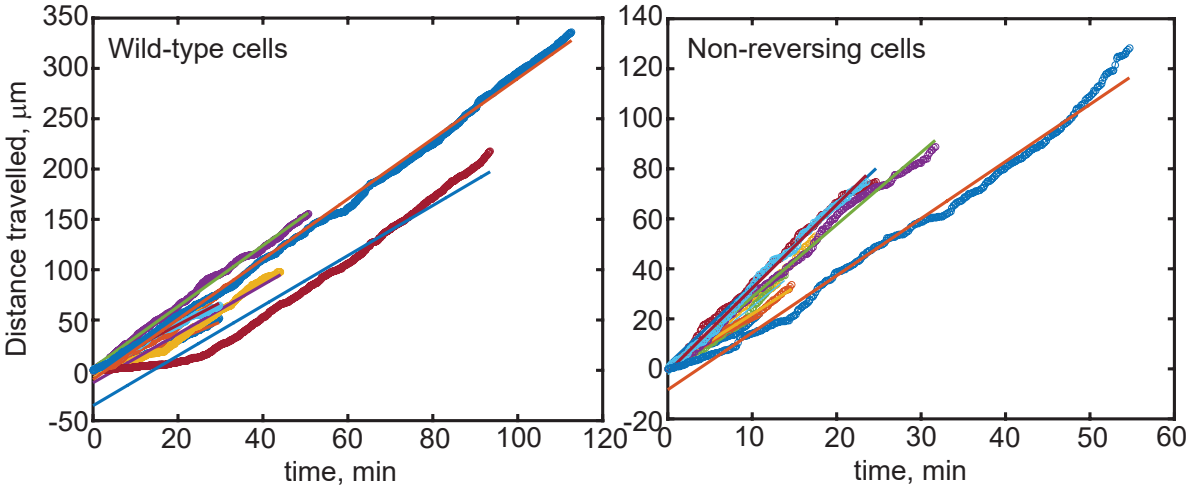


Figure E.12: Cell cumulative travel distance with time fit to a linear function for wild-type and non-reversing cells

# Appendix F

# Biophysical cell model implementation using Box2D physics engine

## Rigid body simulation in Box2D physics engine

### Box2D physics engine

Box2D is a 2-dimensional rigid-body physics engine (simulation library) that simulates the motion of rigid bodies based on Newtonian dynamics. It was developed by Erin Catto [172] to add physics based motion effects in 2-D games. Additionally it supports kinematic objects, static objects and motion constraints on bodies. We use Java port of Box2D library(LiquidFun [217]) for our simulation. Description of various features of Box2D library and how these features are utilized in our simulation are presented below.

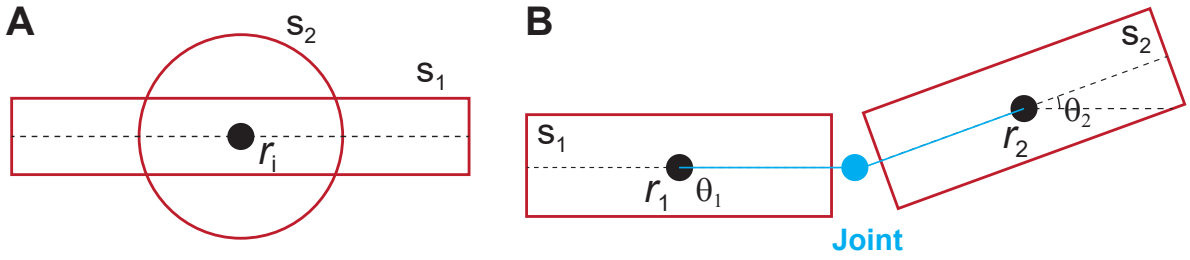


Figure F.1: Rigid body representation in Box2D physics engine. Each rigid body $i$ is represented by a point particle at center with position ($r_i$) and orientation ($\theta_i$). Multiple shapes ($S_1, S_2$) can be associated with a single body. Shapes are attached to the center particle through a fixture object. Fixture objects define material properties of the body (density, friction coefficient, restitution etc.). Mass of the body ($m_i$) can be either specified or automatically calculated by the density and associated shape of the body.

**Rigid bodies**

Rigid bodies in Box2D are point particles (specified by their position, $\boldsymbol{r}_i$ and orientation $\theta_i$ in the physics world Fig. F.1A) with shapes (fixtures) attached to them. Mass of the object is determined by the the shape and dimension of the the fixture attached. Rigid bodies also define other properties such as body type (Dynamic, Kinetic, Static), linear damping coefficient, angular damping coefficient etc.

**Fixture**

Fixtures attach to the body and define its shape (using Shape object - Circle, Polygon) and other material properties such as density, friction, restitution. Multiple fixtures can be attached to a single body to create complex shaped bodies.

**Joints**

Joints connect two bodies and impose constraints on their motion (removes degrees of freedom, see Fig. F.1B). Various type of joints in Box2D available. E.g. Revolute joint restricts relative motion between the connected objects to rotation; Distance joint restricts the distance between connected bodies; Prismatic joint restricts relative motion of connected bodies to a specified axis of translation; Weld joint attaches the two bodies removing all degrees of freedom.

**Physics World**

All the bodies in Box2D are contained in the physics world. Additionally it defines the direction and magnitude of gravity. Physics world object computes the motion of all the bodies contained in it based on the forces acting on the bodies and their movement constraints defined by the joints. Further it provides collision detection between bodies and resolves collisions by applying additional forces on the bodies to separate the colliding objects.

**Restrictions of Box2D**

Box2D can only simulate motion of rigid bodies. Soft/deformable bodies and bodies with changing shapes can not be simulated in Box2D. Dimension of any dynamic body should be with in 0.1 to 10 units to keep the error of Box2D physics solver within tolerance limits. All parameters specified in Box2D solver are in MKS system.

**Rigid body construction in Box2D**

Each rigid body is constructed by creating shape, fixture and body objects. Properties of the each type of object are specified by corresponding definition objects (FixtureDefinition, Body-Definition, JointDefinition etc.).

```
// create shape of the body
CircleShape cshape = new CircleShape();
cshape.radius = 1f;

// create fixture definition for the body
FixtureDef fd = new FixtureDef();
fd.shape = cshape;
fd.density = 1f;
fd.lineardamping = 0f;
fd.friction = 0.1f;

// create body definition
BodyDef bd = new BodyDef();
bd.position.set(new Vec2(0f, 0f));
bd.type = BodyType.DYNAMIC;
// create body
```

```
Body body = physicsWorld.createBody(bd);

// attach fixture to the body
body.attachFixture(fd);
```

**Creating joints between bodies**

```
// creates a revolute joint between two bodies
// create Joint definition
RevoluteJointDef rjd = new RevoluteJointDef();
rjd.bodyA = bodyHead;
rjd.bodyB = bodyTail;
// set anchor position for the joint in bodyA relative to its
   center
rjd.localAnchorA.set(new Vec2(0, 0));
// set anchor position for the joint in bodyB relative to its
   center
rjd.localAnchorB.set(new Vec2(0, 0));

// create joint
RevoluteJoint revJoint = (RevoluteJoint) physicsWorld.
   createJoint(rjd);
```

## *M. xanthus* model cell representation in Box2D

Each model cell is represented by a connected string of rectangular ($N-1$) and circular ($N$) bodies (see Fig. F.2). Each pair of neighbor bodies are connected by revolute joints i.e. 1 revolute joint is created between rectangular and circle bodies at nodes $1, N$ and 3 revolute

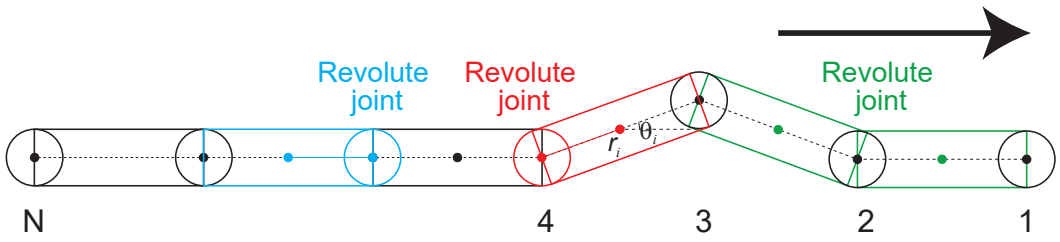


Figure F.2: *M. xanthus* model cell representation as connected rigid bodies in Box2D physics engine. Each pair of neighbor nodes (rectangular-rectangular, rectangular-circle) are connected by revolute joints of Box2D library. 3 revolute joints used at nodes $2, 3, ..N-1$.

joints (between rectangular-rectangular bodies, between rectangular-circular bodies $\times$ 2) are created at nodes $2, ..., N-1$. Each body moves in the physics world due to various forces acting on the bodies subject to joint constraints.

## Physics simulation step in Box2D

At each step of simulation, physics solver iterates through all the bodies in the physics world and computes the position and velocity of the bodies subject to the forces and constraints acting on them. For each body $i$ physics solver accumulates the forces ($\boldsymbol{F}_i$) and torques ($\boldsymbol{T}_i$) acting on it and updates its position ($\boldsymbol{r}_i$), velocity ($\dot{\boldsymbol{r}}_i$) and orientation ($\theta_i$) using following equations of motion based on Newtonian dynamics.

$$\frac{d\dot{\boldsymbol{r}}_i}{dt} = \frac{1}{m_i}\sum_i \boldsymbol{F}_i - \gamma\dot{\boldsymbol{r}}_i$$
$$\frac{d\boldsymbol{r}_i}{dt} = \dot{\boldsymbol{r}}_i$$
$$\frac{d\omega_i}{dt} = \frac{1}{I}\sum_i \boldsymbol{T}_i - \alpha\omega_i$$
$$\frac{d\theta_i}{dt} = \omega_i$$

# Bibliography


[1] I. Couzin and Krause, "Self-organization and collective behavior in vertebrates," *Advances in the Study of Behavior*, vol. 32, pp. 1–75, 2003.

[2] I. Giardina, "Collective behavior in animal groups: theoretical models and empirical studies," *HFSP J*, vol. 2, no. 4, pp. 205–19, 2008.

[3] S. Camazine, *Self-organization in biological systems*. Princeton University Press, 2003.

[4] T. D. Seeley, "When is self-organization used in biological systems?," *Biol Bull*, vol. 202, no. 3, pp. 314–8, 2002.

[5] D. J. Sumpter, "The principles of collective animal behaviour," *Philos Trans R Soc Lond B Biol Sci*, vol. 361, no. 1465, pp. 5–22, 2006.

[6] E. Ben-Jacob, "Bacterial self-organization: co-enhancement of complexification and adaptability in a dynamic environment," *Philos Trans A Math Phys Eng Sci*, vol. 361, no. 1807, pp. 1283–312, 2003.

[7] B. Eshel and H. Levine, "Self-engineering capabilities of bacteria," *Journal of The Royal Society Interface*, vol. 3, no. 6, pp. 197–214, 2006.

[8] N. Verstraeten, K. Braeken, B. Debkumari, M. Fauvart, J. Fransaer, J. Vermant, and J. Michiels, "Living on a surface: swarming and biofilm formation," *Trends Microbiol*, vol. 16, no. 10, pp. 496–506, 2008.

[9] K. K. Jefferson, "What drives bacteria to produce a biofilm?," *FEMS Microbiol Lett*, vol. 236, no. 2, pp. 163–73, 2004.

[10] J. A. Shapiro, "The significances of bacterial colony patterns," *Bioessays*, vol. 17, no. 7, pp. 597–607, 1995.

[11] J. A. Shapiro, “Thinking about bacterial populations as multicellular organisms,” *Annu Rev Microbiol*, vol. 52, pp. 81–104, 1998.

[12] B. Bassler and R. Losick, “Bacterially speaking,” *Cell*, vol. 125, no. 2, pp. 237–246, 2006.

[13] M. Miller and B. Bassler, “Quorum sensing in bacteria.,” *Annu. Rev. Microbiol.*, vol. 55, pp. 165–99, 2001.

[14] A. Persat, C. D. Nadell, M. K. Kim, F. Ingremeau, A. Siryaporn, K. Drescher, N. S. Wingreen, B. L. Bassler, Z. Gitai, and H. A. Stone, “The mechanical world of bacteria,” *Cell*, vol. 161, no. 5, pp. 988–97, 2015.

[15] S. Kjelleberg and S. Molin, “Is there a role for quorum sensing signals in bacterial biofilms?,” *Curr. Opin. Microbiol.*, vol. 5, no. 3, pp. 254–8, 2002.

[16] N. Reading and V. Sperandio, “Quorum sensing: the many languages of bacteria,” *Fems Microbiol Lett*, vol. 254, no. 1, pp. 1–11, 2006.

[17] C. M. Waters and B. L. Bassler, “Quorum sensing: cell-to-cell communication in bacteria.,” *Annu Rev Cell Dev Biol*, vol. 21, pp. 319–46, 2005.

[18] K. Nealson and J. Hastings, “Bacterial bioluminescence: its control and ecological significance.,” *Microbiol Rev*, vol. 43, no. 4, pp. 496–518, 1979.

[19] E. Budrene and H. Berg, “Complex patterns formed by motile cells of escherichia coli.,” *Nature*, vol. 349, no. 6310, pp. 630–3, 1991.

[20] E. O. Budrene and H. C. Berg, “Dynamics of formation of symmetrical patterns by chemotactic bacteria,” *Nature*, vol. 376, no. 6535, pp. 49–53, 1995.

[21] A. A. Polezhaev, R. A. Pashkov, A. I. Lobanov, and I. B. Petrov, “Spatial patterns formed by chemotactic bacteria escherichia coli.,” *Int. J. Dev. Biol.*, vol. 50, no. 2-3, pp. 309–14, 2006.

[22] R. M. Harshey, “Bacterial motility on a surface: many ways to a common goal,” *Annu Rev Microbiol*, vol. 57, pp. 249–73, 2003.

[23] J. W. Costerton, Z. Lewandowski, D. E. Caldwell, D. R. Korber, and H. M. Lappin-Scott, “Microbial biofilms,” *Annu Rev Microbiol*, vol. 49, pp. 711–45, 1995.

[24] D. Boyer, W. Mather, O. Mondragon-Palomino, S. Orozco-Fuentes, T. Danino, J. Hasty, and L. S. Tsimring, “Buckling instability in ordered bacterial colonies,” *Phys Biol*, vol. 8, no. 2, p. 026008, 2011.

[25] A. Siryaporn, M. K. Kim, Y. Shen, H. A. Stone, and Z. Gitai, “Colonization, competition, and dispersal of pathogens in fluid flow networks,” *Curr Biol*, vol. 25, no. 9, pp. 1201–7, 2015.

[26] S. Lecuyer, R. Rusconi, Y. Shen, A. Forsyth, H. Vlamakis, R. Kolter, and H. A. Stone, “Shear stress increases the residence time of adhesion of pseudomonas aeruginosa,” *Biophys J*, vol. 100, no. 2, pp. 341–50, 2011.

[27] W. E. Thomas, L. M. Nilsson, M. Forero, E. V. Sokurenko, and V. Vogel, “Shear-dependent ‘stick-and-roll’ adhesion of type 1 fimbriated escherichia coli,” *Mol Microbiol*, vol. 53, no. 5, pp. 1545–1557, 2004.

[28] W. E. Thomas, V. Vogel, and E. Sokurenko, “Biophysics of catch bonds,” *Annu Rev Biophys*, vol. 37, no. 1, pp. 399–416, 2008.

[29] A. Persat, H. A. Stone, and Z. Gitai, “The curved shape of caulobacter crescentus enhances surface colonization in flow,” *Nat Commun*, vol. 5, p. 3824, 2014.

[30] L. Hamouche, S. Laalami, A. Daerr, S. Song, I. Holland, S. Séror, K. Hamze, and H. Putzer, “Bacillus subtilis swarmer cells lead the swarm, multiply, and generate a trail of quiescent descendants,” *Mbio*, vol. 8, no. 1, pp. e02102–16, 2017.

[31] M. Pearson, D. Rasko, S. Smith, and H. Mobley, "Transcriptome of swarming proteus mirabilis," *Infect Immun*, vol. 78, no. 6, pp. 2834–2845, 2010.

[32] C. Armbruster and H. Mobley, "Merging mythology and morphology: the multifaceted lifestyle of proteus mirabilis," *Nat Rev Microbiol*, vol. 10, no. 11, pp. 743–754, 2012.

[33] H. Berg, "Swarming motility: It better be wet," *Curr Biol*, vol. 15, no. 15, pp. R599–R600, 2005.

[34] M. Trejo, C. Douarche, V. Bailleux, C. Poulard, S. Mariot, C. Regeard, and E. Raspaud, "Elasticity and wrinkled morphology of bacillus subtilis pellicles," *Proc Natl Acad Sci U S A*, vol. 110, no. 6, pp. 2011–6, 2013.

[35] M. Asally, M. Kittisopikul, P. Rue, Y. Du, Z. Hu, T. Cagatay, A. B. Robinson, H. Lu, J. Garcia-Ojalvo, and G. M. Suel, "Localized cell death focuses mechanical forces during 3d patterning in a biofilm," *Proc Natl Acad Sci U S A*, vol. 109, no. 46, pp. 18891–6, 2012.

[36] R. Rusconi, S. Lecuyer, L. Guglielmini, and H. A. Stone, "Laminar flow around corners triggers the formation of biofilm streamers," *J R Soc Interface*, vol. 7, no. 50, pp. 1293–9, 2010.

[37] P. Stoodley, R. Cargo, C. J. Rupp, S. Wilson, and I. Klapper, "Biofilm material properties as related to shear-induced deformation and detachment phenomena," *J Ind Microbiol Biotechnol*, vol. 29, no. 6, pp. 361–7, 2002.

[38] G. O'Toole, H. B. Kaplan, and R. Kolter, "Biofilm formation as microbial development," *Annu Rev Microbiol*, vol. 54, pp. 49–79, 2000.

[39] D. R. Zusman, A. E. Scott, Z. Yang, and J. R. Kirby, "Chemosensory pathways, motility and development in myxococcus xanthus," *Nat Rev Microbiol*, vol. 5, no. 11, pp. 862–72, 2007.

[40] D. E. Whitworth and A. S. for Microbiology., *Myxobacteria : multicellularity and differentiation*. Washington, DC: ASM Press, 2008.

[41] E. M. Mauriello, T. Mignot, Z. Yang, and D. R. Zusman, "Gliding motility revisited: how do the myxobacteria move without flagella?," *Microbiol Mol Biol Rev*, vol. 74, no. 2, pp. 229–49, 2010.

[42] Y. Zhang, A. Ducret, J. Shaevitz, and T. Mignot, "From individual cell motility to collective behaviors: insights from a prokaryote, myxococcus xanthus," *FEMS Microbiol Rev*, vol. 36, no. 1, pp. 149–64, 2012.

[43] B. Nan and D. R. Zusman, "Uncovering the mystery of gliding motility in the myxobacteria," *Annu Rev Genet*, vol. 45, pp. 21–39, 2011.

[44] H. Zhang, Z. Vaksman, D. B. Litwin, P. Shi, H. B. Kaplan, and O. A. Igoshin, "The mechanistic basis of myxococcus xanthus rippling behavior and its physiological role during predation," *PLoS Comput Biol*, vol. 8, no. 9, p. e1002715, 2012.

[45] D. Kaiser, "Coupling cell movement to multicellular development in myxobacteria," *Nat Rev Microbiol*, vol. 1, no. 1, pp. 45–54, 2003.

[46] H. Reichenbach, "The ecology of the myxobacteria," *Environmental Microbiology*, vol. 1, no. 1, pp. 15–21, 1999.

[47] L. Shimkets, M. Dworkin, and H. Reichenbach, "The myxobacteria," *The prokaryotes*, 2006.

[48] M. Dworkin, "Nutritional requirements for vegetative growth of myxococcus xanthus," *Journal of Bacteriology*, 1962.

[49] D. Kaiser, "Bacterial swarming: a re-examination of cell-movement patterns," *Curr Biol*, vol. 17, no. 14, pp. R561–70, 2007.

[50] A. Koch, “Unidirectional movement of flares of cells of myxococcus xanthus,” *Crit Rev Microbiol*, vol. 32, no. 2, pp. 87–90, 2006.

[51] J. E. Berleman, T. Chumley, P. Cheung, and J. R. Kirby, “Rippling is a predatory behavior in myxococcus xanthus,” *J Bacteriol*, vol. 188, no. 16, pp. 5888–95, 2006.

[52] J. E. Berleman, J. Scott, T. Chumley, and J. R. Kirby, “Predataxis behavior in myxococcus xanthus,” *Proc Natl Acad Sci U S A*, vol. 105, no. 44, pp. 17127–32, 2008.

[53] R. Welch and D. Kaiser, “Cell behavior in traveling wave patterns of myxobacteria,” *Proc Natl Acad Sci U S A*, vol. 98, no. 26, pp. 14907–12, 2001.

[54] A. Stevens and S. L, “Making waves: pattern formation by a cell-surface-associated signal,” *Trends in microbiology*, 2005.

[55] B. Sager, “Propagation of traveling waves in excitable media,” *Genes and Development*, 1996.

[56] L. Shimkets and T. Seale, “Fruiting-body formation and myxospore differentiation and germination in mxyococcus xanthus viewed by scanning electron microscopy.,” *Journal of bacteriology*, 1975.

[57] L. Jelsbak and S. L, “Pattern formation: fruiting body morphogenesis in myxococcus xanthus,” *Current opinion in microbiology*, 2000.

[58] D. Kaiser, “Myxococcus-from single-cell polarity to complex multicellular patterns,” *Annu Rev Genet*, vol. 42, pp. 109–30, 2008.

[59] J. Hodgkin and D. Kaiser, “Cell-to-cell stimulation of movement in nonmotile mutants of myxococcus,” *Proc Natl Acad Sci U S A*, 1977.

[60] A. Hodgkin and A. D. Kaiser, “Genetics of gliding motility in myxococcus xanthus (myxobacterales): two gene systems control movement,” *Mol. Gen. Genet.*, vol. 171, pp. 177–191, 1979.

[61] D. Kaiser, “Social gliding is correlated with the presence of pili in myxococcus xanthus,” *Proc Natl Acad Sci U S A*, 1979.

[62] J. Hodgkin and D. Kaiser, “Genetics of gliding motility in myxococcus xanthus (Myxobacterales): genes controlling movement of single cells,” *Molecular and General Genetics MGG*, 1979.

[63] D. Kaiser and C. Crosby, “Cell movement and its coordination in swarms of myxococcus xanthus,” *Cell Motility*, vol. 3, no. 3, pp. 227–245, 1983.

[64] W. Shi and D. R. Zusman, “The two motility systems of myxococcus xanthus show different selective advantages on various surfaces,” *Proc Natl Acad Sci U S A*, vol. 90, no. 8, pp. 3378–82, 1993.

[65] B. Nan, M. Mark J., J. Chen, D. Zusman, and G. Oster, “Bacteria that glide with helical tracks,” *Curr Biol*, vol. 24, no. 4, pp. R169–R173, 2014.

[66] S. T. Islam and T. Mignot, “The mysterious nature of bacterial surface (gliding) motility: A focal adhesion-based mechanism in myxococcus xanthus,” *Semin Cell Dev Biol.*, vol. 46, pp. 143–154, 2015.

[67] L. M. Faure, J. B. Fiche, L. Espinosa, A. Ducret, V. Anantharaman, J. Luciano, S. Lhospice, S. T. Islam, J. Tréguier, M. Sotes, E. Kuru, M. S. Van Nieuwenhze, Y. V. Brun, O. Théodoly, L. Aravind, M. Nollmann, and T. Mignot, “The mechanism of force transmission at bacterial focal adhesion complexes.,” *Nature*, vol. 539, no. 7630, pp. 530–535, 2016.

[68] D. Kearns, “MICROBIOLOGY: bright insight into bacterial gliding,” *Science*, vol. 315, no. 5813, pp. 773–774, 2007.

[69] B. Nan, J. Chen, J. C. Neu, R. M. Berry, G. Oster, and D. R. Zusman, "Myxobacteria gliding motility requires cytoskeleton rotation powered by proton motive force," *Proc Natl Acad Sci U S A*, vol. 108, no. 6, pp. 2498–503, 2011.

[70] M. Sun, M. Wartel, E. Cascales, J. W. Shaevitz, and T. Mignot, "Motor-driven intracellular transport powers bacterial gliding motility," *Proc Natl Acad Sci U S A*, vol. 108, no. 18, pp. 7559–64, 2011.

[71] C. Wolgemuth, E. Hoiczyk, D. Kaiser, and G. Oster, "How myxobacteria glide," *Current Biology*, 2002.

[72] H. Sun, Z. Yang, and W. Shi, "Effect of cellular filamentation on adventurous and social gliding motility of myxococcus xanthus," *Proc Natl Acad Sci U S A*, vol. 96, no. 26, pp. 15178–83, 1999.

[73] O. Sliusarenko, D. R. Zusman, and G. Oster, "Aggregation during fruiting body formation in myxococcus xanthus is driven by reducing cell movement," *J Bacteriol*, vol. 189, no. 2, pp. 611–9, 2007.

[74] T. Mignot, J. W. Shaevitz, P. L. Hartzell, and D. R. Zusman, "Evidence that focal adhesion complexes power bacterial gliding motility," *Science*, vol. 315, no. 5813, pp. 853–6, 2007.

[75] W. Shi and R. Lux, "Focal adhesion: getting a grasp on myxobacterial gliding," *Nat Chem Biol*, vol. 3, no. 4, pp. 205–206, 2007.

[76] M. J. McBride, "Bacterial gliding motility: multiple mechanisms for cell movement over surfaces," *Annu Rev Microbiol*, vol. 55, pp. 49–75, 2001.

[77] D. Zhu, Y. Zhang, P. P. Lam, S. Dolai, Y. Liu, E. P. Cai, D. Choi, S. A. Schroer, Y. Kang, E. M. Allister, T. Qin, M. B. Wheeler, C. C. Wang, W. J. Hong, M. Woo, and H. Y.

Gaisano, “Dual role of vamp8 in regulating insulin exocytosis and islet beta cell growth,” *Cell Metab*, vol. 16, no. 2, pp. 238–49, 2012.

[78] F. Li, S. D. Redick, H. P. Erickson, and V. T. Moy, “Force measurements of the alpha5beta1 integrin-fibronectin interaction,” *Biophys J*, vol. 84, no. 2 Pt 1, pp. 1252–62, 2003.

[79] M. Bowden and H. Kaplan, “The myxococcus xanthus lipopolysaccharide o-antigen is required for social motility and multicellular development,” *Molecular microbiology*, 1998.

[80] A. Lu, K. Cho, W. Black, X. Duan, and R. Lux, “Exopolysaccharide biosynthesis genes required for social motility in myxococcus xanthus,” *Molecular Microbiology*, 2005.

[81] D. Kaiser, “Bacterial motility: How do pili pull?,” *Current Biology*, 2000.

[82] D. Wall and D. Kaiser, “Type IV pili and cell motility,” *Mol Microbiol*, vol. 32, no. 1, pp. 01–10, 1999.

[83] P. Patra, K. Kissoon, I. Cornejo, H. B. Kaplan, and O. A. Igoshin, “Colony expansion of socially motile myxococcus xanthus cells is driven by growth, motility, and exopolysaccharide production,” *PLoS Comput Biol*, vol. 12, no. 6, p. e1005010, 2016.

[84] B. Blackhart and D. Zusman, “” frizzy” genes of myxococcus xanthus are involved in control of frequency of reversal of gliding motility,” *Proc Natl Acad Sci U S A*, 1985.

[85] D. Zusman, “” frizzy” mutants: a new class of aggregation-defective developmental mutants of myxococcus xanthus.,” *Journal of bacteriology*, 1982.

[86] B. Blackhart and D. Zusman, “Analysis of the products of the myxococcus xanthus frz genes.,” *Journal of bacteriology*, 1986.

[87] M. MJ and D. Zusman, “Behavioral analysis of single cells of myxococcus xanthus in response to prey cells of escherichia coli,” *FEMS microbiology letters*, 1996.

[88] O. A. Igoshin, A. Mogilner, R. D. Welch, D. Kaiser, and G. Oster, "Pattern formation and traveling waves in myxobacteria: theory and modeling," *Proc Natl Acad Sci U S A*, vol. 98, no. 26, pp. 14913–8, 2001.

[89] H. Zhang, S. Angus, M. Tran, C. Xie, O. A. Igoshin, and R. D. Welch, "Quantifying aggregation dynamics during myxococcus xanthus development," *Journal of Bacteriology*, vol. 193, no. 19, pp. 5164–70, 2011.

[90] C. Wolgemuth, E. Hoiczyk, D. Kaiser, and G. Oster, "How myxobacteria glide," *Curr Biol*, vol. 12, no. 5, pp. 369–77, 2002.

[91] R. P. Burchard, "Trail following by gliding bacteria," *J Bacteriol*, vol. 152, no. 1, pp. 495–501, 1982.

[92] D. Kaiser, "Signaling in myxobacteria," *Annu Rev Microbiol*, vol. 58, pp. 75–98, 2004.

[93] D. Bretl and J. Kirby, "Molecular mechanisms of signaling in myxococcus xanthus development," *Journal of Molecular Biology*, 2016.

[94] B. Sager and D. Kaiser, "Intercellular c-signaling and the traveling waves of myxococcus.," *Genes & Development*, 1994.

[95] A. Konovalova, S. Wegener-Feldbrugge, and L. Sogaard-Andersen, "Two intercellular signals required for fruiting body formation in myxococcus xanthus act sequentially but non-hierarchically," *Mol Microbiol*, vol. 86, no. 1, pp. 65–81, 2012.

[96] L. J. Shimkets, "Intercellular signaling during fruiting-body development of myxococcus xanthus," *Annu Rev Microbiol*, vol. 53, pp. 525–49, 1999.

[97] O. A. Igoshin and G. Oster, "Rippling of myxobacteria," *Math Biosci*, vol. 188, pp. 221–33, 2004.

[98] O. A. Igoshin, R. Welch, D. Kaiser, and G. Oster, "Waves and aggregation patterns in myxobacteria," *Proc Natl Acad Sci U S A*, vol. 101, no. 12, pp. 4256–61, 2004.

[99] O. Sliusarenko, J. Neu, D. R. Zusman, and G. Oster, "Accordion waves in myxococcus xanthus," *Proc Natl Acad Sci U S A*, vol. 103, no. 5, pp. 1534–9, 2006.

[100] O. Sozinova, Y. Jiang, D. Kaiser, and M. Alber, "A three-dimensional model of myxobacterial fruiting-body formation," *Proc Natl Acad Sci U S A*, vol. 103, no. 46, pp. 17255–9, 2006.

[101] Y. Wu, N. Chen, M. Rissler, Y. Jiang, D. Kaiser, and M. Alber, "Ca models of myxobacteria swarming," in *Cellular Automata*, International Conference on Cellular Automata, pp. 192–203, ACRI, Springer, 2006.

[102] Y. L. Wu, Y. Jiang, D. Kaiser, and M. Alber, "Social interactions in myxobacterial swarming," *Plos Computational Biology*, vol. 3, no. 12, pp. 2546–2558, 2007.

[103] Y. Wu, A. D. Kaiser, Y. Jiang, and M. S. Alber, "Periodic reversal of direction allows myxobacteria to swarm," *Proc Natl Acad Sci U S A*, vol. 106, no. 4, pp. 1222–7, 2009.

[104] J. Starruß, T. Bley, L. Søgaard-Andersen, and A. Deutsch, "A new mechanism for collective migration in myxococcus xanthus," *Journal of Statistical Physics*, vol. 128, no. 1, pp. 269–286, 2007.

[105] A. Janulevicius, M. C. van Loosdrecht, A. Simone, and C. Picioreanu, "Cell flexibility affects the alignment of model myxobacteria," *Biophys J*, vol. 99, no. 10, pp. 3129–38, 2010.

[106] A. Janulevicius, M. van Loosdrecht, and C. Picioreanu, "Short-range guiding can result in the formation of circular aggregates in myxobacteria populations," *PLoS Comput Biol*, vol. 11, no. 4, p. e1004213, 2015.

[107] M. Dworkin, "Lingering puzzles about myxobacteria," *Microbe*, vol. 2, no. 1, pp. 18–24, 2007.

[108] V. Schaller, C. Weber, C. Semmrich, E. Frey, and A. Bausch, “Polar patterns of driven filaments,” *Nature*, vol. 467, no. 7311, pp. 73–77, 2010.

[109] V. Schaller, C. Weber, and B. Hammerich, “Frozen steady states in active systems,” *Proc Natl Acad Sci U S A*, 2011.

[110] Y. Sumino, K. Nagai, Y. Shitaka, D. Tanaka, K. Yoshikawa, H. Chaté, and K. Oiwa, “Large-scale vortex lattice emerging from collectively moving microtubules,” *Nature*, vol. 483, no. 7390, pp. 448–452, 2012.

[111] S. Hu, K. Dasbiswas, Z. Guo, Y. Tee, V. Thiagarajan, P. Hersen, T. Chew, S. A. Safran, Z. Ronen, and A. D. Bershadsky, “Long-range self-organization of cytoskeletal myosin II filament stacks,” *Nat Cell Biol*, vol. 19, no. 2, pp. 133–141, 2017.

[112] M. A. Grant, B. Wacław, R. J. Allen, and P. Cicuta, “The role of mechanical forces in the planar-to-bulk transition in growing escherichia coli microcolonies,” *J. Royal Soc Interface*, vol. 11, no. 97, p. 20140400, 2014.

[113] D. Volfson, S. Cookson, J. Hasty, and L. Tsimring, “Biomechanical ordering of dense cell populations,” *Proc National Acad Sci*, vol. 105, no. 40, pp. 15346–15351, 2008.

[114] M. Delarue, J. Hartung, C. Schreck, P. Gniewek, L. Hu, S. Herminghaus, and O. Hallatschek, “Self-driven jamming in growing microbial populations,” *Nat Phys*, vol. 12, no. 8, pp. 762–766, 2016.

[115] W. Smith, Y. Davit, J. Osborne, W. Kim, K. Foster, and P. Joe, “Cell morphology drives spatial patterning in microbial communities,” *Proc National Acad Sci*, vol. 114, no. 3, pp. E280–E286, 2017.

[116] J. P. Jahnke, J. L. Terrell, A. M. Smith, X. Cheng, and S. D. N, “Influences of adhesion variability on the ”Living” dynamics of filamentous bacteria in microfluidic channels.,” *Molecules*, p. 985, 2016.

[117] H. Wioland, F. Woodhouse, J. Dunkel, J. Kessler, and R. Goldstein, "Confinement stabilizes a bacterial suspension into a spiral vortex," *Phys Rev Lett*, vol. 110, no. 26, p. 268102, 2013.

[118] H. Wioland, E. Lushi, and R. Goldstein, "Directed collective motion of bacteria under channel confinement," *New J Phys*, vol. 18, no. 7, p. 075002, 2016.

[119] E. Lushi and H. Wioland, "Fluid flows created by swimming bacteria drive self-organization in confined suspensions," *Proc Natl Acad Sci U S A*, 2014.

[120] A. Creppy, F. Plouraboué, O. Praud, X. Druart, S. Cazin, H. Yu, and P. Degond, "Symmetry-breaking phase transitions in highly concentrated semen," *J R Soc Interface*, vol. 13, no. 123, p. 20160575, 2016.

[121] A. Doostmohammadi, M. Adamer, S. Thampi, and J. Yeomans, "Stabilization of active matter by flow-vortex lattices and defect ordering," *Nat Commun*, vol. 7, p. 10557, 2016.

[122] F. Farrell, O. Hallatschek, D. Marenduzzo, and B. Waclaw, "Mechanically driven growth of quasi-two-dimensional microbial colonies," *Physical review letters*, 2013.

[123] F. F. Farrell, M. Gralka, O. Hallatschek, and B. Waclaw, "Mechanical interactions in bacterial colonies and the surfing probability of beneficial mutations," *arXiv*, 2017.

[124] A. Czirók, B. E, I. Cohen, and T. Vicsek, "Formation of complex bacterial colonies via self-generated vortices," *Physical Review E*, 1996.

[125] T. Rudge, F. Federici, P. Steiner, A. Kan, and J. Haseloff, "Cell Polarity-Driven instability generates Self-Organized, fractal patterning of cell layers," *Acs Synthetic Biology*, vol. 2, no. 12, pp. 705–714, 2013.

[126] W. Ngamsaad and S. Suantai, "Mechanically-driven spreading of bacterial populations," *Commun Nonlinear Sci*, vol. 35, pp. 88–96, 2016.

[127] R. Leonardo, “Active colloids: Controlled collective motions,” *Nat Mater*, vol. 15, no. 10, pp. 1057–1058, 2016.

[128] C. Bechinger, D. R. Leonardo, and H. Löwen, “Active particles in complex and crowded environments,” *Reviews of Modern Physics*, 2016.

[129] C. M. Marchetti, J. Joanny, S. Ramaswamy, T. Liverpool, J. Prost, M. Rao, and A. R. Simha, “Hydrodynamics of soft active matter,” *Reviews of Modern Physics*, vol. 85, no. 3, p. 1143, 2013.

[130] A. Doostmohammadi, S. Thampi, and J. Yeomans, “Defect-mediated morphologies in growing cell colonies,” *Physical Review Letters*, 2016.

[131] G. Duclos, C. Erlenkämper, J. Joanny, and P. Silberzan, “Topological defects in confined populations of spindle-shaped cells,” *Nat Phys*, vol. 13, no. 1, pp. 58–62, 2016.

[132] T. Vicsek and A. Zafeiris, “Collective motion,” *Physics Reports*, 2012.

[133] P. Ghosh, J. Mondal, and B. E, “Mechanically-driven phase separation in a growing bacterial colony,” *Proc Natl Acad Sci U S A*, 2015.

[134] M. Hagan and A. Baskaran, “Emergent self-organization in active materials,” *Current opinion in cell biology*, 2016.

[135] S. Henkes, Y. Fily, and M. Marchetti, “Active jamming: Self-propelled soft particles at high density,” *Physical Review E*, 2011.

[136] A. Baskaran and M. Marchetti, “Hydrodynamics of self-propelled hard rods,” *Physical Review E*, 2008.

[137] C. D. Nadell, V. Bucci, K. Drescher, S. A. Levin, B. L. Bassler, and J. B. Xavier, “Cutting through the complexity of cell collectives,” *Proc. of The Royal Soceity B*, vol. 280, no. 1755, p. 20122770, 2013.

[138] C. Nadell, K. Drescher, and K. Foster, “Spatial structure, cooperation and competition in biofilms,” *Nat Rev Microbiol*, vol. 14, no. 9, pp. 589–600, 2016.

[139] U. Wilensky and W. Rand, *An introduction to agent-based modeling : modeling natural, social, and engineered complex systems with NetLogo*. Cambridge, Massachusetts ; London, England: The MIT Press, 2015.

[140] E. Bonabeau, “Agent-based modeling: Methods and techniques for simulating human systems,” *Proc Natl Acad Sci U S A*, vol. 99, no. suppl 3, pp. 7280–7287, 2002.

[141] M. Niazi and A. Hussain, “Agent-based tools for modeling and simulation of self-organization in peer-to-peer, ad hoc, and other complex networks,” *IEEE Communications Magazine*, vol. 47, pp. 166–173, Mar. 2009.

[142] S. R. McCandlish, A. Baskaran, and M. F. Hagan, “Spontaneous segregation of self-propelled particles with different motilities,” *Soft Matter*, vol. 8, no. 8, pp. 2527–2534, 2012.

[143] Y. Yang, V. Marceau, and G. Gompper, “Swarm behavior of self-propelled rods and swimming flagella,” *Phys Rev E Stat Nonlin Soft Matter Phys*, vol. 82, no. 3 Pt 1, p. 031904, 2010.

[144] P. Cao and D. Wall, “Circular cell aggregates experimental videos.” Unpublished results, 2016.

[145] R. Balagam, D. B. Litwin, F. Czerwinski, M. Sun, H. B. Kaplan, J. W. Shaevitz, and O. A. Igoshin, “Myxococcus xanthus gliding motors are elastically coupled to the substrate as predicted by the focal adhesion model of gliding motility,” *PLoS Comput Biol*, vol. 10, no. 5, p. e1003619, 2014.

[146] E. Hoiczyk, “Gliding motility in cyanobacterial: observations and possible explanations,” *Arch Microbiol*, vol. 174, no. 1-2, pp. 11–7, 2000.

[147] B. Nan, E. M. Mauriello, I. Sun, A. Wong, and D. R. Zusman, "A multi-protein complex from myxococcus xanthus required for bacterial gliding motility," *Molecular microbiology*, vol. 76, no. 6, pp. 1539–1554, 2010.

[148] M. Chen, E. Cai, J. Huang, P. Yu, and K. Li, "Prognostic value of vascular endothelial growth factor expression in patients with esophageal cancer: a systematic review and meta-analysis," *Cancer Epidemiol Biomarkers Prev*, vol. 21, no. 7, pp. 1126–34, 2012.

[149] A. Chen and V. T. Moy, "Cross-linking of cell surface receptors enhances cooperativity of molecular adhesion," *Biophys J*, vol. 78, no. 6, pp. 2814–20, 2000.

[150] A. J. Merz, M. So, and M. P. Sheetz, "Pilus retraction powers bacterial twitching motility," *Nature*, vol. 407, no. 6800, pp. 98–102, 2000.

[151] M. Clausen, V. Jakovljevic, L. Sogaard-Andersen, and B. Maier, "High-force generation is a conserved property of type iv pilus systems," *J Bacteriol*, vol. 191, no. 14, pp. 4633–8, 2009.

[152] A. Ducret, M. P. Valignat, F. Mouhamar, T. Mignot, and O. Theodoly, "Wet-surface-enhanced ellipsometric contrast microscopy identifies slime as a major adhesion factor during bacterial surface motility," *Proc Natl Acad Sci U S A*, vol. 109, no. 25, pp. 10036–41, 2012.

[153] M. E. Gracheva and H. G. Othmer, "A continuum model of motility in ameboid cells," *Bull Math Biol*, vol. 66, no. 1, pp. 167–93, 2004.

[154] M. Abercrombie, J. E. Heaysman, and S. M. Pegrum, "The locomotion of fibroblasts in culture. 3. movements of particles on the dorsal surface of the leading lamella," *Exp Cell Res*, vol. 62, no. 2, pp. 389–98, 1970.

[155] C. G. Galbraith and M. P. Sheetz, "A micromachined device provides a new bend on fibroblast traction forces," *Proc Natl Acad Sci U S A*, vol. 94, no. 17, pp. 9114–8, 1997.

[156] N. Ofer, A. Mogilner, and K. Keren, "Actin disassembly clock determines shape and speed of lamellipodial fragments," *Proc Natl Acad Sci U S A*, vol. 108, no. 51, pp. 20394–9, 2011.

[157] D. Nakane, K. Sato, H. Wada, M. J. McBride, and K. Nakayama, "Helical flow of surface protein required for bacterial gliding motility," *Proc Natl Acad Sci U S A*, vol. 110, no. 27, pp. 11145–50, 2013.

[158] S. Agarwal, D. W. Hunnicutt, and M. J. McBride, "Cloning and characterization of the flavobacterium johnsoniae (cytophaga johnsonae) gliding motility gene, glda," *Proc Natl Acad Sci U S A*, vol. 94, no. 22, pp. 12139–44, 1997.

[159] C. W. Wolgemuth, "Force and flexibility of flailing myxobacteria," *Biophys J*, vol. 89, no. 2, pp. 945–50, 2005.

[160] C. W. Harvey, F. Morcos, C. R. Sweet, D. Kaiser, S. Chatterjee, X. Liu, D. Z. Chen, and M. Alber, "Study of elastic collisions of myxococcus xanthus in swarms," *Phys Biol*, vol. 8, no. 2, p. 026016, 2011.

[161] A. E. Pelling, Y. Li, S. E. Cross, S. Castaneda, W. Shi, and J. K. Gimzewski, "Self-organized and highly ordered domain structures within swarms of myxococcus xanthus," *Cell Motil Cytoskeleton*, vol. 63, no. 3, pp. 141–8, 2006.

[162] R. Balagam and O. A. Igoshin, "Mechanism for collective cell alignment in myxococcus xanthus bacteria," *PLoS Comput Biol*, vol. 11, no. 8, p. e1004474, 2015.

[163] J. M. Kuner and D. Kaiser, "Fruiting body morphogenesis in submerged cultures of myxococcus xanthus," *J Bacteriol*, vol. 151, no. 1, pp. 458–61, 1982.

[164] D. Wall and D. Kaiser, "Alignment enhances the cell-to-cell transfer of pilus phenotype," *Proc Natl Acad Sci U S A*, vol. 95, no. 6, pp. 3054–3058, 1998.

[165] K. A. O'Connor and D. R. Zusman, "Patterns of cellular interactions during fruiting-body formation in myxococcus xanthus," *J Bacteriol*, vol. 171, no. 11, pp. 6013–24, 1989.

[166] S. K. Kim and D. Kaiser, "Cell alignment required in differentiation of myxococcus-xanthus," *Science*, vol. 249, no. 4971, pp. 926–928, 1990.

[167] J. Starruss, F. Peruani, V. Jakovljevic, L. Sogaard-Andersen, A. Deutsch, and M. Bar, "Pattern-formation mechanisms in motility mutants of myxococcus xanthus," *Interface Focus*, vol. 2, no. 6, pp. 774–785, 2012.

[168] S. Thutupalli, M. Sun, F. Bunyak, K. Palaniappan, and J. W. Shaevitz, "Directional reversals enable myxococcus xanthus cells to produce collective one-dimensional streams during fruiting-body formation," *Journal of The Royal Society Interface*, vol. 12, no. 109, 2015.

[169] F. Peruani, J. Starruss, V. Jakovljevic, L. Sogaard-Andersen, A. Deutsch, and M. Bar, "Collective motion and nonequilibrium cluster formation in colonies of gliding bacteria," *Phys Rev Lett*, vol. 108, no. 9, p. 098102, 2012.

[170] C. W. Harvey, M. Alber, L. S. Tsimring, and I. S. Aranson, "Continuum modeling of clustering of myxobacteria," *New J Phys*, vol. 15, 2013.

[171] F. Peruani, L. Schimansky-Geier, and M. Bar, "Cluster dynamics and cluster size distributions in systems of self-propelled particles," *European Physical Journal-Special Topics*, vol. 191, no. 1, pp. 173–185, 2010.

[172] E. Catto, "Box2d - a 2d physics engine for games," 2012.

[173] F. Ginelli, F. Peruani, M. Bar, and H. Chate, "Large-scale collective properties of self-propelled rods," *Physical Review Letters*, vol. 104, no. 18, p. 184502, 2010.

[174] L. J. Shimkets, “Correlation of energy-dependent cell cohesion with social motility in myxococcus xanthus,” *J Bacteriol*, vol. 166, no. 3, pp. 837–41, 1986.

[175] I. Buttinoni, J. Bialke, F. Kummel, H. Lowen, C. Bechinger, and T. Speck, “Dynamical clustering and phase separation in suspensions of self-propelled colloidal particles,” *Physical Review Letters*, vol. 110, no. 23, p. 238301, 2013.

[176] R. M. Behmlander and M. Dworkin, “Biochemical and structural analyses of the extracellular matrix fibrils of myxococcus xanthus,” *J Bacteriol*, vol. 176, no. 20, pp. 6295–303, 1994.

[177] K. Zhao, B. S. Tseng, B. Beckerman, F. Jin, M. L. Gibiansky, J. J. Harrison, E. Luijten, M. R. Parsek, and G. C. Wong, “Psl trails guide exploration and microcolony formation in pseudomonas aeruginosa biofilms,” *Nature*, vol. 497, no. 7449, pp. 388–91, 2013.

[178] H. Reichenbach, H. Heunert, and H. Kuczka, “Schwarmentwicklung und morphogenese bei myxobakterien - archangium, myxococcus,chondrococcus,chondromyces,” 1965. Film 893.

[179] H. Reichenbach, “Ber. dtsch. bot. ges.,” 1965.

[180] P. Cao, A. Dey, C. Vassallo, and D. Wall, “How myxobacteria cooperate,” *Journal of molecular biology*, 2015.

[181] D. T. Pathak, X. Wei, A. Bucuvalas, D. H. Haft, D. L. Gerloff, and D. Wall, “Cell contact-dependent outer membrane exchange in myxobacteria: Genetic determinants and mechanism,” *PLoS Genet*, vol. 8, no. 4, p. e1002626, 2012.

[182] D. Wall, “Kin recognition in bacteria,” *Annu. Rev. Microbiol.*, vol. 70, no. 1, pp. 143–160, 2016.

[183] B. Jakobczak, D. Keilberg, K. Wuichet, and S. Lotte, "Contact- and protein Transfer-Dependent stimulation of assembly of the gliding motility machinery in myxococcus xanthus," *PLoS Genetics*, vol. 11, no. 7, p. e1005341, 2015.

[184] D. Wall, "Molecular recognition in myxobacterial outer membrane exchange: functional, social and evolutionary implications," *Mol. Microbiol.*, vol. 91, no. 2, pp. 209–20, 2014.

[185] G. Vasquez, F. Qualls, and D. White, "Morphogenesis of stigmatella aurantiaca fruiting bodies.," *Journal of bacteriology*, 1985.

[186] C. Xie, H. Zhang, L. J. Shimkets, and O. A. Igoshin, "Statistical image analysis reveals features affecting fates of myxococcus xanthus developmental aggregates," *Proc Natl Acad Sci U S A*, vol. 108, no. 14, pp. 5915–20, 2011.

[187] C. Cotter, O. A. Igoshin, H. B. Schuttler, and L. J. Shimkets, "Quantification of cell behaviors, robustness, and compensatory mechanism during m. xanthus fruiting body formation," *submitted*, 2016.

[188] L. Jelsbak and S. Lotte, "Cell behavior and cell–cell communication during fruiting body morphogenesis in myxococcus xanthus," *J Microbiol Meth*, vol. 55, no. 3, pp. 829–839, 2003.

[189] B. Sager and D. Kaiser, "Two cell-density domains within the myxococcus xanthus fruiting body.," *Proc Natl Acad Sci U S A*, vol. 90, no. 8, pp. 3690–3694, 1993.

[190] W. Shi, F. Ngok, and D. Zusman, "Cell density regulates cellular reversal frequency in myxococcus xanthus.," *Proc Natl Acad Sci U S A*, vol. 93, no. 9, pp. 4142–4146, 1996.

[191] L. Jelsbak and S. Lotte, "Pattern formation by a cell surface-associated morphogen in myxococcus xanthus," *Proc National Acad Sci*, vol. 99, no. 4, pp. 2032–2037, 2002.

[192] S. L and D. Kaiser, “C factor, a cell-surface-associated intercellular signaling protein, stimulates the cytoplasmic frz signal transduction system in myxococcus xanthus.,” *Proc Natl Acad Sci U S A*, vol. 93, no. 7, pp. 2675–2679, 1996.

[193] S. Lotte, “Cell polarity, intercellular signalling and morphogenetic cell movements in myxococcus xanthus,” *Curr Opin Microbiol*, vol. 7, no. 6, pp. 587–593, 2004.

[194] D. Astling, J. Lee, and D. Zusman, “Differential effects of chemoreceptor methylation-domain mutations on swarming and development in the social bacterium myxococcus xanthus,” *Molecular microbiology*, 2006.

[195] V. Bustamante, M. Irma, H. Vlamakis, and D. Zusman, “Analysis of the frz signal transduction system of myxococcus xanthus shows the importance of the conserved c-terminal region of the cytoplasmic chemoreceptor FrzCD in sensing signals,” *Mol Microbiol*, vol. 53, no. 5, pp. 1501–1513, 2004.

[196] Q. Xu, W. Black, and E. Mauriello, “Chemotaxis mediated by NarX–FrzCD chimeras and nonadapting repellent responses in myxococcus xanthus,” *Molecular Microbiology*, 2007.

[197] A. Scott, E. Simon, S. Park, and P. Andrews, “Site-specific receptor methylation of FrzCD in myxococcus xanthus is controlled by a tetra-trico peptide repeat (TPR) containing regulatory domain of the FrzF methyltransferase,” *Molecular Microbiology*, 2008.

[198] Y. Li, V. Bustamante, R. Lux, D. Zusman, and W. Shi, “Divergent regulatory pathways control a and s motility in myxococcus xanthus through FrzE, a CheA-CheY fusion protein,” *Journal of Bacteriology*, 2005.

[199] J. E. Berleman, J. J. Vicente, A. E. Davis, S. Y. Jiang, Y. Seo, and D. R. Zusman, “FrzS regulates social motility in myxococcus xanthus by controlling exopolysaccharide production,” *PloS one*, vol. 6, no. 8, p. e23920, 2011.

[200] C. W. Harvey, H. Du, Z. Xu, D. Kaiser, I. Aranson, and M. Alber, "Interconnected cavernous structure of bacterial fruiting bodies," *PLoS Comput Biol*, vol. 8, no. 12, p. e1002850, 2012.

[201] E. Holmes, "Are diffusion models too simple? a comparison with telegraph models of invasion," *The American Naturalist*, 1993.

[202] A. Gallegos, B. Mazzag, and A. Mogilner, "Two continuum models for the spreading of myxobacteria swarms," *Bull Math Biol*, vol. 68, no. 4, pp. 837–61, 2006.

[203] J. Monod, "The growth of bacterial cultures," *Annual Reviews in Microbiology*, 1949.

[204] Y. Deng, P. Coen, M. Sun, and J. W. Shaevitz, "Efficient multiple object tracking using mutually repulsive active membranes," *PLoS One*, vol. 8, no. 6, p. e65769, 2013.

[205] W. Hastings, "Monte carlo sampling methods using markov chains and their applications," *Biometrika*, 1970.

[206] D. P. Landau and K. Binder, *A Guide to Monte Carlo Simulations in Statistical Physics*. Cambridge University Press, 2005.

[207] R. Yu and D. Kaiser, "Gliding motility and polarized slime secretion," *Mol Microbiol*, vol. 63, no. 2, pp. 454–67, 2007.

[208] A. M. Spormann and A. D. Kaiser, "Gliding movements in myxococcus xanthus," *J Bacteriol*, vol. 177, no. 20, pp. 5846–52, 1995.

[209] M. Hendrata, Z. Yang, R. Lux, and W. Shi, "Experimentally guided computational model discovers important elements for social behavior in myxobacteria," *Plos One*, vol. 6, no. 7, p. e22169, 2011.

[210] C. A. Schneider, W. S. Rasband, and K. W. Eliceiri, "Nih image to imagej: 25 years of image analysis," *Nat Methods*, vol. 9, no. 7, pp. 671–5, 2012.

[211] E. Meijering, O. Dzyubachyk, and I. Smal, "Methods for cell and particle tracking," *Methods Enzymol*, vol. 504, pp. 183–200, 2012.

[212] S. Wang, H. Arellano-Santoyo, P. A. Combs, and J. W. Shaevitz, "Actin-like cytoskeleton filaments contribute to cell mechanics in bacteria," *Proc Natl Acad Sci U S A*, vol. 107, no. 20, pp. 9182–5, 2010.

[213] F. Czerwinski, A. C. Richardson, and L. B. Oddershede, "Quantifying noise in optical tweezers by allan variance," *Opt Express*, vol. 17, no. 15, pp. 13255–69, 2009.

[214] A. C. Richardson, S. Reihani, and L. B. Oddershede, "Non-harmonic potential of a single beam optical trap," *Opt. Express*, vol. 16, pp. 15709–15717, 2008.

[215] M. Ester, H.-P. Kriegel, J. Sander, and X. Xu, "A density-based algorithm for discovering clusters in large spatial databases with noise," in *Proceedings of 2nd International Conference on Knowledge Discovery and Data Mining*, 1996.

[216] F. Pedregosa, G. Varoquaux, A. Gramfort, V. Michel, B. Thirion, O. Grisel, M. Blondel, P. Prettenhofer, R. Weiss, V. Dubourg, J. Vanderplas, A. Passos, D. Cournapeau, M. Brucher, M. Perrot, and E. Duchesnay, "Scikit-learn: Machine learning in python," *Journal of Machine Learning Research*, vol. 12, pp. 2825–2830, 2011.

[217] "Liquidfun - java port of box2d; http://google.github.io/liquidfun/."